CONSTRAIN NEUTRON STAR PROPERTIES WITH SπRIT EXPERIMENT

By

Chun Yuen Tsang

A DISSERTATION

Submitted to
Michigan State University
in partial fulfillment of the requirements
for the degree of

Physics – Doctor of Philosophy

2022

**ABSTRACT**

CONSTRAIN NEUTRON STAR PROPERTIES WITH SπRIT EXPERIMENT

By

Chun Yuen Tsang

The study of nuclear matter is an interdisciplinary endeavor that is relevant to both astrophysics and nuclear physics. Astrophysicists need to understand the properties of nuclear matter for neutron stars are made of mostly nuclear material. Properties of nuclear matter is also fundamental to the understanding of nuclear physics. They are critical to our understanding of the existence of nuclei, their composition and also the dynamics of nuclear collisions.

Recent measurements of gravitational waves from binary neutron star mergers open a new channel for physicists to study nuclear matter. Such astronomical observations of neutron stars are sensitive to nuclear matter at high density that is usually inaccessible on earth. One of the ways physicists are able to reach such high density in laboratory is through heavy-ion collision. Transport calculations show that head-on collisions of heavy nuclei at high beam energy compress them momentarily to densities comparable to the interior density of neutron stars.

To study neutron star where number of neutrons far exceeds that of protons, the dependence of nuclear properties on neutron to proton ratio ($N/Z$) needs to be understood. This dependence is quantified as the symmetry energy, which describes the difference in binding energy between pure neutron matter and symmetric matter, matter with equal number of protons and neutrons. Internal neutron star pressure that supports itself from gravitational collapse depends on symmetry energy.

Most of the existing heavy-ion collision data come from collisions of stable isotopes. This limits the range of available $N/Z$ in nuclear experiments. Extending results to a wider range of $N/Z$ is the goal of SπRIT experiment using projectiles provided by the cutting-edge Radioactive Isotope Beam Factory in RIKEN, Japan. SπRIT time projection chamber (TPC) is developed to measure charged pions spectra from the collision of neutron-rich system ($132$Sn + $^{124}$Sn), neutron-poor system ($^{108}$Sn + $^{112}$Sn) and intermediate system ($^{112}$Sn + $^{124}$Sn) at 270 AMeV. By comparing

fragmentation patterns for reactions with different number of neutrons, symmetry energy effects can be isolated. Previous results from the analysis of pion spectra is reviewed. In this work, we focus on light fragments spectra that are also available from the TPC data. The data analysis software, with highlights on correction of some major detector aberrations, is discussed in details. Monte Carlo simulation of the S$\pi$RIT TPC is performed to understand the behavior of S$\pi$RIT data and validate the data analysis procedure.

Bayesian analysis is performed to compare some selected light fragment observables to transport model simulations using Markov-Chain Monte Carlo and Gaussian emulators. These observables are chosen to minimize systematic uncertainty from both the experiment and model. This provides comprehensive constraints on numerous symmetry energy parameters. When previous results from the analysis of pion spectra alone is combined with results from light fragment observables in this analysis, the uncertainty on the slope of symmetry energy is reduced by 39%. Its implication on neutron star is briefly studied to demonstrate the importance of data from rare isotope heavy-ion collisions.

# ACKNOWLEDGEMENTS

Your acknowledgements here.

# TABLE OF CONTENTS

# LIST OF TABLES

# LIST OF FIGURES

# CHAPTER 1

## INTRODUCTION

## 1.1   Nuclear equation of state (EoS)

Unification is a general goal pursued by all physicists. Isaac Newton unified gravity on Earth with the trajectory of celestial objects and James Maxwell unified magnetism and electricity through the famous Maxwell's equations. The beauty of unification is that it ties seemingly unrelated phenomena together with a single description. In the study of nuclear equation of state (EoS) presented in this work, we hope to unify astronomical observations, which is the study of massive celestial objects, with heavy-ion collision measurements, which is the study of tiny invisible nucleus. The masses of interest in these two fields differ by 55 orders of magnitude, and yet they are related in a unify description of nuclear EoS.

The key is to realize that the environment in the interior of neutron star (NS) is similar to that in the core of ordinary nucleus. Ordinary matters we find in our everyday life are supported by the electrostatic repulsion of electrons, but the gravitational pull is too strong for neutron star matter to be supported by electrostatic force. The extreme environment forces electrons and protons to merge and form neutrons. Such homogeneous matter of nucleons is called *nuclear matter* and is supported by nuclear degeneracy pressure due to Pauli exclusion principal. This is similar to nucleus during heavy-ion collision where part of it is being compressed to supersaturation density. Our knowledge on nuclear collisions can be extrapolated to predict properties of NS.

Properties of nuclear matter are described quantitatively by nuclear EoS. It is an equation that relates various state variables such as pressure, volume and internal energy. One of the simplest yet powerful approximation to nuclear EoS is the semi-empirical mass formula (SEMF). It models nucleus as an in-compressible drop of nuclear matter [9] which yields the following formula,

$$E_B = a_V A - a_S A^{2/3} - a_C \frac{Z^2}{A^{1/3}} - a_A \frac{(N-Z)^2}{A} + \delta(N, Z).  \tag{1.1}$$

Here $E_B$ is the binding energy, $Z$ is the number of protons, $N$ is the number of neutrons and $A = N + Z$ is the total number of nucleons. The five terms in SEMF can be understood as follows: The first term with coefficient $a_V$ is called the *volume* term which accounts for the increased interactions due to proportionally increased number of nucleons. The second term with coefficient $a_S$ is called the surface term and is negative to account for the fact that nucleons on the surface have less neighbors to interact with, so overall strength of interaction is reduced. The third term with coefficient $a_C$ is called the Coulomb term which accounts for the Coulomb repulsion between protons. This term resembles Coulomb potential once you realize that average distance between nucleons $\propto A^{1/3}$ and charge of nucleus $\propto Z$. The fourth term with coefficient $a_A$ is called the asymmetry term which arises due to asymmetry in number of protons and neutrons. If the number of protons and neutrons are the same, they share the same Fermi energy. However if there are more neutrons than protons, some neutrons are forced to occupied higher energy level due to Pauli exclusion principal. Although Fermi energy of proton is reduced, the overall internal energy is raised which resulted in a reduction of binding energy. The final term is called the pairing term which is caused by spin-coupling. For the purposes of this thesis, the pairing term will not be discussed.

The SEMF was developed to approximately describe the mass and stability of atomic nucleus. It's agreement with measured binding energies of various nuclei is satisfactory for some best fitted values coefficients [10]. If we naively approximate NS as one giant nucleus with $A \to \infty$, EoS for NS can be written as,

$$\frac{E_B}{A} = E_{is} + E_{iv}\delta^2, \tag{1.2}$$

with $E_{is} = a_V$, $E_{iv} = a_A$ and $\delta = (N - Z)^2/A$. These terms are relabelled to emphasize that the first term is the *isoscalar term* which makes no distinction between protons and neutrons, and the second term is the *isovector term* which accounts for the effects of having an unequal amount of protons and neutrons. Such approximated NS EoS is inaccurate in predicting NS properties because baryon density in ordinary nucleus is different from NS. Baryon density in ordinary

nucleus is roughly $\rho \approx \rho_0 = 0.155\,\mathrm{fm}^{-3}$ where $\rho_0$ is called the *saturation density*. However, density inside a NS changes with depth. NS density is zero on the surface and can be up to multiple times the saturation density at its center. The parameters in SEMF are fitted with data from ordinary nucleus so the equation is only valid for nuclear matter at $\rho \approx \rho_0$. Despite the shortcomings, it is still instructive to see how EoS decomposes into isoscalar and isovector terms.

To overcome the over-simplifications in SEMF, we incorporate density dependence to equation (1.2),

$$E(\rho, \delta) = E_{is}(\rho) + \delta^2 E_{iv}(\rho) + O(\delta^4), \tag{1.3}$$

The isovector term is often denoted as $S(\rho)$ and is sometimes referred to as the *symmetry energy term*. Measurements of collective flow and Kaon production in energetic nucleus-nucleus collisions have constrained $E_{is}$ to densities up to $4.5\rho_0$ [11–13]. Specifically, the symmetric matter constraints on pressure vs. density were determined from the measurements of transverse and elliptical flow from Au + Au collisions over a range of incident energies from 0.3 to 1.2 GeV/u [11]. These constraints were confirmed in an independent analysis of elliptical flow data [14]. Similar constraint from $1.2\rho_0$ to $2.2\rho_0$ was obtained from the Kaon measurements [12, 13]. These heavy-ion constraints are consistent with the Bayesian analyses of the NS mass-radius correlation [15].

This is in stark contrast to constraints on $E_{iv}$ as it is constrained only at densities near or below $\rho_0$. Since NS composed mostly of neutrons, $E_{iv}$ should play a prominent role. Indeed studies found that NS properties is sensitive to $E_{iv}$ at $2\rho_0$ [16]. The purpose of this study is to constrain the $E_{iv}$ at high density using heavy-ion collision. In a medium-energy heavy-ion collision, the colliding part of the nucleus is compressed and experience higher density than $\rho_0$, and when it expands afterward it temporarily experiences density below $\rho_0$. Complete knowledge of nuclear EoS across different densities is needed for nuclear theory to accurately predicts collision observables.

There are multiple ways of parameterizing nuclear EoS, such as Skyrme type EoS [3], polytropes [17] and Meta-modelling EoS [1]. Nuclear structure probes are generally sensitive to the density region around saturation [18–21], so derivatives of EoS with respect to density at this point

3

are often used as empirical parameters to characterize the density and isospin dependence of the EoS. These derivatives are commonly expressed as coefficients in the Taylor expansion when EoS is expanded in terms of $x = (\rho - \rho_0)/(3\rho_0)$:

$$E_{is}(\rho) = E_0 + \frac{1}{2}K_{\text{sat}}x^2 + \frac{1}{3!}Q_{\text{sat}}x^3 + \frac{1}{4!}Z_{\text{sat}}x^4 + ... \tag{1.4}$$

$$E_{iv}(\rho) = S_0 + Lx + \frac{1}{2}K_{\text{sym}}x^2 + \frac{1}{3!}Q_{\text{sym}}x^3 + \frac{1}{4!}Z_{\text{sym}}x^4 + ... \tag{1.5}$$

For some EoS families, energy depend on density and asymmetry in a way that cannot be separated into the sum of two terms, but the isoscalar term is always well-defined:

$$E_{is}(\rho) = E(\rho, \delta = 0). \tag{1.6}$$

The isovector term can be defined as the second order Taylor expansion coefficient in $\delta$ around $\delta = 0$ (not to be confused with Taylor EoS expansion coefficients which expands in $x$),

$$E_{iv}(\rho) = \frac{1}{2}\frac{\partial^2 E(\rho, \delta)}{\partial \delta^2}\bigg|_{\delta=0}. \tag{1.7}$$

Likewise Taylor EoS coefficients can always be extracted from any nuclear EoS. This allows for comparison of variables across families of EoS.

## 1.2 Neutron Star

The matter in the interior of a NS is one of the densest material besides black hole in the universe. This matter is so dense that it becomes energetically favorable for protons and electrons to combine and form neutrons. At densities ranging from somewhat below saturation density ($\rho_0 = 0.155 \, \text{fm}^{-1}$) to $3\rho_0$, it is reasonable to describe NS matter as locally uniform nuclear matter composed mostly of neutrons. Study of NS is of great relevance to nuclear physics because it provides unique information on the properties of asymmetric nuclear matter at high density. Refs. [22–24] provide more in depth discussions on the subjects.

Astrophysical NS properties, combined with constraints from nuclear observations, have provided a rough understanding of nuclear EoS. Typical temperatures of NSs are low with $k_BT < 1\,\mathrm{MeV}$, thus finite temperature effect is small, but the uncertainty in the relation between the pressure and energy density of nuclear matter at various baryon densities remains large [25].

Recent gravitational wave observations from LIGO collaboration [26] opened a new window for understanding neutron-star matter. Specifically, the LIGO observation provides estimation for *tidal deformability*, also known as *tidal polarizability*, a quantity that bears direct relevance to nuclear EoS. When a NS orbit around another NS, tidal force deforms its companion star. The mass quadrupole that developed in response to the external quadrupole gravitational field emerges as:

$$Q_{ij} = -\lambda E_{ij}. \tag{1.8}$$

Here $E_{ij}$ is the external gravitational field strength and $\lambda$ is the tidal deformability. The orbital period of the in-spiral differs from point mass calculations because tidal deformation contributes to an overall orbital energy loss and changes the rotational phases. This difference is used to extract the dimensionless tidal deformability ($\Lambda$) of a NS [27, 28]. Throughout this thesis, tidal deformability given below always refers to the dimensionless tidal deformability $\Lambda$ defined as,

$$\Lambda = \frac{\lambda c^{10}}{G^4 M^5} = \frac{2}{3} k_2 \left(\frac{c^2 R}{GM}\right)^5, \tag{1.9}$$

where $k_2$ is the second Love number [29, 30]. This whole expression, including the Love number, is sensitive to the nuclear EoS [26, 31, 32]. Steps necessary to calculate $\Lambda$ for a given EoS are detailed in Appendix A.1. With the gravitational wave observation of a neutron star merger event 170817, LIGO group first constrained this value to $\Lambda < 800$ [26], and later refined to $\Lambda = 190^{+390}_{-120}$ with additional assumption on the functional form of EoS [33]. The quantitative relation between constraint on $\Lambda$ and EoS parameters will be explored in this thesis.

## 1.3 Heavy-ion collision

Another source of constraints on density dependence of the symmetry energy comes from heavy-ion collision (HIC). When nucleus collide, part of the target and projectile nucleons overlap
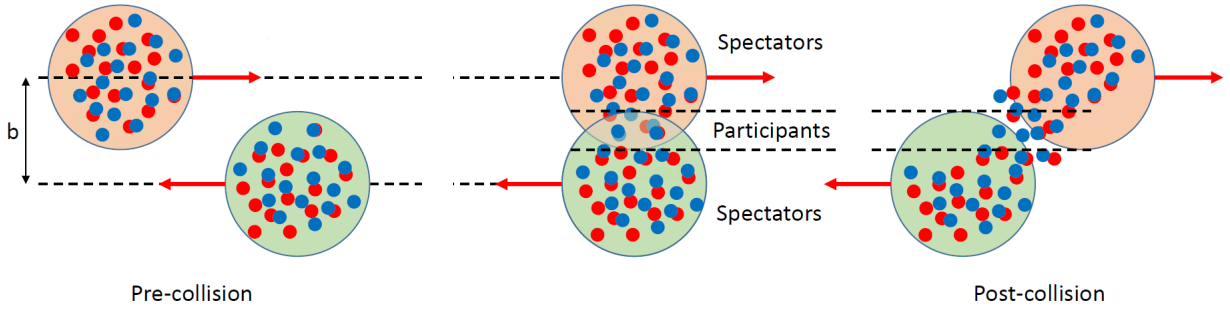
Figure 1.1: Cartoon illustration of impact parameter b, spectator and participant nucleons. Taken from Ref. [2].

with each other. The collision pushes the density of the overlapping region to well above $\rho_0$, sometime to density as high as $2\rho_0$ [2]. The nucleons in the overlapping region is commonly referred to as the *participant nucleons* whereas those not directly in the path of collision is referred to as *spectator nucleons*. The two types of nucleons are illustrated in Fig. 1.1. The patterns at which participant nucleons emerges as light fragments will shed light into the nuclear EoS.

Before the advancement of Rare-Isotope (RI) beams, only stable nucleus can be studied which limits the range of neutron to proton ratio in a reaction. With the development of modern RI beam facility, it is now possible to collide unstable nuclei with a higher neutron to proton ratios than before. By comparing results from reactions at various neutrons to protons ratios, the asymmetry contribution to EoS can be studied.

The perpendicular distance between target and projectile is called the *impact parameter b*. Events with small $b$ are called central events while those with large $b$ are called peripheral events. Collision dynamics changes with impact parameter so different observables are used for central and peripheral events to study nuclear EoS [11, 34–36]. Recently, pion observables on central events (will be detailed on Chapter 4.4) have been compared to theory to successfully constrain symmetry energy term at high density [37].

Most of these analyses explored a few parameters at a time. For instance, Ref. [11] vary only the curvature parameter $K_{sat}$ while keeping other parameters, such as in-medium cross-section

and effective mass fixed. Different experiments have led to different one-variable constraints or two-variable correlation constraints. Ref. [37] only varies two variables ($L$ and $\Delta m_{np}$), with other parameters such as in-medium cross-section or $K_{\mathrm{sym}}$ restricted to best fitted values from other experiments. Due to the complexity of nuclear dynamics, observables rarely depend on only one or two parameters. If certain parameters are fixed, the potential constraining power of the observable on those parameters are lost. Improvements can be made by constraining multiple parameters with multiple observables simultaneously.

## 1.4 Organization of Dissertation

To probe the density dependence of symmetry energy term, a set of Sn + Sn heavy-ion experiments were preformed in 2016 at RIKEN with a time projection chamber (TPC) called S$\pi$RIT placed inside the SAMURAI magnet. Constraints have been extracted from pion yield and ratios [37], but it can still be improved by incorporating other observables involving light fragments. TPC was used under magnetic field as it can distinguish $\pi^+$ from $\pi^-$, measure the momentum of high energy fragments and provide a large geometrical coverage, but the analysis of TPC data is complicated as Chapter 3.2 shows. In this thesis I will demonstrate the improvements on data analysis and Monte Carlo simulation for light fragments observables, develop an efficient algorithm to search for best fits in multi-dimensional parameter space and perform correlation analysis between EoS parameters and deformability $\Lambda$. This correlation will be the connection between nuclear physics, represented by EoS parameters, and astrophysics, represented by $\Lambda$ from LIGO experiment.

The organization of the dissertation is as follows: In Chapter 2, the correlation between nuclear EoS and neutron star properties is studied. Then a brief introduction to the set up of S$\pi$RIT experiment and data analysis software are presented in Chapter 3. The results from the experiment are shown next in Chapter 4. Monte Carlo simulation of the S$\pi$RIT TPC is discussed in details in Chapter 5 to verify the accuracy of our analysis software. Bayesian analysis is then performed in Chapter 6 to translate experimental results into constraints on nuclear EoS parameters. Its implication on NS properties will be discussed. Finally a brief summary is given in Chapter 7.

# CHAPTER 2

# NEUTRON STAR CALCULATIONS

In this chapter, we will explore the correlation between tidal deformability and Taylor expansion parameters. Previous studies have explored the constraints on different 2D parameter planes [16, 20], on a diverse set of models [38–40], and with Bayesian analysis on EoSs from chiral effective field theory [41]. In this study, we will expand the analysis by using EoSs that are commonly used in HIC and exploring a larger parameter space by employing a less restrictive form of EoS.

A family of theoretical EoS is needed to correlate the Taylor expansion parameters with the predicted $\Lambda$. One widely used family in astrophysics is the piece-wise polytropes [17], but it is not suitable in this study because a Taylor expansion assumes that the EoS is analytic over the range of interest. As long as there is only one polytrope, a Taylor expansion is valid, but its validity does not extend past the point of connection between the original polytrope and the next.

A commonly used family of EoS used in nuclear physics is the Skyrme interactions [3]. It derives from simplified approximate nuclear interaction and relies on 15 free parameters in its expanded form. Many different Skyrme interactions have been developed to calculate nuclear properties and these studies are well documented in the literature [3, 19, 42]. Most of the compiled Skyrme interactions used in this work has been tested to be consistent with certain nuclear properties. Due to its prevalence in nuclear physics, we will review how the new merger observable such as the tidal deformability correlates with nuclear physics parameters in nuclear EoS constructed from commonly used Skyrme interactions and how the insights gained can be used to guide the nuclear physics experiments designed to constrain the symmetry energy term of the nuclear EoS.

Recently, Meta-modelling EoS [1] is proposed as an alternative to Skyrme EoS. Its functional form is less restrictive and would be suitable for understanding the effect from higher order terms. Due to their unique advantage, we will also study the correlations between high order Taylor parameters and NS properties using Meta-modelling EoS.

## 2.1 Structure of a NS and modifications on the nuclear EoS

Neutron stars are more than a "giant nucleus". There are structural changes at various density regions as a result of a competition between the nuclear attraction, chemical potential of various particle species and the Coulomb repulsion. The dynamics of the outermost layer of NSs is described mostly by the Coulomb repulsion and nuclear masses, where nuclei arrange themselves in a crystalline lattice. As the density increases, it becomes energetically favorable for the electrons to capture protons, and the nuclear system evolves into a Coulomb lattice of progressively more exotic, neutron-rich nuclei that are embedded in a uniform electron gas. This outer crustal region exists as a solid layer of about 1 km in thickness [32].

At intermediate densities of sub-saturation, the spherical nuclei that form the crystalline lattice start to deform to reduce the Coulomb repulsion. As a result, the system exhibits rich and complex structures that emerge from a dynamical competition between the short-range nuclear attraction and the long-range Coulomb repulsion [43].

At densities of about half of the nuclear saturation, the uniformity in the system is restored and matter behaves as a uniform Fermi liquid of nucleons and leptons. The transition region from the highly ordered crystal to the uniform liquid core is very complex and not well understood. At these regions of the inner crust which extend about 100 meters, various topological structures are thought to emerge that are collectively referred to as "nuclear pasta". Despite the undeniable progress [44–57] in understanding the nuclear-pasta phase since their initial prediction over several decades ago [58–60], there is no known theoretical framework that simultaneously incorporates both quantum-mechanical effects and dynamical correlations beyond the mean-field level. As a result, a reliable EoS for the inner crust is still missing.

The matter in the core region of NS can be described as uniform nuclear matter where neutron, proton, electrons and muons exist in beta equilibrium [43]. Although a phase change and exotic matter such as hyperons [43, 61, 62] could appear in the inner core region, there is currently no direct evidence of their existence. In this work, we calculate the EoS in this region by assuming that the neutron-star matter is composed of nucleons and leptons only.

Due to the rich structure of NS, the nuclear EoS needs to be contextualized before it can be used for NS properties calculation. To begin with, crustal EoS should be used at density below transition density $\rho_T$. Normally the determination of $\rho_T$ requires complicated thermodynamic calculations, but some simple relationship has been found between transition densities and Taylor parameters of the EoS [63] that greatly simplifies its calculation. In this study, the following equation is used to determine $\rho_T$:

$$\rho_T = (-3.75 \times 10^{-4}L + 0.0963) \text{ fm}^{-3}. \tag{2.1}$$

Outer and inner crust exhibit different physical properties and should be described by different EoSs. For the outer crust, EoS provided by Ref. [64] is used in this analysis. For the inner crust, either a Fermi-gas EoS (used in Section 2.2) or spline interpolation (used in Section 2.3) is used. Its main purpose is to connect the outer crust and outer core. The outer crust is used in the region of $0 < \rho < 0.3\rho_T$ and the inner crust in $0.3\rho_T \leq \rho < \rho_T$. The transition density at $0.3\rho_T$ is chosen ad-hoc and this connection region cannot precisely describe crustal dynamics, properties of the neutron star core such as tidal deformability does not appear to be sensitive to the choice of the crustal EoS [32, 65, 66].

The outer core region $\rho > \rho_T$ is characterized by the EoS of a beta equilibrated system of protons, neutrons, electrons and muons. Proton and neutrons are collectively described by nuclear EoS while electrons and muons are modeled as relativistic Fermi gases. Equilibrium is attained by minimizing the Helmholtz free energy at different densities. Beyond a certain high density threshold $\rho_c$, the EoS of outer core may not be applicable. To complete the description of NS EoS, polytropes (used in Section 2.2) or EoS with speed of sound equals to speed of light (used in Section 2.3) can be used to extend the EoS to the central density region of a neutron star. The high density region mainly affects the maximum neutron star mass and does not affect the relevant properties of the 1.4 solar mass neutron stars considered here.

To summarize, EoS of the neutron-star matter is formulated as follows:

$$P(\mathcal{E}) = \begin{cases} P_{\text{outer crust}}(\mathcal{E}), & \text{if } 0 < \rho < 0.3\rho_T \\ P_{\text{connection}}(\mathcal{E}), & \text{if } 0.3\rho_T < \rho < \rho_T \\ P_{\text{outer core}}(\mathcal{E}), & \text{if } \rho_T < \rho < \rho_c \\ P_{\text{inner core}}(\mathcal{E}) & \text{if } \rho_c < \rho. \end{cases} \tag{2.2}$$

In the above equation, $P_{\text{outer crust}}$ is the pressure from outer crustal EoS and $P_{\text{outer core}}$ is the pressure from beta-equilibrated nuclear EoS. $P_{\text{connection}}$ is the intermediate equation that smoothly connects $P_{\text{crust}}(\mathcal{E}_{\text{crust}}(0.3\rho_T))$ to $P_{\text{outer core}}(\mathcal{E}_{\text{outer core}}(\rho_T))$.

## 2.2 Neutron stars from Skyrme EoS

In this section, a collection of 248 Skyrme interactions from Refs. [3, 19, 21] are used to form the outer core EoS. The outer core is assumed to be valid until $\rho_c = 3\rho_0$, where a transition to inner core occurs. A polytropic EoS of the form $K'\rho^\gamma$ is used to extend the EoS to the central density region of a neutron star. The constants $K'$ and $\rho_0$ are fixed by the conditions that the pressure at thrice the normal nuclear density, $P_{\text{inner core}}(\rho_c)$ matches the pressure from the Skyrme density functionals $P_{\text{outer coure}}(\rho_c)$ and that the polytrope pressure at $7\rho_0$ is such that the EoS can support a 2.17 solar-mass neutron star, the maximum neutron star mass predicted from the neutron star merger event [67].

The EoS in different density regions are presented by the different color curves in Fig. 2.1. At the lowest densities, the EoSs, describing the outer crust, are represented by yellow lines. The Fermi-gas EoS that connect the crust to the inner core are represented by the green curves. As a vehicle in connecting nontrivial nuclear physics observables to 1.4 solar mass neutron-star observables, we use the Skyrme interactions (green curves) [3, 19, 42] at densities found in the inner core region (between $0.5\rho_0$ to $3\rho_0$) that represent the nuclear matter environment where such interactions can apply. The polytropic EoS above $3\rho_0$ are plotted in red. The Skyrme interactions that generate negative pressure at $3\rho_0$ or otherwise would not support a 2.17 solar mass neutron
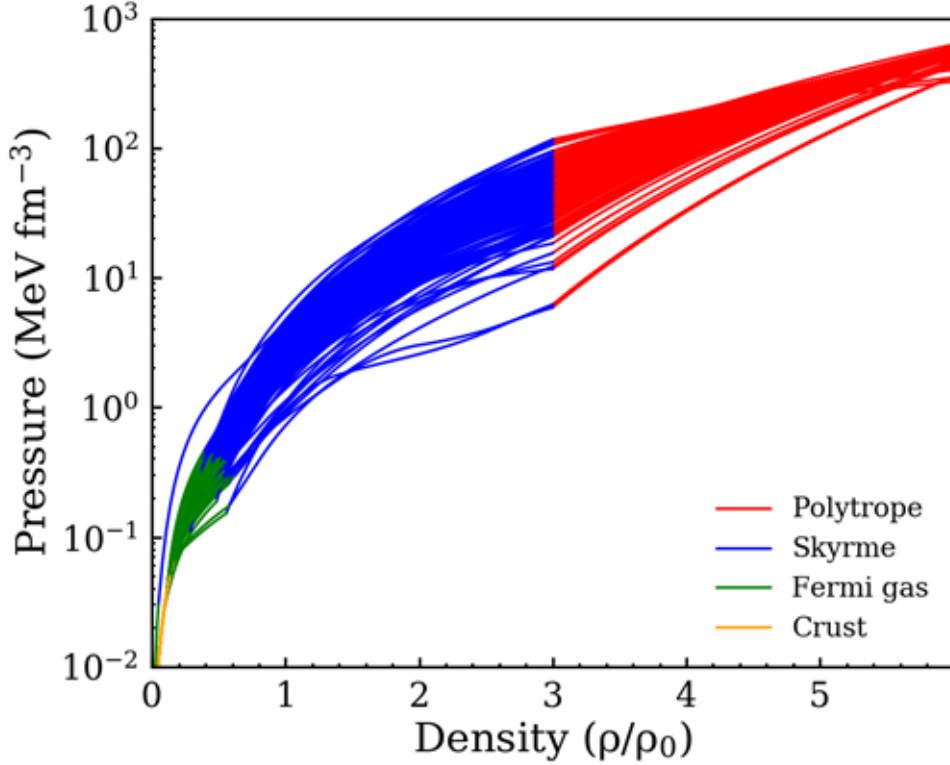
Figure 2.1: Composition of EoSs in different density regions in the neutron star. The outer crust EoS is represented by the yellow line, relativistic Fermi gas polytropic EoSs by the green lines, Skyrme EoSs by the blue lines and high density polytropes by the red lines. See text for details.

star are excluded as they are not realistic.

### 2.2.1 Results for a 1.4-solar mass NS

From the collection of Skyrme EoSs, only 182 of them can support a 2.17 solar mass neutron star. Each EoS, represented by an open circle in Fig. 2.2, gives rise to a unique prediction for the neutron-star radius and tidal deformability. The trend exhibited by the open circles reflects the fact that tidal deformability and neutron-star radius are correlated as described by Eq. (1.9). Tidal deformability is sensitive to pressure at density region region of $(0.5 - 3)\rho_0$ [17, 41, 68]. If we neglect the crust in our calculations, we arrive at the blue dashed curve. Above $\Lambda > 600$, calculations including a crust produce larger radii. The phenomenon that the crust adds to the radii has been also observed in other calculations [67, 68].
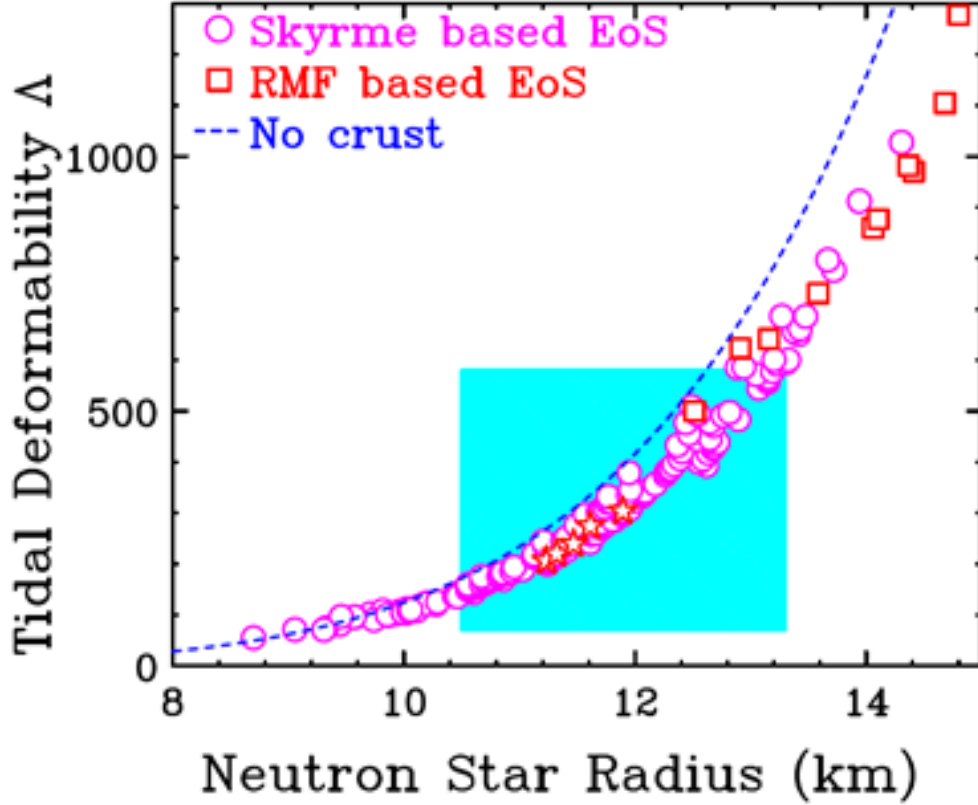
Figure 2.2: Correlation between neutron-star tidal deformability and radius from current calculations are represented by open circles and those from Ref. [3] by open squares. The light blue shaded area represents constraint from recent GW170817 analysis [4]. Five interactions, KDE0v1, LNS, NRAPR, SKRA, QMC700, deemed as the best in Ref. [3] in describing the properties of symmetric matter and calculated pure neutron matter, are plotted as red stars. The dashed curve is the best fit to our results if no crust is included in our neutron star model.

The increase in crustal thickness with neutron star radius is consistent with Ref. [69], which shows that the crust thickness increases inversely with neutron star compactness ($M/R$). The reason is that crust thickness contributes to the total radius but does not affect the total mass and depends little on uncertainties in the crustal EoS. In the region of large tidal deformability, our results are consistent with those from EoSs based on relativistic mean-field interactions [4] following analogous methodology and represented by the open red squares in Fig. 2.2. The range of the updated values $\Lambda = 70 - 580$ and $R = 10.5 - 13.3$ km obtained from the GW170817 analysis [33] is represented by the light blue-shaded square there. Our calculations lie nearly diagonally across the box with about 130 interactions inside.

One advantage of Skyrme nuclear density functionals is that many different Skyrme interactions have been developed to calculate nuclear properties and these studies are well documented in the literature [3, 19, 42]. Most of the compiled Skyrme interactions used in this work has been tested to be consistent with some nuclear properties. As described in Ref. [3], eleven constraints that represent the properties of symmetric nuclear matter and pure neutron matter are used to assess 240 Skyrme interactions. Five interactions, KDE0v1, LNS, NRAPR, SKRA, QMC700, which satisfy nearly all the eleven constraints, are highlighted as red stars in all the figures in this section. The $\Lambda$ values ($\sim 250$) they yield, with the associated radii ($\sim 11.3$ km), are well within the GW constraint.

As mentioned in Section 1.1, it is customary to expand EoS in Taylor parameters expanded at saturation density. By taking advantage of the large range of Skyrme parameter used in this work, we can explore the correlations of the set ($K_{sat}$, $Q_{sat}$, $S_0$, $L$, $K_{sym}$, $Q_{sym}$) to the neutron star properties, specifically, the tidal polarizability, $\Lambda$. Since $\Lambda$ is monotonically related to the neutron star radius $R$, we observe similar correlation between $R$ and the set ($K_{sat}$, $Q_{sat}$, $S_0$, $L$, $K_{sym}$, $Q_{sym}$) even though the latter correlations are not discussed below.

First we explore the connection to the parameters in $E_{is}$. Fig. 2.3 shows the plots of $\Lambda$ vs $K_{sat}$ (left panel) and $Q_{sat}$ (right panel). The value of $K_{sat}$, also known as compressibility, has been fairly well determined experimentally to be $230 \pm 30$ MeV [3]. Most of the Skyrme interactions studied here cluster around $K_{sat} \sim 240$ MeV and, within this tight bound on $K_{sat}$, show no obvious correlation with $\Lambda$. $Q_{sat}$ values cluster around $\sim -380$ MeV and again show no correlation with $\Lambda$. This observation that $\Lambda$ is not strongly connected to $K_{sat}$ and $Q_{sat}$ that characterize the symmetric matter, is consistent with conclusions of previous studies [70]. This implies that it would be difficult to extract properties of the symmetric nuclear matter from the dipole deformability of the neutron star alone.

Next we explore the importance of the parameters in symmetry energy term, $S_0$, $L$, $K_{sym}$, and $Q_{sym}$ in Fig. 2.4. The abscissa scales are chosen to represent the respective ranges of values found in Ref. [3] and that the correlations between the plots are comparable. The correlations between $\Lambda$ and symmetry energy parameters are stronger than those for symmetric nuclear matter. The
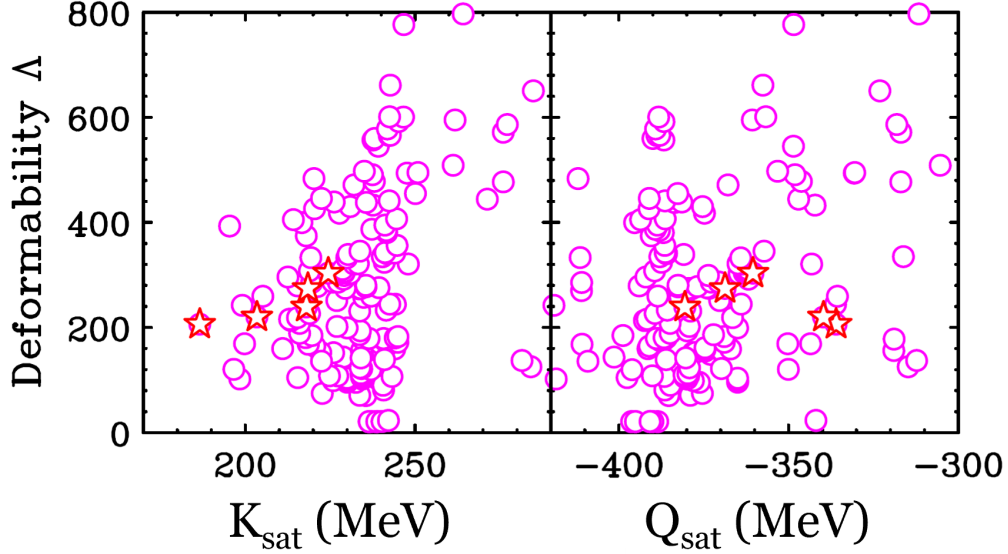
Figure 2.3: Correlation between the neutron star deformability $\Lambda$ and the compressibility parameter $K_{\mathrm{sat}}$ (left panel) and skewness parameter $Q_{\mathrm{sat}}$ (right panel) defined in Eq. (1.5) for the symmetric matter EoS of Skyrme functionals used in the study. The red stars in both panels represent the five interactions, KDE0v1, LNS, NRAPR, SKRA, and QMC700 that satisfy nearly all 11 constraints of Ref. [3].

correlation is strongest in $K_{\mathrm{sym}}$ followed by $L$. The slope $L$ mainly characterizes the vicinity of saturation density region as it is the first derivative, also known as the slope. Since the second-order term, $K_{\mathrm{sym}}$ impacts more the higher densities, it is not surprising that $K_{\mathrm{sym}}$ should have stronger influence on $\Lambda$. The much weaker sensitivity to $Q_{\mathrm{sym}}$ probably reflects that $Q_{\mathrm{sym}}$ impacts density above $3\rho_0$. Different models may have different correlations between $S_0$, $L$, $K_{\mathrm{sym}}$, and $Q_{\mathrm{sym}}$. Thus the correlations observed here may not be universal. It would be interesting to examine these correlations with other density functionals and, in particular, with interactions that have different correlations between density regions than those that are implicitly contained in the Skyrme.

### 2.2.2 Neutron star of different masses

Fig. 2.2 shows the power-law relationship between the tidal deformability and the radius for 1.4 solar mass neutron star. If mass of the neutron star changes, a different power law relationship is expected. The left panel of Fig. 2.5 shows the tidal deformability as a function of neutron star radius for neutron-star mass of 1 (closed violet circles), 1.2 (open violet circles), 1.4 (closed blue
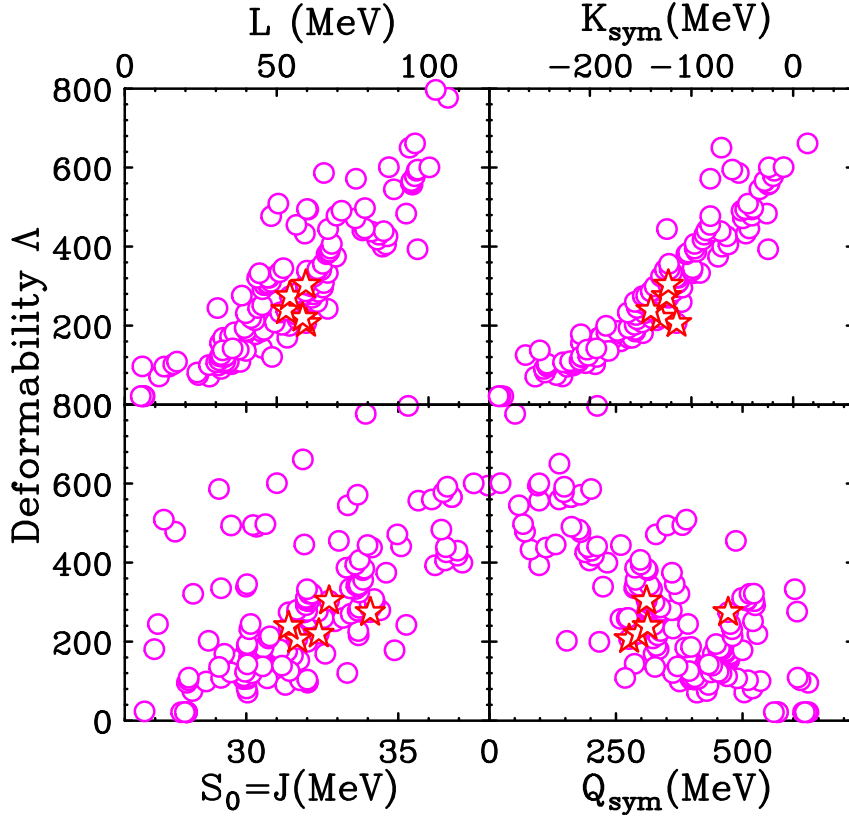
Figure 2.4: The four panels show the correlation between the neutron star deformability $\Lambda$ and Taylor expansion coefficients $S_0$ (lower left), $L$ (upper left), $K_{sym}$ (upper right) and $Q_{sym}$ defined in Eq. (1.5) for the symmetry energy and obtained for the Skyrme functionals used in the study. The symbols follow the same convention as in Figs. 2.2 and 2.3

squares), 1.6 (open blue squares), 1.8 (closed red triangles) and 2 (open triangle) solar masses. A universal relationship with the tidal deformability is obtained if the mass is taken into account as shown in the right plot of Fig. 2.5 where the radius is replaced by the compactness factor $(M/R)$. As expected, the tidal deformability has an inverse power law relationship to the compactness factor $(M/R)$. For a fixed solar mass, the range of the compactness factor is limited since the radius of the neutron star mostly span a range from about 8 to 14 km. Thus it is easier to deform a smaller star giving rise to larger deformability than to deform a star with larger mass.
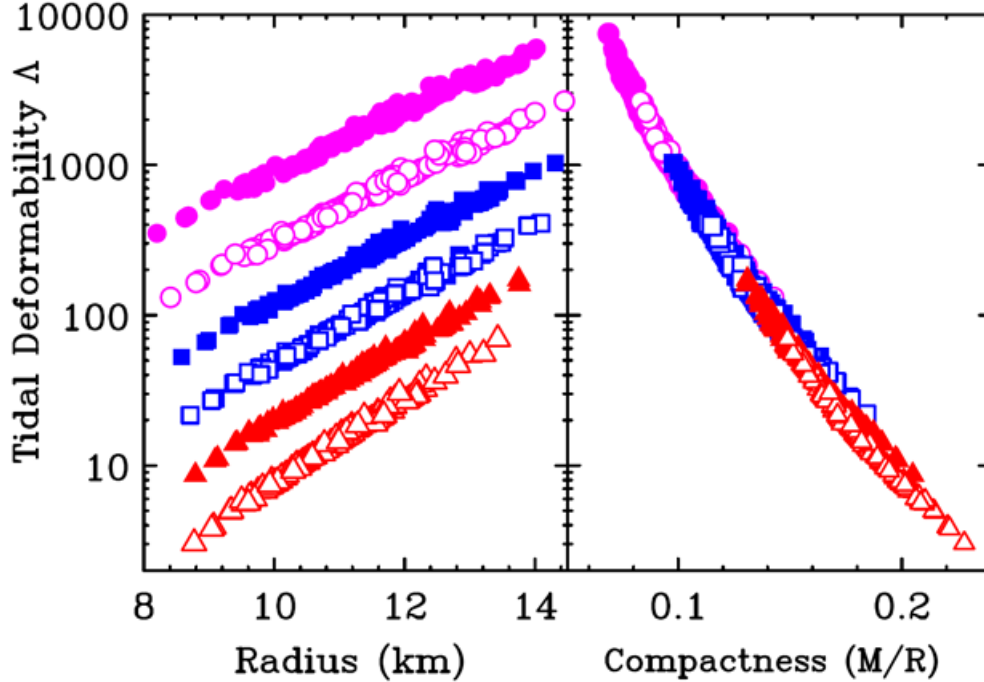
Figure 2.5: Left panel: Correlation between neutron-star tidal deformability and radius for neutron stars with different masses. From top: closed and open circles, closed and open squares, closed and open triangles represent neutron star mass of 1, 1.2, 1.4, 1.6, 1.8 and 2 solar masses. Right panel: Universal relationship between neutron-star tidal deformability and compactness ($M/R$) for neutron stars with different masses as plotted in the left panel.

## 2.3 Neutron stars from Meta-modelling EoS

While Skyrme EoS provides numerous advantages, it is difficult to explore new physics from the Taylor expansion parameters because they are strongly constrained by the form of the Skyrme interaction itself. It is difficult to access the functional dependencies of the Taylor expansion parameters that are not contained in the original choice for the Skyrme functional form [71, 72]. This can be overcome with Meta-modelling EoS from Ref. [1]. Such metamodels for the EoS can be easily constructed with only Taylor expansion parameters and effective masses. Their derivatives of different orders are independent of each other by construction.

Four different *empirical local density functionals* (ELF) meta-models are proposed in Ref. [1]: ELFa, ELFb, ELFc and ELFd. ELFa does not produce vanishing energy as density approaches zero. ELFb does not converge to a typical Skyrme EoS even when identical Taylor parameters are

17

used. ELFc does not have the shortcomings of EFLa and ELFb and closely resembles Skyrmes with similar Taylor parameters. Although ELFd agrees with Skyrmes better than ELFc, it relies on high density information that is not well constrained by experiments.

From the above considerations, we adopt ELFc in this study. Similar choice is also made in other recent studies [68, 73]. The formulation of ELFc is detailed in Appendix A.2. The following choices of parameters have been accurately constrained by nuclear experiment and are fixed in the analysis [1]: $E_{\text{sat}} = -15.8\,\text{MeV}$, $\rho_0 = 0.155\,\text{fm}^{-3}$.

Apart from the usual Taylor series coefficients, another important quantity that characterizes nuclear matter properties in Meta-modelling is the effective mass $m^*(\rho, \delta)$. It is used to characterize the momentum dependence of nuclear interaction and it can be different for protons $m_{\text{p}}^*(\rho, \delta)$ and neutrons $m_{\text{n}}^*(\rho, \delta)$ depending on the environment under which the nuclear matter is subjected to. It is generally assumed that $m_{\text{p}}^* = m_{\text{n}}^*$ in SNM.

Comparison of effective masses is commonly carried out through the comparison of two quantities: the nuclear effective mass in SNM at saturation $m_{\text{sat}}^*$ and the splitting in neutron and proton effective masses in pure neutron matter (PNM) at saturation $\Delta m^* = m_{\text{n}}^* - m_{\text{p}}^*$. The choice of the two quantities mirrors the spirit of splitting EoS into isoscalar term and isovector term in Eq. (1.3) where contribution from SNM is separated from the correction factor that arises due to asymmetry in numbers of protons and neutrons.

Sometimes it is more convenient to express $m_{\text{sat}}^*$ and $\Delta m^*$ in terms of $\kappa_{\text{sat}}$, $\kappa_{sym}$ and $\kappa_v$:

$$
\begin{aligned}
\kappa_{\text{sat}} &= \frac{m}{m_{\text{sat}}^*} - 1 = \kappa_s, \\
\kappa_{\text{sym}} &= \frac{1}{2}\left(\frac{m}{m_n^*} - \frac{m}{m_p^*}\right), \\
\kappa_v &= \kappa_{\text{sat}} - \kappa_{\text{sym}}.
\end{aligned}
\tag{2.3}
$$

The parameter $\kappa_v$ plays the role of the enhancement factor in Thomas-Reiche-Khun sum rule and depends on the energy region of the resonance energy [74]. In this analysis, the effective masses will be expressed in terms of $m_{\text{sat}}^*/m$ and $\kappa_v$.

NS EoSs are constructed from Meta-modelling EoS using procedure detailed in Section 2.1,

with spline interpolation as the connection EoS and beta-equalibrated EFLc as the EoS for outer

core. The inner core is represented by the "stiffest" possible EoS in this section where speed of

sound is equal to the speed of light. The determination of transition density from outer to inner

core will be outlined below.

Additional characteristics of nuclear matter can be inferred using thermodynamic equations

once an EoS is specified. The pressure at various densities $P(\rho)$ is related to the derivative of the

energy:

$$P(\rho) = \rho^2 \frac{\partial E(\rho, \delta)}{\partial \rho}. \tag{2.4}$$

The adiabatic speed of sound can then be calculated [75]:

$$\left(\frac{v_s}{c}\right)^2 = \left(\frac{\partial P}{\partial \mathcal{E}}\right)_S, \tag{2.5}$$

where $\mathcal{E} = \rho(E + mc^2)$ is the energy density of the material, including mass density. This implies

any thermodynamic stable EoS must satisfy $\left(\frac{\partial P}{\partial \mathcal{E}}\right)_S > 0$. Furthermore, since information cannot

travel faster than the speed of light due to causality, the inequality $v_s < c$ must hold for all densities

relevant to NS. This may not be always true for ELFc. To keep the EoS valid, we will switch from

ELFc to an expression for the stiffest possible EoS whenever causality is violated:

$$P_{\text{inner core}}(\mathcal{E}, v_s, \mathcal{E}_0, P_0) = \left(\frac{v_s}{c}\right)^2 (\mathcal{E} - \mathcal{E}_0) + P_0. \tag{2.6}$$

This equation represents a EoS with constant speed of sound $v_s$, with $v_s = c$ yields the stiffest

possible EoS [76]. Here $\mathcal{E}_0$ and $P_0$ are reference values of energy density and pressure, respectively.

The reference values can be adjusted to match the conditions at a specific density where energy

density and pressure are known. The switch in EoS avoids superfluous rejection when causality is

considered.

### 2.3.1 Bayesian inference

We use Bayesian inference to study the influence of tidal deformability constraints from LIGO

on nuclear-matter EoS parameters. These parameters are sampled uniformly within reasonable

ranges and are then transformed into samples of neutron-star matter EoSs. Through solving TOV equation, we are able to calculate the corresponding tidal deformabilities. By combining their prior distribution, which is our initial believe on parameter values based on findings from literature, and likelihood, which indicates the compatibility between the calculated and the observed tidal deformability, Bayesian inference will assign probability for each EoS parameters with Bayes theorem:

$$P(\mathcal{M}) = \frac{1}{V_{\text{tot}}} w(\mathcal{M}) p(\Lambda(\mathcal{M})) \prod_i g_i(m_i). \tag{2.7}$$

In this equation, $\mathcal{M}$ is the set of all EoS parameters, $m_i \in \mathcal{M}$ is the $i^{\text{th}}$ EoS parameters, $V_{\text{tot}}$ is the normalization constant, $p(\Lambda(\mathcal{M}))$ is the likelihood of a EoS calculated from its predicted $\Lambda$, $g_i$ is the prior distribution of the $i^{th}$ parameter and $w(\mathcal{M})$ is the filter condition that filters out EoSs that are nonphysical.

The likelihood of EoS is the probability of having the observed LIGO event with the assumption that the given theoretical EoS is the ultimate true EoS. We will model the likelihood function as an asymmetric Gaussian distribution base on the extracted $\Lambda = 190^{+390}_{-120}$ [33] for 1.4-solar mass NS from GW170817.

$$p(\Lambda) = \begin{cases} \frac{1}{V} \exp(-\frac{(\Lambda - 190)^2}{2 \times 120^2}), & \text{if } \Lambda \leq 190 \\ \frac{1}{V} \exp(-\frac{(\Lambda - 190)^2}{2 \times 390^2}), & \text{if } \Lambda > 190. \end{cases} \tag{2.8}$$

In the above, $V$ is the feature scaling constant such that the likelihood function integrates to 1.

The sought function is the probability distribution of EoS parameters rather than that for $\Lambda$, so prior distribution $g_i$ is required to convert between the two using Bayes theorem. A commonly used prior is the Gaussian distribution:

$$g_i(m_i) = \frac{1}{\sqrt{2\pi\sigma_i^2}} \exp\left(-\frac{(m_i - m_{i,\text{prior}})^2}{2\sigma_i^2}\right), \tag{2.9}$$

where $m_{i,\text{prior}}$ and $\sigma_i$ are the prior mean and standard deviation of the free parameters, respectively. They should be chosen to reflect our current understanding of those free parameters.

Some parameter sets may yield nonphysical EoSs due to various additional considerations. The filter condition $w(\mathcal{M})$ takes that into account; it is set to 1 if the following three conditions of stability, causality and maximum mass, are all satisfied and it is set to 0, if not.

The stability condition rejects EoSs whose pressure decreases with energy density. Above the crust-core transition density, we require the EoSs to be mechanically stable with thermodynamical compressibility greater than zero, which means that the pressure of homogeneous matter does not decrease with density. For EoSs with negative compressibilities at density above the crust-core transition densities predicted by Eq. (2.1), they will be rejected as being inconsistent with experimental information.

The requirement of causality rejects EoSs whose speed of sound is greater than the speed of light in the core region of their respective heaviest NS. The maximum mass condition rejects EoSs that fail to produce a NS of at least 2.04 solar mass in accordance with observation. [77, 78].

Using the fact that the binary NS merger GW170817 detected by LIGO did not promptly produce a black hole, the heaviest possible NS should be around 2.17 solar mass [67]. Other sources put the maximum mass at around 2.15-2.40 solar masses [79–84]. Neither of these constraints have been adopted in here but can be implemented in the future.

The calculated probability distribution from Eq. (2.7) is referred to as the posterior distribution. By comparing prior to posterior distribution, we will be able to infer the sensitivity of various EoS parameters to NS tidal deformability. By construction, priors of different free parameters in meta-modeling EoS are not correlated with each other, so any correlations in the posterior reflect the collective sensitivity of the Taylor expansion parameters to NS tidal deformability.

Prior distributions of the parameters should reflect our initial belief of those quantities before information on tidal deformability is taken into account. For this, we rely on Ref. [1] which summarizes the distributions of EoS parameters from three phenomenological families, Skyrme, relativistic mean field (RMF) and relativistic Hartee-Fock (RHF). The mean and standard deviation of the parameters for each family are tabulated in the first six rows of Table 2.1. In this study, the prior means and standard deviations are the weighted average values of the three families,

with weights of 0.500, 0.333, 0.167 respectively. The weights reflect our confidence in of the models. We give Skyrme EoS the most weight as it is the most heavily employed parametrization in a myriad of nuclear predictions [3]. These relative weights are ad-hoc, but should cover most plausible parameter spaces. Prior means and standard deviations are listed in the seventh and eighth row in Table 2.1 respectively.

Table 2.1: Summary information of various models in Ref. [1]. The bottom half shows characteristics of the prior and posterior distribution respectively.

| | $L$ $(MeV)$ | $K_{\text{sym}}$ $(MeV)$ | $K_{\text{sat}}$ $(MeV)$ | $Q_{\text{sym}}$ $(MeV)$ | $Q_{\text{sat}}$ $(MeV)$ | $Z_{\text{sym}}$ $(MeV)$ | $Z_{\text{sat}}$ $(MeV)$ | $\frac{m^*_{\text{sat}}}{m}$ | $\kappa_v$ |
|---|---|---|---|---|---|---|---|---|---|
| Skyrme Average | 49.6 | -132 | 237 | 370 | -349 | -2175 | 1448 | 0.77 | 0.44 |
| Skyrme $\sigma$ | 21.6 | 89 | 27 | 188 | 89 | 1069 | 510 | 0.14 | 0.37 |
| RMF Average | 90.2 | -5 | 268 | 271 | -2 | -3672 | 5058 | 0.67 | 0.40 |
| RMF $\sigma$ | 29.6 | 88 | 34 | 357 | 393 | 1582 | 2294 | 0.02 | 0.06 |
| RHF Average | 90.0 | 128 | 248 | 523 | 389 | -9956 | 5269 | 0.74 | 0.34 |
| RHF $\sigma$ | 11.1 | 51 | 12 | 237 | 350 | 4156 | 838 | 0.03 | 0.07 |
| Weighted Average | 69.0 | -45.3 | 248 | 367 | -114 | -3990 | 3310 | 0.712 | 0.42 |
| Weighted $\sigma$ | 20.1 | 70.8 | 18.3 | 214 | 200 | 1530 | 989 | 0.06 | 0.17 |
| Posterior Average | 71.6 | -76.9 | 245 | 436 | -97 | -3410 | 3490 | 0.74 | 0.41 |
| Posterior $\sigma$ | 16.5 | 66.0 | 23 | 219 | 202 | 1710 | 970 | 0.07 | 0.25 |

The EoSs are sampled uniformly within ranges of plus or minus $2\sigma$ from the mean values from the seventh and eighth of Table 2.1. Each EoS is weighted by the product of filter condition, prior and likelihood of Eq. (2.7). A total of 1,500,000 EoSs have been sampled and 682,652 of them satisfy all of our constraints. Only 11,711 EoSs apply to all densities without switching to the stiffest EoS.

### 2.3.2 Results for a 1.4-solar mass NS

After incorporating the constraint on $\Lambda$ from gravitational wave observation of the merger of two 1.4-solar mass NSs by LIGO, posterior distributions of Taylor expansion parameters are shown in Fig. 2.6. The lower triangular plots show the bivariate distributions for two parameters. The

diagonal plots show the prior (blue curves) and marginalized posterior distributions (red curves) for each individual parameter. The upper triangle displays the Pearson correlation coefficients for parameter pairs defined as,

$$\rho_{X,Y} = \frac{\mathbf{E}[(X - \bar{X})(Y - \bar{Y})]}{\sigma_X \sigma_Y}, \tag{2.10}$$

where $\mathbf{E}$ is the expectation value and $\sigma_X$ and $\sigma_Y$ are the standard deviations of the parameters distributions. The Pearson coefficient ranges from -1 to 1 and its absolute value reflects the strength of the correlation. A positive value close to 1 indicates a strong correlation and a negative value close to -1 indicates strong anti-correlation while a value close to 0 indicates lack of correlation [85]. Only bivariate distributions between $L$, $K_{\mathrm{sym}}$, $K_{\mathrm{sat}}$, $Z_{\mathrm{sym}}$ and $Z_{\mathrm{sat}}$ are shown because the higher order parameters do not seem to be influenced by our tidal deformability constraints. The full correlation plot is included in Appendix A.3. Characteristics of the probability distributions are summarized in the bottom two rows of Table 2.1.

Fig. 2.7 shows the mean and $2\sigma$ region of pressure at different densities spanned by the EoSs in the posterior. The $2\sigma$ region converge to a line for $\mathcal{E} \lesssim 20\,\mathrm{MeV/fm^3}$, which corresponds to the outer crust. Since we connect all EoSs to the crustal EoS given by Ref. [64], this convergence is expected. From around $20\,\mathrm{MeV/fm^3}$ to $70\,\mathrm{MeV/fm^3}$, the spline connection kicks in and manifests in the broadening of pressure.

The cut-offs in the lower left corner of $Z_{\mathrm{sym}}$ vs. $Z_{\mathrm{sat}}$ distribution and the upper left corner of $K_{\mathrm{sym}}$ vs. $L$ distribution in Fig. 2.6 are the consequence of stability condition. At such extreme values, speed of sound may be imaginary when extrapolating to NS of 2.04 solar masses. This is evident in Fig. 2.8 in which 50 randomly selected EoSs from the cut-off region in $K_{\mathrm{sym}}$ vs. $L$ are shown in the lower panel. The pressure for those EoSs do not increase monotonically with the energy density and become mechanically unstable. These EoSs are discarded.

The posterior distributions of $K_{\mathrm{sym}}$ and $Z_{\mathrm{sym}}$ differ from the prior distributions significantly. The tidal deformability constraint favors lower $K_{\mathrm{sym}}$ region. The inference also narrows the range of possible $L$. Parameters such as $K_{\mathrm{sat}}$ and $Z_{\mathrm{sat}}$, whose posterior distributions are not altered significantly reflect that they are not sensitive to the tidal deformability constraints.
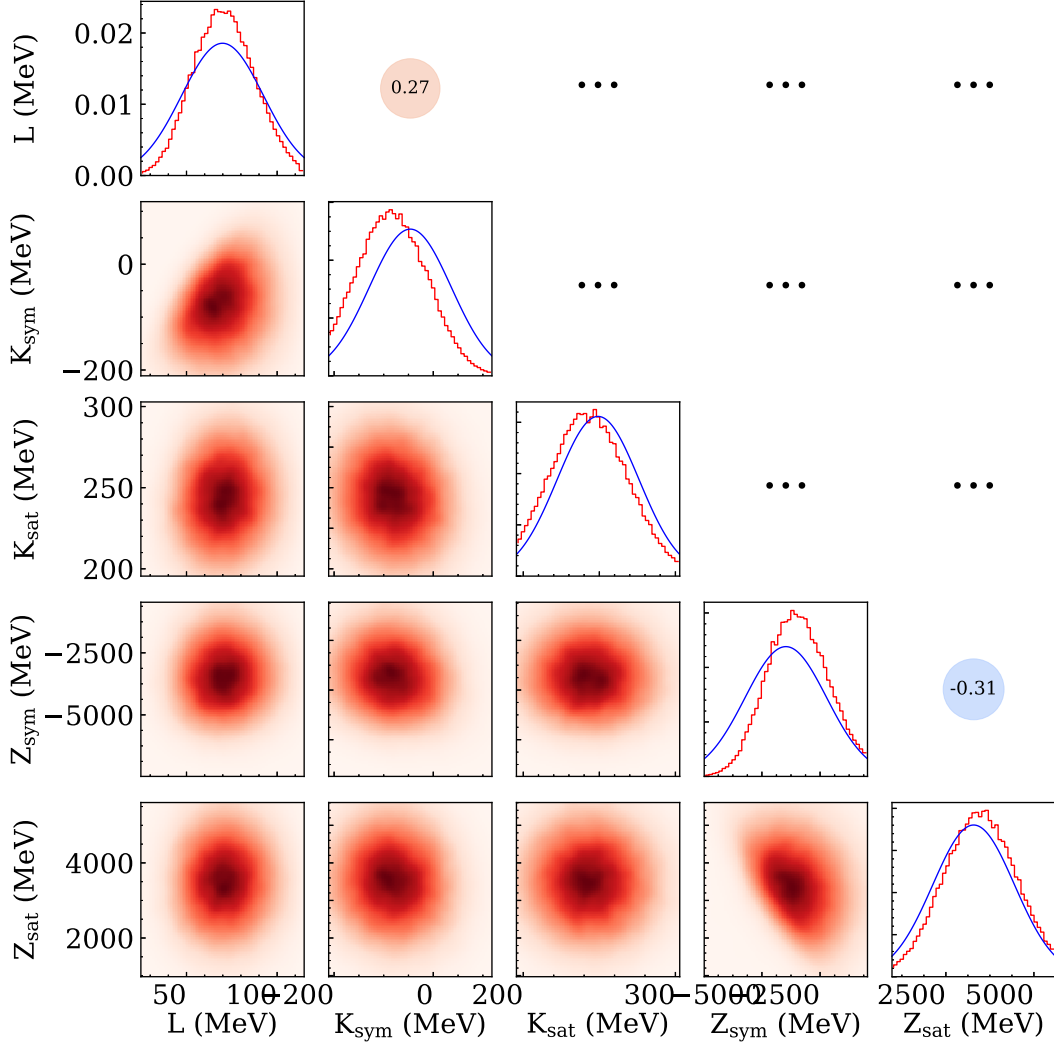
Figure 2.6: Bivariate characteristics of posterior likelihood distributions. Three regions can be distinguished. The lower triangle panels show likelihood distributions, with intensity proportional to distribution value, for pairs of Taylor parameters. The diagonal panels display prior (blue) and marginalized posterior (red) distributions for each parameter. The upper triangular region shows Pearson correlation coefficient for parameter pairs. Three dots indicate weak correlations with magnitude less than 0.1.

While this Bayesian analysis is well suited to discuss the sensitivity of the deformability to the Taylor expansions parameters $L$, $K_{sym}$, $K_{sat}$, etc., it has some limitations. In particular, we note that the prior and posterior distributions of $\Lambda$ as shown in Fig. A.3.1 (row 2 column 10 in Appendix A.3) are drastically different, probably as a consequence of the narrow prior distributions of the Taylor expansion parameters listed in Table 2.1. This reflects the strong sensitivity of $\Lambda$ to
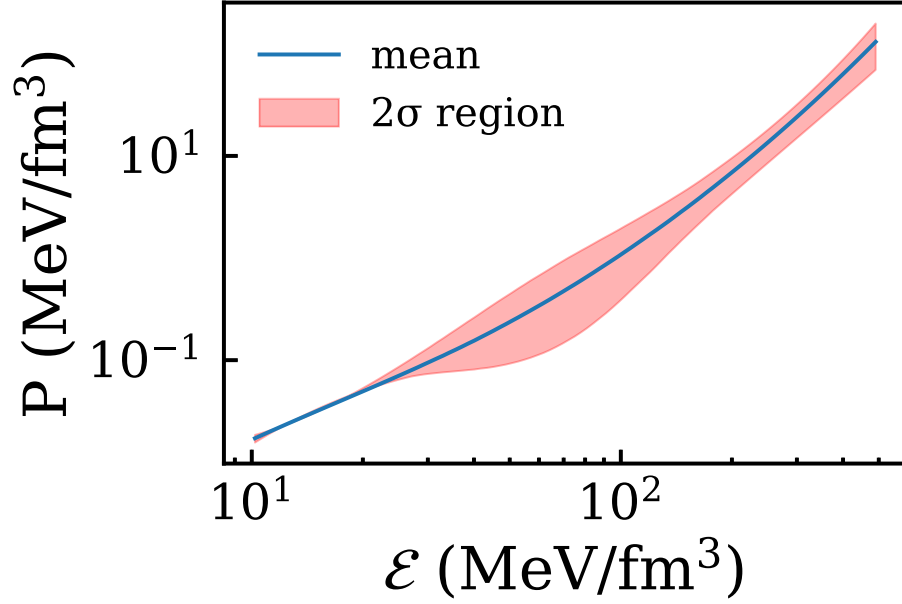
Figure 2.7: Distribution of EoSs sampled from the posterior. The divergence above energy density $\sim> 20\,\mathrm{MeV/fm^3}$ coincides with the transition from outer crust to spline connection.
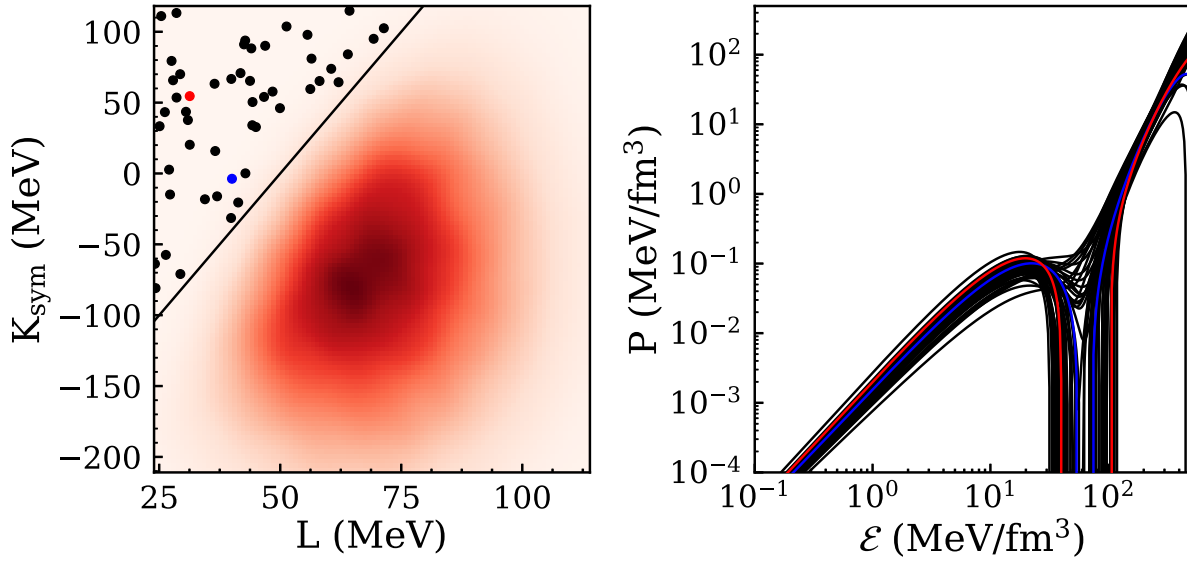


Figure 2.8: Upper panel: The 50 dots in the upper left hand corner of $K_{\mathrm{sym}}$ vs. $L$ correspond to 50 randomly chosen parameter space within the stability cut-off region. Lower panel: Unstable EoSs that correspond to the 50 dots. The red and blue lines correspond to the red and blue points in the upper panel respectively. They are highlighted to showcase how a typical EoS in the cut-off region looks like.

Table 2.2: Predicted tidal deformability for NS of different masses

| | $\Lambda(1.2)$ | $\Lambda(1.4)$ | $\Lambda(1.6)$ | $\Lambda(1.8)$ | $\Lambda(2.0)$ |
|---|---|---|---|---|---|
| Posterior Average | 1490 | 624 | 281 | 132 | 64 |
| Posterior $\sigma$ | 310 | 129 | 61 | 31 | 17 |

the prior distributions of the EoS. Furthermore, the posterior distribution of $\Lambda$ is much sharper and peaked at $624 \pm 129$ which exceeds the value of $190^{+390}_{-120}$ from the analysis of the GW170817 [33]. While the GW constraint reflects the high density of NS core, the prior distributions of the Taylor expansion parameters do not have rigorous laboratory constraints at high density region where $\Lambda$ is determined.

### 2.3.3 Neutron star of different masses

In anticipation that more merger events involving different NS masses than the nominal NS mass of 1.4 solar mass will be observed in the future [86], we use the posterior EoS distributions to predict deformability of NS with different masses.In Table 2.2, we provide our predictions for the tidal deformabilities for NS with 1.2, 1.4, 1.6, 1.8 and 2 solar mass using this group of EoSs weighted by their posterior distributions. To show the sensitivity of these predictions to the Taylor parameters, the bivariate distributions between the Taylor parameters from the posterior and the predicted tidal deformabilities on different stellar masses are shown in Fig. 2.9. We find that $\Lambda$ is more strongly correlated with $L$ and $K_{\text{sym}}$ than it is with higher order Taylor expansion parameters. The sensitivity to $K_{\text{sym}}$ increases, while the sensitivity to $L$ decreases, with stellar mass.

To quantify this dependence of sensitivity on mass, the Pearson correlation coefficients for a few selected Taylor parameter pairs are shown in Fig. 2.10. A gradual reduction in correlation between $L$ and tidal deformability is observed as the mass of a NS increases. This is expected as relevant average density for more massive stars shift upward and away from those directly impacted by $L$. A high density parameter $P(2\rho_0)$, the pressure for pure neutron matter at twice the saturation density, is also included in Figs. 2.9 and 2.10. The strong correlation between tidal deformability and
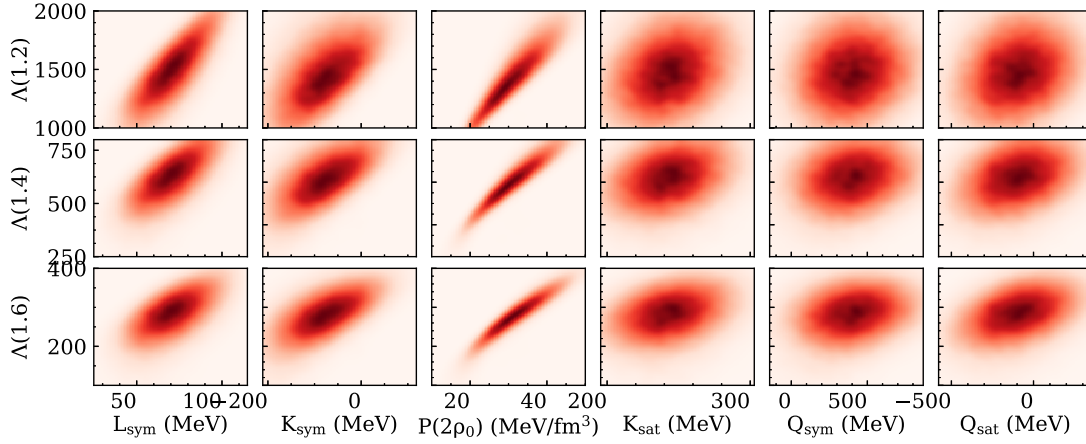
Figure 2.9: Bivariate distributions between deformabilities with NS of different masses and Taylor parameters. Correlation with tidal deformability is clearly seen with $L$, $K_{sym}$ and $P(2\rho_0)$.
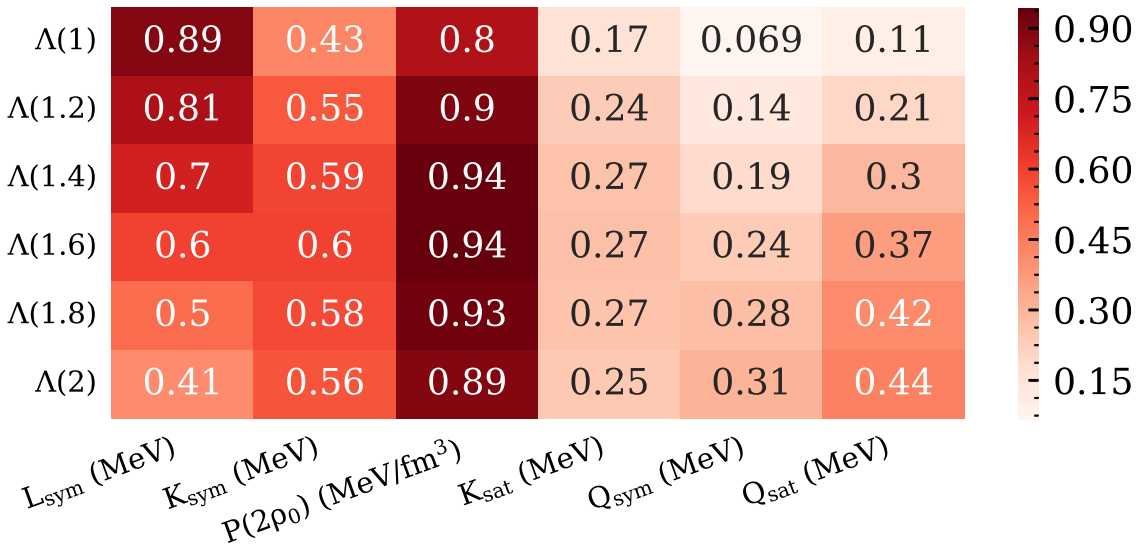


Figure 2.10: Pearson correlations for different NS masses.

$P(2\rho_0)$ is consistent with prior work [17, 33, 41, 87]. While this strong correlation is maintained for both heavy and light NS, the slope of the correlation becomes smaller reflecting the decrease in average values and variations of $\Lambda$ with stellar mass.

Such decrease is correlated with an increase in stellar compactness. Using the posterior distributions of Taylor expansion parameters, predictions can be made on the relation between
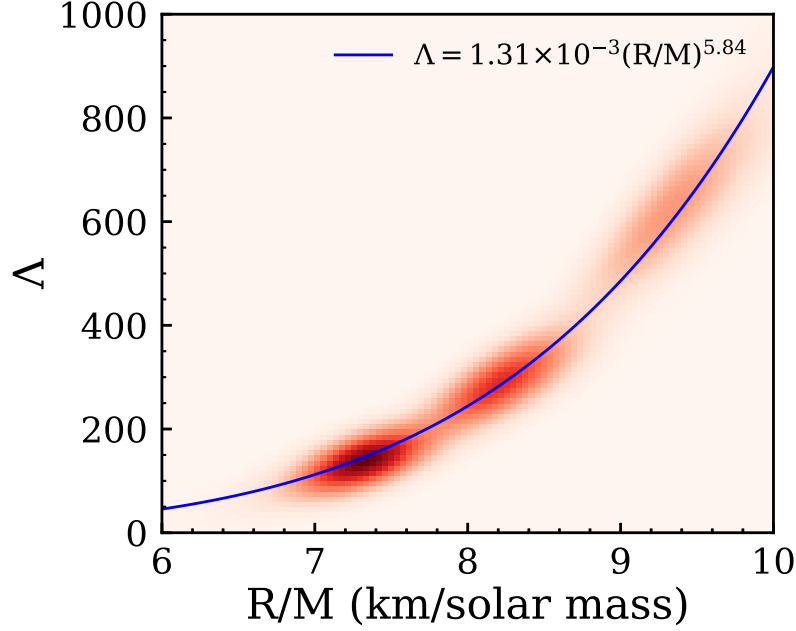
Figure 2.11: Tidal deformability vs. inverse compactness for 1.2, 1.4, 1.6, 1.8 solar mass NS.

stellar mass and inverse compactness ($R/M$). Fig. 2.11 shows tidal deformability plotted against inverse compactness, with calculation results for 1.2, 1.4, 1.6 and 1.8 solar mass NS all combined together. It is consistent with Eq. (1.9) where $\Lambda \propto k_2 (R/M)^5$. The best fitted power law has an index of 5.84 due to additional interdependence of tidal Love number $k_2$ and $R/M$. The result is consistent with Refs. [32, 88, 89].

We found that independently and in parallel, Ref. [73] conducts a very similar analysis using ELFc. Our work examines correlations between more parameters and our study extends to higher mass neutron star. Ref. [73] uses much wider priors while our prior is more restrictive and provide finer details in a smaller phase-space. In addition, they apply additional constraints on the EoS using data from $\chi$EFT approach and ISGMR collective mode. Even though their extracted $Q_{\text{sat}}$ and $K_{\text{sym}}$ values are consistent with our extracted values, details in the correlations are not the same. The subtle differences suggest that Bayesian analysis results depend on the choice of priors and constraints applied to the EoS.

# CHAPTER 3

# SπRIT DATA ANALYSIS

## 3.1  SπRIT experiment

Nuclear EoS has been studied with heavy-ion collision experiments where heavy-ions are accelerated by particle accelerator(s) and guided by magnets to collide with target nucleus. Particle detector(s) records the collision fragment distributions, from which observables are constructed from the data and compared to transport models. The properties of nucleus and constraints on nuclear EoS can then be inferred.

In the SπRIT heavy-ion experiment, the particle accelerators are provided by the Radioactive Isotope Beam Factory (RIBF) at RIKEN, JAPAN. Tin isotopes are accelerated to 270 AMeV. The target is an isotopically highly enriched stationary Tin foils and the main particle detector is the SπRIT time projection chamber (TPC). In this chapter, the configuration and working principle of the accelerators and SπRIT TPC will be briefly described. Details can be found in Ref. [90].

### 3.1.1  Radioactive Isotope Beam Factory (RIBF)

RIBF produces rare Tin isotope beams from relatively stable primary beams. This primary beam is created by accelerating the primary ion progressively by a linear accelerator (RILAC) and four coupled cyclotrons (RRC, fRC, IRC and SRC) to reach a beam energy of 345AMeV. The ions are guided to hit a rotating Be target, which breaks the primary ion down to smaller fragments, and in some events one of these fragments is the desired Tin isotope. For the creation of neutron-rich $^{132}$Sn and $^{124}$Sn beams, $^{238}$U primary ion is used and for more symmetric $^{112}$Sn and $^{108}$Sn beams, $^{124}$Xe is used.

The fragments are selected by the BigRIPS spectrometer, which is a series of dipole magnets, slits and wedge degraders arranged in such a way that only particles within a narrow range of magnetic rigidity ($B\rho = p/Z$, where $p$ is the momentum magnitude and $Z$ is the charge) can pass
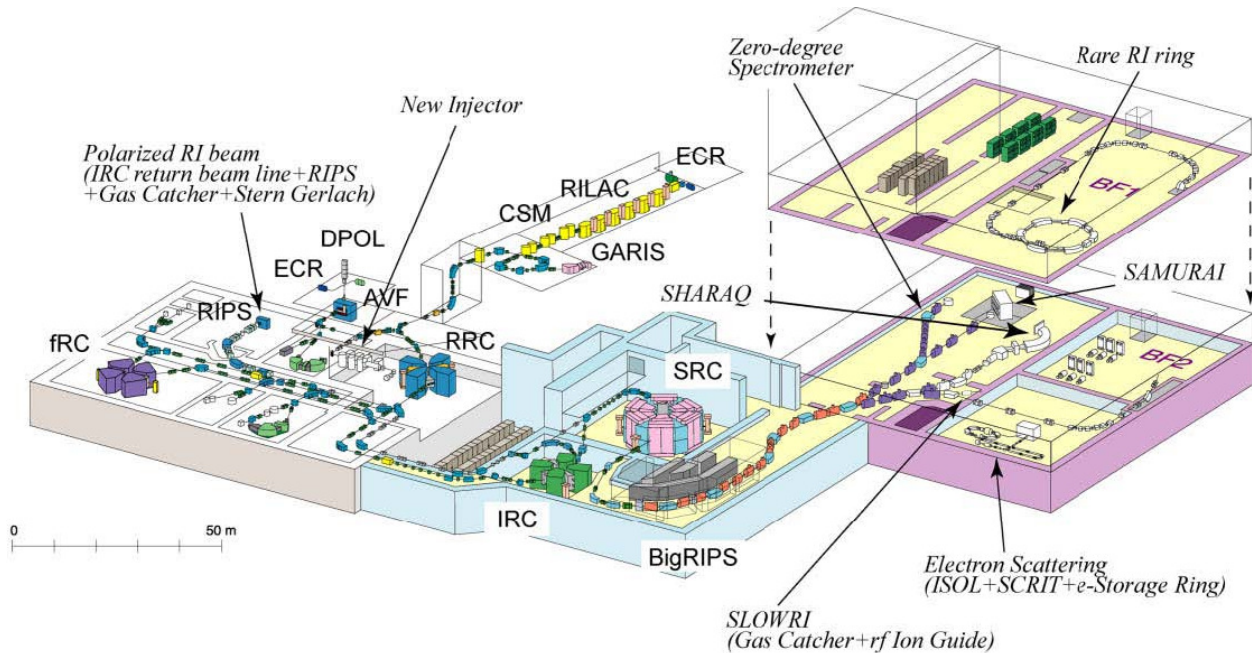
Figure 3.1: An overview of RIBF extracted from Ref. [5], with accelerators on the left, fragment separator BigRIPS in the middle and SAMURAI spectrometer on the top right.

through. It filters out most of the undesirable fragments, but some contaminating isotopes can still pass through. To select events from a particular isotope, scintillators and ion chambers are set-up along the beam line after the spectrometer. They measure the time-of-flight (ToF) and charge number (Z) of isotopes that reaches the S$\pi$RIT detector respectively. $B\rho$ is calculated from ToF information and magnet settings in BigRIPS, and when it is used in conjunction with the charge state information we can identify the isotope that passes through BigRIPS event by event. This beam selection process is described in Ref. [2]. In this work, only events from the desired Tin isotope are analyzed.

The configuration of RIBF is illustrated in Fig. 3.1. The BigRIPS guided the Sn beam towards SAMURAI spectrometer, inside of which was the S$\pi$RIT TPC.

### 3.1.2 S$\pi$RIT Time Projection Chamber (TPC)

The S$\pi$RIT TPC is a rectangular detector designed to measure momentum distributions of pions and other light fragments from a fixed target collision with an activae gas volume of dimensions
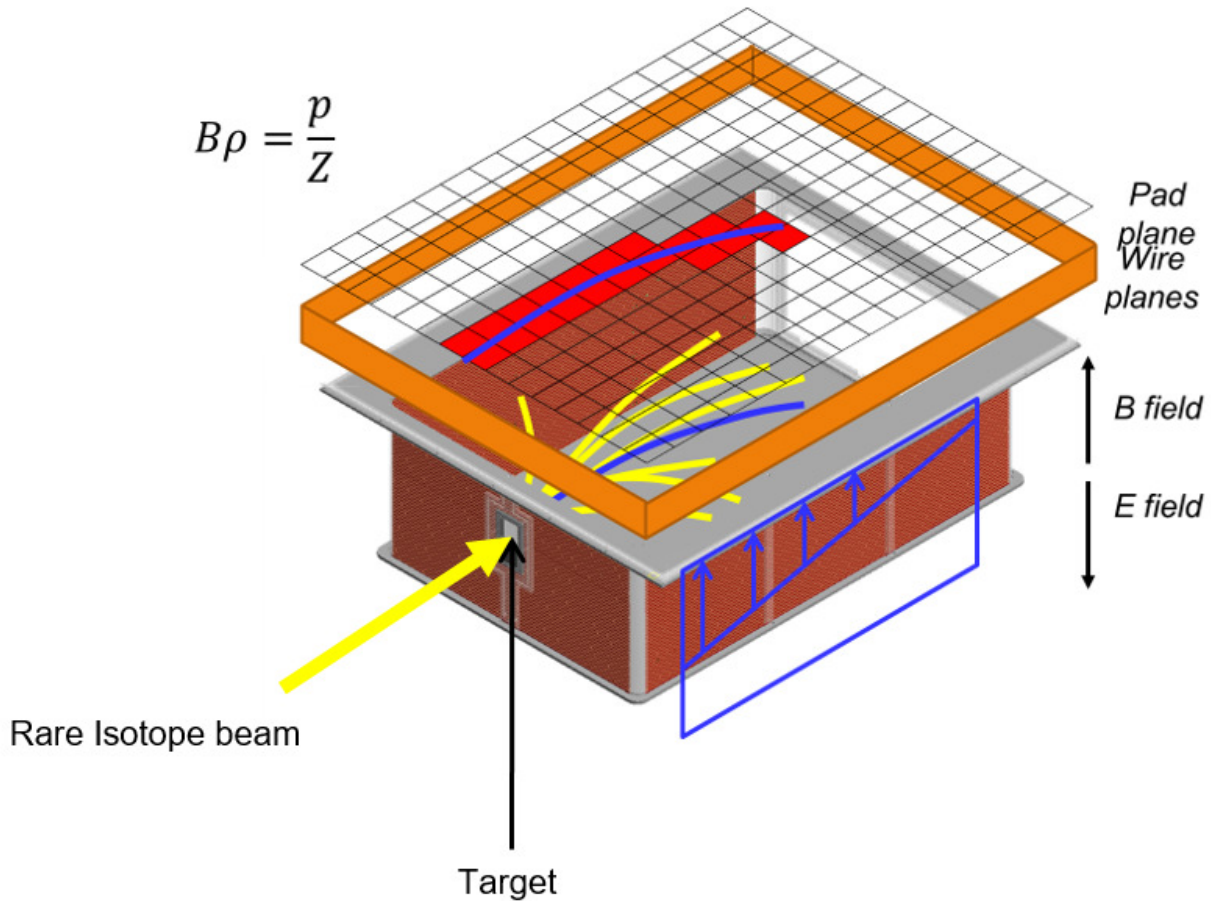
Figure 3.2: A cartoon illustration of SπRIT TPC. The pads are not drawn to scale.

86.2 cm × 51.3 cm × 134.4 cm (width, height, length). It was surrounded by auxiliary trigger detectors on both sides and downstream. It is placed inside the SAMURAI dipole magnet which provides a near uniform 0.5 T magnetic field for the TPC. Please refers to Ref. [91] for details of SAMURAI spectrometer.

Fig. 3.2 is a simplified cartoon that illustrates its working principle. The detection volume was filled with 90% Ar and 10% $CH_4$ (P10 gas) at atmospheric pressure. When charged particles pass through the detector volume, they interact with and ionize the gas molecules, leaving behind trails of free electrons and positive ions.

Magnetic and electric fields inside the detection volume force trailing electrons to drift upward and positive ions downward. The electric field is created by the walls of the TPC, called the *field cage*, which is made of PCBs and depicted as the brown vertical walls in Fig. 3.2. The field cage

consists of 50 vertically stacked layers of copper strips, with each layer wraps around the detection area horizontally and is electrically isolated from nearby layers. During operation, maximum voltage is applied to the top layer and gradually lowered voltages are applied to each successive lower layers. This potential gradient on the boundary creates a uniform electric field.

Once the drift electrons reach the top of the TPC, they enter the *wire plane*, which consists of three planes of *gating grid*, *anode wire* and *ground wire* from bottom to top. When drift electrons enter the volume between anode and ground wires, they are accelerated to speed high enough to ionize gas molecules by the large potential difference between these two layers. Electrons from these ionized molecules are also accelerated to create more electrons. This electron multiplying process is called *avalanche* and it amplifies the signal from the drift electrons, but a lot of unwanted positive ions are also created. They drift back into the detection volume by electrostatic force and if too many are presence, the uniform electric field will be distorted. To maintain the uniformity of electric field, the gating grid is placed below anode wire to prevent excessive electrons from entering the anode in the first place. One of the major source of excessive electrons is collision events that do not satisfy trigger conditions. The gating grid consists of a series of parallel wires. When trigger condition is not met, the grid is set to "close" configuration such that the voltages of the wires are staggered. Electrons approaching the grid are pushed towards and absorbed by gating grid wires with lower voltage. When trigger condition is satisfied, the grid is set to "open" configuration such that voltages of all wires are identical. This allows electrons to move upward unimpeded. Simulation shows that average transparency is 100% in "open" position and 0% in "close" position [8]. The movement of drift electrons when gating grid is "open" and "close" are illustrated in Fig. 3.3.

The induced electrons from avalanche enters the *pad plane*, which consists of pads (pixels) that detect the amount of drifting electrons they come into contact with. There are 112 layers of pads along $z$-direction and 108 rows along $x$-direction, with the size of each pad being $1.2\,\text{cm} \times 0.8\,\text{cm}$ (length, width). Signal from all pads can be combined to trace the two-dimension projection of the fragment trajectory along the horizontal ($x$-$z$) plane. This is illustrated in Fig. 3.2 where the
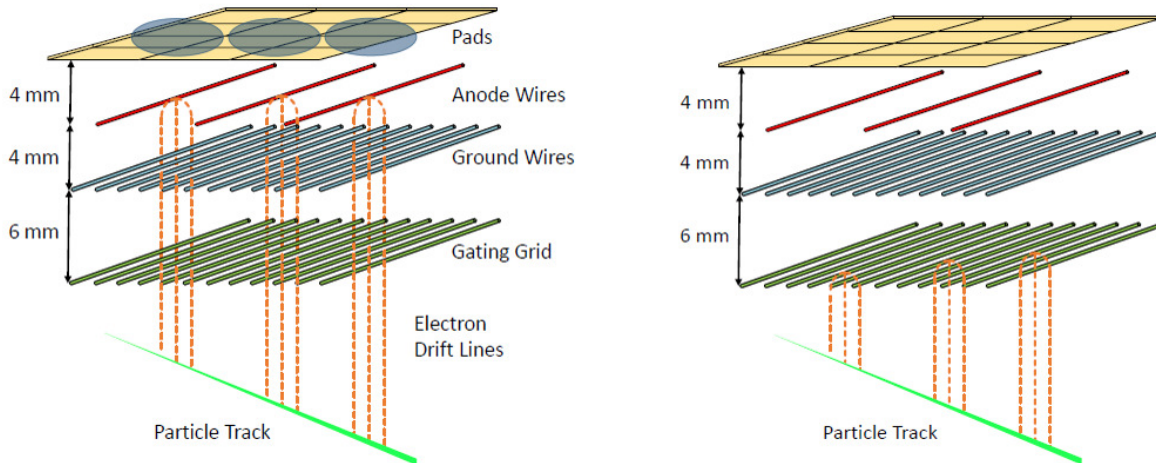
Figure 3.3: Cartoon depiction of grating grid in "open" configuration (left) and "close" configuration (right).

red cells corresponds to pads with signal and the blue curve corresponds to the two dimension projection of a fragment track on the pad plane. Vertical information for each track can be inferred from the signal detection time on each pad relative to the start counter time-stamp. Electrons drift at a constant speed of $5.42\,\text{ns}/\mu\text{m}$ in S$\pi$RIT TPC [92] so electrons that originate from lower vertical position takes longer to reach the top.

Trajectories of charged fragments inside the TPC are curved due to magnetic field. The curvature of each track is indicative of their corresponding momentum over charge ($p/Z$) value. With appropriate curve fitting routine, we can reconstruct momentum distributions of various fragments. Such procedures will be described in details in later chapters.

### 3.1.3 Beam Drift Chambers (BDC)

To boost the momentum distributions from laboratory frame to center-of-mass frame, we need to measure the projectile angle of incidence for each event. This is achieved with a pair of Walenta-type detectors called Beam Drift Chambers (BDCs). They are placed upstream of the target along the beam pipe.

These chambers consist of two sets of Parallel Plate Avalanche Counters (PPACs). They are approximately 1 m apart along the beam line. PPAC records the location of the beam particle as

it passes through, therefore two readings from the two PPACs can be interpolated to estimate the angle of incidence. The uncertainty in BDC beam angle of the order of magnitude of 0.1 µrad [2].

### 3.1.4   KYOTO array and KATANA veto bars as trigger detectors

The four major triggers in the S$\pi$RIT experiment are the Scintillating Beam Trigger (SBT), Active Veto Array, KYOTO Multiplicity array and KATANA veto bars. Given that the primary objective of the experiment is to measure pions created in central collisions [93], the triggers are set-up to favor central collision events and disproportionately rejects peripheral events.

SBT is located 4.5 m upstream of the detector. It is a plastic scintillator that serve as a start counter when a beam particle registers a hit. Active veto array consists of four plastic scintillators immediately upstream of the target forming a rectangular shape with a rectangular hole in the middle. The hole allows for beam particles with small angle of incidence from BigRIPS to pass through. Veto array is hit only if beam particle arrives off-center so events with a signal from veto array are rejected. These two detectors are set-up to maintain beam quality on recorded events.

The remaining two detectors, KYOTO array and KATANA veto bars, are set-up to disproportionately accept central events by selecting high multiplicity and low projectile mass events. They are depicted as the transparent walls surrounding the TPC in Fig. 3.4. These conditions skew the multiplicity distribution away from what is expected from geometric cross-section.

The KYOTO multiplicity arrays are the two arrays flanking the left and right sides of the S$\pi$RIT chamber. Each side consists of 30 tightly packed rectangular plastic scintillator bars with dimensions of $450 \times 50 \times 10 \, \text{mm}^2$. The hardware specifications are detailed in Ref. [94].

Krakow KATANA veto bars are three sintillating paddles at the downstream end of the S$\pi$RIT chamber, shifted slightly left of the beam axis to intercept the heavy residue traversing the magnetic field [2, 95]. The signal amplitude is proportional to the charge state $Z$ of the residue. The trigger condition is to only accept events where charge of heavy residue hitting KATANA is lower than $Z \approx 20$ and four or more KYOTO bars are being hit simultaneously.
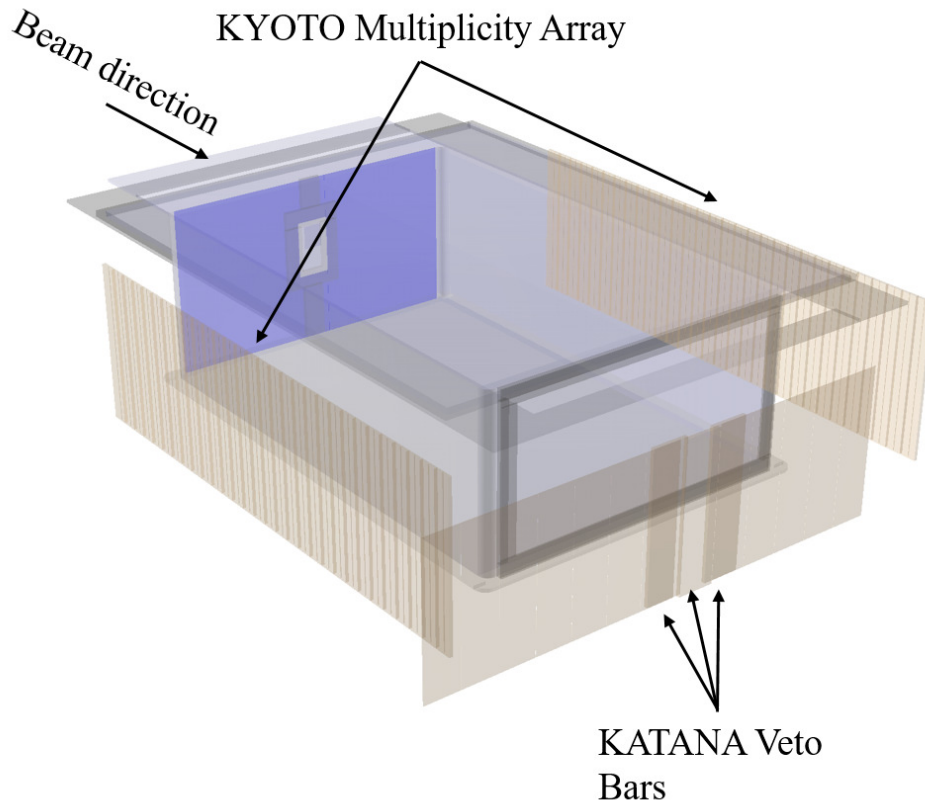
Figure 3.4: Illustration of KATANA and KYOTO arrays. KYOTO arrays surround the chamber on the left and right sides and the KATANA array is immediately downstream. For the KATANA array, the two narrow strips with deeper shade of brown and the one between them are the veto paddles used in trigger condition.

## 3.2 Data analysis

The S$\pi$RITROOT framework is developed to analyze data from S$\pi$RIT TPC [96]. It is developed based on the FAIRROOT framework which offers modular design pattern with different tasks running sequentially to convert raw electronic signal to physical observables step-by-step. These tasks can be classified into two groups: track level tasks and particle level tasks. The former deals with recognizing tracks from pad signals and the latter deals with reconstructing observables given the fitted tracks. Track level tasks for all fragments and particle level tasks for pions are detailed in Refs. [2, 8] so they are only reviewed briefly here. Particle level tasks for light fragments are newly developed and will be discussed in more details.

## 3.3 Track Level analysis

The following tasks are required to recognize particle tracks from pad signals,

1. Decoder task.

2. Pulse Shape Analysis (PSA) task.

3. Helix Finding task.

4. Correction task.

5. Space charge task.

6. Track fitting and vertex reconstruction (GENFIT task).

These tasks are run sequentially, in the order that is listed above. Each task has access to output of any tasks that are executed before itself.

### 3.3.1 Decoder, PSA and Helix and correction task

The *Decoder task* translates the raw data in binary files into a C++ readable data structure called the *STRawEvent* class [6]. This class contains multiple instance of *STPad* class, each corresponds to an individual pad. STPad class encapsulates the digitized electric pulses.

The *PSA task* uses data from STRawEvent class to identify the amount and arrival time of drift electrons for all pads. Pulse from a single packet of drift electrons follows a standard shape whose height is proportional to the amount of electrons in that packet. Since it is common to have multiple tracks passing under a pad at different height, the detected pulse is often a linear combination of multiple standard pulses, each with different amplitudes and different rise time. PSA Task de-convoluted the combined signal into its constituent single pulses as illustrated in Fig. 3.5. We called each of these pulse a *hit*. The fitted amplitude and start time will be stored in a data structure called the *STHit* class. Vertical location is then calculated from the start time.

To the first order approximation, locus of charged particles under magnetic field is the arc of a circle. *Helix task* uses Riemann track finding algorithm to group hits from each event into disjoint
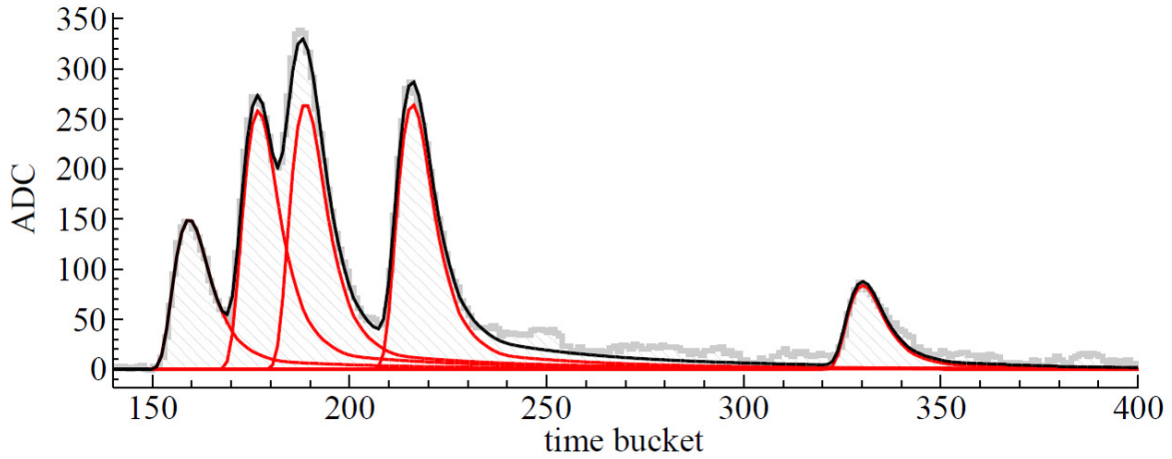
Figure 3.5: An example result from pulse analysis. Taken from Ref. [6].

sets such that hits from each set forms an arc [97]. The fitted arc and the grouping of hits are stored in another data structure called *STHelixTrack* class.

The next task is the *correction task* which extends the dynamic ranges of $dE/dx$. The signal strength in some pads are off-scale high (i.e. the digitized signal saturates at the maximum ADC channel) which renders its energy loss information unreliable, but usually such pads are surrounded by multiple pads with lower signal amplitude. Avalanche electrons spread across an area and these nearby pads detect the tails of the electron distribution. The correction task uses signals from these nearby pad to estimate the expected signal amplitude on the saturated pads [98].

### 3.3.2 Space Charge effect

Space charge effect is a distortion caused by the accumulation of positive ions in the detection region. Reaction cross-section of Sn + Sn collision is so small that 98% of incoming projectile passes through the target foil without a collision [92]. When these un-reacted and highly charged projectiles transverse the detector volume, they ionized a lot of gas molecules. The ionized electrons are pushed upwards by the E- and B-field. They drift relatively quickly and are promptly removed by gating grid or anode wire. The massive positive ions, however, drift downward at much slower speed. Ions from a projectile do not have time to clear the height of the TPC before the next
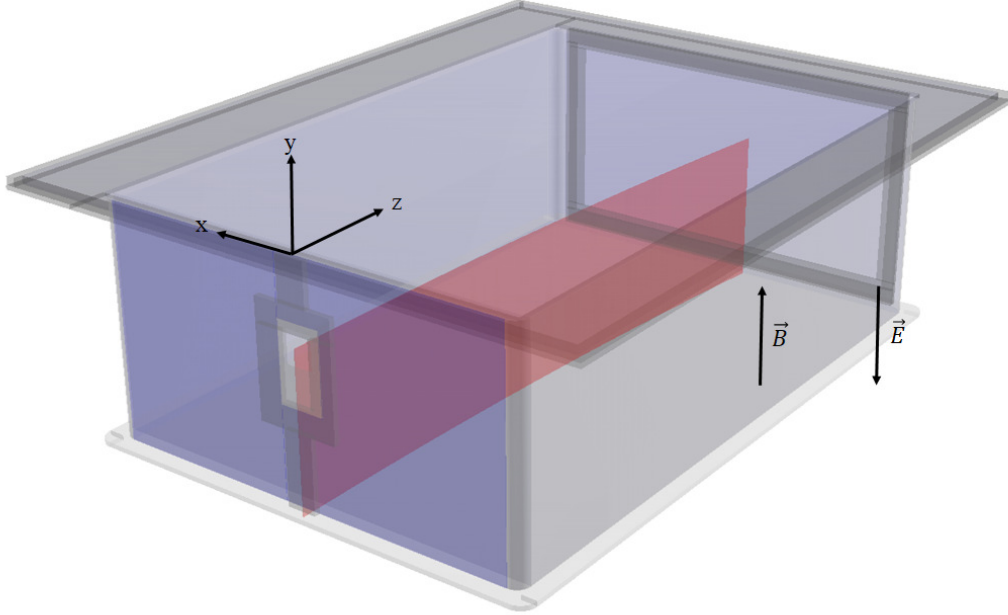
Figure 3.6: The drak red sheet illustrates the expected approximate shape of the positive ion distribution inside the S$\pi$RIT TPC.

projectile enters the detector, which causes ions to accumulate. The resultant charge configuration can be approximately described as a sheet charge extending downward from the beam track as Fig. 3.6 illustrates. The figure also shows the coordinate systems for S$\pi$RIT data, where the origin is located at middle of the front edge of the active pads and at the same height as the pad-plane. The sheet charge is expected to be approximately uniform as drift velocity of ions is constant.

Their presence in the detection area distorts the otherwise uniform E-field. This slight distortion has negligible impact on trajectories of reaction fragments due to their strong inertia, but the same cannot be said for electron drift. Electrons acquire a "side-way" component to its drift velocity which distort the observed curvatures on pad plane. Other TPCs, such as STAR, detect such distortion directly with lasers [99], but such equipment was not available during the S$\pi$RIT experimental campaign. Below are two strange features from our data that can be attributed to space charge effect.

Fig. 3.7 is the proton center of mass momentum distribution for forward emitting (i.e. $P_{\text{CMz}} > 0$)

38
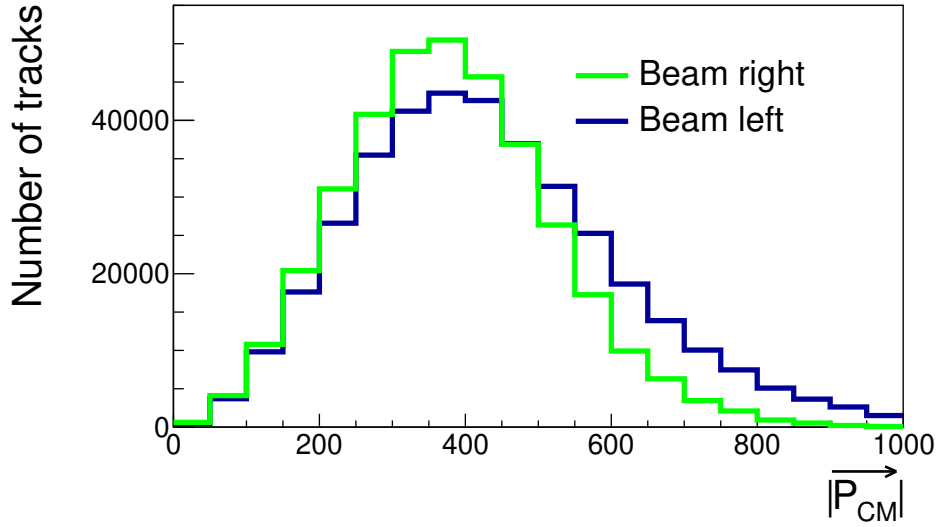
Figure 3.7: Proton momentum distribution when gated on particles with $P_x > 0$ (Beam left) and $P_x < 0$ (Beam right). The two distributions are expected to be identical due to cylindrical symmetry of the reaction.

tracks. The procedure needed to identify proton, correct for efficiency and transform into center of mass frame will be discussed later in Section 3.4. Only tracks with azimuth of $-30° < \phi < 20°$ (beam left) are selected in the blue distribution and only tracks with azimuth $160° < \phi < 210°$ (beam right) are selected in the green distribution. It is important to note that the $x$-axis is defined with respect to detector orientation instead of the reaction plane for each event, and $x$-axis points to the left when looking downstream of the beam. The coordinate system is illustrated in Fig. 3.6 above the target entrance. The two distributions should be similar due to cylindrical symmetry arguments, but they are not.

Another curious feature is found when distance to vertex distribution is examined. The reconstructed tracks can be extrapolated back to the target plane and the extrapolated point should agree with the measured vertex location from BDC. The displacement vector between the extrapolated vertex and the measured BDC vertex location is denoted as $\vec{\Delta V}$. The definition of this vector is illustrated in Fig. 3.8a.

The distribution of $x$-component of $\vec{\Delta V}$, denoted as $\Delta V_x$, should be Gaussian-like with peak
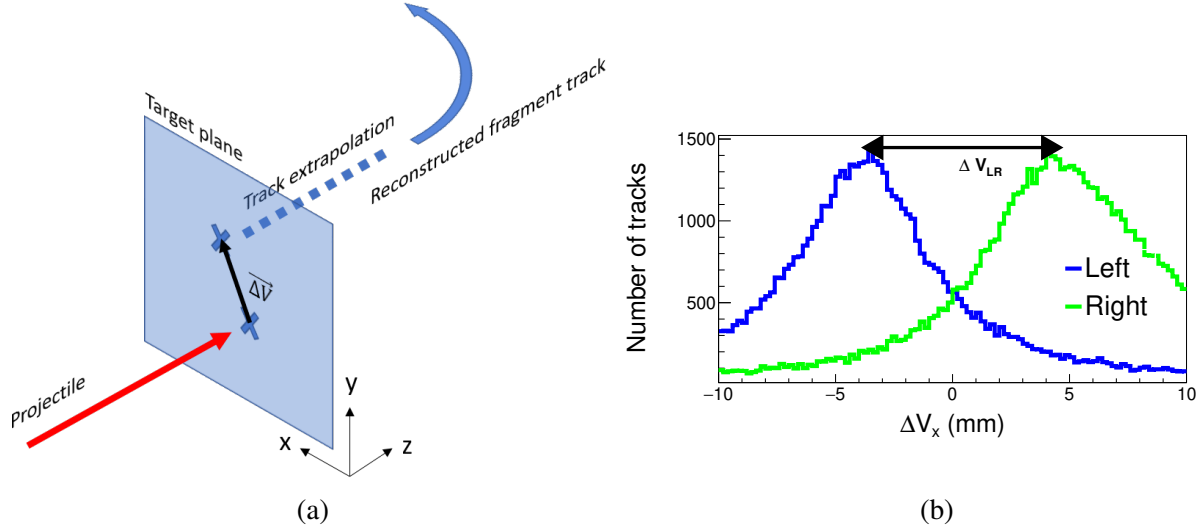
Figure 3.8: (a): Cartoon illustration of the definition of $\vec{\Delta V}$. (b): The distribution of $DeltaV_x$ for particles with $\theta > 40°$. Blue histogram is drawn with tracks going beam left and green histogram with tracks going beam right. The definition of $\Delta V_{LR}$ is illustrated on the plot as the distance between the peak locations of blue and green histograms.

centers at zero. Our data, however, shows that the peak location changes with on track azimuth. Fig. 3.8b shows the $\Delta V_x$ distributions for fragments going in beam left and beam right direction for tracks with polar angle $\theta > 40°$, and neither distribution peaks at $0\,\text{mm}$.

Evidence that supports space charge as the causative effect for these features can be found by correlating $\vec{\Delta V}$ with beam intensity. Denote $\Delta V_{LR}$ as the separation between the two peaks of $\Delta V_x$ distributions in Fig. 3.8b. It is observed that $\Delta V_{LR}$ is directly proportional to the beam intensity of the run. This correlation is shown in Fig. 3.9 and since the strength of space charge effect is also proportional to the beam intensity, it is an indication that our observed features are related to space charge.

If space charge is indeed responsible for our observations, we should be able to correct for it as the effect of space charge is described by well established equations: To begin with we need to solve for the distorted E-field with Poisson's equation. The field follows Dirichiet boundary condition as field cage fixes potential on boundaries of the TPC. The sheet charge distribution is approximated as uniform and its magnitude is denoted as $\sigma_{\text{SC}}$, whose value will be determine later. The curvature of the sheet is easily calculated as it follows the trajectory of un-reacted Tin projectile. After that
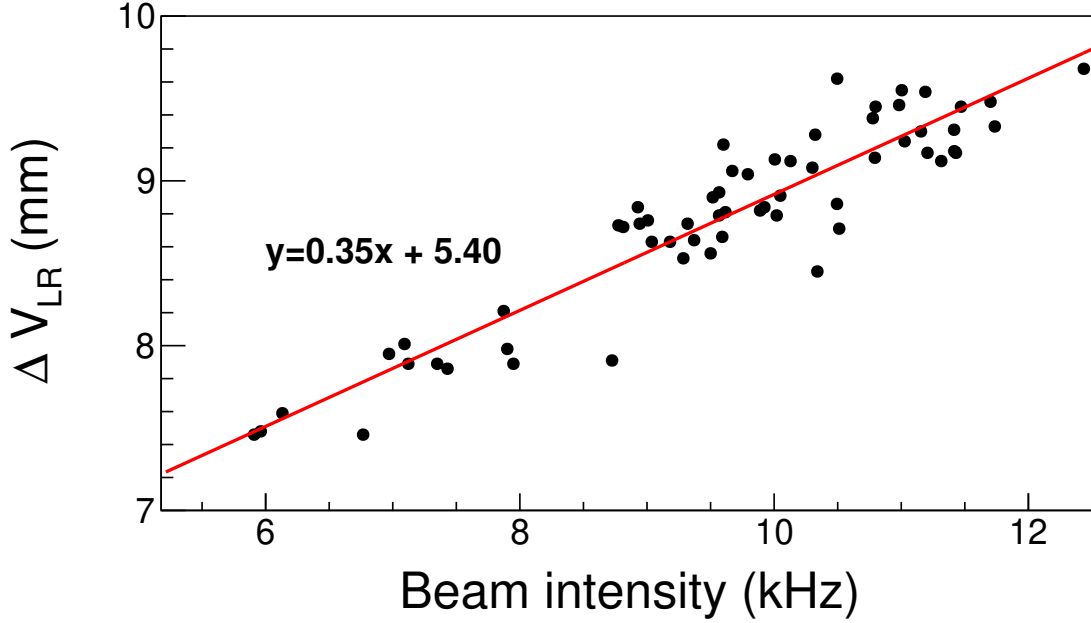
Figure 3.9: Difference in peak location $\Delta V_{LR}$ is plotted against beam intensity and it shows a strong positive correlation.

we calculate the expected lateral electron movement with Langevin equation,

$$\frac{d\vec{x}}{dt} = \frac{\mu}{1 + (\omega\tau)^2}\left(\vec{E} + \omega\tau\frac{\vec{E} \times \vec{B}}{|\vec{B}|} + \omega^2\tau^2\frac{\vec{E} \cdot \vec{B}}{|\vec{B}|^2}\vec{B}\right). \tag{3.1}$$

This equation describes the averaged motion of charged particles moving through gaseous medium under E- and B-field. $\omega = eB/m$ is the cyclotron frequency, $\tau$ is the mean free time between collisions and $\mu = e\tau/m$, where $m$ and $e$ are the mass and the signed electric charge of electrons/ions respectively. This equation can be solved to find the expected amount of literal movement acquired by drift electron when initial conditions are given, and during track reconstruction the measured hit points will be shifted literally in the opposite direction to compensate for space charge distortions.

The remaining loose end is the determination of $\sigma_{SC}$. Since $\Delta_{LR}$ is expected to center at zero when space charge effect is corrected, we vary $\sigma_{SC}$ in track reconstruction until $\Delta_{LR} = 0$. This procedure of varying $\sigma_{SC}$ is computationally intensive as track reconstruction algorithms need to be run multiple times for each run, so only five runs with wildly different beam intensities are
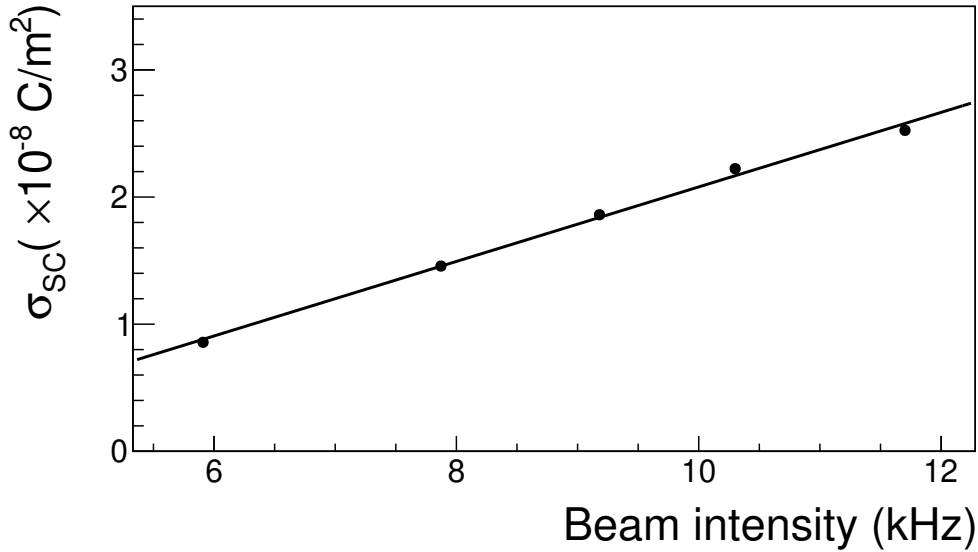
Figure 3.10: The recovered sheet charge density $\sigma_{SC}$ is plotted against beam intensity for five selected runs. The fitted linear line is used to approximate the sheet charge magnitude for the other runs.

determined this way. The $\sigma_{SC}$ for these five runs are plotted against beam intensities in Fig. 3.10. This linear relation will be used as an estimation of $\sigma_{SC}$ for all other runs. When center of mass momentum for proton is plotted after space charge effect correction in Fig. 3.11, the distributions of beam left and beam right particles now agree with each other.

### 3.3.3 Leakage Space Charge effect

Due to design issues, the gating grid does not extend all the way to the end of the field cage. The gap between the end of gating grid and field cage allows secondary electrons from highly charged heavy residue fragment to leak into the avalanche region as Fig. 3.12 illustrates. The induced positive ions leak back into the field through the same gap. Ions pour out of the gap continuously as they drift steadily from the top to the bottom of the TPC, forming a sheet like positive charge configuration. This type of sheet charge will be referred to as "leakage" space charge $\sigma_{leak}$ to distinguish itself from the "beam" space charge described in previous section.
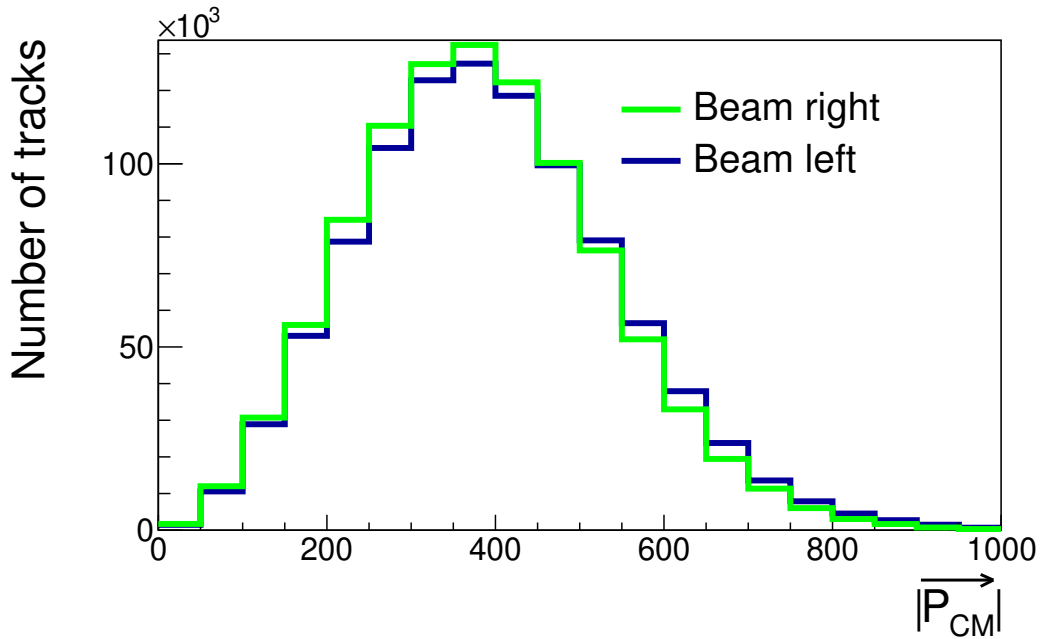
Figure 3.11: Center of mass proton momentum distribution for experimental data with $P_z > 0$ after space charge effect is corrected. "Beam left" histogram is populated only with tracks emitted at $-30° < \phi < 20°$ and "Beam right" histogram is populated with tracks emitted at $160° < \phi < 210°$. The two histograms agree with each other much more than in Fig. 3.7.
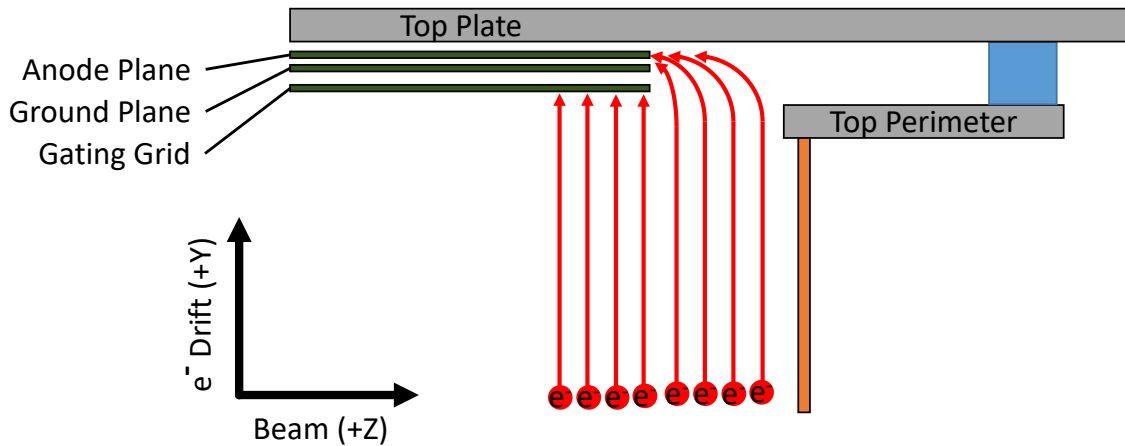


Figure 3.12: Sketch of gating grid near the rear end of S$\pi$RIT TPC, taken from Ref. [7]. Electrons, represented as the red points, leak into the anode plane from the gap between gating grid and top perimeter and induce position ions.
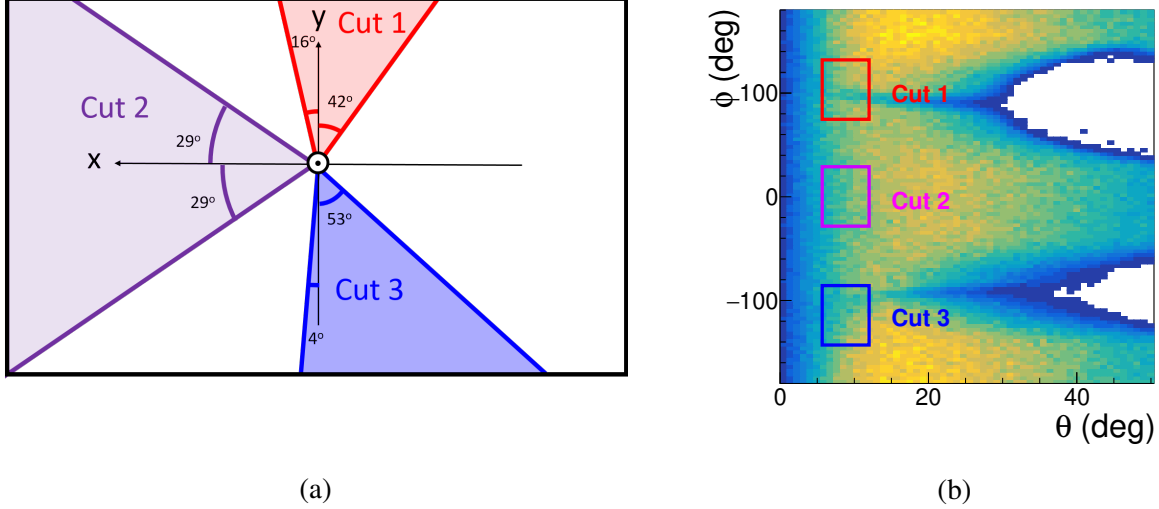
Figure 3.13: (a): The three azimuthal angle cuts when viewed into the beam axis. Beware that $x$-axis points toward the left in our right-handed coordinate system and $z$-axis points into the page, as indicated by the circle with a dot in the center of the image. (b): The three cuts with their respective azimuth and polar angle conditions are drawn as red, magenta and blue rectangle on $\phi$ vs. $\theta$ phase space. The background colored histogram is the proton phase space distribution from experiment. See text for details. We will revisit this phase space plot in Fig. 3.21

The presence of leakage space charge means that even after correcting for beam space charge effect, experimental momentum distributions of particles at some phase space regions are still unreasonable. This can be demonstrated by comparing momentum distributions in three different azimuthal regions in Fig. 3.13a where Cut 1 corresponds to $74° < \phi < 132°$, cut 2 corresponds to $-29° < \phi < 29°$ and cut 3 corresponds to $-86° < \phi < -143°$.

With an ideal detector, the momentum distributions in all three cuts should be identical due to cylindrical symmetry. With S$\pi$RIT TPC, however, we expect momentum distributions to agree with each other only when polar angle cut of $6° < \theta < 12°$ is imposed because tracks with large polar angle suffer from geometric coverage issues. The TPC is shorter than it is wide, so large polar angle tracks with $\phi \approx \pm 90°$ (move sideways) will leave a shorter trail of ionized electrons in the field cage than those with $\phi \approx 0°$ or $\phi \approx 180°$ (move up or down). Shorter tracks are reconstructed less efficiently due to the lack of hit points. Tracks with small polar angle do not escape from the sides so the average track length in the three cuts should be similar with the polar angle condition. Fig. 3.13b shows the three cuts in $\phi$ vs. $\theta$ plots, with experimental proton distribution of $^{132}$Sn +

44
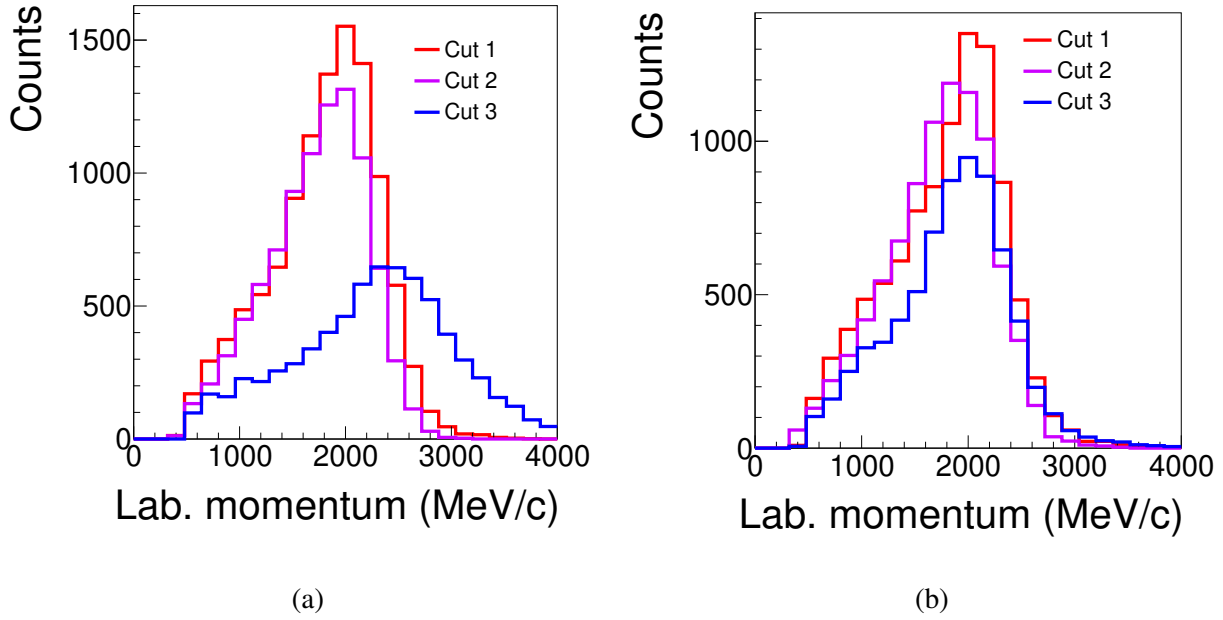
Figure 3.14: Triton momentum distributions in the three azimuth cuts at $6° < \theta < 12°$ after space charge correction is applied. (a): Track reconstructed with all available hit points. (b): Track reconstructed only with hit points at $z \leq 100\,\text{cm}$.

$^{124}$Sn with number of clusters $> 15$ and distance to vertex $< 15$ (the definition of these conditions will be detailed in Section 3.3) is plotted in the background. Unfortunately, even with $6° < \theta < 12°$ imposed, the momentum distribution in cut 3 still looks different from that in cuts 1 and 2, contrary to our expectation. The Triton distributions in all three cuts are plotted in Fig. 3.14a. Triton is selected as it has the highest average $p/Z$ value among all light fragments and the discrepancy is the most prominent.

Although the behavior of both leakage and beam space charge can be described by Eq. (3.1), they affect tracks in different phase space regions due to differences in their charge configuration. The expected shapes of the two sheets are shown in Fig. 3.15 with leakage space charge located at the rear end of the detector, therefore hit points in the forward half of the detector should not be affected by leakage charge. Furthermore, charge density of leakage space charge is much higher than beam space charge due to the magnifying effect of the avalanche. Detailed analysis in the later sections reveals that the charge density of leakage space charge is 9.8 times that of normal beam
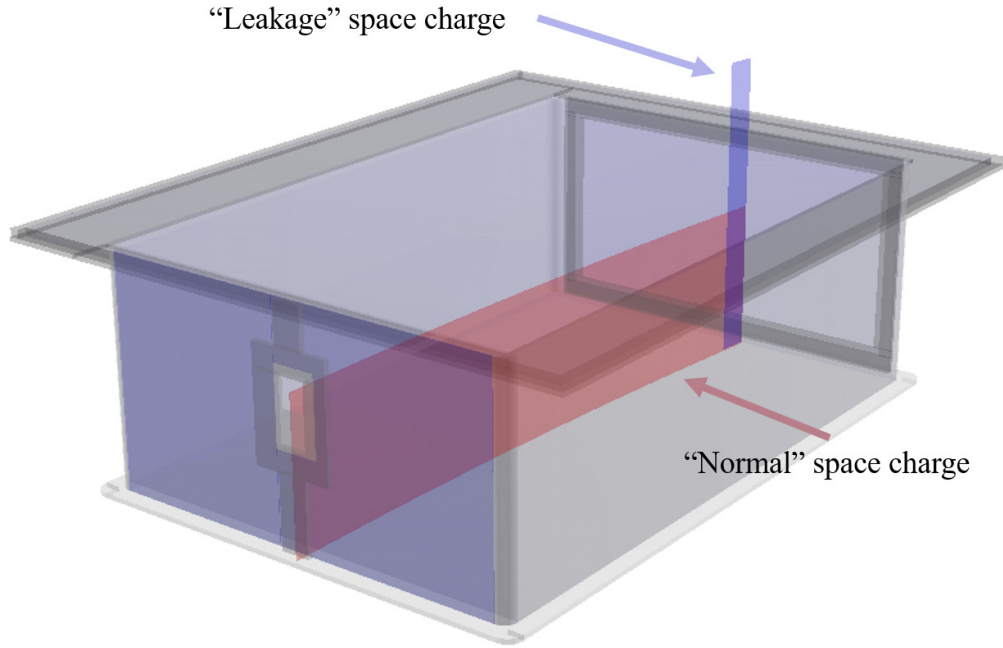
Figure 3.15: Approximate shape of the leakage sheet charge and normal sheet charge. The width of the leakage space charge is only 3.96 cm and extend all the way from top to bottom of the TPC.

space charge.

There is strong evidence that leakage space charge is the cause of the discrepancy in Fig. 3.14a. First and foremost, most detector distortions, such as the beam space charge and geometric ineffi-ciencies, have been corrected for or circumvented with our correction algorithms and polar angle cuts. Second, if we plot Fig. 3.14a again but with hit points beyond $z = 100$ cm discarded during track reconstruction, we get Fig. 3.14b and the discrepancy in momentum distributions among the three cuts are eliminated. The causative agent of the distortion must be located at the downstream end of the detector. Third, if we include additional leakage sheet charge in the space charge correction algorithm, it eliminates the discrepancy without discarding any hit points.

To incorporate leakage charge into space charge correction, we need to estimate its shape and charge density. The shape, as illustrated in Fig. 3.15, is approximated as the last 3.96 cm of normal beam sheet charge but extended all the way to the top of the TPC. Charge estimation is more complicated as the procedure in Section 3.3.2 for beam space charge cannot be used for leakage

space charge. In previous section, $\sigma_{SC}$ is varied until $\Delta V_{LR} = 0$, but this cannot be done for leakage charge as it is located at the downstream side of the detector while the vertex is located at upstream. As an alternative, we will vary the leakage charge density until the reconstructed momentum remains unchanged before and after discarding hit points downstream.

The reconstructed Triton momentum in cut 3 changes as the $z$ coordinate threshold varies, the threshold beyond which hit points are discarded. When reconstructed Triton momentum with a particular $z$ threshold is plotted against that with another $z$ threshold track-by-track inside cut 3, we get a two-dimensional distribution. The two dimensional plot needs to be simplified such that results with different $z$ thresholds can be overlaid on a single graph for direct comparison. To do this, the distribution is cut into slices along $x$-axis and only the mean y-values is shown for each $x$-slice. For comparison sake, momentum reconstructed with various $z$ thresholds are all against that with a standard $z < 100$ cm threshold, the threshold at which momentum distributions in all three cuts agree with each other. Fig. 3.16a is the comparison plot with different $z$ thresholds, and the slope of each line will be referred to as "Triton consistency". Without leakage space charge, Triton consistency should always be one. Deviation from unity indicates distortions in track reconstruction. Triton consistencies are plotted against their respective $z$ thresholds in Fig. 3.16b, which shows that it is monotonically increasing with $z$-cut value, with a sudden change in slope at $z$-cut $= 120$ cm.

The goal is to vary the leakage charge density in the space charge correction task until Triton consistency stays at one regardless of $z$ threshold values. It is computationally expensive to estimate $\sigma_{\text{leak}}$ for each run, so instead we assumed that $\sigma_{\text{leak}} \propto \text{Beam rate} \propto \sigma_{\text{beam}}$. This approximation stems from the fact that leakage charge is induced by beam particles. The proportionality factor between $\sigma_{\text{leak}}$ and $\sigma_{\text{norm}}$, denoted as $a$, is assumed to be constant across runs with different beam-intensities. Fig. 3.17a demonstrates how Triton consistency vs. $z$-cut changes with $a$ by scanning through multiple test values.

The desired slope and y-intercept for all plots in Fig. 3.16b are zero and one respectively. These two conditions allow us to determine $a$ in two ways: Interpolate slope as a function of $a$ and find

47
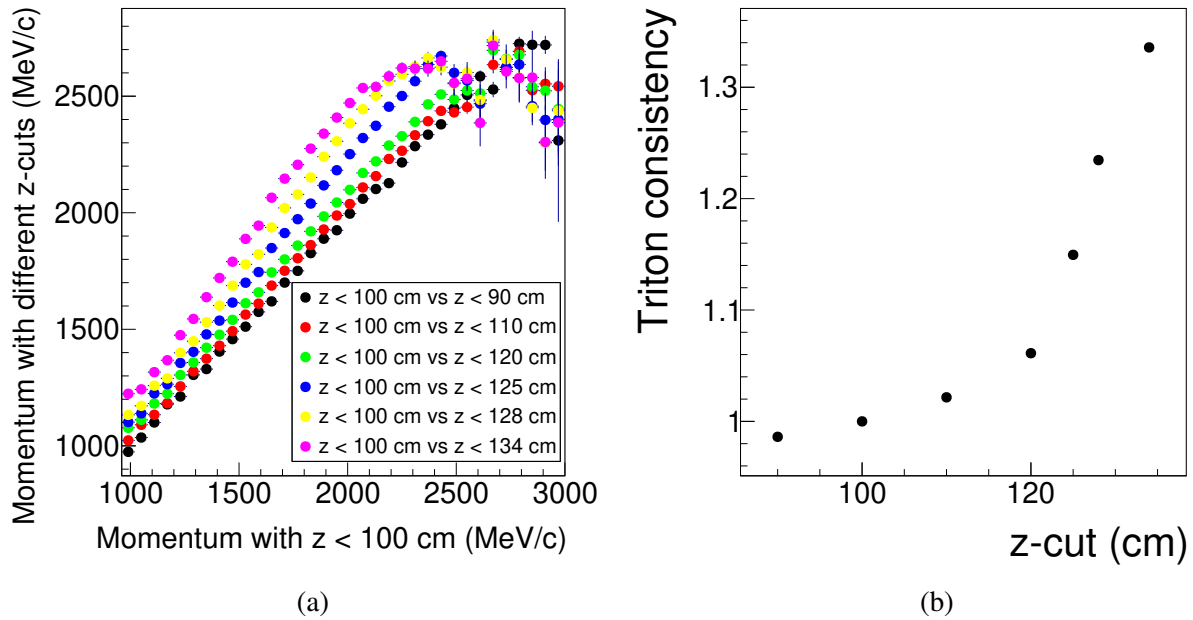
Figure 3.16: (a) shows the mean values for the sliced distributions of Triton momentum reconstructed with different $z$-thresholds against that with a standard $z$-threshold of 100 cm. (b) shows the slopes (labelled as Triton consistency) for each line in (a) as a function of their respective $z$-threshold.
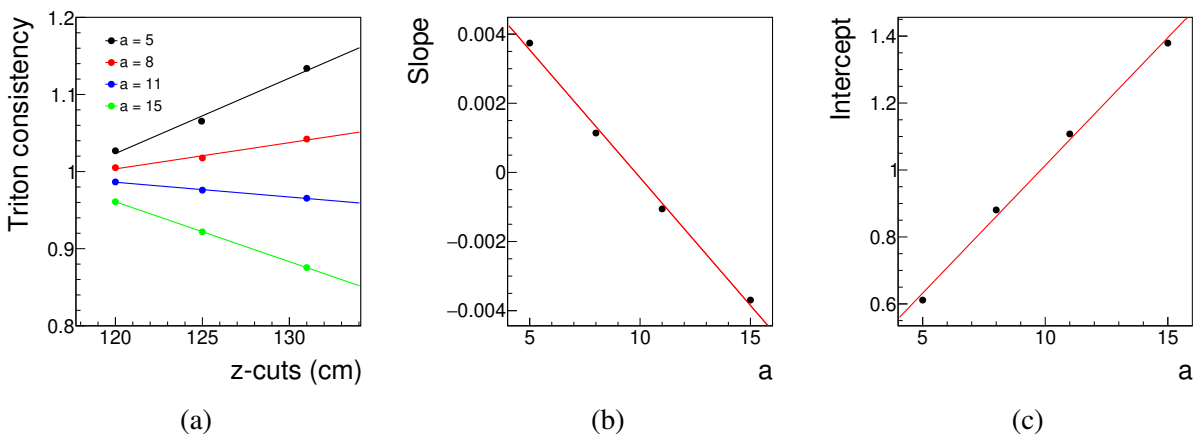


Figure 3.17: (a): Triton consistency vs. $z$-threshold when different values of $a$ are used. Ideally we want $a$ to be set such that Triton consistency is always one at all $z$-thresholds. (b) and (c): Slopes and intercepts of the linear fits of the four lines in (a).
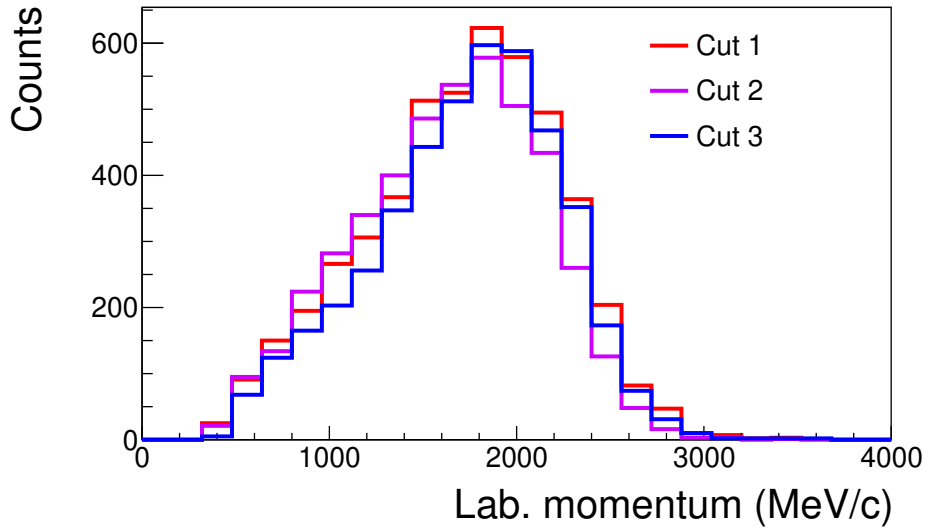
Figure 3.18: Same as Fig. 3.14 (a), but leakage space charge has been corrected with $a = 9.8$.

where slope = 0 corresponds to or interpolate y-intercept as a function of $a$ and find where intercept = 1 corresponds to. The former is performed in Fig. 3.17b and the latter is performed in Fig. 3.17c. Both methods yield $a = 9.8$. It is verified in Fig. 3.18, which is the same as Fig. 3.14a but with leakage correction performed at $a = 9.8$, that the correction is able to eliminate the discrepancy in momentum distributions. The gating grid is modified after the last experiment and extends to the end of the field cage [7]. Future experiments involving SπRIT TPC will not suffer from leakage space charge distortion.

### 3.3.4 GENFIT task

The corrected hit points are passed onto the final *GENFIT task*. It uses a well established tracks fitting routine called GENFIT to reconstruct the momentum for each track [100]. It offers greater reconstruction accuracy than Helix task as it takes energy loss in the medium and non-uniformity of the magnetic fields into account. The grouping of hits and rough momentum estimates from Helix task will be used as initial guess for GENFIT. Another function of GENFIT task is to find the location of vertex using the RAVE vertex finding package [101]. Events where vertex is located

too far upstream or downstream of the target plane will be rejected from the analysis.

Hit clusters that are too close to the edges of the detector volume are not used for track recognition as they suffer from edge effects that render their cluster location unreliable [8]. Furthermore, there are too many clusters close to each other near the reaction vertex. The chances of these clusters being misidentified for the wrong track are high, so they are also not used in the track fitting. For a cluster to be used in momentum reconstruction, all of the following conditions must be satisfied,

$$|x| \leq 420 \,\text{mm}, -522 \,\text{mm} \leq y \leq -64 \,\text{mm},$$

$$\left(\frac{x}{120 \,\text{mm}}\right)^2 + \left(\frac{y - y_{\text{beam height}}}{100 \,\text{mm}}\right)^2 + \left(\frac{z - z_{\text{target foil}}}{220 \,\text{mm}}\right)^2 > 1.$$

The numbers are expressed using the coordinate system in Fig. 3.6. The condition on the second line represents an ellipsoid cut centers at reaction vertex. Geometric measurement of our experimental set-up shows that $y_{\text{beam height}} = -260 \,\text{mm}$ and $z_{\text{target foil}} = -11.9 \,\text{mm}$.

This task is executed twice. It is first run without using vertex location from BDC measurement in curve fitting, and then again with the inclusion of vertex location. The purpose of the first run is to isolate tracks that do not converge to a common vertex and the second is to improve momentum resolution by incorporating accurately know vertex location from BDC into GENFIT routine.

## 3.4 Particle level analysis

### 3.4.1 Track and event selection

Tracks with poor detection quality must be removed for accurate results. One of the track quality condition used in the analysis is to remove tracks with number of clusters $< 20$ for pions and $< 15$ for other light fragments. Number of clusters of a track is the sum of number of row clusters and number of layer clusters. Row refers to the pad numbering along $x$-direction and layer refers to pad numbering along $z$-direction. Number of layer clusters is the number of layer of pads that register hits for a track when its yaw angle, defined as the angle between the projected track on $x$-$z$ plane and $z$-axis, is less then $45°$ [8]. An illustration about the way clusters are counted is provided in Fig. 3.19. In this example, the track spans five layers but the last layer is not counted because
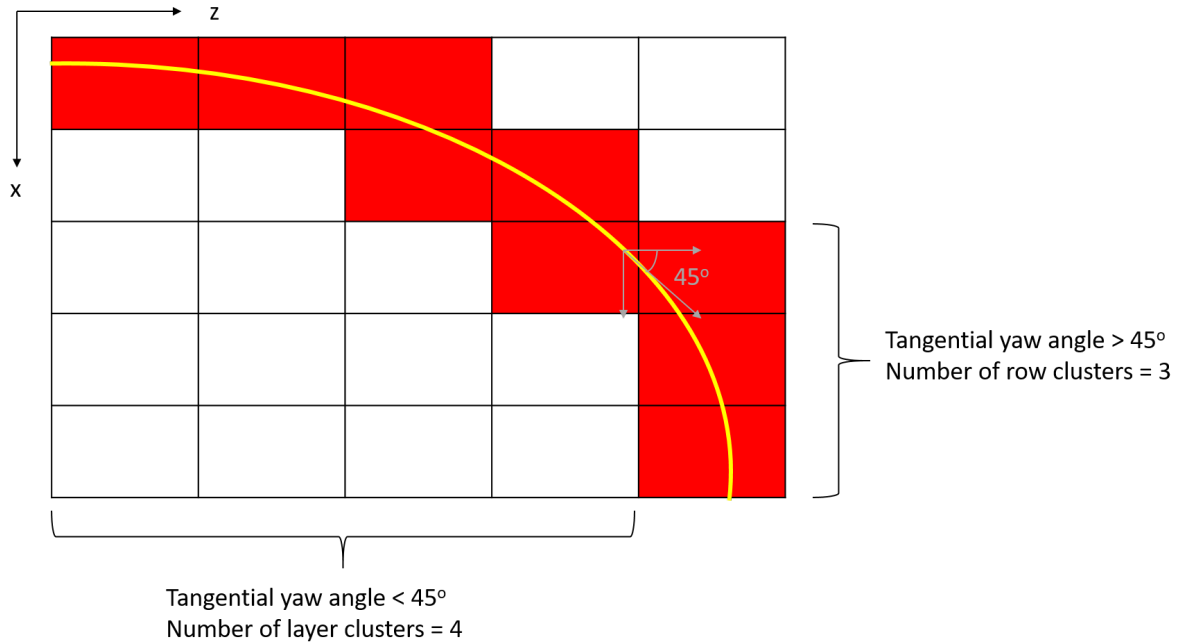
Figure 3.19: An not-to-scale illustration of how numbers of row and layer clusters are defined. The yellow line corresponds to the track trajectory projected on $x - z$ plane and the cells that are labelled red are pads directly on top of the track.

yaw of the track exceeded $45°$ beyond the $4^{\text{th}}$ layer, therefore the number of layer clusters = 5. In similar fashion, number of row clusters is the number of row of pads that register hits for a track when its yaw angle exceeds $45°$. In our example figure, number of row clusters = 3 and the number of clusters is $4 + 3 = 7$. Number of clusters corresponds to the number of points GENFIT used for curve fitting. Momentum resolution will be poor for tracks with inadequate points to fit. The number of clusters threshold is imposed to filter out tracks with unreliable momentum values.

The second condition is to remove tracks with distance to vertex > 20 mm for pions and > 15 mm for all other light fragments. Distance to vertex is the closest distance between reconstructed track and vertex when extrapolated back to the target, as illustrated in Fig. 3.20. If the distance to vertex is too large, then either the track does not originate from the same reaction as other tracks or the is badly fitted. Either way these tracks are not good enough to be counted towards the final spectrum and are removed.

The third condition is to only accept tracks with $-40° < \phi < 20°$ or $160° < \phi < 220°$, where

51
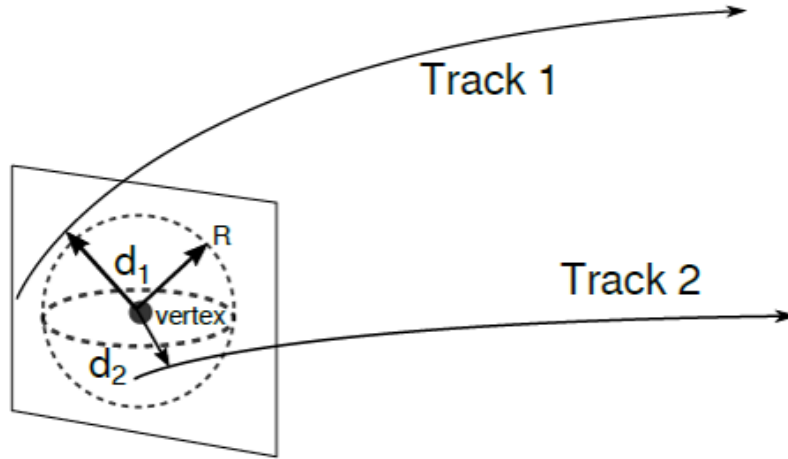
Figure 3.20: Illustration of distance to vertex, taken from Ref. [8].

$\phi$ is the particle azimuth. The S$\pi$RIT detector is wider than it is tall, so tracks that are emitted in the general upward or downward direction escape the detection volume quicker than those emitted sideways and leaves less hit points. After imposing the number of cluster cut, tracks that are emitted at $\phi \sim \pm 90°$ are mostly be cut away. Fig. 3.21 shows the distribution of $\phi$ vs $\theta$ for all protons with number of clusters > 15. The cluster condition completely rejects all tracks near $\phi \sim \pm 90°$ when $\theta > 40°$. This phase-space cut-off boundary is not simple and the resultant geometric bias will be difficult to correct for. Thus we decide to reject tracks emitted in those poorly accepted $\phi$ ranges entirely.

The fraction of particles removed by these cut conditions must be accounted for if we want to accurately count the yield of particles. The efficiency loss due to the number of clusters and distance to vertex conditions can be accurately calculated through efficiency unfolding procedure discussed in Sections 3.4.4. For the azimuth condition we can simply multiply the result by a constant factor of $((220 - 160) + (20 + 40))/360 = 3$ since the reaction should exhibit cylindrical symmetry.

The beam particles could react with nuclei such as the counter gas other than those from the target. These events have to be removed from the analysis. To ensure projectile reacts with the desired Tin nucleons, cuts on vertex locations are made. A $z$-coordinate cut is applied to vertex
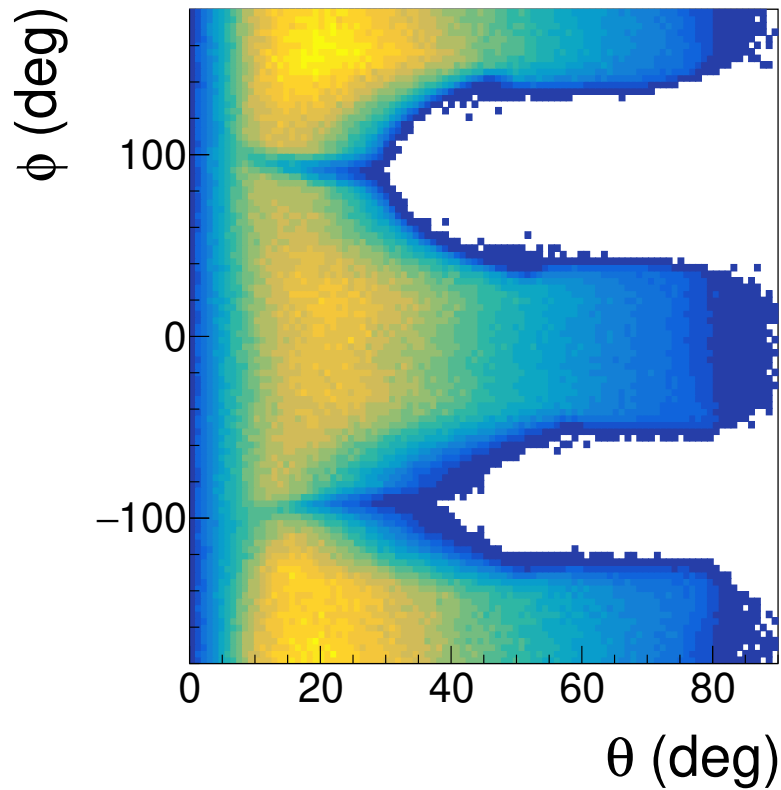
Figure 3.21: Distribution of $\phi$ against $\theta$ for protons with distance to vertex cut < 15 mm and number of cluster cut > 15. Data is taken from $^{132}$Sn + $^{124}$Sn after gating on beam purity.

fitted from tracks to make sure the reaction does not originate up-stream or down-stream of the target foil. Cuts in $x$- and $y$-coordinate are applied to BDC extrapolated vertex position to make sure the beam does not hit the frame of the target.

All cut conditions are tabulated and summarized in Section 3.4.5. Unless otherwise specified, analysis in the following sub-sections are done after vertex, number of clusters and distance to vertex cut have been applied and corrected for.

### 3.4.2  Particle identification

As particle traverse the TPC, it loses energy and ionizes the detector gas molecules. The amount of energy loss depends on particle velocity and electric charge according to Bethe-Bloch equation
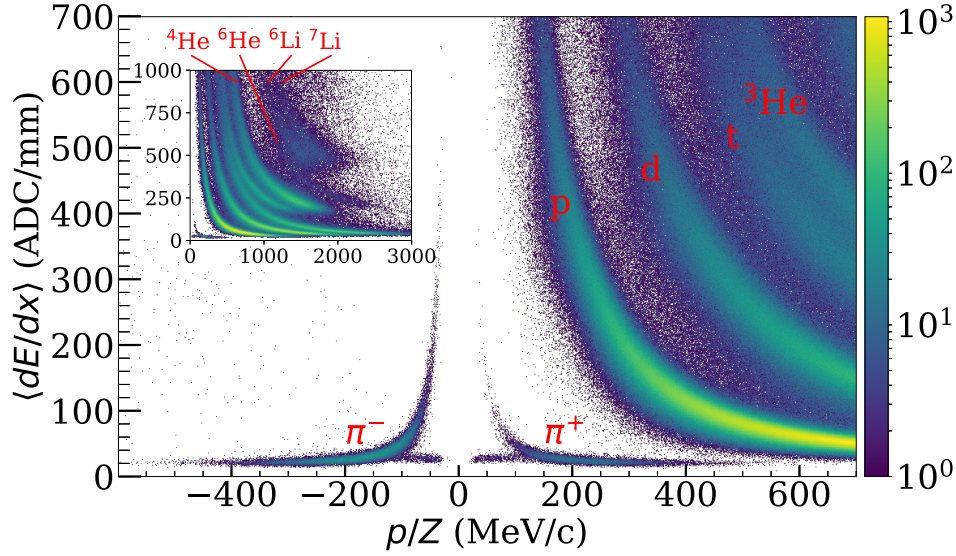
Figure 3.22: Particle identification plot with all events in $^{132}$Sn + $^{124}$Sn.

(BBE) [102],

$$-\left\langle \frac{dE}{dx} \right\rangle = \frac{KZ^2}{\beta^2} \left[ \ln\left( \frac{C\beta^2}{1-\beta^2} \right) - \beta^2 \right] \qquad (3.2)$$

Where $K$ and $C$ are constants that depend only on the properties of detector gas, $\beta = v/c$ is the particle's velocity over speed of light and $Z$ is the absolute particle electric charge in multiples of the electron charge. This allows for different particle types to be identified through a plot of average energy loss per unit length vs. momentum, commonly referred to as the PID plot. Different elements are separated into lines of different height as $dE/dx \propto Z^2$. Isotopes with equal velocity lose the same amount of energy, but they have different momentum due to mass differences and therefore isotopes are also separated into distinguishable lines in PID plot.

PID plot for $^{132}$Sn + $^{124}$Sn reaction is shown in Fig. 3.22. There are slight overlap between some particle species, most noticeably the Triton line and $^3$He line are very close at $p/Z < 700$ MeV/c. To estimate the degree of cross-contamination and to classify particle type for each tracks, we follow the Bayesian PID method outlined in Ref. [103].

Instead of classifying each track as a single type of particle, this method tabulates the probability

of a track being each type of isotope. A single track can be identified as multiple isotopes with varying probability near the ambiguous region of PID. For a track with observed momentum magnitude $p$, the likelihood of detecting energy loss $E$ given that it comes from a particle of type $H_i$ is given by,

$$P(E|p, H_i) = \frac{1}{\sqrt{2\pi}\sigma(p, H_i)} e^{-\frac{(E - \hat{E}(p, H_i))^2}{2\sigma(p, H_i)^2}} . \tag{3.3}$$

In the equation, $\hat{E}(p, H_i)$ is the expected energy loss and $\sigma(p, H_i)$ is the measured width of PID line. The resolution in both momentum and $dE/dx$ measurement contribute to the width of PID lines [8]. Using Bayes theorem, it can be inverted to give the probability of the track being $H_i$ given the energy loss and momentum value,

$$P(H_i|p, E) = \frac{P(E|p, H_i)Pr(p, H_i)}{\sum_{k=P,D,T,...} P(E|p, H_i)Pr(p, H_i)}. \tag{3.4}$$

$Pr(H_i)$ is the prior in the above equation. Following Ref. [103], an iterative procedure will be used in which the priors in the first iteration are assumed to be constants. The posterior distributions from this initial run will be used as prior for the next iteration. This is repeated until the posterior converges.

The expected energy loss $\hat{E}(p, H_i)$ and measured resolution $\sigma(p, H_i)$ are fitted empirically. To do this a crude graphical cut is made to each PID line. The mean and standard deviation of $dE/dx$ at different momentum bins inside the cut will be fitted with ad-hoc functions to represent $\hat{E}(p, H_i)$ and $\sigma(p, H_i)$. Any functions that fit data good enough will work, and in this case $\hat{E}(p, H_i)$ takes the form of a modified BBE,

$$\hat{E}(p, H_i) = \frac{A_i + B_i\beta}{\beta^2} \left[ \ln \left( C_i + \left( \frac{m}{\beta} \right)^{D_i} \right) - \beta^{E_i} + F_i \right]. \tag{3.5}$$

Here $\beta = p/\sqrt{p^2 + m}$ is the velocity, $A_i, B_i, C_i, D_i, E_i$ and $F_i$ are parameters to be fitted. The reason for a modified BBE is that the measured $dE/dX$ is the truncated mean energy loss instead of the real averaged energy loss. The truncation is needed to minimize the effect of outliner energy
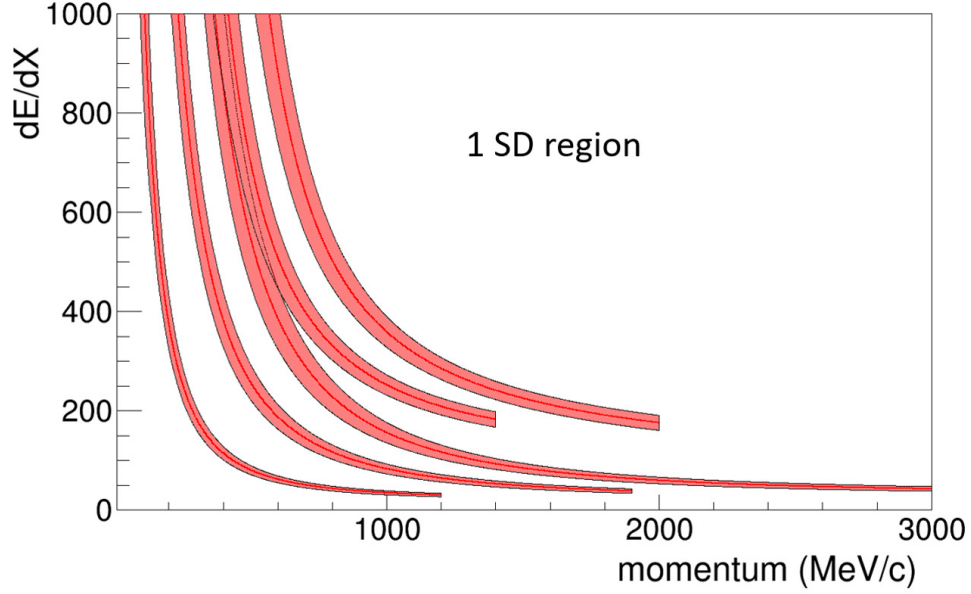
Figure 3.23: The fitted $\hat{E}(p, H_i)$ and $\sigma(p, H_i)$. The red line in the center of the red shaded region corresponds to $\hat{E}(p, H_i)$ and the width of the shaded region on each side the line corresponds to $1\sigma(p, H_i)$ (1 SD).

loss data point caused by delta electrons [98]. The truncation skews the distribution to the point where the original BBE is not a good enough fit. The $\sigma(p, H_i)$ takes the following form,

$$\sigma(p, E_i) = \frac{\alpha_i}{p^{\beta_i}} + \gamma_i, \qquad (3.6)$$

where $\alpha_i, \beta_i$ and $\gamma_i$ are parameters to be fitted. The result fitted from $^{132}$Sn + $^{124}$Sn data is shown in Fig. 3.23

The classification results for $^{132}$Sn + $^{124}$Sn is shown in Fig. 3.24, where the left panel shows $dE/dx$ distributions within a narrow range of momentum and the right panel shows where the range of momentum is on the PID plot. Histograms for each particle type on the left panel are weighted distributions, with each track weighted by the probability of it being a particular particle type. For instance, a track can be 50% proton and 50% deuteron and is counted as 0.5 count in both proton and deuteron distributions. The tails of the distributions overlap with each other in a way that make intuitive sense. When observables for light fragments are constructed in Chapter 4, only tracks with $P(H_i|p, E) > 0.7$ and $\sigma(p, E_i) < 2.2$ are counted. These conditions are chosen by analysis of
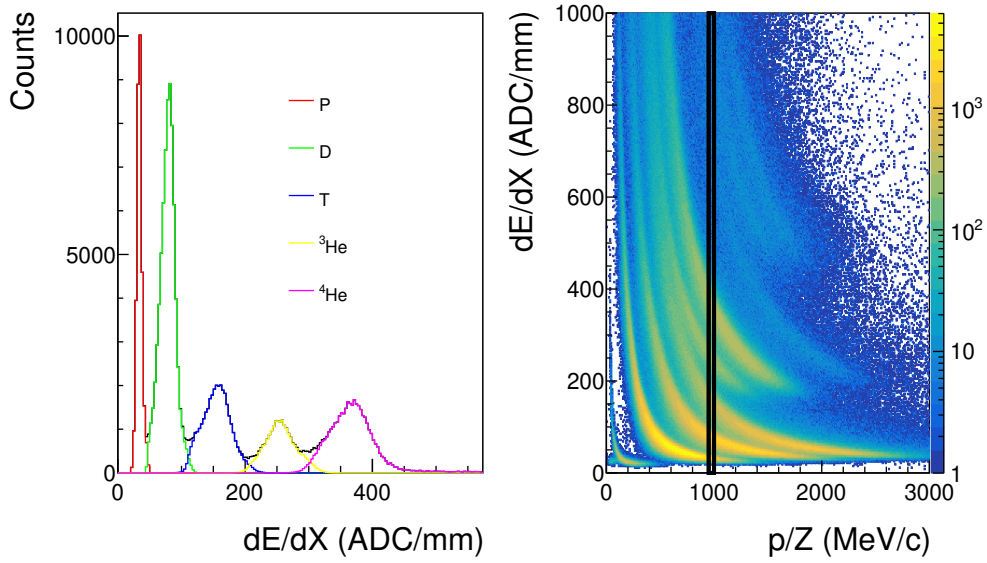
Figure 3.24: Particle selection of Bayesian PID on a selected momentum range. Left: Distributions of $dE/dX$, with each track weighted by the probability of it being a particular isotope. Right: PID plot with a rectangular box indicating where the momentum cut is set in the making of $dE/dX$ distribution on the left.

systematic errors from PID selection, in which fragments observables are found to not vary much within a range of $P$ and $\sigma$ thresholds that centers around 0.7 and 2.2 respectively [104].

Special care must be taken in pion selection because pion PID lines are contaminated by electron and positron PID lines. The Lepton PID lines are not described well by Eq. (3.5) and therefore a different fitting procedure is needed to estimate the amount of contamination for pions. The details on pion selection are described in Ref. [98] and the threshold is set to $P(H_i|p, E) > 0.2$. This is laxer than for light fragments because pion lines are far away from the PID lines of other isotopes.

### 3.4.3 Frame transformation

Center of mass frame is the most convenient reference frame for analysis. To transform measured momentum from laboratory to center of mass frame, it is first rotated such that the beam is traveling in the direction of $z$-axis in the rotated frame. BDC measures the location and angle of incidence of beam particle in each event, and this information is used to properly rotate the coordinate system.

The 4-momentum vector, defined as $\mathbf{P} = (E/c, p_x, p_y, p_z)$, is constructed for each track and is then boosted back to center of mass frame with Lorentz transformation.

We need to know the mass of each fragment to construct the 4-momentum because $E^2 = m^2 c^4 + p^2 c^2$, where $m$ is the mass of the fragment and $c$ is the speed of light. During particle identification, a track can be identified as multiple isotopes simultaneously with different probabilities. The mass of the most probable isotope in particle identification is used as the fragment mass during frame transformation.

The initial beam energy from BigRIPS is inferred from Time-of-Flight (ToF) measurement. On average, nuclear collision are assumed to occur in the middle of the target foil along the beam axis, so the final beam energy for Lorentz transformation is the expected energy after the beam particle traverses half the thickness of the target foil, calculated from LISE++ program [105].

### 3.4.4  Efficiency unfolding

Particle yields are often underestimated due to inefficiencies of the detector. However, detection efficiency can be accurately estimated with Monte Carlo (MC) embedding techniques, details of which will be described later in Section 5.9.1. In this section it is sufficient to know that for particles with a given initial momentum, MC embedding returns the percentage of them being recognized in track recognition and their distribution of reconstructed momentum. Reconstructed momentum is not identical to the initial momentum due to detector resolution.

The naive approach to correct for efficiency loss is simply to weigh each track by the inverse of fraction of recognized tracks over all embedded tracks. Efficiency depends strongly on track momentum so it must be taken into account. To construct efficiency as a function of momentum phase space, MC embedding calculation is repeated across a range of initial momentum. The phase space can be divided into finite bins, with each bin populated by the number of detected tracks over that of initial tracks. Such seemingly innocuous procedure, however, suffers from ambiguity stemming from the fact that detected momentum is not identical to initial momentum given the finite resolution in track fitting routine, so looking efficiency up with detected momentum may

results in inaccuracies.

To demonstrate this effect, denote $R_i$ as the number of tracks with *reconstructed* momentum inside the $i^{\text{th}}$ phase space bin and $T_i$ as the number of tracks with *true* momentum inside the $i^{\text{th}}$ phase space bin. In other words, $R_i$ is the reconstructed momentum distribution and $T_i$ is the true momentum distribution. A fraction of tracks with true momentum in bin $i$ end up with reconstructed momentum in bin $j$ due to finite resolution. Denote $M_{i,j}$ as the fraction of tracks that migrate from bin $i$ to $j$ after track reconstruction such that,

$$
\begin{aligned}
R_i &= T_i M_{i,i} + \sum_{i \neq j} T_j M_{j,i} \\
&= \sum_{\text{All } j} T_j M_{j,i}.
\end{aligned}
\tag{3.7}
$$

$R_i$ is detected in the experiment and the goal of efficiency unfolding is to extract $T_i$ from it. Beware that some tracks are lost in reconstruction due to detector inefficiencies and track quality cut, so it is expected that $\sum_i M_{j,i} \leq 1$. $M_{j,i}$ can be calculated from MC embedding from the following procedure: MC embedding is performed with $C$ initial tracks on each momentum bin such that,

$$
R_i^{\text{embed}} = \sum_{\text{All } j} T_j^{\text{embed}} M_{j,i} = C \sum_{\text{All } j} M_{j,i},
\tag{3.8}
$$

since $T_i^{\text{embed}} \equiv C$. Note that the embedded tracks have to pass track quality conditions to be counted towards $R_i^{\text{embed}}$. Efficiency $E_i$ is defined as,

$$
E_i = \frac{R_i^{\text{embed}}}{T_i^{\text{embed}}} = \sum_{\text{All } j} M_{j,i}.
\tag{3.9}
$$

It is tempting to divide the number of experimental reconstructed tracks by $E_i$ bin-by-bin to recover the true momentum distribution, but such division does not always yield the correct distribution. Denote $EC_i$ (stands for efficiency corrected) as the result of division for bin $i$,

$$
EC_i = \frac{R_i}{E_i} = \frac{\sum_j T_j M_{j,i}}{\sum_j M_{j,i}}.
\tag{3.10}
$$

There are only two ways $EC_i$ equals to $T_i$: If $M_{i,j} = A_i\delta_{i,j}$ or if $T_i$ is a constant. The former corresponds to zero bin migration, in other words perfect momentum resolution, and the latter corresponds to uniform particle distribution in momentum space. Neither is true in general, but if bin migration is small enough, $EC_i$ will be very close to $T_i$. Let $M_{i,j} = A_{i,j}\delta_{i,j} + \sigma_{i,j}$ where $\sigma_{0,0} = 0$ and $\sigma_{i,j} \ll A_{i,j}$, we have,

$$
\begin{aligned}
EC_i &= \frac{\sum_j T_j (A_{j,i}\delta_{j,i} + \sigma_{j,i})}{\sum_j (A_{j,i}\delta_{j,i} + \sigma_{j,i})} \\
&= \frac{A_{i,i}T_i + \sum_j \sigma_{j,i}T_j}{A_{i,i} + \sum_j \sigma_{j,i}} \\
&= A_{i,i}^{-1}\left(A_{i,i}T_i + \sum_j \sigma_{j,i}T_j\right)\left(1 + \frac{\sum_j \sigma_{j,i}}{A_{i,i}}\right)^{-1} \\
&= \left(T_i + \frac{\sum_j \sigma_{j,i}T_j}{A_{i,i}}\right)\left(1 - \frac{\sum_j \sigma_{j,i}}{A_{i,i}}\right) + O(\sigma_{j,i}^2) \\
&= T_i + \frac{\sum_j (T_j - T_i)\sigma_{j,i}}{A_{i,i}} + O(\sigma_{j,i}^2) \\
&= T_i + O(\sigma_{j,i})
\end{aligned}
\tag{3.11}
$$

$EC_i \approx T_i$ to the first order of $\sigma$, but the accuracy can be improved with an iterative procedure where each embedded particles are weighted by $EC_i$. This iterative procedure will be referred to as *unfolding* and will be repeated until the efficiency corrected histogram converges. Let $\epsilon_i = \sum_j (T_j - T_i)\sigma_{j,i}/A_{i,i}$, the embedding tracks are weighted as follows,

$$
\begin{aligned}
T_i^{\text{embed}(2)} &= T_i^{\text{embed}(1)} EC_i^{(1)} \\
&= C(T_i + \epsilon_i) + O(\sigma^2),
\end{aligned}
\tag{3.12}
$$

The number in the parenthesis on superscript states the order of iteration. Following Eq. (3.8),

$$
\begin{aligned}
R_i^{\text{embed}(2)} &= \sum_{\text{All } j} T_j^{\text{embed}(2)} M_{j,i} \\
&= C\sum_j (T_j + \epsilon_j)(A_{j,i}\delta_{j,i} + \sigma_{j,i}) + O(\sigma^2) \\
&= C\left(A_{i,i}T_i + A_{i,i}\epsilon_i + \sum_j T_j\sigma_{j,i}\right) + O(\sigma^2)
\end{aligned}
\tag{3.13}
$$

The new efficiency is,

$$
\begin{aligned}
E_i^{(2)} &= \frac{R_i^{\text{embed}(2)}}{T_i^{\text{embed}(2)}} \\
&= \frac{C(A_{i,i}T_i + A_{i,i}\epsilon_i + \sum_j T_j\sigma_{j,i}) + O(\sigma^2)}{C(T_i + \epsilon_i) + O(\sigma^2)} \\
&= \frac{A_{i,i}(C(T_i + \epsilon_i)) + C\sum_j T_j\sigma_{j,i} + O(\sigma^2)}{C(T_i + \epsilon_i) + O(\sigma^2)} \\
&= A_{i,i} + \frac{\sum_j T_j\sigma_{j,i} + O(\sigma^2)}{T_i + \epsilon_i + O(\sigma^2)} + O(\sigma^2).
\end{aligned}
\tag{3.14}
$$

Make use of the fact that $\epsilon_i \sim O(\sigma)$, the efficiency becomes,

$$
\begin{aligned}
E_i^{(2)} &= A_{i,i} + \frac{\sum_j T_j\sigma_{j,i} + O(\sigma^2)}{T_i + O(\sigma)} + O(\sigma^2) \\
&= A_{i,i} + \frac{\sum_j T_j\sigma_{j,i} + O(\sigma^2)}{T_i}(1 - O(\sigma)) + O(\sigma^2) \\
&= A_{i,i} + \frac{\sum_j T_j\sigma_{j,i}}{T_i} + O(\sigma^2).
\end{aligned}
\tag{3.15}
$$

The efficiency corrected histogram in the second iteration is,

$$
\begin{aligned}
EC_i^{(2)} &= \frac{\sum_j T_j(A_{j,i}\delta_{j,i} + \sigma_{j,i})}{A_{i,i} + \frac{\sum_j T_j\sigma_{j,i}}{T_i} + O(\sigma^2)} \\
&= \frac{T_i(A_{i,i} + \frac{\sum_j T_j\sigma_{j,i}}{T_i})}{A_{i,i} + \frac{\sum_j T_j\sigma_{j,i}}{T_i} + O(\sigma^2)} \\
&= T_i + O(\sigma^2)
\end{aligned}
\tag{3.16}
$$

Iteration improves the accuracy by a factor of $\sigma$. Eventually the procedure will converge to a stable $EC_i$. To prevent tracks with extremely small efficiency from blowing up the histogram, tracks with the unfolded efficiency smaller than 0.15 will be discarded.

### 3.4.5 Conditions for event and track selections

Event and track conditions described in the last three sub-sections are summarized in Table 3.1. The track lost due to number of clusters, distance to vertex and detector inefficiencies should be

Table 3.1: Cut conditions used in event and track selection for reconstruction of particle distributions.

| Track conditions | Light fragments | Pions |
|---|---|---|
| Number of clusters | > 15 | > 20 |
| Distance to vertex | < 15 mm | < 20 mm |
| PID probability | > 0.7 | > 0.2 |
| PID $\sigma$ | > 2.2 | Not imposed |
| Efficiency | > 0.15 | |
| Azimuth range | $-40° < \phi < 20°$ or $160° < \phi < 220°$ | |

| Vertex conditions | | | |
|---|---|---|---|
| System | z(mm) | BDC-x(mm) | BDC-y(mm) |
| $^{108}$Sn + $^{112}$Sn | $-14.8 \pm 3.1$ | $0.0 \pm 2.5$ | $0.0 \pm 2.4$ |
| $^{108}$Sn + $^{112}$Sn | $-14.8 \pm 3.7$ | $0.0 \pm 3.0$ | $0.0 \pm 2.3$ |
| $^{108}$Sn + $^{112}$Sn | $-14.3 \pm 2.6$ | $0.0 \pm 2.5$ | $0.0 \pm 3.0$ |
| $^{108}$Sn + $^{112}$Sn | $-14.8 \pm 3.7$ | $0.0 \pm 2.8$ | $0.0 \pm 2.5$ |

corrected by efficiency unfolding. The multiplicative factor of 3 due to azimuth range cuts will be imposed after efficiency unfolding. Although Monte Carlo simulation is able to recreate the shape of particle PID to an certain extent, it is not accurate enough to be used for calculating the amount of track lost due to PID cuts. The performance of MC PID will be discussed in Section 5.9.2.

### 3.4.6 Reaction plane determination

Reaction plane is the plane that the beam axis and the displacement vector between target and projectile span. Estimation of reaction plane azimuth $\Phi$ is needed in the determination of *collective flow*, which was the focus of numerous previous studies [11, 106–108]. Flows are expected to shed light into the properties of nuclear matter. Collective flow indicates the degree of non-uniformity in azimuth distribution with respect to reaction plane. In this work, Q-vector method [109] is used to approximate reaction plane angle, which stated that the azimuth of $\vec{Q}$ defined as,

$$\vec{Q} = \sum w(y_z)\vec{p_T},\tag{3.17}$$

is a good approximation to $\Phi$. Here $w = 1$ for $y_z > 0.4y_{\text{beam CM}}$, $w = -1$ for $y_z <$

$-0.4y_{\text{beam CM}}$ and $w = 0$ otherwise. Fragments with $|y_{\text{beam CM}}| < 0.4$ are not used as mid-rapidity fragments do not contribute to reaction plane determination [110]. When applied to S$\pi$RIT data, the number of clusters cut is relaxed to $> 7$ and no azimuth range cuts are applied to minimize bias in azimuth acceptance. Denote $\Phi_r$ as the approximated reaction plane angle. Q-vector method work best for detectors with uniform azimuth acceptance, but given that S$\pi$RIT TPC does not exhibit cylindrical symmetry the acceptance is non-uniform. Fragments emitted at some angles are less efficiently detected than the others, leading to under-representation of particles in those angular ranges. There are multiple ways to correct for such bias, and in this analysis we expand the distribution of $\Phi_r$ as a Fourier series and shifts reaction plane angles event-by-event in a way that makes the final distribution isotropic [111]. This shift is achieved by first normalizing each component of Q-vector to have zero mean and unit standard deviation,

$$\hat{Q}_i = (Q_i - \langle Q_i \rangle)/\sigma_{Q_i}, \tag{3.18}$$

where $i$ denotes the component of Q-vector and can be either $x$ or $y$. Define $\hat{\vec{Q}} = \hat{Q}_x \hat{x} + \hat{Q}_y \hat{y}$, then the $n^{\text{th}}$ Fourier components of the azimuth distribution of $\hat{\vec{Q}}$ is,

$$
\begin{aligned}
a_n &= -\frac{2}{n} \langle \sin(n\phi(\hat{\vec{Q}})) \rangle, \\
b_n &= \frac{2}{n} \langle \cos(n\phi(\hat{\vec{Q}})) \rangle.
\end{aligned}
\tag{3.19}
$$

To correct for acceptance bias, reaction plane angles are shifted to erase the contributions of each Fourier component by the following amount,

$$\Phi_{\text{flat}} = \phi(\hat{\vec{Q}}) + \sum_n [a_n \cos(n\phi(\hat{\vec{Q}})) + b_n \sin(n\phi(\hat{\vec{Q}}))]. \tag{3.20}$$

The effect of Eq. (3.20) is demonstrated in Fig. 3.20 where the Q-vector azimuth distributions from $^{108}$Sn + $^{112}$Sn before and after bias correction are plotted. This correction is verified to flatten the reaction plane distributions for all reaction systems in S$\pi$RIT experiment.

Although the flattened reaction plane angle $\Phi_{\text{flat}}$ provides a reasonable estimation of reaction plane angle $\Phi$, they are still not identical due to stochastic nature of nuclear reaction, particle
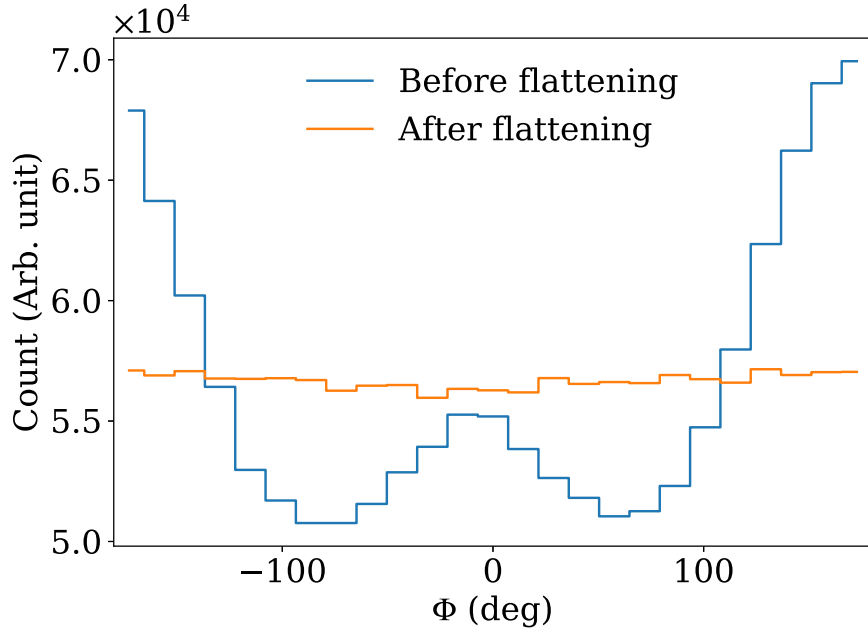
Figure 3.25: Distributions of reaction plane azimuth before (blue) and after (orange) correction of Eq. (3.20) is made. The selected events come from $^{108}$Sn + $^{112}$Sn.

detection resolution and efficiency effects. Fortunately, as we will show in Section 4.4.4, flow observables can be accurately determined from inaccurate reaction plane angle as long as reaction plane resolution is given. It can be calculated with the *sub-event* methods which quantifies the resolution as $\langle\cos(i(\Phi - \Phi_{\text{flat}}))\rangle$ for $i = 1, 2, \ldots$.

In sub-event method, fragments in each events are grouped randomly into two disjoint sub-events with equal multiplicity, which we denote as group $a$ and $b$. Denote $\Phi_{\text{flat}}^a$ and $\Phi_{\text{flat}}^b$ as the reconstructed Q-vector reaction plane angle for events in group $a$ and $b$ respectively and $\chi_m = \langle\cos(\Phi_{\text{flat}}^a - \Phi_{\text{flat}}^b)\rangle/\sqrt{2}$, then the relation between reaction plane angle and sub-event reaction plane angles can be approximated as,

$$
\begin{aligned}
\langle\cos(\Phi - \Phi_{\text{flat}})\rangle &= 0.626657\chi_m - 0.09694\chi_m^3 + 0.02754\chi_m^4 - 0.002283\chi_m^5, \\
\langle\cos(2(\Phi - \Phi_{\text{flat}}))\rangle &= 0.25\chi_m^2 - 0.011414\chi_m^3 - 0.034726\chi_m^4 + 0.006815\chi_m^5.
\end{aligned}
\tag{3.21}
$$

These equations are then solved numerically. For full derivation of sub-event method please refers to Ref. [109].

64

# CHAPTER 4

## EXPERIMENTAL RESULT

## 4.1 Introduction

The goal of the S$\pi$RIT experiment is to study the properties of nuclear matter such that our understanding of neutron star, which is composed mostly of nuclear matter, can be improved. Experimental results will be compared against theoretical predictions to constrain nuclear EoS parameters. Using the S$\pi$RITROOT analysis framework, various spectra of pions and light fragments can be reconstructed.

Theoretical predictions are made using *transport models*, a class of semi-classical algorithm that describes the dynamics of nuclear collisions from Fermi to relativistic energies. A review on the different transport models can be found in Ref. [112].

In this chapter, a brief summary on transport models will be provided, followed by results from the S$\pi$RIT experiment.

## 4.2 Transport model

The idea of transport model is to extend the classical Vlasov equation for one-body phase-space distribution with a Pauli-blocked Boltzmann collision term. The resulting equation, called Boltzmann-Uehling-Uhlenbeck (BUU) equation, is formulated as,

$$\left( \frac{\partial}{\partial t} + \vec{\nabla}_p \epsilon \cdot \vec{\nabla}_r - \vec{\nabla}_r \epsilon \cdot \vec{\nabla}_p \right) f_a(\vec{r}, \vec{p}, t) = I_{\text{coll}} \left[ f_a(\vec{r}, \vec{p}, t), \frac{d\sigma_{ab}^{\text{med}}}{d\Omega} \right]. \tag{4.1}$$

In this equation, $f_a(\vec{r}, \vec{p}, t)$ is the one-body phase-space distribution for particle $a$, $\epsilon[f_a]$ is the single-particle energy function, $I_{\text{coll}}[f_a, d\sigma_{ab}^{\text{med}}/d\Omega]$ is the two-bodies collision integral and $d\sigma_{ab}^{\text{med}}/d\Omega$ represents all the in-medium nucleon-nucleon differential scattering cross sections between particle $a$ and $b$. $\epsilon$ and in-medium cross sections are inputs that must be provided by the

user. In particular, $\epsilon$ is governed by the mean-field potential which contains contributions from nuclear EoS. The collision term for the collision $p_a + p_b \rightarrow p_a' + p_b'$ is,

$$I_{\text{coll}} \left[ f_a(\vec{r}, \vec{p}, t), \frac{d\sigma^{\text{med}}}{d\Omega_{ab}} \right] = \sum_b \frac{g_b}{(2\pi\hbar)^3} \int d^3 p_b v_{ab} \frac{d\sigma_{ab}^{\text{med}}}{d\Omega_b} [(1 - f_a)(1 - f_b) f_a' f_b'$$
$$- f_a f_b (1 - f_a')(1 - f_b')], \quad (4.2)$$

where $v_{ab}$ is the relative velocity between particle $a$ and $b$, $g_b$ is the spin degeneracy and the summation over $b$ corresponds to summation over all neutrons and protons. The collision term is solved by performing stochastic collisions. In each time step, we first check if two test particles are close enough to incur a collision and then check if the final state of the collision is permitted by Pauli-exclusion principle.

There are two types of transport models, namely the quantum molecular dynamics (QMD) models [113–121] and the stochastic extensions of Boltzmann-Lagevin type [122–127]. They mainly differ in how fluctuations and many-body correlation are introduced. Only QMD models are described here as the availability of transport codes due to their availability to our group.

QMD models approximate the many-body wave-function as a product of multiple Gaussian wave-packets with fixed width. The one-body Wigner function, which is the phase space distribution for the corresponding many-body wave-function, is,

$$f(\vec{r}, \vec{p}) = \sum_i^A f_i(\vec{r}, \vec{p}), \text{ with}$$
$$f_i(\vec{r}, \vec{p}) = \left( \frac{\hbar}{\Delta x \Delta p} \right)^3 \exp \left[ -\frac{(\vec{r} - \vec{R}_i(t))^2}{2\Delta x^2} - \frac{(\vec{p} - \vec{P}_i(t))^2}{2\Delta p^2} \right]. \quad (4.3)$$

The centroid position $\vec{R}_i(t)$ and $\vec{P}_i(t)$ are treated as variational parameters. This summarizes how QMD type models simulate nuclear dynamics, but the details in collision simulation and mean field formulation differ from code to code. We will briefly describe ImQMD, dcQMD and UrQMD in the next three subsections as these three models are used in different part of our analysis.

66

### 4.2.1 ImQMD

ImQMD was first developed at China Institute of Atomic Energy (CIAE) by the group of Prof. Zhuxia Lia. It was improved by Yingxun Zhang in 2003 [121, 128–130]. Its mean field derives from Skyrme energy density functional with explicit Skyrme-type momentum-dependent interaction [131]. Collision between nucleons is only attempted when their transverse distance is less than $\sqrt{\sigma^{\mathrm{med}}/\pi}$, where $\sigma^{\mathrm{med}} = (1 - \eta\rho/\rho_0)\sigma^{\mathrm{free}}$ and $\eta$ is a free parameter, and their longitudinal distance is less than $v_{ij}\gamma\delta t/2$, where $v_{ij}$ is the relative velocity, $\gamma$ is the Lorentz factor and $\delta t$ is the length of time step. It is suitable for the study of Skyrme interaction, a commonly used EoS family in low-energy nuclear physics, including neutron star calculations.

### 4.2.2 UrQMD

UrQMD was first developed in the mid-1990s at Frankfurt [132]. It was extended to include 50 different baryon species and 35 different meson species and is commonly used to study collisions over vast energy ranges. Different versions of UrQMD use different mean field formulations for the study of different topics in heavy-ion experiments [133–140]. The mean field of UrQMD in sections 5.8 and 5.9.3 uses Skyrme type mean field with in-medium cross-section equals to cross-section in free space [141].

### 4.2.3 dcQMD

dcQMD was adapted from TuQMD, which was first developed in the 90s in Tubingen, Germany [142, 143]. TuQMD includes the degrees of freedom for a lot of particle species [144]. It was extended to dcQMD for the study of asymmetric part of nuclear EoS at a few hundred AMeV [145, 146]. The mean-field of dcQMD was formulated to introduce independent variations of compressibility or slope parameters in EoS. It allows the isospin-dependent potential of nucleon to be different from that of $\Delta(1231)$ which has a large impact on pion multiplicities [147]. Therefore this flexibility makes dcQMD suitable for the comparison of pion observables. A collision

is attempted when $\pi d_{\mathrm{min}}^2 \leq \sigma$, with $\sigma$ being the scattering cross-section. A particular feature of dcQMD is that it considers the total energy balance due to in-medium potential in a collision. This condition shifts the production threshold based on differences between the initial and final potential energy [148].

## 4.3 Coalescence

After transport model propagates nucleons to their final position, *clusterization* (also called *coalescence*) algorithm will be used to group nucleons into light fragments such as Deuteron and Triton. It usually involves combining neutrons and protons with small relative distance and speed into isotopes. This procedure is unreliable as the physical fragment production mechanism involves many body correlations that are not well understood [149, 150].

In some models, clusterization algorithms are handled better and yield more consistent results with data. Most prominently, the Asymmetrized Molecular Dynamic (AMD) propagate nucleons and calculate cluster formation in one unified step. Its predictions on light fragment yield was shown to agree with data to a satisfactory extent [149, 151]. For all the transport models that will be used for comparison with data in this manuscript, however, use the less reliable clusterization process and therefore energy spectra of light fragments cannot be compared directly.

To overcome this issue, observables must be chosen carefully to minimize their sensitivity to clusterization. To be more precise, we want to construct observables whose values depend weakly on the clusterization process. This can be achieved by one of the following ways:

1. Consider particles that do not form elements or isotopes.

2. Sum up protons from all light fragments to reconstruct the primary nucleon distribution before clusterization.

3. Take ratio of the same observables between different reaction systems. The division could potentially cancel systematic errors from clusterization.

Various observables have been constructed with those methods. In this chapter, those observables will be described and their measured values from S$\pi$RIT experiment will be shown.

## 4.4 Pion Observables

Since pions do not form isotopes with other particles, their yields should be independent of the clusterization process. Furthermore, pion observables are believed to be sensitive to nuclear EoS at high density due to pion's unique production mechanism: In nucleon-nucleon collisions, some interactions are energetic enough to form excited $\Delta(1323)$ baryon resonance ($NN \leftrightarrow \Delta$) which then promptly decay into pions. The high production threshold of $\Delta$ resonance ($1232 \, \mathrm{MeV/c^2}$) at the early stage of the reaction ensures that pions originate from high density region. S$\pi$RIT data on pion momentum spectra in central collisions have been published [37, 147] and their results will be reviewed. It will be followed by data on other new pion observables.

### 4.4.1 Pion yield of central events

The most straight-forward pion observable to extract is the total yields of charged pions. Although they are measured reliably in S$\pi$RIT experiment, comparison with theory is hard to carry out because a lot of different physical processes must be taken into account for the prediction of total pion yields to be accurate. Some of these processes are not well understood which introduce additional uncertainties in quantifying the relation between pion yield and symmetry energy. These issues can be mitigated by using the ratio of $Y(\pi^-)$ to $Y(\pi^+)$ instead. The division cancels out contributions from physical processes that act on both $\pi^-$ and $\pi^+$ in similar way while magnifying the symmetry energy effects which act on $\pi^-$ and $\pi^+$ with opposite sign.

The study of pion yields is the focus of Ref. [147]. The S$\pi$RIT experiment measured the pion ratios of $^{108}$Sn + $^{112}$Sn, $^{112}$Sn + $^{124}$Sn and $^{132}$Sn + $^{124}$Sn systems. The total neutron to proton ratio $N/Z$ of these three systems are 1.36, 1.2 and 1.56 respectively. Due to limited geometric coverage of the S$\pi$RIT TPC, only pions with $p_z \geq 0$ in center of mass frame are measured. The observed pion yield only covers the forward $2\pi$ solid angle instead of the complete $4\pi$. The effects of incomplete
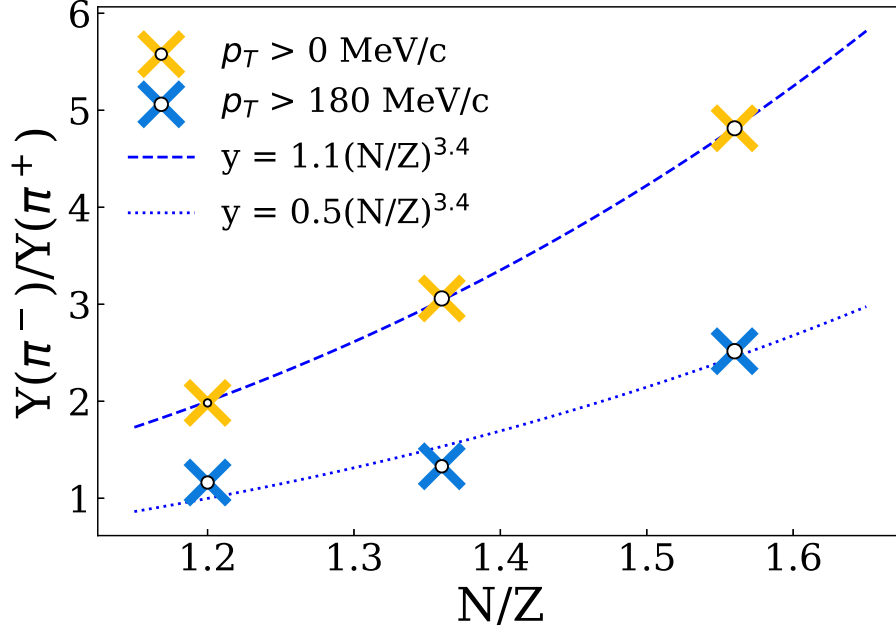
Figure 4.1: Yield of $\pi+$ over that of $\pi^-$ in $b < 3\,\text{fm}$ events for pions with $p_z > 0$ in center of mass frame, plotted as a function of $N/Z$. The yellow crosses show the yield ratios with no transverse momentum cut while the blue crosses shows that with $p_T > 180\,\text{MeV/c}$. The radius of circle inside each cross represents the statistical uncertainty of the ratio. The dashed blue line and dotted blue line corresponds to best fitted power functions of $N/Z$ for $p_T > 0$ and $p_T > 180\,\text{MeV/c}$ pion ratios respectively.

coverage should be minimized when ratios between yields of $\pi^-$ and $\pi^+$ are taken. To impose centrality gate, only events with multiplicity larger than 50 are considered. This corresponds to an impact parameter cut of $b < 3\,\text{fm}$.

With a $\Delta$ resonance model for pion production, one would expect that $Y(\pi^-)/Y(\pi^+)$ follows a $(N/Z)^2$ dependence [35, 152]. However, the measured pion ratios in Fig. 4.1 (yellow cross with circle marker) follows $N/Z$ with a best fitted power index of 3.4 instead. The radius of the circle in the center of each cross is the uncertainty of yield measurement. The discrepancy indicates the presence of dynamical factors beyond a simple $\Delta$ resonance model. If transverse momentum cut of $p_T > 180\,\text{MeV/c}$ is imposed, the result (blue crosses with circle marker) still shows a $(N/Z)^3.4$ dependence instead of the expected $(N/Z)^2$. The effects unexplained by $\Delta$ resonance model persist even for high momentum pions.

### 4.4.2 Pion ratio spectra of central events

The analysis of pions momentum spectra in central collisions is the focus of Ref. [37]. Their results will be briefly summarized in this section.

dcQMD's predictions will be compared against the measured pion spectrum to constrain nuclear EoS. As described in Section 4.2.3, dcQMD is suitable for describing pion emissions due to its flexibility in adjusting $\Delta$ potential independently from that of nucleons. This is essential as it was found that if $\Delta$ potential is set to equal to that of nucleons, the predicted yield of $\pi^-$ and $\pi^+$ will be incorrect [147, 153]. The potential depth at saturation density is adjusted until dcQMD is able to reproduce experimental pion yields and mean kinetic energies [153].

Only $L$ and the scaled difference between neutron and proton effective mass $\Delta m_{np}^* = [m_n^* - m_p^*]/(m\delta)$ are allowed to vary to simplify the analysis. Other EoS parameters are fixed to the best fit values from other analysis. Following results in Ref. [154], $K_{\mathrm{sat}}$ is set to 250 MeV and $Q_{\mathrm{sat}}$ is set to $-350$ MeV. Following results from nuclear mass and radius measurements [19, 20], $L$ will be correlated with $K_{\mathrm{sym}}$ via $K_{\mathrm{sym}} = -488 + 6.728L \, (\mathrm{MeV})$ and $S(\rho = 0.1 \, \mathrm{fm}^{-3})$ is fixed to 25.5 MeV.

When the measured $\pi^+$ and $\pi^-$ transverse momentum $(p_T)$ spectra in $^{108}$Sn + $^{112}$Sn and $^{132}$Sn + $^{124}$Sn reactions for events with impact parameter $b < 3$ fm are compared against dcQMD predictions in Fig. 4.2, it is found that pion potential is required to describe pions accurately. Only pions with $p_z > 0$ in center of mass frame are counted due to acceptance limitations of the S$\pi$RIT TPC. The black markers correspond to measured spectra and both the blue and red lines correspond to dcQMD calculations with $L = 80$ MeV, $\Delta m_{np}^* = 0$ and optimized $\Delta$ potential depth. The difference between the two curves is that pion optical potential is used on the red curves but not the blue curves.

Next we focus on the single ratio spectrum $SR(\pi^-/\pi^+) = [dN(\pi^-)/dp_T]/[dN(\pi^+)/dp_T]$. This ratio magnifies symmetry energy effects as the contribution of symmetry energy to isovector mean field potential is opposite in sign for $\pi^-$ and $\pi^+$, similar to our rationale for taking ratios of total yield in the previous section. We use dcQMD to predict single ratios at 12 different points in the $L$ vs. $\Delta m_{np}^*$ space, forming a regular lattice. The value of $L$ in the lattice is either 15, 60, 106
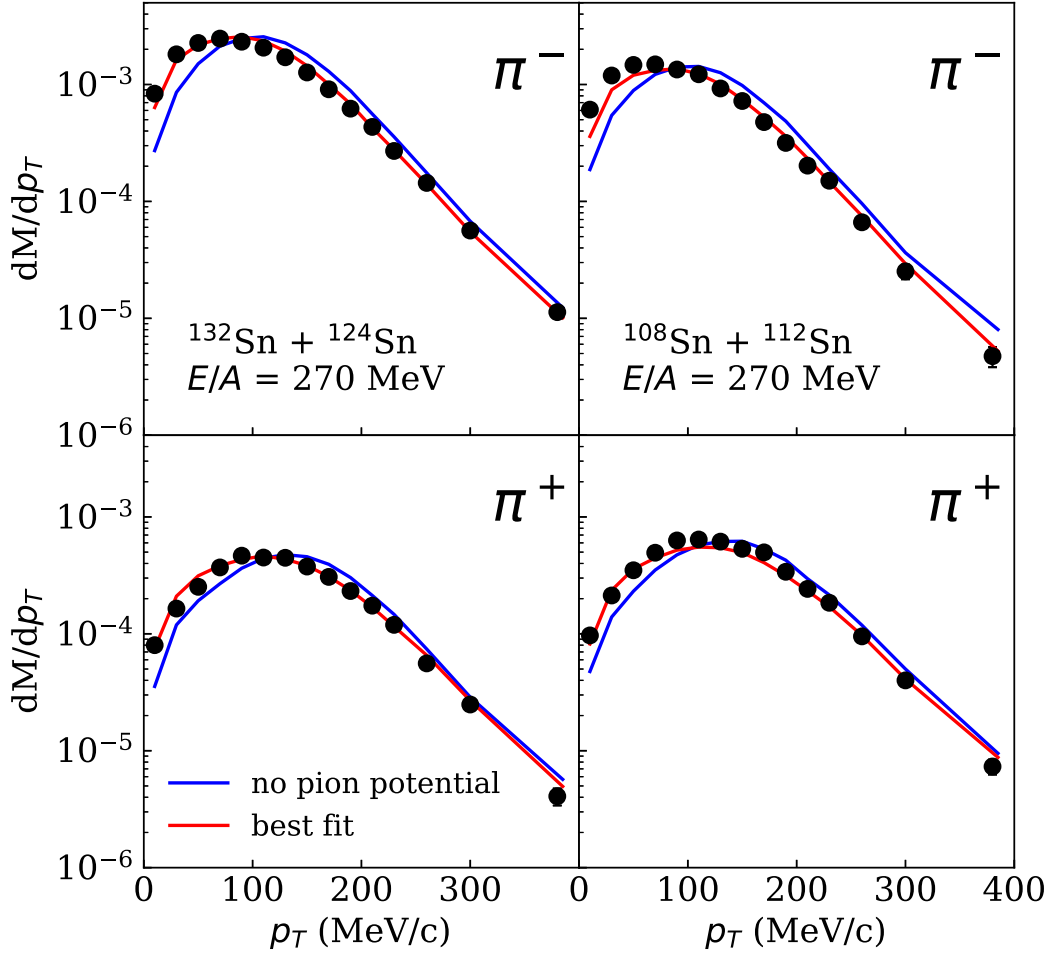
Figure 4.2: Measured $p_z > 0$ pion spectra for $b < 3\,\mathrm{fm}$ events. Red curves show dcQMD predictions with best fitted pion potential. The blue curves are identical except that no pion potential is used.

or $151\,\mathrm{MeV}$ and $\Delta m^*_{np}/\delta$ is either -0.33, 0 or 0.33.

A few selected calculations and the measured single ratios are shown in Fig. 4.3. The $(L, \Delta m^*_{np})$ values of solid blue line is $(60, -0.33\delta)$, dashed blue line is $(60, -0.33\delta)$, solid red line is $(151, -0.33\delta)$ and dashed red line is $(151, -0.33\delta)$. Coulomb effect dominates the low $p_T$ region which cause a steep rise in measured ratios at $p_T < 200\,\mathrm{MeV}$. All calculations at $p_T < 200\,\mathrm{MeV}$ disagree with data, which could be caused by inaccuracies in the simulation of Coulomb interac-
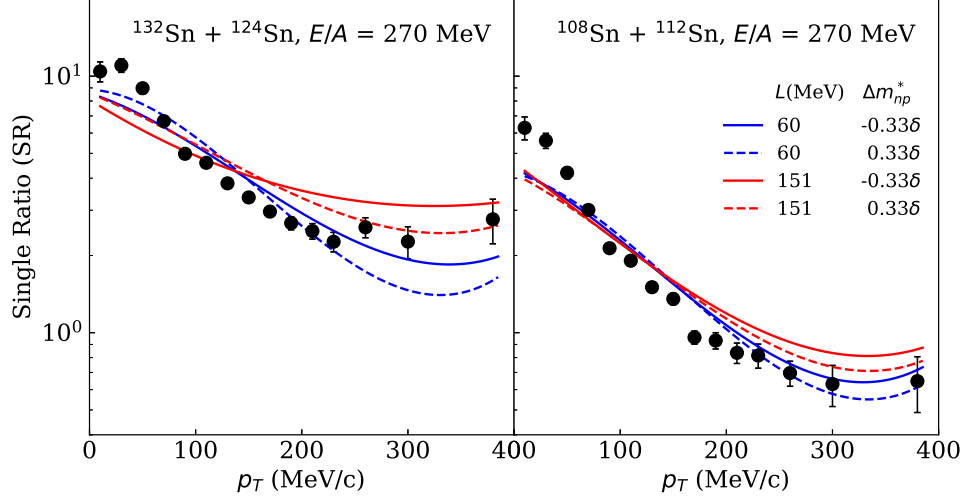
Figure 4.3: Single pion spectral ratios in $^{132}$Sn + $^{124}$Sn (left) and $^{108}$Sn + $^{112}$Sn (right) reactions with four selected dcQMD predictions overlay on top. See text for details.

tions or pion optical potential above saturation density. At $p_T > 200$ MeV, the Coulomb effects diminishes and the ratios should be good probes to the symmetry energy effect.

The predicted single ratios at $p_T > 200$ MeV are interpolated with 2D cubic splines over $(L, \Delta m_{np}^*)$ space. The interpolated predictions are compared against experimental measurement through a chi-square analysis. The resultant multivariate constraint on $L$ and $\Delta m_{np}^*$ is shown in Fig. 4.4 where the green shaded region is the one-sigma confidence interval and the area enclosed by the two blue dashed curve is the two-sigma confidence interval. Without any constraints on the effective mass, the best fitted value is $L = 79.9 \pm 37.6$ MeV. The correlation between $\Delta m_{np}^*$ and $L$ suggests that tighter constraint on $L$ can be made if $\Delta m_{np}^*$ is constrained better.

### 4.4.3 Pion yield dependence on impact parameter

Using the machine learning algorithm described later in Section 5.9.3, events are separated into impact parameter bins from 0 to 10 fm with bin size of 1 fm. The pion yield is plotted against impact parameter for $^{132}$Sn + $^{124}$Sn and $^{108}$Sn + $^{112}$Sn systems in Fig. 4.5. Due to limitations in geometric acceptance of SπRIT TPC, only pions with $p_z > 0$ in center of mass frame are counted. The pion yields decrease with increasing impact parameters where the overlapping zone between
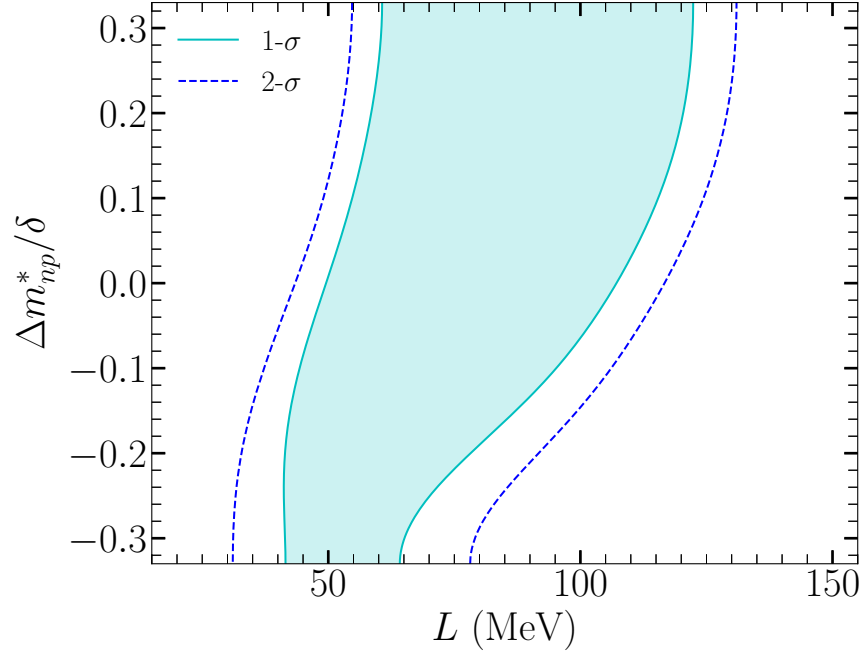
Figure 4.4: Correlation constraint between $L$ and $\delta m_{np}^*/\delta$ extracted from pion single ratio at $p_T > 200\,\text{MeV/c}$ in both the neutron deficient $^{108}\text{Sn} + {}^{112}\text{Sn}$ and the neutron excess $^{132}\text{Sn} + {}^{124}\text{Sn}$ systems. The green shaded region corresponds to 68% confidence interval while the dashed blue lines denote the contours of 95% confidence interval.

projectile and target (also known as the participant zone) decreases. The neutron rich system of $^{132}\text{Sn} + {}^{124}\text{Sn}$ generates the largest difference between $\pi^-$ and $\pi^+$ yields. While $\pi^+$ yields is nearly the same for both systems, the $\pi^-$ is a factor of 2 larger for the neutron rich systems.
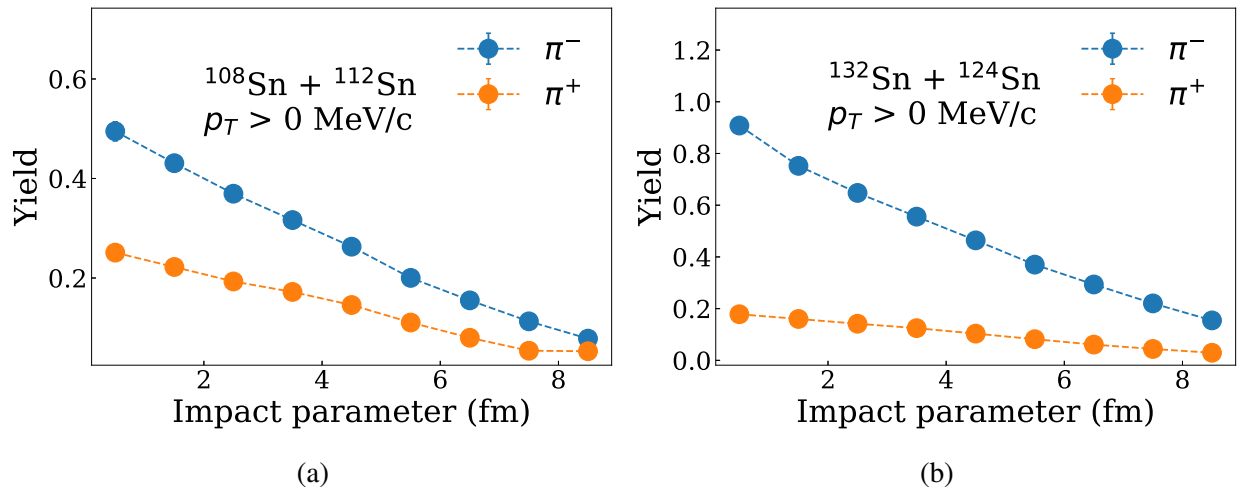


Figure 4.5: Pion yield of (Left) $^{108}\text{Sn} + {}^{112}\text{Sn}$ and (Right) $^{132}\text{Sn} + {}^{124}\text{Sn}$.
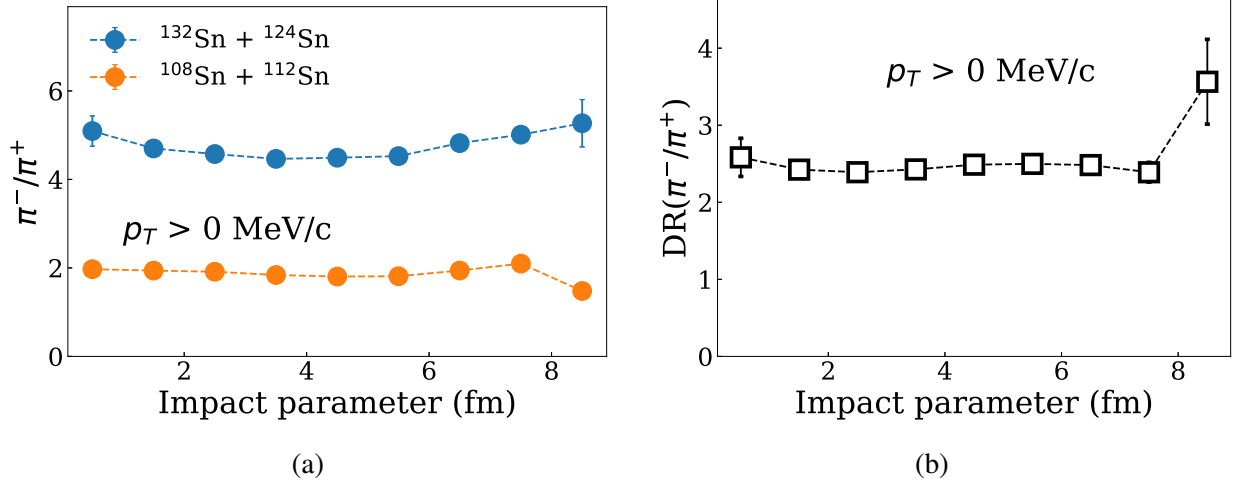
Figure 4.6: (a): Single ratios of $\pi^-/\pi^+$ as a function of impact parameter for $^{132}$Sn + $^{124}$Sn (orange circle) and $^{108}$Sn + $^{112}$Sn (blue circle) reactions. (b): Double ratio of $\pi^-/\pi^+$ from $^{132}$Sn + $^{124}$Sn over $^{108}$Sn + $^{112}$Sn as a function of impact parameter.

The predicted pion yield may suffers from systematic errors due to incomplete description of nuclear dynamics. To minimize such effect, ratio of yields ($\pi^-/\pi^+$) can be used to cancel out the contribution of systematic errors. To further minimize the errors, the double ratio of $\pi^-/\pi^+$ of $^{132}$Sn + $^{124}$Sn over that of $^{108}$Sn + $^{112}$Sn can be used for comparison with models.

These single and double ratios are shown in Fig. 4.6. It is interesting to note the the double ratio is almost constant across all impact parameters.

As described in the previous sections, pions with high transverse momentum provide a clearer signal to symmetry energy as other undesirable effects, such as Coulomb, diminishes. The analysis is repeated with $p_T > 180$ MeV/c and the results are shown in Figs. 4.7 and 4.8. They are identical to Figs. 4.5 and 4.6 respectively except that only pions with $p_T > 180$ MeV/c are counted. Within statistical errors, the impact parameter dependence of single and double ratio is still nearly flat, and the double ratio for the high $p_T$ region is slightly higher than that without $p_T$ cut.

### 4.4.4 Pion direct flow

Collective flow in nuclear collisions have been the focus of numerous studies [11, 106–108] and was demonstrated to be a sensitive probe for nuclear EoS. It is quantified as the Fourier coefficient
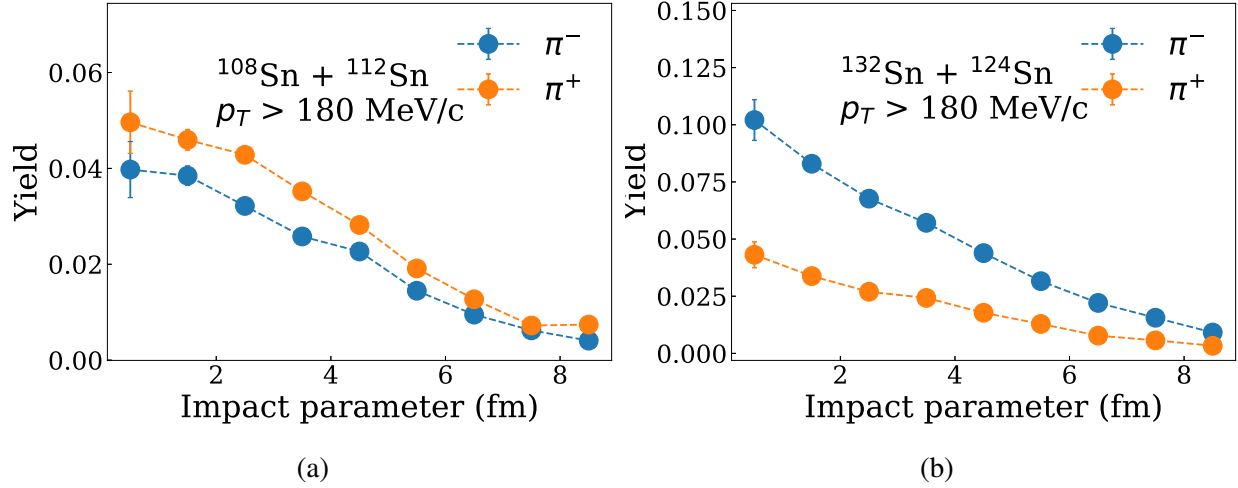
Figure 4.7: Same as Fig. 4.5 except only pions with $p_T > 180\,\text{MeV}$ are counted.
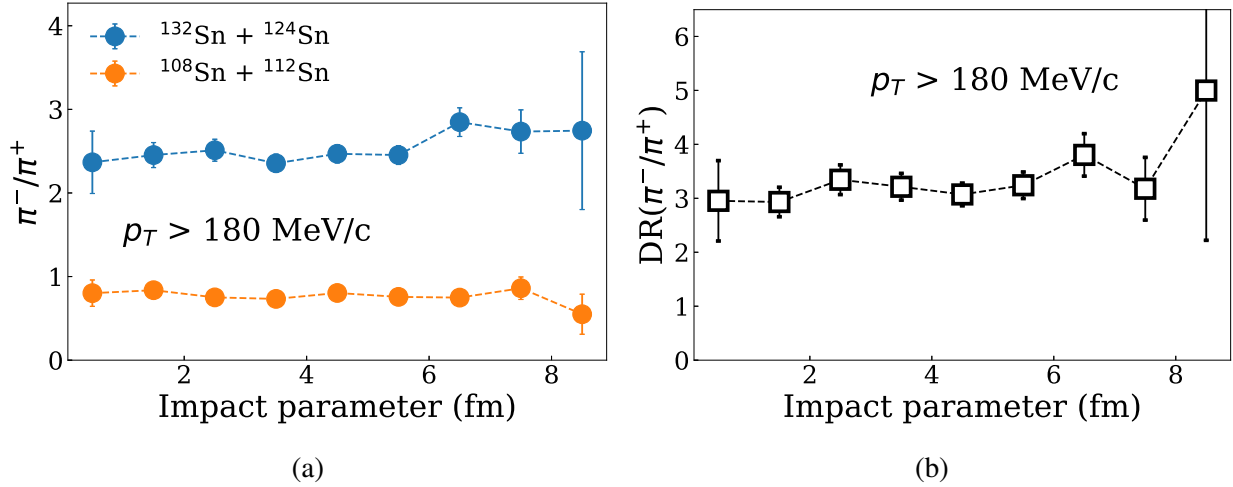


Figure 4.8: Same as Fig. 4.6 except only pions with $p_T > 180\,\text{MeV}$ are counted.

of the fragments' azimuthal distribution with respect to reaction plane azimuth $\Phi$ [109],

$$\frac{dN}{d(\phi - \Phi)} \propto 1 + 2v_1 \cos(\phi - \Phi) + 2v_2 \cos(2(\phi - \Phi)) + ... \qquad (4.4)$$

Here $\phi$ is the fragment azimuths, $v_1$ is the *direct flow* and $v_2$ is the *elliptical flow*. Azimuthal distribution of nuclear fragment is not isotropic because in mid-central collisions, emission near reaction plane is blocked by spectator nucleons. Nucleons outside of the overlapping region between projectile and target nucleus along the beam line are called *spectator nucleons* and those inside are called *participant nucleons*. If the mean field is highly repulsive, participant nucleons experience

76

higher pressure in the collision which leads to early emission. The spectator nucleons do not have time to leave and blocks emission of particle near the reaction plane azimuth, leading to stronger flow. Vice versa for when mean field is less repulsive [11].

The observed direct and elliptical flow are calculated as follows,

$$v_1^{\text{obs}} = \langle \cos(\phi - \Phi_{\text{flat}}) \rangle$$
$$v_2^{\text{obs}} = \langle \cos(2(\phi - \Phi_{\text{flat}})) \rangle$$

$$(4.5)$$

The observed value $v_i^{\text{obs}}$ is smaller than the true $v_i$ due to non-zero resolution in the determination of reaction plane by Q-vector. Fortunately $v_i$ can be reconstructed using resolution information from sub-event method,

$$v_i = v_i^{\text{obs}} / \langle \cos(i(\Phi - \Phi_{\text{flat}})) \rangle.$$

$$(4.6)$$

It is customary to plot observables as a function of normalized rapidity $y_0 = y_{\text{CM}}/y_{\text{NN}}$. Here $y_{CM} = 0.5 \ln((E + p_z)/(E - p_z))$ is the center-of-mass rapidity for fragments in consideration and $y_{\text{NN}}$ is the relative rapidity of nucleons between projectile and target. In fixed target experiment like S$\pi$RIT, target is stationary in laboratory frame so the relative rapidity is simply half of beam rapidity in laboratory frame, $y_{\text{NN}} = 0.5 y_{\text{Beam Lab}}$.

Fig. 4.9 shows pion direct flow ($v_1$) from S$\pi$RIT experiment for $^{108}$Sn + $^{112}$Sn and $^{132}$Sn + $^{124}$Sn reactions at average impact parameter of 5.1 fm ($28 < M \leq 49$) and 5.2 fm ($31 < M \leq 49$) respectively. The flow of $\pi^-$ is positive while that of $\pi^+$ is negative with larger amplitude. Such characteristics are not reproduced by current transport models. The direct flow of pion is expected to be sensitive to the pion potential so further studies are warranted. There is not enough statistics to extract $v_2$ and higher order terms with satisfactory accuracy.
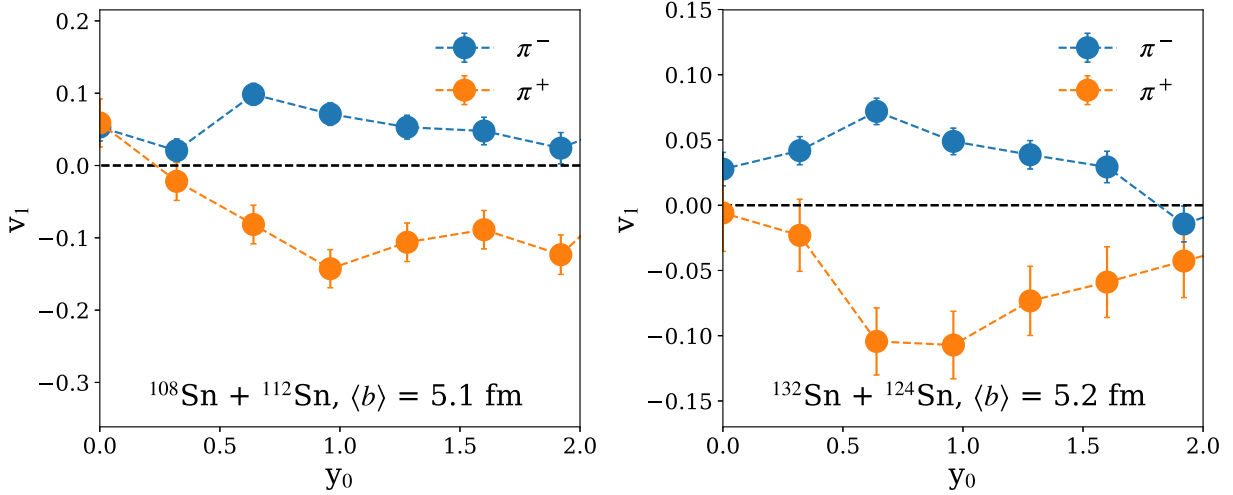
Figure 4.9: $v_1$ of $\pi^+$ and $\pi^-$ as a function of rapidity $y_0$ for $^{108}$Sn + $^{112}$Sn (left) at $\langle b \rangle = 5.2$ fm and $^{132}$Sn + $^{124}$Sn (right) reactions at $\langle b \rangle = 5.1$ fm

## 4.5 Light fragments observables

### 4.5.1 Coalescence invariant proton spectrum

For most transport models, spectrum of individual light fragment cannot be compared between data and model. However, when all proton contributions from light fragments are summed up, it should reproduce the primary proton distribution before the clusterization process. Neutron-to-proton spectrum ratio constructed this way has been successfully used to constraint nuclear EoS in previous experiment [155]. By summing the rapidity distributions for light fragments, we get the *coalescence invariant proton spectrum* (CIP). In the S$\pi$RIT experiment, protons from light fragments up to $^4$He are summed,

$$Y_{\text{CIP}} = Y_{\text{p}} + Y_{\text{d}} + Y_{\text{t}} + 2Y_{^3\text{He}} + 2Y_{^4\text{He}}. \tag{4.7}$$

The scaling factor of 2 in front of Helium isotopes reflects the fact that Helium consists of two protons. Isotope heavier than $^4$He are not counted since their yields are low. Furthermore, due to the geometric constraints of S$\pi$RIT TPC, only fragments emitted in the direction of the beam ($p_z > 0$) are measured. This is problematic as we need to know how many nucleons are
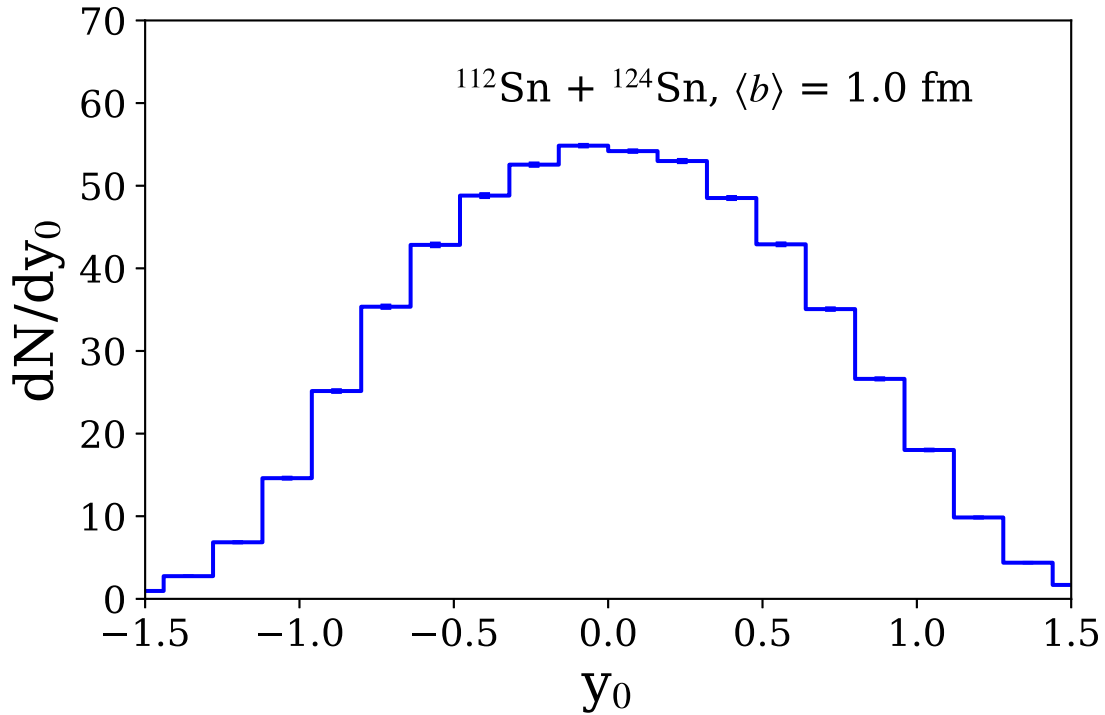
Figure 4.10: Coalescence invariant proton spectrum of $^{112}$Sn + $^{124}$Sn at $b = 1.0\,\text{fm}$ from the SπRIT experiment.

recovered in the summation. It is imperative that most protons are being counted in the CIP for such reconstruction of initial proton distribution to be accurate. For $^{132}$Sn + $^{124}$Sn and $^{108}$Sn + $^{112}$Sn, this estimation cannot be done but fortunately for $^{112}$Sn + $^{124}$Sn, the mirrored reaction $^{124}$Sn + $^{112}$Sn systems are available. The full CIP spectrum can be reconstructed by flipping spectrum of $^{124}$Sn + $^{112}$Sn along $y_0 = 0$ and then combining with spectrum of $^{112}$Sn + $^{124}$Sn system.

Fig. 4.10 shows the complete CIP of $^{112}$Sn + $^{124}$Sn at $\langle b \rangle = 1.0\,\text{fm}$. The impact parameter selection is done with multiplicity cut of $M > 55$. 93% of all the protons in the reaction are accounted for.

### 4.5.2 Stopping

The observable *VarXZ* is believed to be sensitive to the *transparency*, or *stopping*, of heavy-ion collision [36]. Stopping refers to the degree of equilibrium between target and projectile. This

observable allows us to quantify the deviation of reality from a completely stopped scenario, an assumption that were made previously using a hydrodynamic model [36]. It is also useful in understanding the nuclear shear viscosity [156]. Define *VarX* and *VarZ* as the variance of particle rapidity distributions in $x$-direction (transverse direction) and $z$-direction (longitudinal direction) respectively, then *VarXZ = VarX/VarZ*. The $x$-axis in VarX is an arbitrary laboratory axis and not reaction plane azimuth. If the target and projectile are completely equilibrated in the collision, the information on beam axis is lost and we expect the variance in either $x$- or $z$-direction to be identical, thus VarXZ = 1. On the other hand, if target and projectile do not interact at all, which is the case for complete transparency, there is no collision and VarXZ should be 0.

Although S$\pi$RIT TPC cannot detect backward emitting particles, a complete $4\pi$ particle distribution for $^{112}$Sn + $^{124}$Sn reaction can be reconstructed by combining it with results for $^{124}$Sn + $^{112}$Sn in a fashion identical to how coalescence invariant proton distribution is constructed in previous section. Experiment on mirror system of $^{108}$Sn + $^{112}$Sn is not performed in the S$\pi$RIT campaign, but particle distributions are expected to be approximately symmetric around $y_0 = 0$ as the mass number of target and projectile are similar. The $y_0 < 0$ portion of the rapidity distribution is approximated as a mirror image of $y_0 > 0$ part of the distribution. VarXZ from $^{132}$Sn + $^{124}$Sn is not calculated as the mass difference between target an projectile is too large for the mirror image approximation to hold. Fig. 4.11 shows *VarXZ* for proton, Deuteron and Triton for $^{108}$Sn + $^{112}$Sn with centrality gate of $\langle b \rangle = 1.1$ fm ($M > 55$) and $^{112}$Sn + $^{124}$Sn at $\langle b \rangle = 1.0$ fm ($M > 55$). VarXZ decreases with increasing atomic mass on hydrogen isotopes, which is consistent with Au + Au results from FOPI [36] who called this phenomena *stopping hierarchy*.

### 4.5.3 Isospin Tracing

Global equilibrium is not reached in central heavy-ion collision. These non-equilibrium effects are expected to be influenced by a myriad of processes, such as in-medium effects and deflections in momentum-dependent mean fields. To quantify the extent of non-equilibrium, Isospin Tracing was proposed in Ref. [157] to constrain the magnitude of in-medium cross-section with data from the
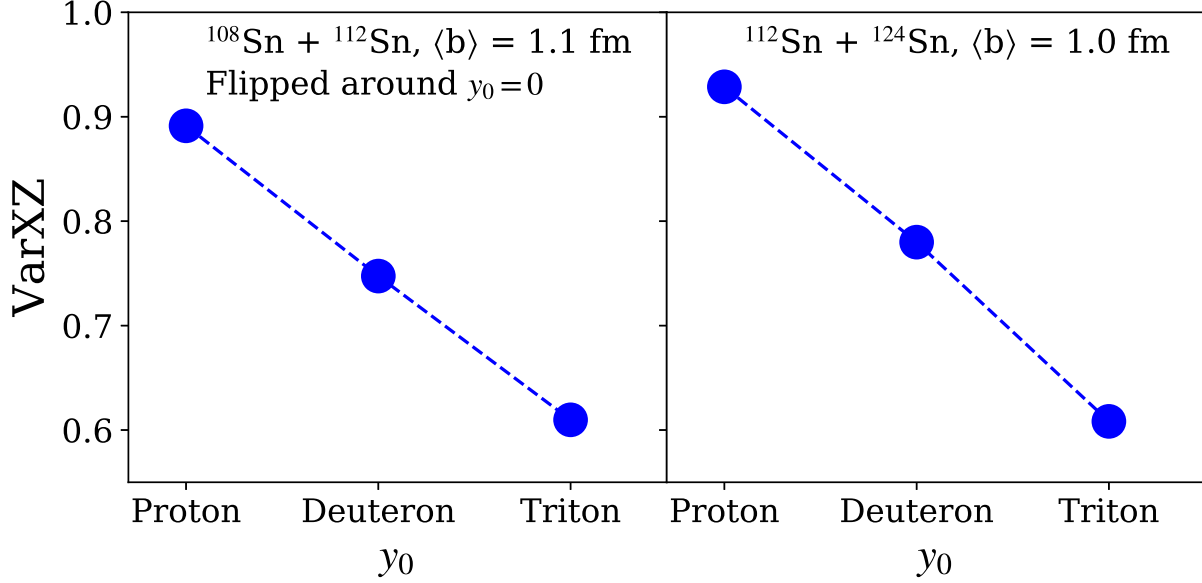
Figure 4.11: Left: *VarXZ* for $^{108}$Sn + $^{112}$Sn at $b = 1.1$ fm from the S$\pi$RIT experiment. Right: *VarXZ* for $^{112}$Sn + $^{124}$Sn at $b = 1.0$ fm.

FOPI experiment [157]. In this section, the construction of Isospin Tracing will be described and the measured values from S$\pi$RIT experiment will be presented.

Isospin Tracing $R_x$ is a meta-observable that is defined with respect to an observable $x$ as follows:

$$R_x = \frac{2x^{AB} - x^A - x^B}{x^A - x^B}. \tag{4.8}$$

In this equation, $x^{AB}$, $x^A$ and $x^B$ are the observable values for $A + B$, $A + A$ and $B + B$ reactions respectively. $R_x$ takes the value of $+1$ if $A + B$ behaves like $A + A$ and $-1$ if it behaves like $B + B$. If global equilibrium is reached, it should take the value of $0$ everywhere in the phase-space. $R_x$ quantifies how well target and project are "mixed".

In the case of Ref. [157], $A = $ Ru and $B = $ Zr. $R_x$ is tested with $x$ being either Triton to Helium-3 ratio (t/$^3$He) or coalescence-invariant proton spectrum ($Z$). $R_{t/^3\text{He}}$ and $R_Z$ both increase monotonically as a function of impact parameter $b$. This trend agrees with the general belief that reactions are more equilibrated in central than peripheral collisions. Furthermore, when a centrality gate of $b \leq 1.3$ fm is imposed, $R_Z$ is observed to be proportional with rapidity $y_0$, with $R_Z = 0$

at $y_0 = 0$. It indicates that equilibrium is reached at mid-rapidity, but not so for fragments with high rapidity. Transport model calculations showed that the slope at which $R_Z$ increases with $y_0$ in central events is sensitive to in-medium cross-section [157].

### 4.5.3.1 Adapting Isospin Tracing for S$\pi$RIT

Due to acceptance issues with S$\pi$RIT TPC, particle data at $p_z < 0$ is only available for $^{112}$Sn + $^{124}$Sn reaction, which comes from data of the mirrored system $^{124}$Sn + $^{112}$Sn. As a result, isospin tracing will only be calculated on that system. In this section, $x$ is chosen to be coalescence-invariant proton spectrum. It is tempting to repeat the analysis of Ref. [157] simply by substituting $A$ with $^{112}$Sn and $B$ with $^{124}$Sn, but it cannot be done due to the absence of data for symmetric reactions.

The calculation of $R_Z$ requires data for $^{112}$Sn $+^{112}$ Sn and $^{124}$Sn $+^{124}$ Sn reaction, which are not performed in the S$\pi$RIT experiment. Fortunately these distributions can be approximated by linear combinations of distributions for reaction systems performed in the experiment. Denote $Z^A$ as CIP for $A + A$ reaction and $Z^{AB}$ as CIP for $A + B$ reaction. To begin with, the distribution $Z^{112\text{Sn}} + Z^{124\text{Sn}}$ can be approximated as $Z^{112\text{Sn}124\text{Sn}} + Z^{112\text{Sn}124\text{Sn}}$. The two distributions are mirror image along $y_0 = 0$. The heuristic reason for the approximation is the fact that the total masses of the target and projectile between L.H.S. and R.H.S. of the equation are equal.

This takes care of the second and the third term on the numerator of Eq. (4.8). With the help of data for $^{132}$Sn $+^{124}$ Sn reaction, the terms on the denominator can also be approximated. Using the mass summing heuristic, $0.5 * (Z^{132\text{Sn}124\text{Sn}} + Z^{112\text{Sn}124\text{Sn}}) \approx Z^{124\text{Sn}}$ since the average projectile mass of L.H.S. = $0.5 * (132 + 112) = 122$, which is close to the desired projectile mass of 124. These approximated distributions will be referred to as *proxy*, as oppose to the real distributions calculated with data from the symmetric systems. The accuracy of proxy will be verified with transport model.

The last variation from Ref. [157] is that we scaled the amplitude of each distribution by the inverse of total system mass to eliminate any effect caused by mass difference between the symmetric and mixed systems. This step is not needed in Ref. [157] because their target and
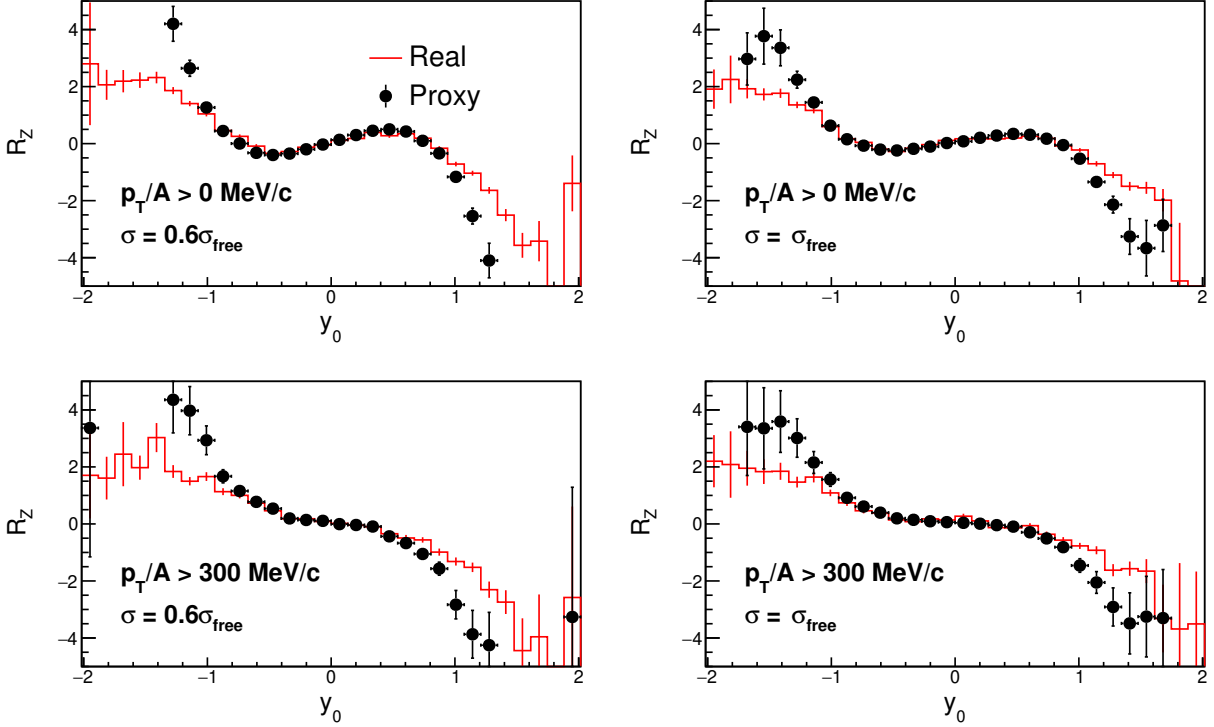
Figure 4.12: Isospin tracing from dcQMD with different parameters. Top left: $p_T/A > 0\,\mathrm{MeV/c}$ and $\sigma = 0.6\sigma_{\mathrm{free}}$. Top right: $p_T/A > 0\,\mathrm{MeV/c}$ and $\sigma = \sigma_{\mathrm{free}}$. Bottom left: $p_T/A > 300\,\mathrm{MeV/c}$ and $\sigma = 0.6\sigma_{\mathrm{free}}$. Bottom right: $p_T/A > 300\,\mathrm{MeV/c}$ and $\sigma = \sigma_{\mathrm{free}}$.t

projectile are chosen to be of the same mass.

Using dcQMD [153], proxies and real distributions are compared in Fig. 4.12. These distributions are generated at $b = 1\,\mathrm{fm}$. From left to right, the in-medium cross-section is increased from $0.6\sigma_{\mathrm{free}}$ to $\sigma_{\mathrm{free}}$. The distributions become flatter, albeit subtlety. This is expected as increasing cross-section should push the reaction closer to equilibrium. For the two graphs on the bottom, only fragments with transverse momentum per nucleon $p_T/A > 300\,\mathrm{MeV/c}$ are used. The slope of $R_z$ at mid-rapidity increases with $p_T/A$ threshold, which reflects an enhancement of transparency for high momentum fragments. $R_Z$ from proxies in all four cases are very close to those from real distributions when $|y_0| < 1$.

Proxies results from the S$\pi$RIT experiment are shown in Fig. 4.13. As expected, the slope of $R_z$ increases with the $p_T/A$ threshold. When $p_T/A$ cut is absent, data disagrees with dcQMD predictions regardless of in-medium cross-section but when $p_T/A > 300\,\mathrm{MeV/c}$ is imposed, data
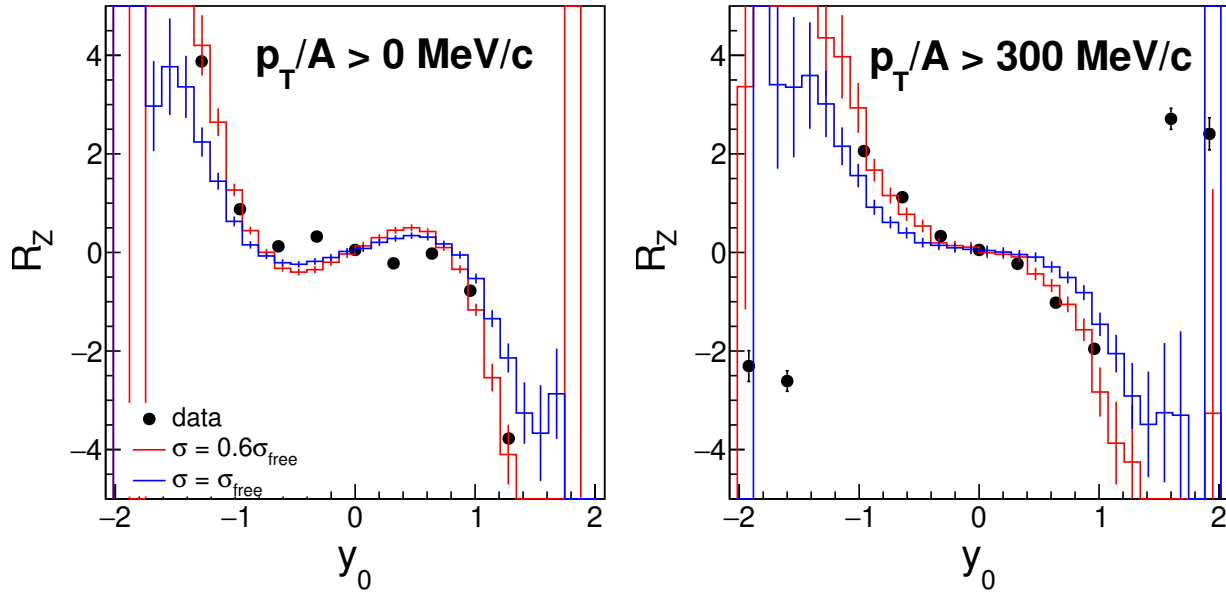
Figure 4.13: Isospin tracing from S$\pi$RIT experiment at $b = 1$ fm. On the left no $p_T/A$ cut is imposed and on the right $p_T/A > 300$ MeV/c is imposed. The legend on the lower left hand corner on the left plot is also applicable to the right plot.

agree with predictions for $\sigma = 0.6\sigma_{\text{free}}$ better that for $\sigma = \sigma_{\text{free}}$. This demonstrates the momentum dependence of in-medium cross-section. By varying the $p_T/A$ slices, it may be possible to constrain this dependence in the future.

In summary, we have demonstrated the viability of using Isospin Tracing on S$\pi$RIT data. Using proxies, $R_z$ can be constructed despite the absence of experimental data for symmetric systems. A comparison between dcQMD predictions and experimental data reveals a possible momentum dependence of in-medium cross-section and future studies are warranted to construct a comprehensive constraint on the in-medium effects.

### 4.5.4   Direct and elliptical flow

Fig. 4.14 shows the direct and elliptical flow for $^{108}$Sn + $^{112}$Sn and $^{132}$Sn + $^{124}$Sn reactions at average impact parameter of 5.1 fm ($28 < M \leq 49$) and 5.2 fm ($31 < M \leq 49$) respectively. The methods used to determine collective flows for light fragments are identical to that for pions detailed in Section 4.4.4. Only $y_0 > -0.5$ are plotted due to limitations of detector acceptance. Figs. 4.14c

and 4.14d show $v_1$ as a function of $p_T/A$ and are both gated on $0.2 < y_0 < 0.8$. The rapidity cut is imposed to increase sensitivity as it is observed that $v_1 \sim 0$ when $y_0 \sim 0$. Finally $v_2$ as a function of $y_0$ for the two systems are shown in Figs. 4.14e and 4.14f.

Direct and elliptical flows of light fragments are also influenced by the coalescence process. Similar to the construction of coalescence invariant proton spectrum, the results can be made less dependent on coalescence by summing proton contributions from all light fragments. The Coalescence invariant flow (C.I. flow) distributions are constructed by taking weighted average of cosines in Eq. (4.5) for all Hydrogen and Helium isotopes, with Helium isotopes weighted twice as much as hydrogen isotopes. Fig. 4.15 shows C.I. flow for $^{108}$Sn + $^{112}$Sn and $^{132}$Sn + $^{124}$Sn reactions.

(a)

(b)

(c)

(d)

(e)

(f)
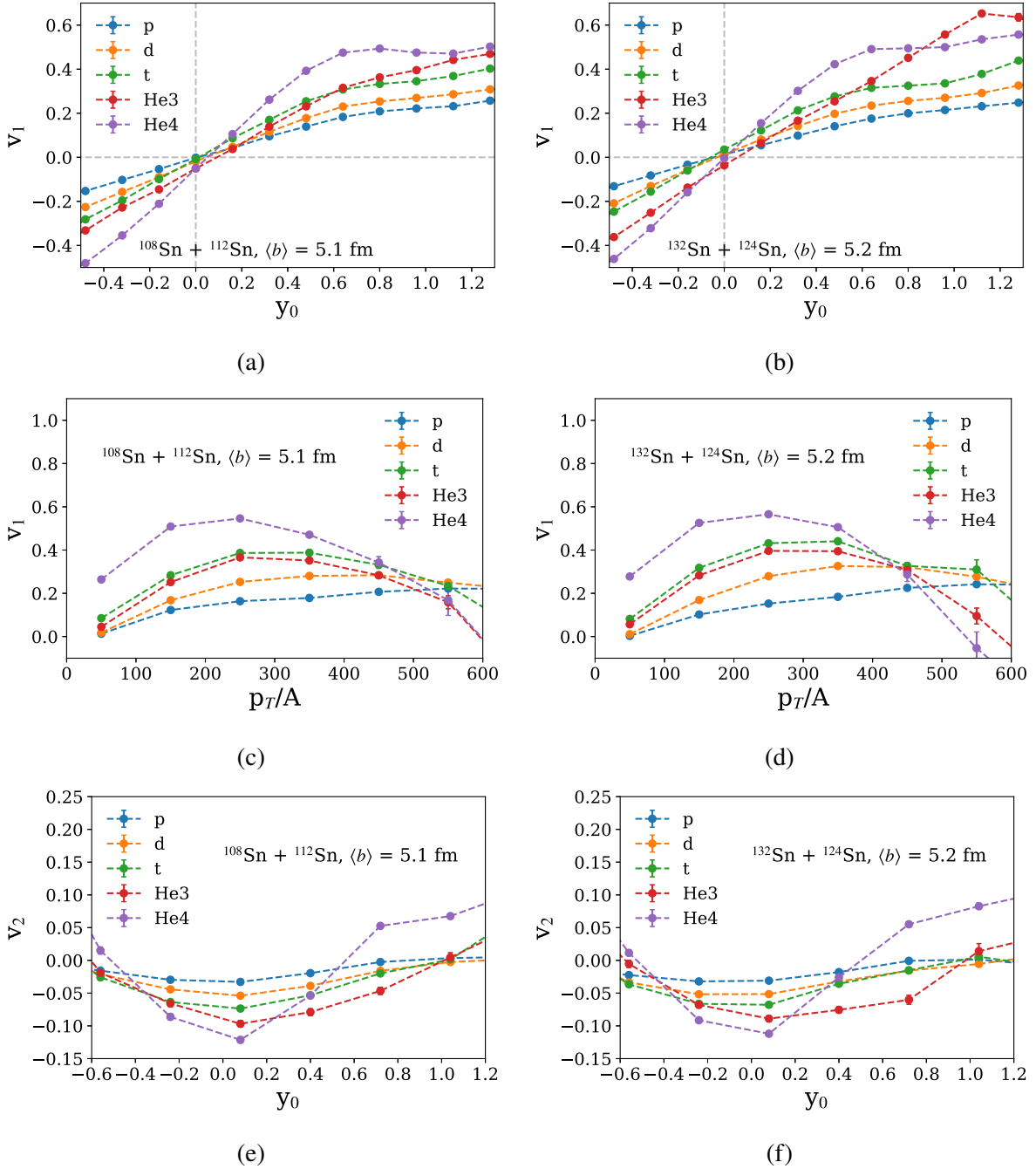
Figure 4.14: (a): Direct flow $v_1$ of $^{108}$Sn + $^{112}$Sn plotted as a function of $y_0$ at average impact parameter of 5.1 fm. (c): Direct flow $v_1$ of $^{108}$Sn + $^{112}$Sn is plotted as a function of $p_T/A$ and gated on $0.3 < y_0 < 0.8$. (e): Elliptical flow $v_2$ as a function of $y_0$ of $^{108}$Sn + $^{112}$Sn. (b), (d) and (f) are the same as (a), (c) and (e) respectively but with results from $^{132}$Sn + $^{124}$Sn, all at average impact parameter of 5.2 fm.

(a)



(b)



(c)
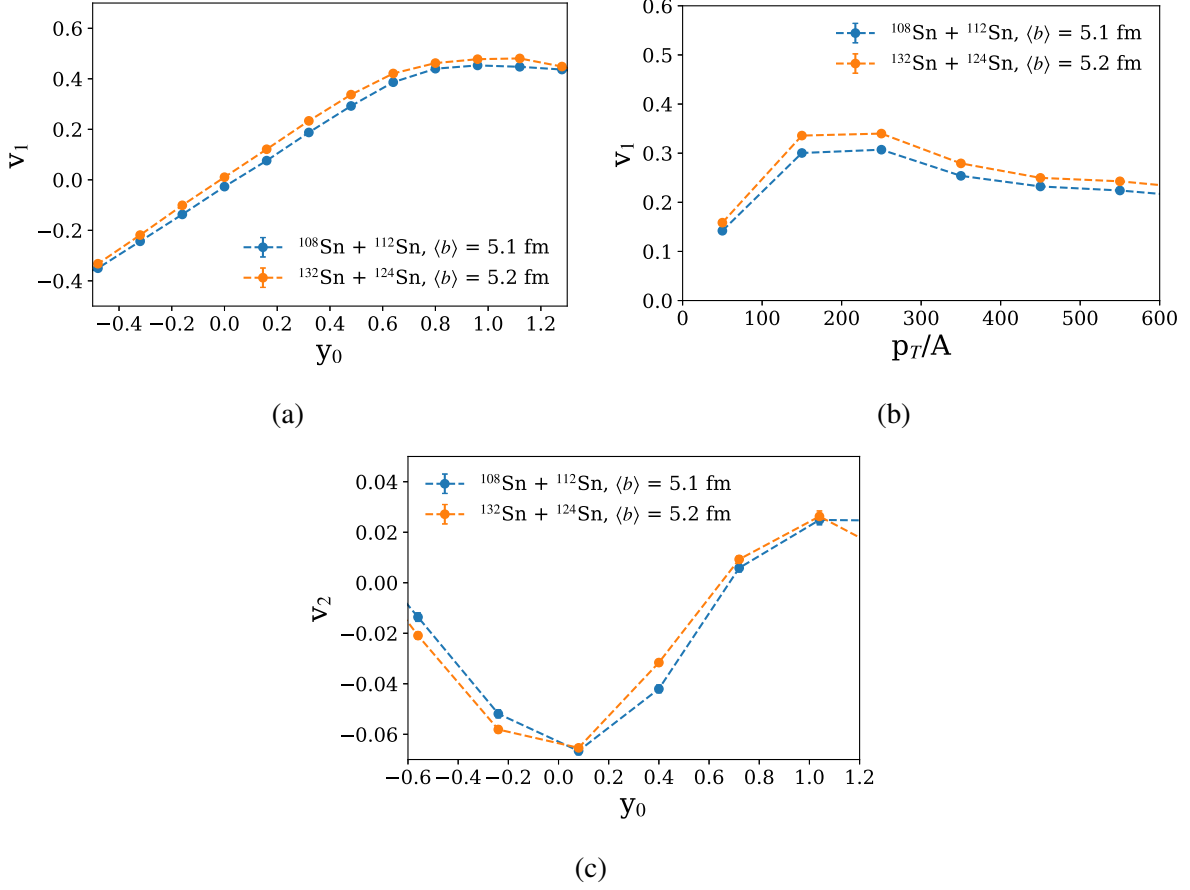
Figure 4.15: (a): Coalescence invariant direct flow $v_1$ as a function of rapidity. (b): Coalescence invariant direct flow $v_1$ as a function of transverse momentum $p_T$, gated on $0.3 < y_0 < 0.8$. (c): Coalescence invariant elliptical flow $v_2$ as a function of rapidity.

# CHAPTER 5

# MONTE CARLO SIMULATION

## 5.1  Introduction

The goal of an experiment is to extract knowledge on the physical world by comparing measured results with theoretical predictions. This comparison is made complicated by the fact that detector resolutions, inefficiencies and abbreviations often skew the observed data. It is imperative that the impact of detector effects be understood to ensure the accuracy of the reconstructed values. This is achieved with Monte Carlo (MC) simulation.

MC simulation for S$\pi$RIT is developed as a part of S$\pi$RITROOT framework to simulate the working principle of S$\pi$RIT TPC. It incorporates known detector effects to generate electronic signals from a given initial particle distribution. The signals can be analyzed as if they are experimental data. Due to the stochastic nature of the physical processes, simulation needs to be repeated for multiple events sampled from the initial particle distribution to understand the average performance of the TPC.

MC simulation routine follows a task-based sequential pipeline structure, similar to that of data analysis routine in Section 3.2. The routine mainly consists of 7 tasks:

1. Geant4 Virtual Monte Carlo

2. Space Charge task

3. Drift task

4. Pad Response task

5. Beam Saturation task

6. Electronic task

7. Trigger task

These tasks will be described in this chapter.

## 5.2 Geant4 Virtual Monte Carlo

The first task, "Geant4 Virtual Monte Carlo", uses Geant4 (version 10-02-patch-01) to simulate the interaction between detector material and the particle fragments. The geometry, material of and magnetic field map in S$\pi$RIT TPC are taken into consideration. Geant4 simulation covers most of the important physical processes in particle-gas interaction and scattering from detector walls, like particle transport, energy loss, multiple scattering and particle decays [158]. The output of this task is the amount of energy loss in keV/cm and the location of interaction (x,y,z).

## 5.3 Space Charge Task

In Section 3.3.2, we showed two idiosyncrasies in experimental data that are caused by the space charge effect. To recap briefly, the first idiosyncrasy is the fact that the peak location of $\Delta V_x$ distribution differs between beam left particles and beam right particles. The second is the fact that that center of mass momentum distribution for beam left and beam right particles are not in agreement when they should be due to cylindrical symmetry arguments.

Here we will try to recreate these idiosyncrasies by distorting the Monte Carlo hit points with space charge effect without correct for it in the analysis of simulated data. It serves as a confirmation that space charge effect distorts detector measurements in ways that matches our expectations.

By integrating Eq. (3.1), the expected lateral displacement for each drift electron as it drifts toward pad plane can be calculated. Each MC interaction points will be displaced accordingly. Unlike in the correction for experimental data where $\sigma_{SC}$ is a measured quantity, we are free to choose the value of $\sigma_{SC}$ in simulation. All simulations in this sub-section will be performed with an ad-hoc value of $\sigma_{SC} = 4 \times 10^{-8}\,\text{C/m}^2$, which is approximately the average $\sigma_{SC}$ for all runs in $^{132}\text{Sn} + ^{124}\text{Sn}$.

As stated previously, the two main features of space charge effect are disagreement of momentum distributions in Fig. 3.7 and $\Delta V_x$ distributions in Fig. 3.8b between left-going tracks and right-going tracks. With space charge distortion included in MC simulation and space charge correction disabled in track reconstruction, both features can be reproduced in Fig. 5.1a and Fig. 5.1b. Both figures are
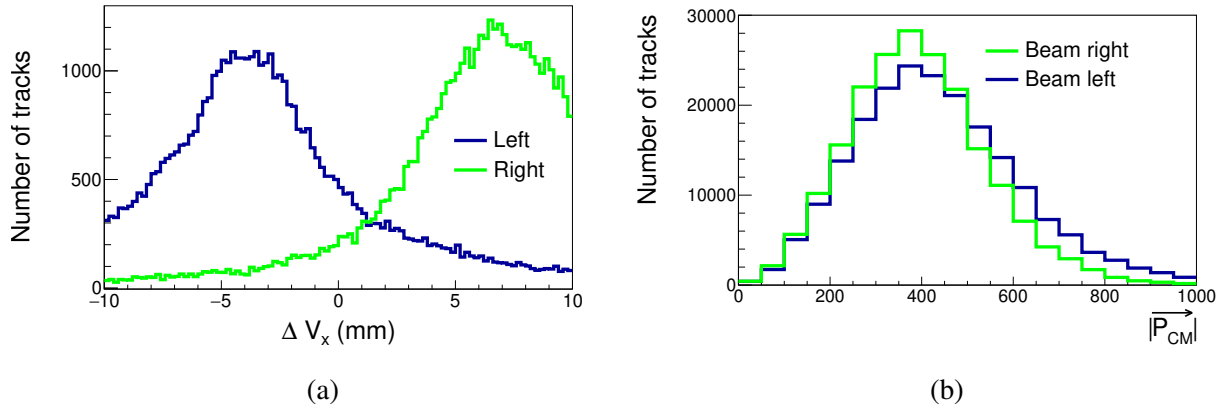
Figure 5.1: (a): *x*-component of distance to vertex on target plane distributions. (b): Center-of-mass momentum distributions. Both distributions are populated with simulated data after the inclusion of space charge effect. Cut conditions are identical to what is being used in Fig. 3.7 and Fig. 3.8b.

drawn with cut conditions identical to that of Fig. 3.7 and Fig. 3.8b.

The space charge simulation procedure can also be used to simulate leakage space charge, which is described in Section 3.3.3. The only modification needed is to include the sheet charge geometry and density for the leakage in electric field calculation. The multiplicative factor of 9.8 found in experiment that converts $\sigma_{SC}$ to leakage sheet charge is used here. Therefore the simulated leakage charge is $9.8\sigma_{SC} = 3.92 \times 10^{-7}\,\mathrm{C/m^2}$. After the inclusion of leakage charge, results from Monte Carlo simulation exhibit inconsistencies in reconstructed Triton momentum in ways that are similar to what is being observed in experimental data. Simulated Triton momentum distributions inside the three azimuth cuts are plotted in Fig. 5.2 which shows that the momentum distribution in cut 3 disagrees with that in cuts 1 and 2 when leakage charge simulation is enabled. To recap the cut conditions, cut 1 corresponds to $74° < \phi < 132°$, cut 2 corresponds to $-29° < \phi < 29°$ and cut 3 corresponds to $-86° < \phi < -143°$. On top of the azimuth cuts, a polar angle cut of $6° < \theta < 12°$ is imposed on all three cuts. The dependence of Triton consistency on *z*-threshold, first shown in Fig. 3.16b for experimental data, is roughly recovered in simulation as Fig. 5.3 showed.
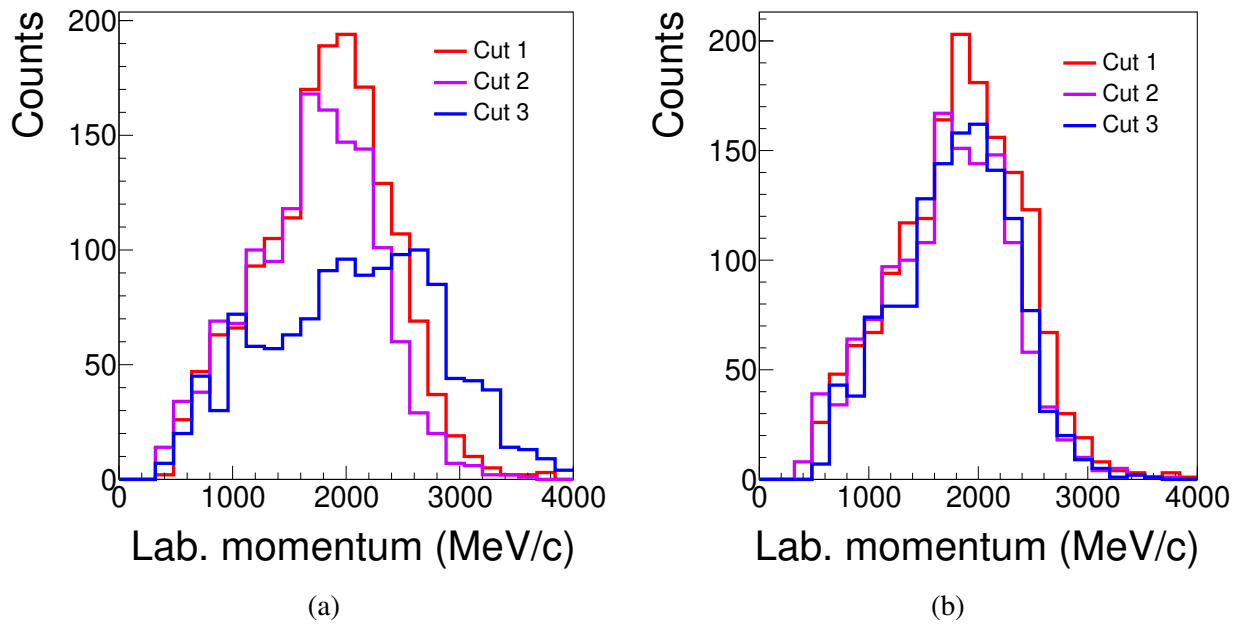
Figure 5.2: Simulated Triton momentum distributions in the three azimuth cuts. (a): Momentum distributions when "leakage" space charge is simulated. (b): Momentum distributions when "leakage" space charge is not simulated.
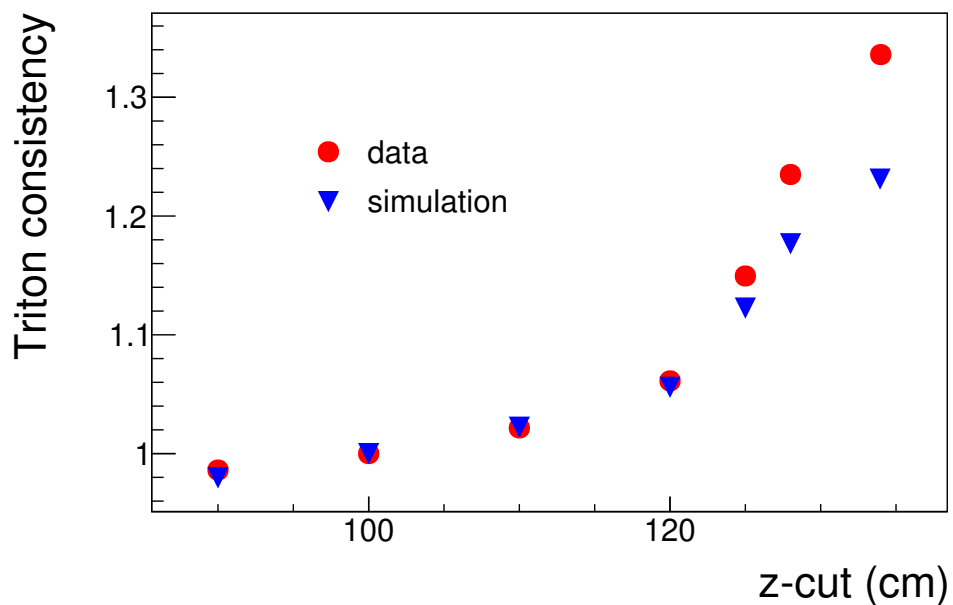


Figure 5.3: Triton Consistency from Monet Carlo simulation (blue inverted triangle) and experimental data (red circle) after including leakage charge. It shows a sharp increase in values beyond $z$-cut = 120 cm, which is consistent with real data.

## 5.4 Drift task

The "Drift task" then converts the interaction points to secondary ionized electrons. The amount of electrons $N_{e^-}$ created in an interaction is described by the following equation,

$$N_{e^-} = \frac{\Delta E}{I}, \tag{5.1}$$

where $\Delta E$ is the energy loss from Geant4 task and $I$ is the ionization coefficient of P-10 gas, which is $26.2\,\text{eV}$. Electrons frequently collide with gas molecules and diffuse as they drift upward, therefore each secondary electron is displaced by a random vector $\vec{\Delta r}$. The random vector is sampled from the following random distribution,

$$\Delta r_i \sim \text{Gaus}(0, c_i \sqrt{L}). \tag{5.2}$$

In this equation, $L$ is the vertical distance between interaction point and the anode wires and $i$ is the component index which can either be $t$, the transverse direction or $l$, the longitudinal direction relative to fragment trajectory. $c_i$ represents the diffusion coefficient along the two directions, whose values are $c_t = 240\,\mu\text{m/cm}^{1/2}$ and $c_l = 340\,\mu\text{m/cm}^{1/2}$ according to Garfield++ calculation [159].

## 5.5 Pad Response task

The "Pad task" calculates the signal amplitude for each pad. Due to the spread of avalanche electrons in the anode wires, some pads that are not directly over but near the secondary electrons will also register signals with lowered amplitudes. It is determined from data that signal amplitude depends on the horizontal displacement between hit points and the pad location as a two-dimension Gaussian function, whose width depends on trajectory direction. The width as a function of trajectory angle is determined empirically [8]. For each secondary electron from the drift task, this empirical function is used to distribute signals amplitude on different pads. If multiple signals are registered at the same time bucket on the same pad, their amplitudes will be summed.

## 5.6   Beam Saturation task

Most incoming beam particles do not react with the target and pass through the TPC detection volume unimpeded. Even when collision occurs, most of them are peripheral as geometric cross-section of peripheral events is larger than that of central events. In most peripheral collisions, projectile nucleus is not broken up effectively which results in heavy residues with high atomic number. When the highly charged particles from either un-reacted beam or heavy residues interact with detector gas, large amount of electrons will be created. They saturate the pads directly on top such that hit points directly below the particle trajectory are not recorded. Furthermore, some pads that were saturated in previous events may not have time to recover before the next collision event occurs. Those pads will be unresponsive for the entire duration of some events. The purpose of Beam Saturation task is to simulate such saturation modes.

The effects of this saturation mode can be seen in Fig. 5.4 which shows the $\phi$ vs. $\theta$ (phase space) distribution for protons in laboratory frame. The creases at $\phi \approx \pm 90°$ demonstrate the inefficiencies created by the saturated of pads by heavy residues. To accentuate beam saturation at large polar angle, no cut is set on number of clusters and only distance to vertex cut of $< 15\,\mathrm{mm}$ is applied.

The naive approach to simulate beam saturation is to include heavy-fragments in event generator. Pad saturation is already handled by the simulation without needing a dedicated beam saturation task. However this approach suffers from performance and memory issues. Heavy-fragments spawn orders of magnitude more ionized electrons than light fragments due to its high electric charge. Since each electron is simulated individually in drift task, this approach consumes a lot of computational powers. It crashes the simulation on our available computation hardware due to excessive memory consumption.

As a result, empirical approach where pads are saturated randomly according to some given probability distributions is preferred. The saturation effect of heavy-fragment is manifested in two ways which we called *complete beam saturation* and *normal beam saturation*. A pad suffers from complete beam saturation when it is unresponsive for the entire duration of an event, which happens when the pad has not recovered from saturation in previous events. In normal beam saturation, the
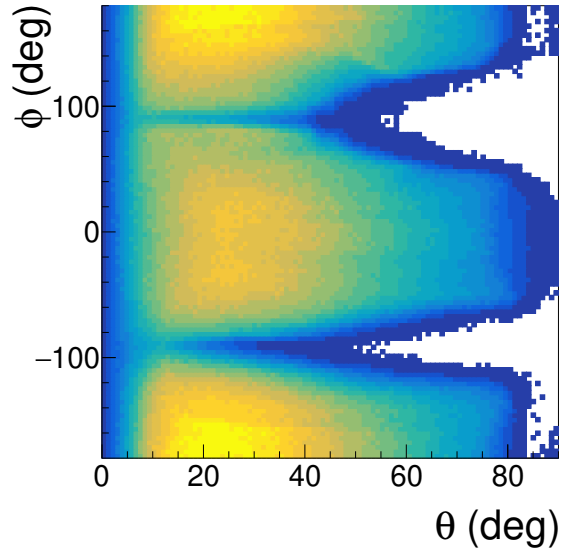
Figure 5.4: $\phi$ against $\theta$ for protons. It is similar to Fig. 3.21, but here no number of clusters cut is applied.

pad is responsive before secondary electrons from the heavy-fragment reach the pad plane. Both saturation modes are needed to accurately reproduce the observed creases.

To simulate complete beam saturation, we tabulate the experimental fraction of events for each pad where it is unresponsive from the beginning of an event. This unresponsive event fraction for each pad is visualized in Fig. 5.5. The empirical fraction is used as probability for each pad to be saturated randomly at the beginning of each simulated event.

To simulate normal beam saturation, we register a large signal amplitude, large enough to saturate the pads, to pads directly on top of the projectile track at time bucket that corresponds to height of the beam. This direct injection of signal circumvent the need to simulate electrons in drift task. This algorithm do not capture all the physics of heavy residues, but it is accurate enough for simulation to reproduce the creases in Fig. 5.4.

Fig. 5.6a shows phase space distribution of simulated protons when only complete beam saturation is applied. Although creases appear, the one at $\phi = -90°$ is not deep enough when compared to experimental result. After normal beam saturation is enabled, a deeper crease is observed at $\phi = -90°$ in Fig. 5.6b. This indicates that both saturation modes are present in the
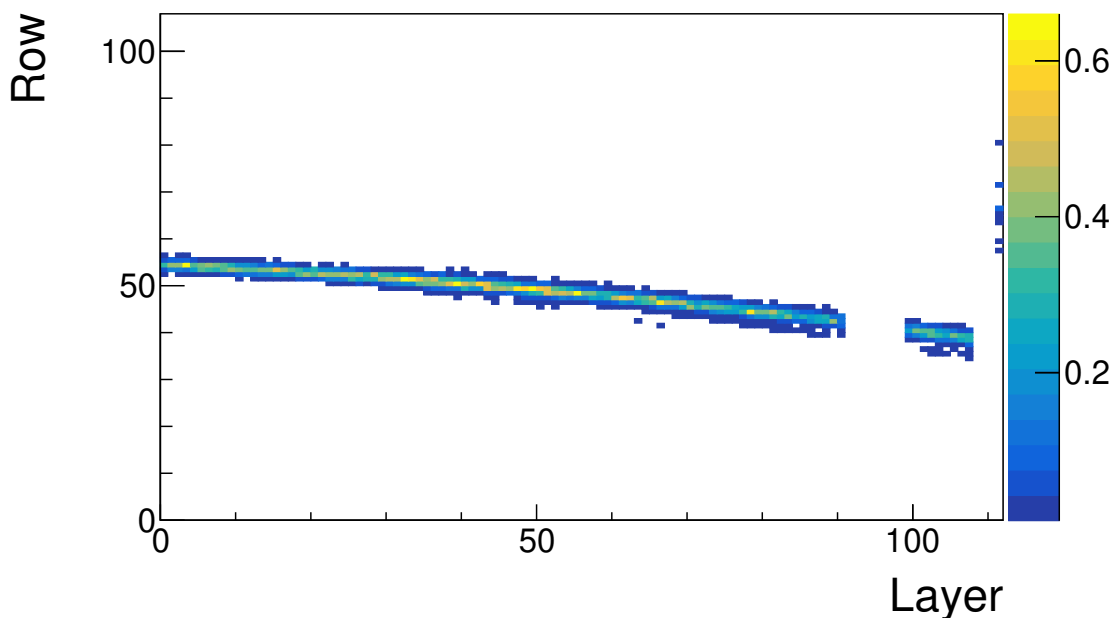
Figure 5.5: The unresponsive event fraction for each pad. The color scale on each pixel corresponds to the fraction of total experimental events where each pad is completely unresponsive. Pads on white pixels are never saturated at the beginning of any events.

experiment.

## 5.7 Electronic task

The "Electronic task" converts signal amplitudes from previous tasks into electronic pluses. The pluses are stored as analogue-to-digital (ADC) readings at different time buckets. Since pulse shape does not vary significantly from pulse to pulse apart from its height, a standard template pulse shape can be extracted empirically. Electronic task takes this template pulse, scales its height according to signal amplitude and displaces its start time to give the simulated pulse [8]. If there are more than one interaction point below a pad, pulses from those interactions are superimposed to form a complete pulse. If total pulse amplitude exceeds the dynamic range of ADC, a saturated template pulse will be appended at the saturation time. All signals beyond saturation time will be discarded.
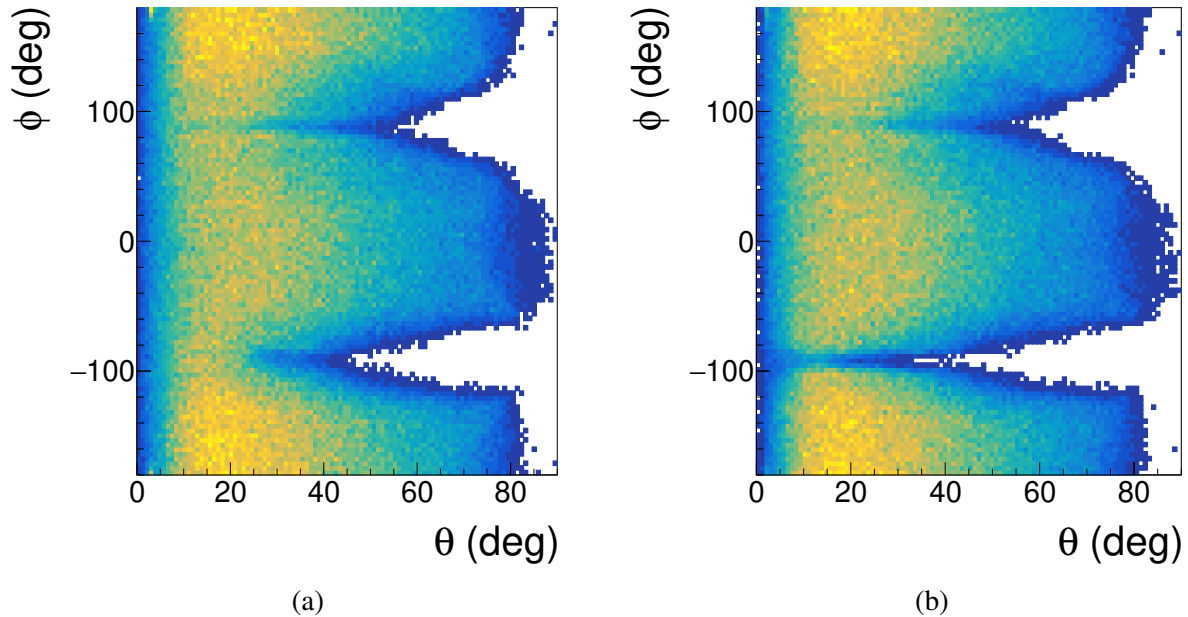
Figure 5.6: Simulated proton $\phi$ vs $\theta$ distribution when (a): only dead pads are simulated, (b): both dead pads and the beam are simulated.

## 5.8 Trigger task

Trigger conditions lead to biases due to their tendency to disproportionately rejects certain type of events. To estimate and understand the effect of *trigger bias*, simulation of triggers have to be implemented. Here the simulated triggers will be described and simulated results will be compared against experimental data.

The geometry and material of KATANA and KYOTO arrays are imported into Geant4 Virtual Monte Carlo task, which allows for the interaction between fragments and the triggers to be simulated. It is possible to convert energy loss in KATANA veto bars and KYOTO arrays to simulated electronic pulses to be reconstructed with S$\pi$RITROOT, but since we are only interested in studying the qualitative effects of trigger bias, approximations can be made to reduce complexities in analysis and simulation. To begin with, the electric charge of heavy-residue is not calculated from energy loss amplitude in KATANA veto bars, rather the exact charge $Z$ of fragments that passes through KATANA veto bars is saved to files. Similarly, the energy depositions in KYOTO arrays will not be converted to electric signal. Any energy deposition inside a KYOTO bar counts

as a hit in trigger and the total number of KYOTO bar being hit is saved to disk. This approximation is reasonable as KYOTO efficiency is measured to be about 99% [160].

To simulate nuclear dynamics, events are generated from Ultra-relativistic Quantum Molecular Dynamic (UrQMD) for $^{132}$Sn $+^{124}$Sn reactions at 270 AMeV with soft EoS of Ref. [141]. The impact parameter distribution follows the geometric cross-section $d\sigma = 2\pi b db$ from $b = 0 - 10$ fm. These events are converted to electronic signals using S$\pi$RITROOT and are reconstructed with tracking algorithms, identical to what is being done with experimental data. The multiplicity distribution of the reconstructed UrQMD simulation will be referred to as *simulated* multiplicity distribution whereas that of experimental data will be referred to as *real* multiplicity distribution. For comparison sake, both real and simulated multiplicity distributions are normalized to unit area.

The simulated multiplicity distribution without any trigger conditions is plotted in Fig. 5.7 as the blue histogram. The steep rise at low multiplicity reflects the fact that cross-section increases with impact parameter. In contrast, the real distribution (black markers) shows a suppression of low multiplicity events due to trigger bias.

When trigger conditions are applied, the simulated distribution resembles real distribution better. The blue curve in Fig. 5.8 is created with the conditions that KYOTO hits $\geq$ 4 and KATANA $Z \geq 20$, which are the same trigger conditions in S$\pi$RIT experiment. On the high multiplicity ($\geq$ 50) side, there are more events in simulation than data, but that is most likely caused by inaccuracies in clusterization of UrQMD rather than problems with trigger simulation. It is well-known that UrQMD, like other similar QMD type models, over predicts light fragment yields [149]. This was discussed in Chapter 4 when transport models were introduced.

On the low multiplicity side ($\leq$ 40), the simulated distribution underestimates the yield of peripheral events. This is also caused by inaccuracies in clusterization process: if the $Z$ distribution of heavy residues is inaccurate, the events rejected by KATANA simulation will not reflect the event selection bias accurately. To compensate for this, the KATANA charge threshold in simulation is raised from $\leq$ 20 to $\leq$ 35. This new threshold is chosen to match the simulated multiplicity distribution on the low multiplicity side to real distribution. The red histogram in Fig. 5.8 shows
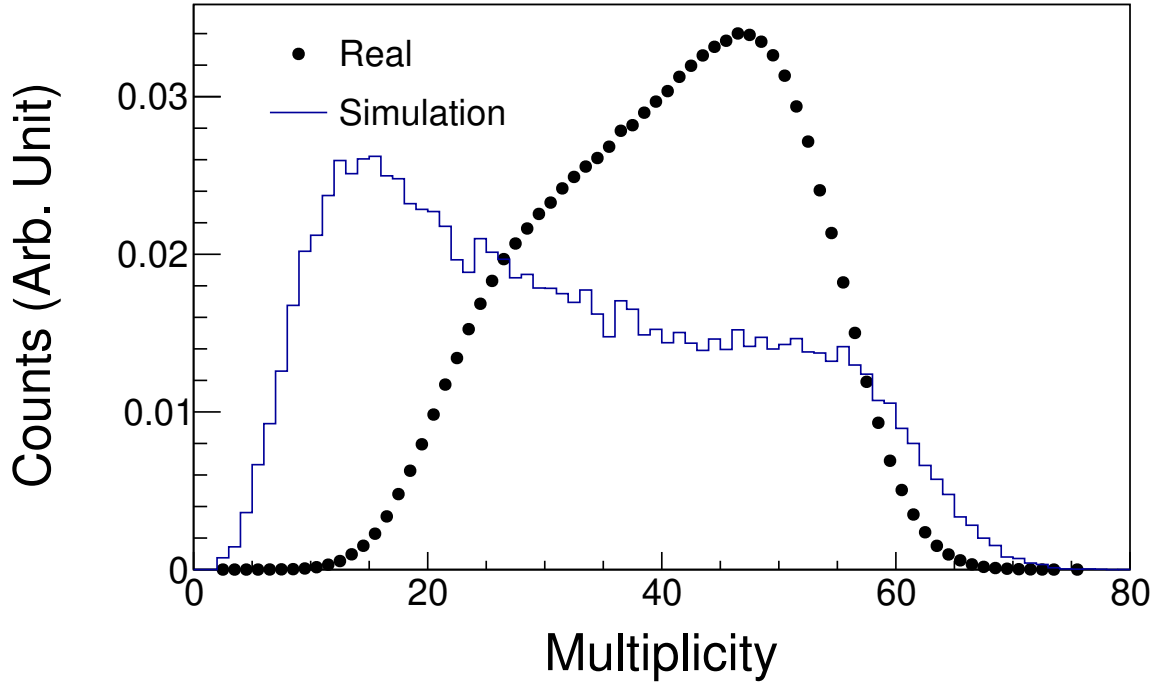
Figure 5.7: *Simulated* multiplicity distribution (blue line) and *real* multiplicity distribution (black points). The *y*-axis are normalized such that areas under the curves are always one.

simulated multiplicity distribution after the charge threshold is raised.

To conclude, the shape of multiplicity distribution depends strongly on the trigger conditions. We have reproduced the approximate shape of multiplicity distribution with trigger simulation. The remaining differences between simulation and data that can be attributed to inaccuracies in UrQMD and the rough implementation of trigger simulations. Hopefully with advancements on nuclear models in the future, the agreement between data and simulation can be improved.

## 5.9 Application of Monte Carlo Simulation

One of the important applications of MC is *embedding efficiency calculation*. Simulation is used to generate electric pulses of S$\pi$RIT TPC for a single particle. Those pulses will be appended to pulses from experimental events in a process called *embedding*, and the embedded events will be analyzed with S$\pi$RITROOT. The fraction of events in which S$\pi$RITROOT successfully identifies the embedded simulated particle is the efficiency of the detector. This technique is also use in
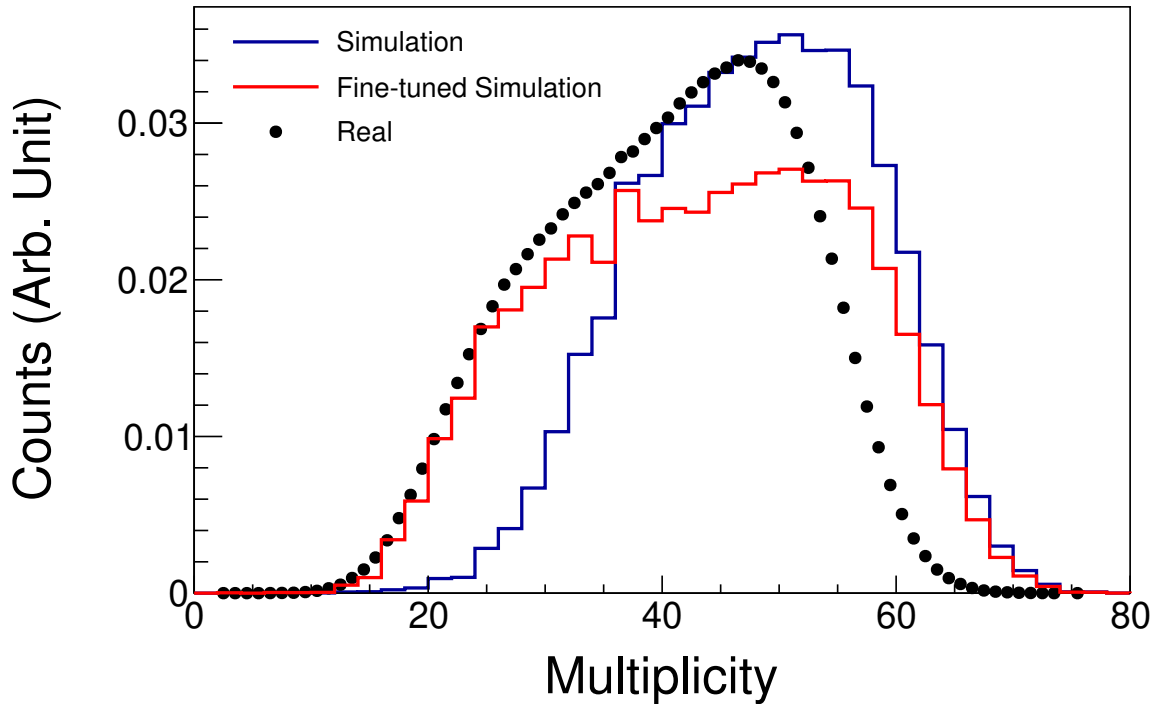
Figure 5.8: *Simulated* multiplicity distribution (blue line) and *real* multiplicity distribution (black points). The *y*-axis are normalized such that area under the curves are always one.

STAR TPC [161].

It can also be used for *Closure testing*. Analysis routine reconstructs Monte Carlo data as if it is experimental data, and the extracted observable values will be compare against the true value from event generator. This step is essential in demonstrating the validity and precision of the analysis routine, as well as revealing any potential issues the analysis may have missed.

The Monte Carlo routine was developed after the 2016 S$\pi$RIT experiment. While it could not be used for the design of S$\pi$RIT TPC and the current experiment, the code will be indispensable for future experiment planning by testing the accuracy in reconstructing the purposed observables. The effects of any modifications to the detector can also be studied in advance. Other experiments also use Monte Carlo simulation for *Detector Design and Optimization* and *Software and Computing Design and Testing* [162].

In this chapter, the various applications of Monte Carlo simulation in S$\pi$RIT experiment will

be reviewed.

### 5.9.1 Efficiency calculation with track embedding

Embedding is a special type of Monte Carlo simulation, used mainly for detector efficiency calculation. If we only consider single track events, efficiency can be calculated without the need for special embedding techniques. It is simply the amount of reconstructed tracks divided by that of initial tracks.

However, real events are rarely single track events. The multiplicities of S$\pi$RIT events are often close to 50. The particle distributions affect detector efficiency due to varying degree of saturation or overlapping of electric pulses. If we want to calculate efficiency with ordinary Monte Carlo simulation (i.e. simulate all ~ 50 tracks in an event and see how many are reconstructed), the events from event generator needs to accurately imitate real events. This is very hard to do, especially when there are many different correlations between particles that are not yet studied. On top of that, cosmic ray background which may affects the overall efficiency is also absent from the simulation.

Single track embedding is developed to overcome those difficulties. Instead of simulating the entire event, only one particle is simulated per event. The simulated signals will be appended to signals of a real event, unless the pad it tries to embed onto is already saturated. The combined event is reconstructed as normal. The detector efficiency is the fraction of events where appended tracks are correctly identified.

Special routine is developed to handle the pulse appending procedure (embedding) and to single out the appended tracks from all the other tracks after track reconstruction. Fig. 5.9 shows a simplified flow diagram for the embedding procedure.

For a track to be identified as the embedded track among all reconstructed tracks, it has to satisfy two conditions that quantify how similar the selected reconstructed and the initial MC track is. The first condition is $N_{MC} > 5$, the fitted track has to make use of at least 5 row or column pad clusters from the MC simulation. The second condition is $N_{MC}/N_{total} > 0.5$, at least half of the clusters used to reconstruct the track has to originate from MC simulation.
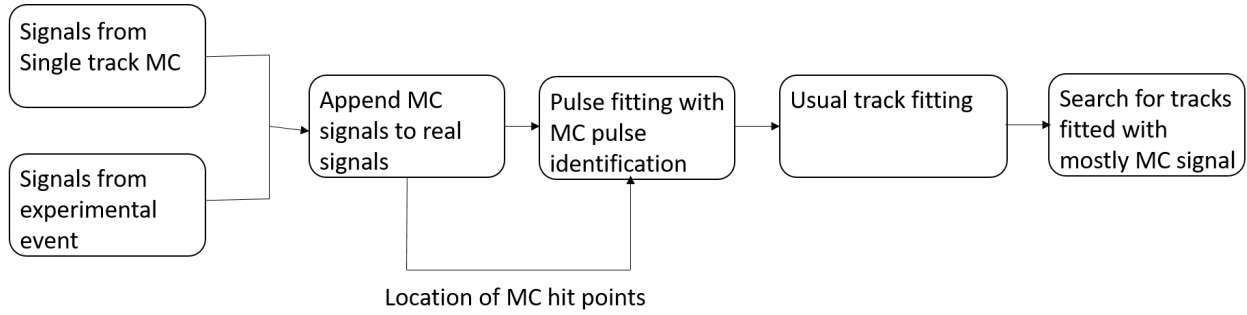
Figure 5.9: Flow diagram for the embedding software.
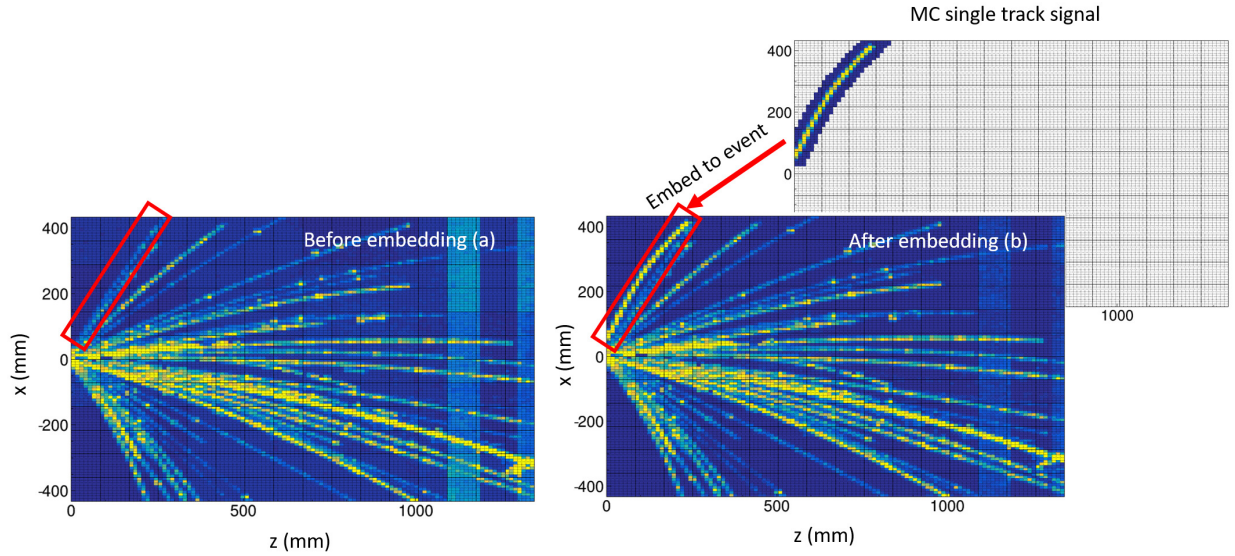


Figure 5.10: Top-down hit pattern before (a) and after (b) embedding. The plot behind (b) shows signal generated by MC simulation.

Naturally this rises the question of how pad clusters from MC and data are differentiated. Clusters are designated as MC cluster if at least one pulse in a cluster originates from MC. The identification of MC pulses is done in PSA task in two steps. The first is to tag all pulses that satisfy following two criteria as "not MC pulse": $|(Q_{\text{Exp}} - Q_{\text{Exp + embed}})/Q_{\text{Exp}}| < 0.05$ and $|t_{\text{Exp}} - t_{\text{Exp + embed}}| < 3$ where $Q$ and $t$ represent the charge and time of the hit point respectively. The subscript "Exp" means fitted pulses from only experimental data and "Exp + embed" means that from the embedded data. The second is to tag the all remaining pulses that satisfy $|t_{\text{Embed}} - t_{\text{Exp + embed}}| < 3$ as MC pulses. If there are more than one track that satisfy all the similarity conditions, the one with the smallest distance to vertex is chosen.

101

### 5.9.2 Verification of data analysis pipeline

Although each step in our data analysis pipeline is tested vigorously, it remains to be seen if they can work in unison to reconstruct observables accurately. By analyzing data from Monte Carlo simulation of S$\pi$RIT TPC, any errors in the software can be caught by comparing the reconstructed observables with the *ground truth*, which is the expected observable values from the event generator. In this section, simulation refers to the simulation of S$\pi$RIT TPC responses instead of QMD simulation.

Particle distributions are constructed in such a way that the expected observable values equal to some initial chosen values. These chosen values are called ground truth. Event generator will sample particles from the particle distributions, and then be simulated and reconstructed with S$\pi$RITROOT analysis framework. How close the reconstructed values is to the ground truth is by definition the accuracy of the analysis.

The $p_T$ vs. $y_0$ distributions of proton, Deuteron, Triton, $^3$He and $^4$He for $^{112}$Sn + $^{124}$Sn reaction are reconstructed from experimental data. These reconstructed distributions will be used as ground truth for event generator in the Monte Carlo simulation of S$\pi$RIT TPC. Only distributions from $^{112}$Sn + $^{124}$Sn system are used because that is the only system where complete $4\pi$ distribution can be recovered by combining experimental results for $^{112}$Sn + $^{124}$Sn with the mirror system $^{124}$Sn + $^{112}$Sn. Due to computational limitations, only events with $^{112}$Sn as the target and $^{124}$Sn as the projectile are simulated at different impact parameters. Since the accuracy and resolution of S$\pi$RIT TPC are intrinsic properties of the detector and do not depend strongly on reaction systems, our conclusion from $^{124}$Sn + $^{112}$Sn reaction can be applied to other reactions.

We first test the performance of rapidity distributions reconstruction. Accurate rapidity distributions are needed in reconstructing VarXZ and Coalesence invariant proton spectrum. The ground truth $p_T$ vs. $y_0$ distributions come from data with centrality gate of $\langle b \rangle = 2.1$ fm as the observables of interest are sensitive to central collision. The particle azimuth are assumed to be uniformly distributed for simplicity. It will be fined when collective flow is considered.

The particles from event generator are converted to ADC pulses. These simulated pulses are
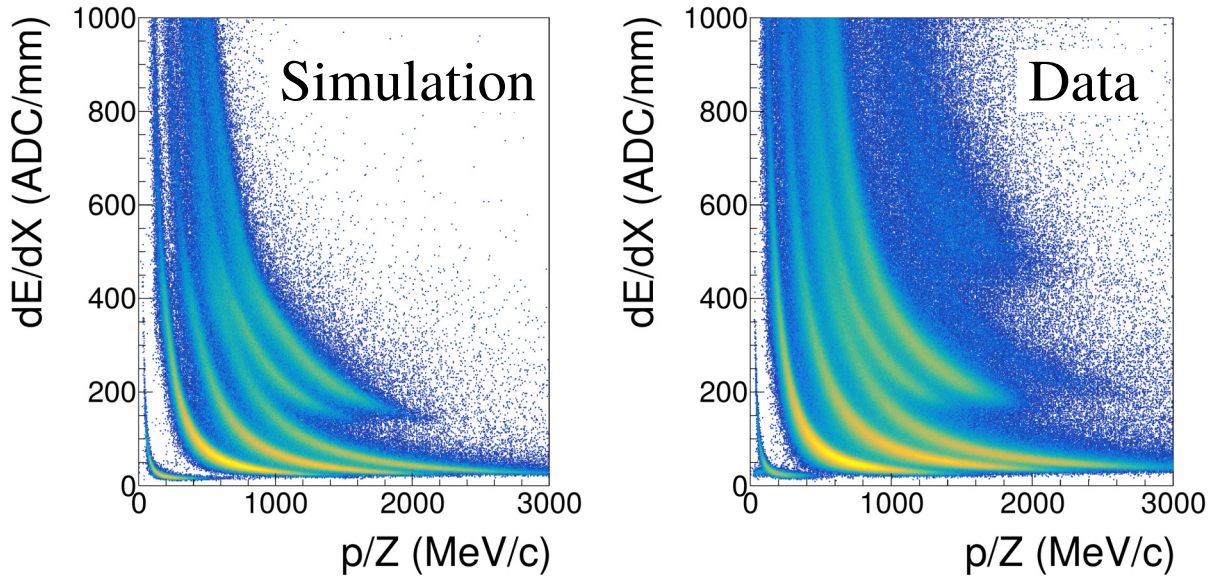
Figure 5.11: PID from simulation (left) and experimental data (right). The plots on the left shows not PID lines for fragments heavier than $^4$He because heavy fragments are not simulated in S$\pi$RITROOT, but otherwise the two look qualitatively similar.

treated as experimental data in the analysis pipeline. Cut conditions described in Table 3.1 are also used in the analysis of simulated data to keep the settings consistent between simulated and real data. However, due to imperfections in simulation, a few adjustments must be made. The PID lines are refitted with simulated data as the shape of simulated PID lines is not exactly identical to that of real PID lines. PID of simulated and experimental data are plotted side-by-side in Fig. 5.11 which shows that, at first glance, the two look very similar. However, the exact $dE/dX$ values for each isotopes are slightly different and there are no PID lines for isotopes heavier than $^4$He as they are not simulated in S$\pi$RITROOT due to computational constraint. Furthermore, since cosmic rays are not included in the simulated data, the amount of background junk tracks in real data differs from simulation. Therefore embedding efficiency is also recalculated, this time with simulated event as the background for single tracks to embed onto.

The reconstructed rapidity distributions and true distributions for proton, Deuteron and Triton are plotted from left the right in that order in Fig. 5.12. Due to geometric coverage limitations of S$\pi$RIT TPC, particles with $y_0 < -0.6$ are poorly detected so only spectrum with $y_0 > -0.6$ are shown. The upper half of each subplot in Fig. 5.12 is the rapidity distribution, with red histograms

103
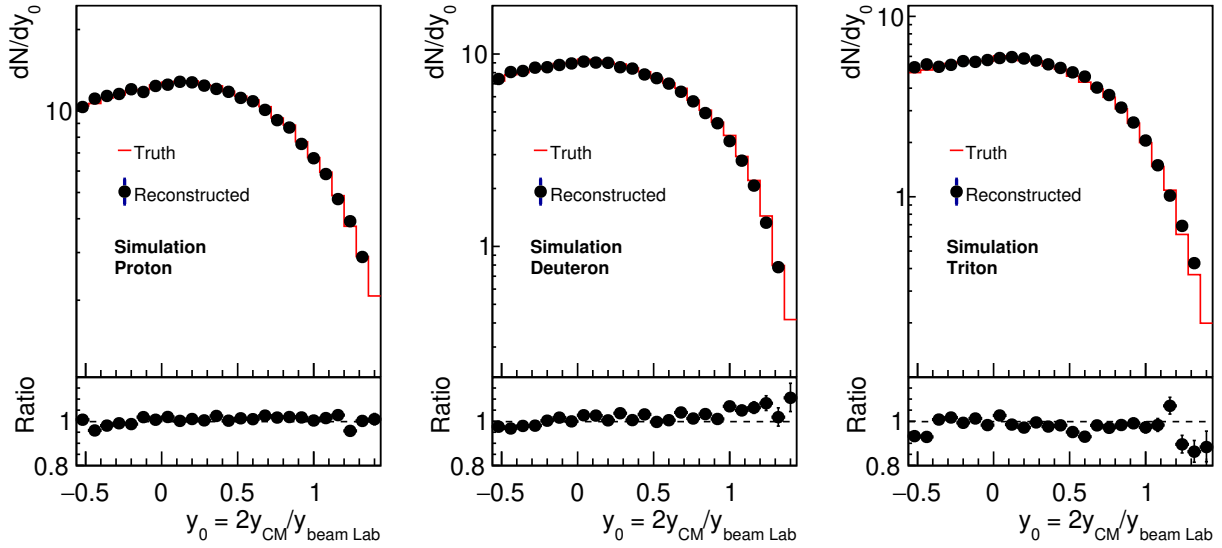
Figure 5.12: From left to right: Rapidity distributions of proton, Deuteron and Triton. The red lines correspond to the initial distribution from event generator and the black points correspond to the rapidity distributions reconstructed with results from simulation of SπRIT TPC. The ratio plots on the bottom of each graphs show the ratio of the true distribution over reconstructed distribution.

being the ground truth and black solid circle being the reconstructed spectrum. The lower half is the ratio of ground truth over reconstructed spectrum, which is very close to the expected value of one. This comparison shows no significant errors in the data analysis.

Next we test the performance of flow reconstruction. The $p_T$ vs. $y_0$ distributions are extracted from data with centrality gate that gives $\langle b \rangle = 5.2$ fm as flow is more sensitive to mid-peripheral than central events. Additional steps are needed to generate collective flow from the event generator.

Let $\Phi$ be the reaction plane azimuth, $\phi_i$ be the azimuth of the $i^{\text{th}}$ particle in an event, $v_{1i}$ be the ground truth direct flow value for particle $i$, we can define function $F(x)$ as,

$$F(x) = x + 2v_{1i} \sin x. \tag{5.3}$$

Although not explicit in the formulation, $v_{1i}$ does not need to be constant. It can be a function
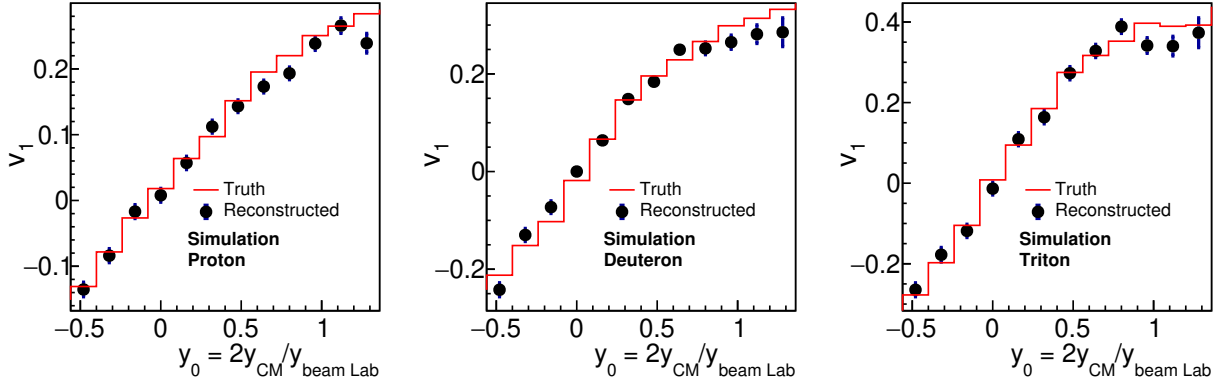
Figure 5.13: From left to right: Direct flow $v_1$ of proton, Deuteron and Triton as a function of $y_0$. The red lines correspond to the initial $v_1$ from event generator and the black points correspond to $v_1$ reconstructed with results from simulation of S$\pi$RIT TPC. The estimation of reaction plane angle with Q-vector or the estimation of reaction plane angle with sub-event method are re-calculated for simulated data.

of $y_0$ of particle $i$. The desired flow can be incorporated if $\phi_i$ is being sampled as follows,

$$\Phi \sim \mathcal{U}(0, 2\pi),$$

$$\phi_i = \Phi + \phi_i' + F^{-1}(\phi_i') \quad \text{where} \quad \phi_i' \sim \mathcal{U}(0, 2\pi),$$

(5.4)

where $\mathcal{U}$ is the uniform distribution and $F^{-1}(x)$ is the inverse of the function $F(x)$. In the following analysis, the ground truth $v_{1i}$ follows the reconstructed $v_1$ vs. $y_0$ correlation from $^{112}$Sn + $^{124}$Sn at $\langle b \rangle$ = 5.2 fm. The dependence of $v_1$ on $p_T$ and any higher order flow term are not included in the ground truth for simplicity.

The simulated data is again analyzed as if it is real data. Bias correction and reaction plane resolution of real data cannot be used since flow distributions in the simulation is simplified not to include dependence on $p_T$ and higher order terms. They need to be re-calculated "empirically" from the simulated data following steps in Section 3.4.6. Fig. 5.13 shows that the reconstructed flow matches the true flow reasonably well.

### 5.9.3 Impact parameter determination with Machine Learning algorithm

Impact parameter cannot be measured directly, but can be inferred from other indirect observables. Traditionally, the inference is done with the help of an observable that depends on impact parameter monotonically. Examples of such observables include total charged multiplicity and ratio of total transverse kinetic energy to longitudinal kinetic energy (ERAT) [34]. With the assumption of geometric cross-section $d\sigma = 2\pi r dr$, impact parameter can be calculated from the cumulative distribution of such observable using the following formula [2],

$$b = b_{\max}\sqrt{\frac{N_{O \geq O_C}}{N_{\text{total}}}}, \tag{5.5}$$

where $O_C$ is the current observable value, $N_{O \geq O_C}$ is number of observed events with observable value $\geq O_C$, $N_{\text{total}}$ is the total number of observed events and $b_{\max}$ is the maximum impact parameter. $b_{\max}$ is calculated from the empirical total reaction cross-section. The method of impact parameter determination using charged particle multiplicity in equation (5.5) will be referred to as *traditional method* in the following sections.

Recent developments of machine learning (ML) algorithms demonstrated their potential in impact parameter determination. Ref. [141] specificity shows that with a perfect detector, algorithms based on Convolutional Neural Networks (CNN) and Light Gradient Boosting Machine (Light-GBM) can be used to predict impact parameter of Au + Au collisions at various beam energies with simulated data generated from ultra-relativistic quantum molecular dynamics (UrQMD) model, and the prediction error is smaller than traditional method.

With the development of Monte Carlo simulation for S$\pi$RIT TPC, such ML algorithms can be extended beyond perfect detector by providing realistic simulation of detector response. In this section, such algorithms will be developed and applied to real experimental data. A few key observables will be compared to gauge the quality of the impact parameter selection.

#### 5.9.3.1 Machine Learning Algorithms

Ref. [141] shows that performance metrics of LigthGBM is slightly better than CNN with perfect detector, trained on events from UrQMD. Base on this, LightGBM is selected for this study. The training data set consists of 135,000 UrQMD $^{132}$Sn $+^{124}$Sn events at $E/A = 270$ MeV for $b = 0 - 10$ fm is used. The reaction is chosen to align with the experimental settings of the S$\pi$RIT experiment. UrQMD is configured to use the parameter set "SM-F", in which the compressibility $K_{\text{sat}} = 200$ MeV and the nucleon-nucleon elastic scattering cross-section in free space is used as the in-medium cross-section.

Following Ref. [141], the following seven observables are chosen as features for the algorithm to infer impact parameter: (i) Total multiplicity of charged particles. (ii) Transverse kinetic energy of hydrogen and helium isotopes. (iii) Ratio of total transverse-to-longitudinal kinetic energy. (iv) Total number of hydrogen and helium isotopes. (v) Averaged transverse momentum of hydrogen and helium isotopes. (vi) Number of free protons at mid-rapidity $|y_z/y_{beam}| \leq 0.5$. (vii) Averaged transverse momentum of free protons at mid-rapidity $|y_z/y_{beam}| \leq 0.5$.

Mean deviation (Bias) and standard deviation (S.D.) of the predicted impact parameter will be used to quantify the quality of the algorithm. Intuitively, bias and S.D. corresponds to accuracy and precision, respectively, and are defined as:

$$\text{Bias}\,(b^{\text{pred}}) = \overline{b^{\text{pred}} - b^{\text{true}}}$$
$$\text{S.D.} = \sqrt{\text{Var}\,(b^{\text{pred}} - b^{\text{true}})}. \tag{5.6}$$

$b^{\text{true}}$ is the true impact parameter used in event generation and $b^{\text{pred}}$ is the predicted impact parameter from the LightGBM. To study the performance as a function of impact parameter, events are binned according to their $b^{\text{true}}$ values. The averaging is done over all events in the same bin.

#### 5.9.3.2 Results on simulated events

Fig. 5.14 shows bias (top panel) and S.D. (bottom panel) as a function of impact parameter ($b^{true}$). LightGBM is used to train and test on two data sets: one includes the response of the S$\pi$RIT
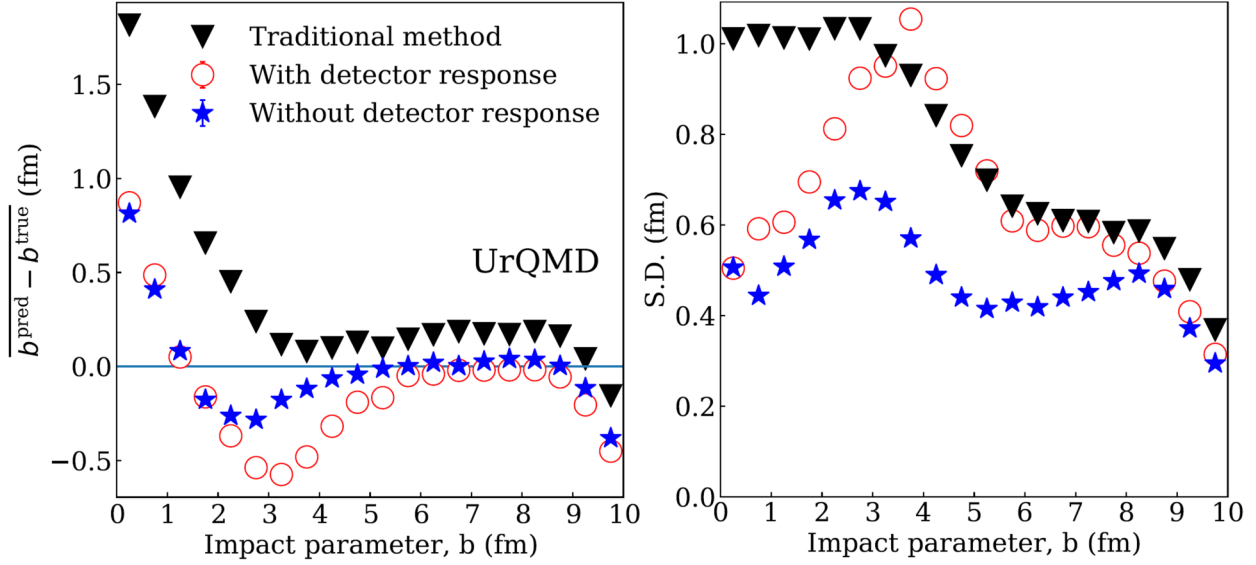
Figure 5.14: Impact parameter dependence of bias (upper panel) and S.D. (lower panel) predicted by LightGBM without detector response (solid stars) and with detector response (open circles).

experiment (open red circles) and one without (blue solid stars). Both the training and the testing data sets use the same UrQMD input parameter set of SM-F. As expected both bias and S.D. worsens with the inclusion of detector response, especially in the mid-peripheral regions. Around $b$=3 fm, both bias and S.D. worsen by a factor of 2 when detector response is included. The worsening in bias and S.D. even when detector response is not included could be related to the physics of transport models. In central collisions (small $b$), nucleon-nucleon scatterings dominate in the collision dynamics while in peripheral collisions (large $b$), the mean field dominates. In the mid-central or mid-peripheral regions ($b$=3-5 fm), accurate treatment of both the mean-field and collisions are very important but transport models may fall short.

The black inverted triangle represent results from traditional method. In general, traditional method performs worse than ML, especially for central collisions. Experimentally, we also see that ML selects central collision events better as discussed below.

If the determination of $b$ is perfect, both bias and S.D. will be zero. That happens for the bias only in the range of $b$=5-8 fm. Over this region, the detector effects are minimal. S.D. never approaches zero over the range of $b$ we investigate. The worsening of both bias and S.D. around $b \approx 0$ fm and $b \approx 10$ fm have been observed with other ML algorithms. This could be due to the

inability of the LightGBM and traditional method to predict accurately near the boundaries of the observable limits.

To verify that application of the LightGBM algorithm trained on the UrQMD simulations is not restricted to only simulations from the UrQMD model and can be generalized to experimental data, we test the algorithm using simulations from four different transport models, Antisymmetrized Molecular Dynamics (AMD) model [163, 164] plus three different families of Quantum Molecular Dynamics (QMD) models, dcQMD [165, 166], IQMD [167, 168] and ImQMD [169]. All these models, including UrQMD, use different techniques and approaches to simulate the nucleus-nucleus collisions. All of them have had various success in describing different aspects of heavy ion collision data. The differences, underlying assumptions and performance between models are detailed in Refs. [170, 171]. In the simulations described here, default physics input parameters for each code are used. This allows us to not only gauge the discrepancy caused by different model assumptions, but also by uncertainty in input parameter values. In addition to these four different models, we also include a different input parameter set for the UrQMD model, labeled as UrQMD/SM-I. It can be considered as a different model.

Tests at $b = 3$ fm are perform to quantify the performance of ML. About 5000 events at 3 fm are generated from each code. LightGBM trained with UrQMD/SM-F data is tasked with predicting the impact parameter of these events. The bias and the corresponding S.D. values are listed in the top, middle, and bottom sections of Table 5.1. The top section contains results from the perfect detector (i.e. without the inclusion of detector response to simulated events) both for training and testing. The middle section contains results from including the detector response for both training and testing. Finally, in the bottom section, we apply the ML algorithm trained with perfect detectors to testing events that include detector response. The last option gives the largest deviation of $b^{true}$ by predicting the mean $b^{pred}$ as nearly 6 fm. Therefore the algorithm not including detector response in the training is unacceptable and would not be discussed any further.

AMD has the largest bias (1.09 fm), reflecting the very different approaches used in simulating HIC in AMD and other QMD-type models. As expected, both the bias and S.D. are larger than

Table 5.1: Statistical properties of $b^{\text{pred}}$ on simulated events from various transport models. Simulated data from UrQMD/SM-F input parameter set are used for training. The bias values are plotted as absolute numbers. All values are in unit of fm.

| Model | AMD | dcQMD | ImQMD | IQMD | Average | UrQMD/ SM-F | UrQMD/ SM-I |
|---|---|---|---|---|---|---|---|
| Perfect detector | | | | | | | |
| $\overline{b^{\text{pred}}}$ | 4.09 | 2.84 | 3.29 | 3.19 | 3.35 | 2.77 | 3.20 |
| S.D. | 0.68 | 1.00 | 0.74 | 0.88 | 0.83 | 0.66 | 0.94 |
| \|Bias\| | 1.09 | 0.16 | 0.29 | 0.43 | 0.49 | 0.23 | 0.20 |
| With realistic detector response | | | | | | | |
| $\overline{b^{\text{pred}}}$ | 4.06 | 3.77 | 3.22 | 2.66 | 3.43 | 2.44 | 2.96 |
| S.D. | 0.91 | 1.22 | 1.02 | 1.03 | 1.04 | 0.94 | 1.05 |
| \|Bias\| | 1.06 | 0.77 | 0.22 | 0.34 | 0.60 | 0.56 | 0.04 |
| Trained with perfect detector, applied to simulation with detector response | | | | | | | |
| $\overline{b^{\text{pred}}}$ | 6.45 | 6.45 | 6.25 | 6.04 | 6.30 | 5.87 | 5.69 |
| S.D. | 0.44 | 0.46 | 0.44 | 0.46 | 0.45 | 0.62 | 0.46 |
| \|Bias\| | 3.45 | 3.45 | 3.25 | 3.04 | 3.30 | 2.87 | 2.69 |

those values listed under UrQMD/SM-F column in Table 5.1 since these transport models were not used to train the events. Except for AMD, the bias and S.D. from different transport models are similar to the results of UrQMD/SM-I where the training and testing data use different input parameter sets. For AMD, while the accuracy worsens, the S.D. values are similar to the reference of UrQMD/SM-F.

As a reference, the best case scenario is LightGBM predictions on UrQMD/SM-F since training and testing data sets come from the same model. When average performance of different models is compared to it, S.D. increases by 20%. The UrQMD/SM-F under-predicts while the other models over-predict $b$. As expected, including the detector response worsens the bias and S.D. for all models. Assuming that the data could be described by the average of the models, then one could expect that the ML algorithm could determine $b$ with a bias of 0.6 fm and S.D. of 1 fm from experimental data.
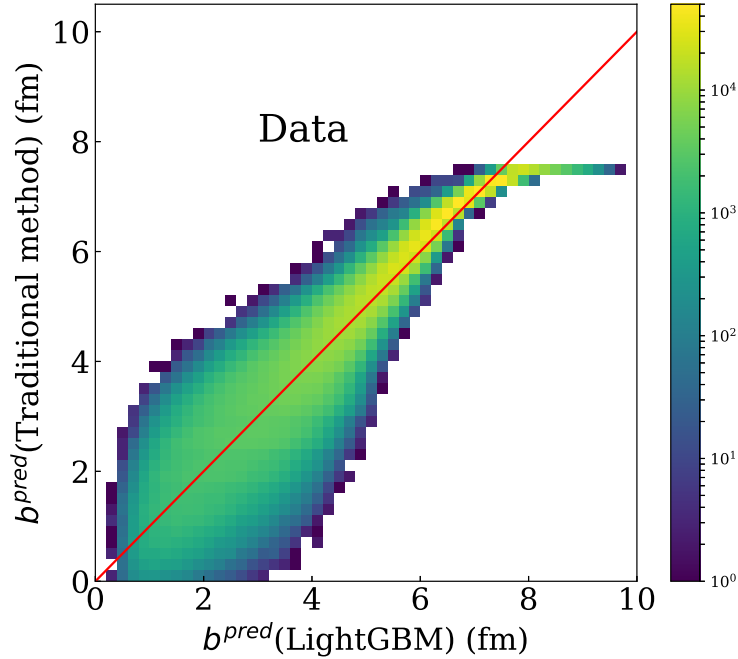
Figure 5.15: Tthe $b^{\text{pred}}$ values from the LightGBM is plotted against that from traditional method. Color represent number of counts in each bin. The red diagonal line shows the expected correlation if impact parameters are determined perfectly.

### 5.9.3.3 Results on experimental data

After extensive tests with transport models, we apply the ML algorithm to experimental data. Fig. 5.15 plots the correlations between $b^{\text{pred}}$ from LightGBM and $b^{\text{pred}}$ from traditional method. Generally, they are in agreement as evidenced by the overall diagonal distribution. Experimental cross-section measurements sets $b_{\text{max}}$ of traditional method to be 7.5 fm while $b^{\text{pred}}$ from the LightGBM extends beyond the sharp cut off limit resulting in a horizontal tail at 7.5 fm. It should be noted that the measured cross-section from which $b_{\text{max}}$ is calculated is smaller than the true geometric cross-section due to trigger bias.

The histogram in Fig. 5.16 shows the experimental impact parameter distributions from the sharp cut off model of eq. (5.5). The impact parameter distribution predicted by the LightGBM (open symbols) exhibits a tail that extends $b^{\text{pred}}$ beyond 7.5 fm. It resembles smearing of the experimental impact parameter distribution which is consistent with the expectation that the experimental data should contain a range of impact parameters that would extend beyond $b_{\text{max}}$. In addition, one would
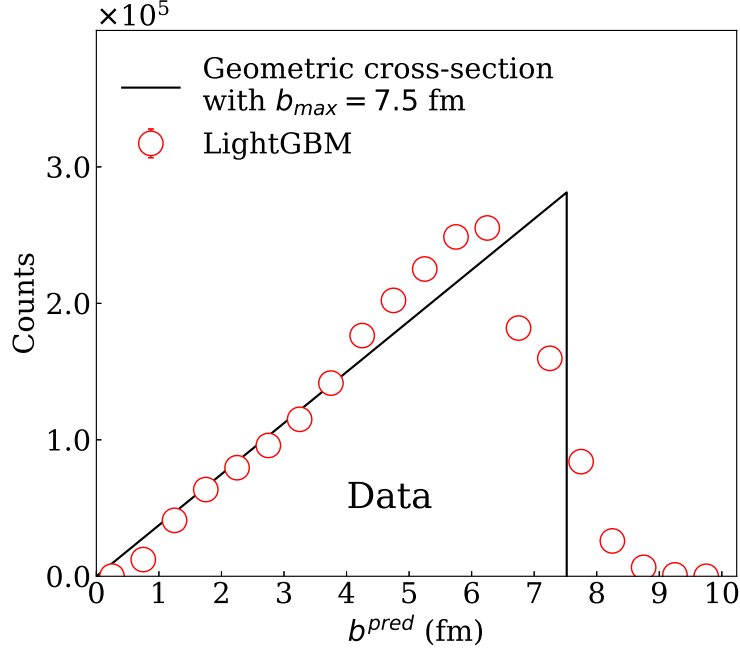
Figure 5.16: Distribution of $b^{\mathrm{pred}}$ made with the LightGBM (open symbols) and sharp cut off model with $b_{\max} = 7.5\,\mathrm{fm}$ (black line).

expect the sharp cutoff model multiplicity distribution should always be equal to or higher than the realistic multiplicity distributions. Fig. 5.16 shows that from 4 to 6.5 fm, there are slightly more events from LightGBM than from traditional method. This apparent discrepancy is not understood. It could be that, not all the detector response has been accurately reproduced. It could also be that the UrQMD is not describing the experimental data accurately enough in this region as is also evidenced by the worsening of the accuracy and broadening of S.D. in Fig. 5.14. Nonetheless, the effects are small.

Unlike events from transport models, we do not have the true value of impact parameter from experimental data so we cannot evaluate the accuracy of $b^{\mathrm{pred}}$ values. Fig. 5.16 suggests that the LightGBM algorithm determines the impact parameter for peripheral events more accurately as it does not have the sharp cutoff limit and the impact parameter smearing occurs naturally. To evaluate the performance at central collisions, we use observables whose qualitative behavior with impact parameter is known.

One such observable is the reaction plane resolution $\langle\cos(\Phi_M - \Phi_R)\rangle$[109]. Here $\Phi_M$ and
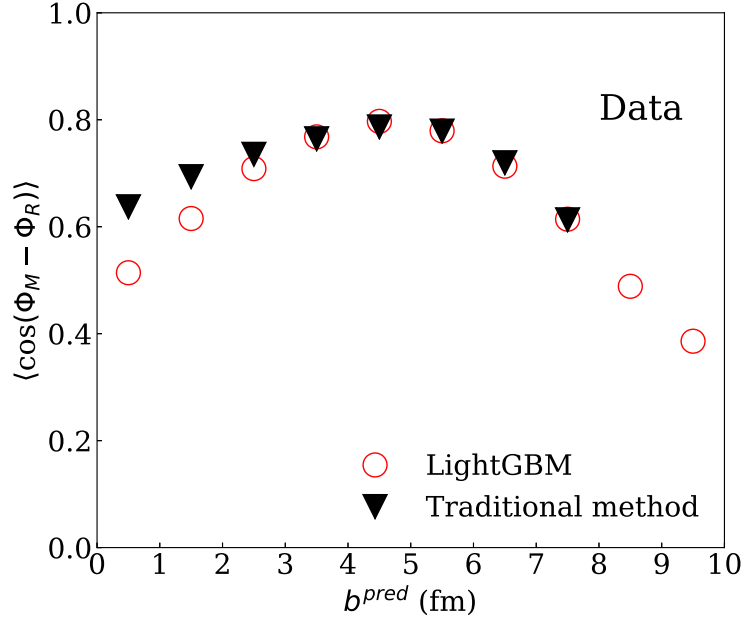
Figure 5.17: The reaction plane angle resolution, $\langle\cos(\Phi_M - \Phi_R)\rangle$ is plotted against $b^{\text{pred}}$. The predictions are made with traditional method (inverted black triangle) and LightGBM (red open circle).

$\Phi_R$ are the measured and the real azimuthal angle of the reaction plane, respectively. The reaction plane should vanish as $b$ approaches zero due to azimuthal symmetry. In a perfect head-on collision ($b = 0$ fm), the fragment emission is isotropic and $\Phi_M$ is reduced to a random number between $0 - 2\pi$, which makes the average of cosine zero.

As shown in Fig. 5.17, the reaction plane resolution $\langle\cos(\Phi_M - \Phi_R)\rangle$ decreases with $b^{\text{pred}}$. However, at $b^{\text{pred}} < 3$ fm the reaction plane resolution is closer to zero if the central event selections are made with LightGBM. This finding supports the assertion that events selected by LightGBM are more central than the corresponding events selected by traditional method, although neither intercepts the $y$-axis at zero.

# CHAPTER 6

## EQUATION OF STATE PARAMETER CONSTRAINTS

## 6.1 Introduction

We are interested in searching for the parameter phase space where model predictions agree with measured observables. The observables described in Chapter 4 are constructed to overcome limitations of clusterization process and should be directly comparable to model predictions. In this analysis, the Improved Quantum Molecular Dynamic (ImQMD) model will be used for constraining nuclear EoS parameters.

We will search in a multi-parameter space, as oppose to the one- or two-parameters search that some other analysis have done to explore the high dimensional correlations between different pairs of parameters. Such a high dimensional search is made with *Bayesian analysis* using *Markov Chain Monte Carlo* (MCMC) sampling. It incorporates our initial believe on parameter values (often results from other analysis) as *prior* and searches the high dimensional parameter space efficiently. This analysis returns the *posterior* distribution, the probability distribution in multivariate parameter space when conditioned on the measured observables. It can be easily projected onto one or two dimensional *marginal probability distribution* for visualization and interpretation.

A downside to such analysis is the intense computational requirement. MCMC sampling asks for model predictions on tens of thousands of parameter sets. Given that ImQMD typically takes half an hour to calculate each one parameter set, MCMC sampling will be prohibitively slow. To speed-up the calculations, we adopt the *Gaussian emulator* [172] and *Principal component analysis* [173]. It is a non-parametric interpolation algorithm that interpolates model predictions from a few tens of parameter sets. The emulator is robust against statistical fluctuations from ImQMD simulation, able to estimate interpolation uncertainty and fast.

In this chapter, we will describe the mathematical background of Bayesian analysis, MCMC, Gaussian emulator and Principal component analysis. These algorithms will be validated with

*closure test*. A constraint on effective mass will be made through Bayesian analysis with ImQMD and SπRIT data. When the constraint is used in conjunction with results from pion spectral yield ratios, the uncertainty on symmetry energy term at $1.5\rho_0$ can be reduced by 39%.

## 6.2    Bayesian analysis

Denote $n$ as the number of free nuclear EoS parameters, $\theta^i$ as the $i^{\text{th}}$ parameter, $m$ as the number of observables, $y_P^j(\vec{\theta})$ as the predicted values for the $j^{\text{th}}$ observable from a given parameter set $\vec{\theta} = \{\theta^1, ...\theta^n\}$, $\sigma_P^j(\vec{\theta})$ as the statistical uncertainty of $y_P^j(\vec{\theta})$, $y_M^j$ as the measured observable value and $\sigma_M^j$ as the experimental uncertainty of $y_M^j$. We will refer to the collection of all predicted and measured observables as $\overrightarrow{y_P}$ and $\overrightarrow{y_M}$ respectively.

From Bayes theorem, the posterior probability distribution is given by $P(\vec{\theta}|\overrightarrow{y_M}) = P(\vec{\theta})P(\overrightarrow{y_M}|\vec{\theta})$. The first term $P(\vec{\theta})$ is referred to as *Prior* and it is the assumed probability distribution of the parameters from prior knowledge, in other words, constraints from other experiments. The second term $P(\overrightarrow{y_M}|\vec{\theta})$ is called the *likelihood*, which is the conditional probability of having the measured observable values given $\vec{\theta}$. It is formulated as,

$$P(\overrightarrow{y_M}|\vec{\theta}) \propto \exp\left(-\sum_{i=1}^{m} \frac{(y_M^i - y_P^i(\vec{\theta}))^2}{2\sigma^{i2}(\vec{\theta})}\right). \tag{6.1}$$

In this expression, $\sigma^{i2}(\vec{\theta}) = \sigma_M^{j\,2} + \sigma_P^{j\,2}(\vec{\theta})$ to incorporate the uncertainty from both the experiment and model simulation.

It is hard to visualize distributions with dimensionality higher than three. To interpret the high dimensional posterior distribution, it is customary to project the distribution onto one or two dimensions such that correlation of any pairs of parameters can be examined. Such projected distributions are called *marginal distributions* and defined as

$$P(\theta_i, \theta_j) = \int \cdots \int_{-\infty}^{\infty} P(\vec{\theta}|\overrightarrow{y_M})\, d\theta_1 \ldots d\theta_{i-1}\, d\theta_{i+1} \ldots d\theta_{j-1}\, d\theta_{j+1} \ldots d\theta_n, \tag{6.2}$$

where $\theta_i$ and $\theta_j$ are the pair of parameters to be visualized. With conventional numerical integration technique, such integration is computationally expensive. This is mitigated by sampling

the posterior with Markov Chain Monte Carlo (MCMC) which randomly walks along the parameter space according to some pre-defined conditions [174]. Those conditions are imposed such that the path of this random walk will converge to posterior distribution. Marginal distributions can be plotted efficiently by filling histograms with parameters from the samples. All posterior distributions in this study are generated with the help of python library PyMC2 [175].

## 6.3 Gaussian emulator

Gaussian process will be used as a surrogate model in lieu of ImQMD in MCMC sampling. It is an interpolation algorithm for arbitrary dimensional input [172]. Only calculations from ImQMD at several tens of randomly distributed parameter sets are needed for the interpolation to work accurately. Gaussian process is better than other interpolation algorithms because it is robust against fluctuations in the training samples and able to estimate interpolation uncertainty. Since ImQMD is a Monte Carlo simulation of nuclear collision, its predictions suffer from statistical fluctuations. Gaussian process is also non-parametric, meaning that the interpolation does not assume any predetermined functional forms. This is advantageous in eliminating potential sources of bias in our choice of regression functions.

Gaussian process takes the form of a high dimension Gaussian distribution, with dimensionality equals to number of training sets [172]. Denote $n$ as the number of training sets, $x_i$ and $y_i$ as the set of nuclear EoS parameters and predicted observable values of the $i^{\text{th}}$ training set respectively. A covariance function $k(x_i, x_j)$ is specified ad-hoc to quantify the covariance between pairs of training sets. The discussion on covariance function is delayed until later sections. Consider the following $n \times 1$ column matrix $f$ with random variable elements that follow multivariate Gaussian distribution,

$$f \sim \mathcal{N}(\mathbf{0}, K(X, X)), \tag{6.3}$$

where $X$ represents the collection of EoS parameters $x_i$ of all $n$ training sets and $K(X, X)$ is a $n \times n$ matrix with elements $K_{i,j} = k(x_i, x_j)$. To predict outcome on a new parameter set $x_{\text{new}}$,

116

Eq. (6.3) can be written as,

$$
\begin{pmatrix} f_{\text{new}} \\ f \end{pmatrix} \sim \mathcal{N}\left( 0, \begin{pmatrix} K(x_{\text{new}}, x_{\text{new}}) & K(x_{\text{new}}, X) \\ K(X, x_{\text{new}}) & K(X, X) \end{pmatrix} \right).
\tag{6.4}
$$

In this equation, $f_{\text{new}}$ is a scalar random variable, $K(x_{\text{new}}, X)$ is a $1 \times n$ row matrix with elements $K_{0,i} = k(x_{\text{new}}, x_i)$, $K(X, x_{\text{new}}) = K(x_{\text{new}}, X)^T$ and $K(x_{\text{new}}, x_{\text{new}}) = k(x_{\text{new}}, x_{\text{new}})$ is a scalar. Gaussian process assumes that the prediction of ImQMD follows $f_{\text{new}}$, with an important twist: since the value of column matrix $f$ is given as the training sets, the distribution of $f_{\text{new}}$ should be conditioned on $f_i = y_i$. Denote $y$ as a column matrix with elements $y_i$. After applying the formula for conditional Gaussian distribution (see Ref. [176]), the probability distribution of $f_{\text{new}}$ becomes,

$$
\mathcal{P}(f_{\text{new}}|f = y) = \mathcal{N}\big(K(x_{\text{new}}, X)K(X, X)^{-1}y,
$$
$$
K(x_{\text{new}}, x_{\text{new}}) - K(x_{\text{new}}, X)K(X, X)^{-1}K(X, x_{\text{new}})\big).
\tag{6.5}
$$

$y_i$ from ImQMD are not exact due to statistical fluctuations. Assume that such random noises follow independent and identically distributed Gaussian function with variance $\sigma^2$, they can be added to the covariance in Eq. (6.3),

$$
\begin{pmatrix} f_{\text{new}} \\ f \end{pmatrix} \sim \mathcal{N}\left( 0, \begin{pmatrix} K(x_{\text{new}}, x_{\text{new}}) & K(x_{\text{new}}, X) \\ K(X, x_{\text{new}}) & K(X, X) + \sigma^2 I \end{pmatrix} \right)
\tag{6.6}
$$

Equation (6.5) has to be modified to accommodate the additional noise,

$$
\mathcal{P}(f_{\text{new}}|f = y) = \mathcal{N}\big(K(x_{\text{new}}, X)[K(X, X) + \sigma^2 I]^{-1}y,
$$
$$
K(x_{\text{new}}, x_{\text{new}}) - K(x_{\text{new}}, X)[K(X, X) + \sigma^2 I]^{-1}K(X, x_{\text{new}})\big).
\tag{6.7}
$$

Covariance function is essential in the construction of Gaussian process [177]. A major assumption in interpolation is that $f_{\text{new}}$ is similar to $y_i$ if $x_{\text{new}}$ is close to $x_i$. The covariance function encodes our assumption on the similarity between points. A commonly used covariance function is the *squared exponential* function,

$$
k(x_1, x_2) = \sigma_f \exp\left( -\sum_{i=1}^{m} \frac{(x_1^i - x_2^i)^2}{2l_i^2} \right).
\tag{6.8}
$$

117

In the equation, $m$ is the number of dimension of EoS parameters, $x^i$ is the $i^{\text{th}}$ component of $x$, $l_i$ is the length-scale and $\sigma_f$ is the covariance amplitude. $l_i$, $\sigma_f$ and $\sigma$ of Eq. (6.6) are free parameters that one need to adjust for optimal performance. In the context of machine learning, they are called *hyperparameters* and the problem of selecting optimal values are called *model selection*. Squared exponential function is used in this chapter.

We will use leave-one-out cross-validation (LOO-CV) for model selection [178]. The idea is to remove a particular parameter set from the training data set. The leave-one-out point, which is usually called the *validation data*, is used to quantify the predictive accuracy with log probability,

$$\log p(y_i|X_{-i}, y_{-i}, \text{hyperparameters}) = -\frac{1}{2}\log(\sigma_{\text{pred}}^2) - \frac{(y_i - y_{\text{pred}})^2}{2\sigma_{\text{pred}}^2} - \frac{1}{2}\log 2\pi. \qquad (6.9)$$

$(X_{-i}, y_{-i})$ denotes the set of training data with $i^{\text{th}}$ set left out and $y_{\text{pred}}$ and $\sigma_{\text{pred}}$ are the predicted values and uncertainty at $x_i$ respectively. The hyperparameters will be adjusted until the sum of log-likelihood over all left-out sets is maximized,

$$\text{hyperparameters} = \text{argmax} \sum_{i=1}^{n} \log p(y_i|X_{-i}, y_{-i}, \text{hyperparameters}) \qquad (6.10)$$

The maximization is performed with Adaptive Movement Estimation (ADAM) algorithm [179]. For a more comprehensive description and derivation of Gaussian process, readers are encouraged to read Ref. [180].

## 6.4 Principal Component Analysis

The output of Gaussian process is usually a scalar. Although multivariate Gaussian process has been developed [181], they are invented recently and we do not have access to such algorithms. This is problematic because our observables are spectrum with different values at different rapidity or momentum bins. The desired output should be a vector of the spectrum values instead of a scalar.

The naive approach is to emulate each bin with an independent Gaussian process, but this approach carries some major drawbacks. If the spectrum is binned finely, a lot of Gaussian

processes are needed which slows down the calculation. The inability to capture the correlated errors between nearby bins in the spectrum is also a potential concern.

Following the approach adopted by the Modeling and Data Analysis Initiative (MADAI) [182], we perform a dimension reduction on the spectrum with Principal Component Analysis (PCA) before interpolation. PCA returns the ranked orthogonal coordinate bases which satisfy the following conditions: the variance of spectrum projections on the first basis is the greatest among all possible orthogonal coordinate bases, and the variance of spectrum projections on the second basis is the greatest among all possible orthogonal coordinate bases that are orthogonal to the first one, etc. These bases are called *principal components* (PC) and only PC with large variance needs to be emulated. Low variance PCs can be approximated as constant without losing too much accuracy.

The formula for PCA is shown here without proof. Readers are encouraged to read Ref. [173] for detailed derivation. Denote $d$ as the number of bins in the spectrum and $\Sigma$ as the $d \times d$ covariance matrix of all bins in spectrum on training data set, and $y_i$ as the $d$-dimensional vector representing the $i^{\text{th}}$ spectrum in the training set. If we only keep the first $k$ components, then $y_i$ can be transformed into a lower dimensional vector $z_i$ by,

$$z_i = \text{eig}(\Sigma, k)(y_i - \overline{y}). \tag{6.11}$$

Here, $\text{eig}(\Sigma, k)$ is the matrix formed by stacking $k$ row-eigenvectors of $\Sigma$ with $k$ largest eigenvalues. $\overline{y}$ is the mean $y$ vector over all the observed data points and $z_i$ is a $k$ dimensional vector. It is important to note that $k \leq d$ since number of eigenvectors equals to the dimension of the covariance matrix. $y_i$ can be approximated by $z_i$ using the following inverse transformation,

$$\hat{y}_i \approx \overline{y} + \text{eig}(\Sigma, k)^T z_i. \tag{6.12}$$

It is guaranteed that $\hat{y}_i \approx y_i$ if $k$ is large enough. To be precise, let $\lambda_i$ be the $i^{\text{th}}$ largest eigenvalue and we use superscript to denote the component of a vector, then $\hat{y}_i$ satisfies the following condition,

$$\frac{1}{n} \sum_{i=1}^{n} \sum_{j=1}^{d} (y_i^j - \hat{y}_i^j)^2 = \sum_{i=k+1}^{d} \lambda_i. \tag{6.13}$$

119

In the above equation, $n$ is the number of training parameter sets. This means that as long as $\lambda_i$ for all $i > k$ are all very small, the averaged square difference between $\hat{y}_i$ and $y_i$ will be very small. Therefore, it is possible to approximate $d-$dimensional spectrum with just $k-$dimensional PCs, where $k \leq d$. Empirical evidence suggests that rarely do we need more than three PCs to emulate a spectrum, even if the spectrum contains as much as fifteen bins.

During MCMC, $k$ emulators are used to interpolate $k$ PCs independently. The interpolated PCs will be transformed back to spectrum with equation (6.12). The emulated uncertainties for each PCs are also transformed to covariance matrix of the spectrum. The truncation error of equation (6.13) is divided by $d$ to estimate the average truncation error of each bin, which will then be added to the diagonal elements of covariance matrix for likelihood estimation.

## 6.5 Sensitivity of each observables

The training data for Gaussian emulator comes from ImQMD predictions on 70 parameter sets. On each parameter set, calculation is repeated for each required reaction system and impact parameter. For each calculation, 3000 events are simulated. The following three classes of observables, totalling in eight spectra, are extracted on each parameter set,

1. Coalescence Invariant Direct flow (C.I. $v_1$) at $b = 5\,\text{fm}$

   a) C.I. $v_1$ as a function of $y_0$ for $^{108}\text{Sn} + {}^{112}\text{Sn}$

   b) C.I. $v_1$ as a function of $p_T$ for $^{108}\text{Sn} + {}^{112}\text{Sn}$ ($0.3 < y_0 < 0.8$)

   c) C.I. $v_1$ as a function of $y_0$ for $^{132}\text{Sn} + {}^{124}\text{Sn}$

   d) C.I. $v_1$ as a function of $p_T$ for $^{132}\text{Sn} + {}^{124}\text{Sn}$ ($0.3 < y_0 < 0.8$)

2. Coalescence Invariant Elliptical flow (C.I. $v_2$) at $b = 5\,\text{fm}$

   a) C.I. $v_2$ as a function of $y_0$ for $^{108}\text{Sn} + {}^{112}\text{Sn}$

   b) C.I. $v_2$ as a function of $y_0$ for $^{132}\text{Sn} + {}^{124}\text{Sn}$

3. Stopping (VarXZ) at $b = 1\,\text{fm}$

a) VarXZ of p,d and t for $^{108}$Sn + $^{112}$Sn (Histograms flipped along $y_0 = 0$)

b) VarXZ of p,d and t for $^{112}$Sn + $^{124}$Sn

The constructions and physic importance of each observable were described in Chapter 4. In addition to symmetry energy term, the momentum dependence of nuclear mean-field potential also influences the properties of nuclear matter [183–189]. This dependence manifests itself as a reduction of nucleon masses. The ratio of effective mass in symmetric matter to free nucleon mass $m_N$ is called the isoscalar effective mass $m_s^*/m_N$. In asymmetric matter, the contribution of isovector (symmetry) mean-field potential causes the neutron and proton effective mass to differ [183, 185, 186], which is quantified in terms of isovector effective mass $m_v^*/m_N$ [184]. The in-medium NN cross sections in ImQMD is formulated as [190],

$$\sigma_{\text{QMD}}^{\text{med}} = \left(1 - \frac{\eta\rho}{\rho_0}\right)\sigma^{\text{free}}, \tag{6.14}$$

where $\sigma^{\text{free}}$ is the NN cross-section in free space taken from Ref. [191] and $\eta$ is the reduction factor to be determined. These parameters, together with $S_0$ and $L$ in density dependence of symmetric energy term, strongly influence the dynamics of nuclear collision. It is expected that the predicted flow and stopping depends on the competing effect of in-medium cross-section, symmetry forces and the momentum dependence in mean-field potential.

70 parameter sets are sampled randomly and with Latin Hyper-cube within parameter space ranges specified in Table 6.1.

| Parameters | Min. | Max. |
|---|---|---|
| $S_0$ (MeV) | 25 | 50 |
| $L$ (MeV) | 15 | 160 |
| $m_s^*/m_N$ | 0.6 | 1 |
| $m_v^*/m_N$ | 0.6 | 1.15 |
| $\eta$ | -0.25 | 0.25 |

Table 6.1: The ranges of parameters for the training of Gaussian emulator.

The sensitivity of each observable group on nuclear EoS parameters can be tested with the *Closure test*, where the analysis is performed by pretending ImQMD prediction from a new parameter set, one that is not used in the training of Gaussian emulator, is the experimental data. If the marginalize posterior distributions does not show narrow peaks around the initial values, it indicates a lack of sensitivity, and vice versa.

This section can be separated into two parts: The first part examine the sensitivity of each individual observable group and the second part tests the maximal constraining power when all observables are combined in a simultaneous global fit. In the first part, Bayesian analysis will be performed three times, each by comparing only one class of observables. Pairwise marginalize probability distributions between all pairs of parameters from the Closure tests will be shown. This analysis illustrates the correlation between parameters and observables qualitatively, so the Closure test is only done on one randomly generated parameter set for brevity. The second part is a quantitative analysis that examines the average performance of the analysis across the entire parameter space. All observables are compared simultaneously for maximum performance. Closure test is repeated 18 times, each with a randomly generated set of parameters to span the entire parameter space uniformly. The one-dimensional marginalized distributions will be fitted with asymmetric Gaussian to estimate predicted averages and uncertainties, which are then compared to the true initial parameter values to gauge the accuracy of the algorithm.

### 6.5.1 Sensitivity of each group of observables

Through out this section, prior is uniform within ranges listed in Table 6.1, and the true parameter values is $S_0 = 37.4\,\mathrm{MeV}$, $L = 47.3\,\mathrm{MeV}$, $m_s^*/m_N = 0.80$, $m_v^*/m_N = 1.11$ and $\eta = 0.13$. The parameter values are chosen at random, and the qualitative dependency of posterior on different groups of observables sheds light into the constraining power of the observables.

The posterior in Fig. 6.1 is the result of closure test when only the first group of observable (C.I. $v_1$) is being compared. It tries to simultaneously fit the spectrum of coalescence invariant proton $v_1$ as a function of $y_0$, and $v_1$ as a function of $p_T$ gated on $0.3 < y_0 < 0.8$ for $^{108}$Sn $+$ $^{112}$Sn and
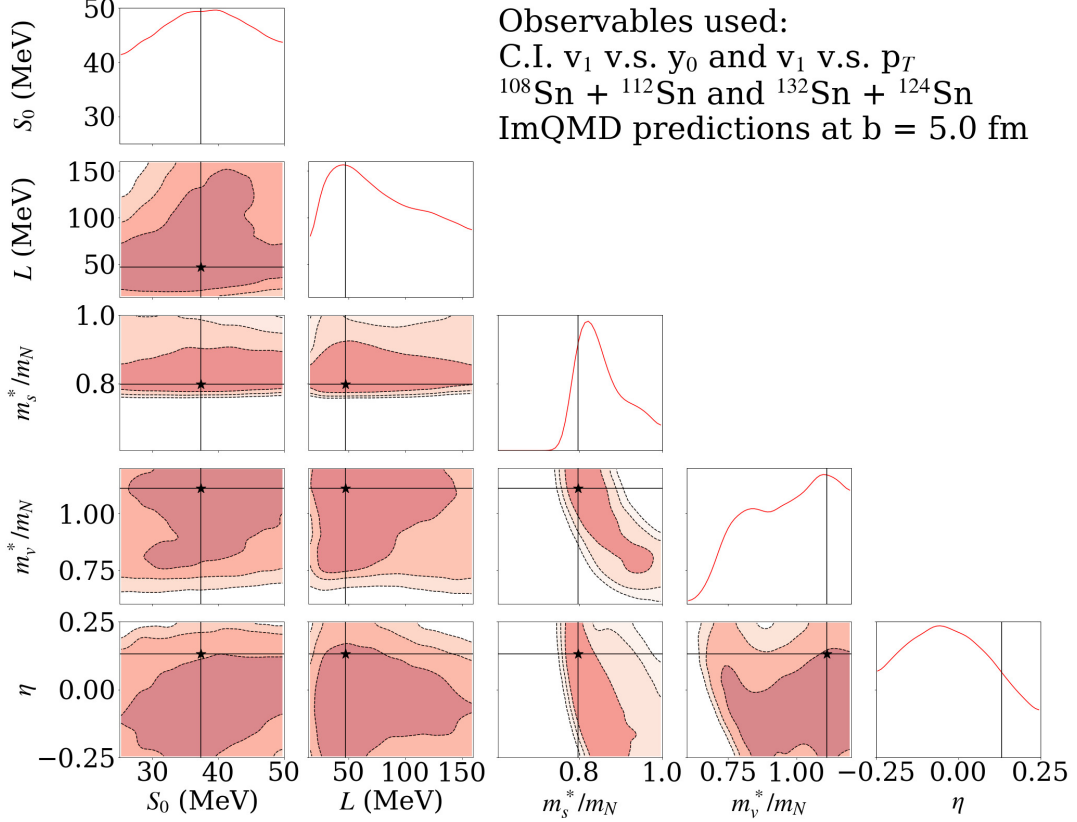
Figure 6.1: Posterior of closure test when all observables in group C.I. $v_1$ are compared. The black line in every plot and the black star in every off diagonal plot shows the initial true parameter values.

$^{132}$Sn + $^{124}$Sn at $b = 5$ fm. The black vertical lines in the diagonal plots and star markers in the off-diagonal plots show the location of the true parameter values as a visual reference. The contour on off-diagonal plots shows 68% (1-$\sigma$) confidence interval, 95% (2-$\sigma$) and 99% (3-$\sigma$) confidence interval with increasingly lighter shades. This posterior peaks narrowly only for $m_s^*/m_N$, which is consistent with the belief that direct flow is related to the momentum dependence of nuclear mean field [11]. There is an anti-correlation between $m_s^*/m_N$ and $m_v^*/m_N$ which demonstrates that increasing $m_s^*/m_N$ and $m_v^*/m_N$ has the opposite effect on coalescence invariant direct flow.

The sensitivity of coalescence invariant elliptical flow in Fig. 6.2 is slightly different. The figure is the posterior of closure test by fitting only the coalescence invariant proton $v_2$ as a function of $y_0$ for $^{108}$Sn + $^{112}$Sn and $^{132}$Sn + $^{124}$Sn at $b = 5$ fm. It reveals a narrow peak on $m_v^*/m_N$ as well as $m_s^*/m_N$, which indicates that higher order flow terms are more sensitive to the isovector
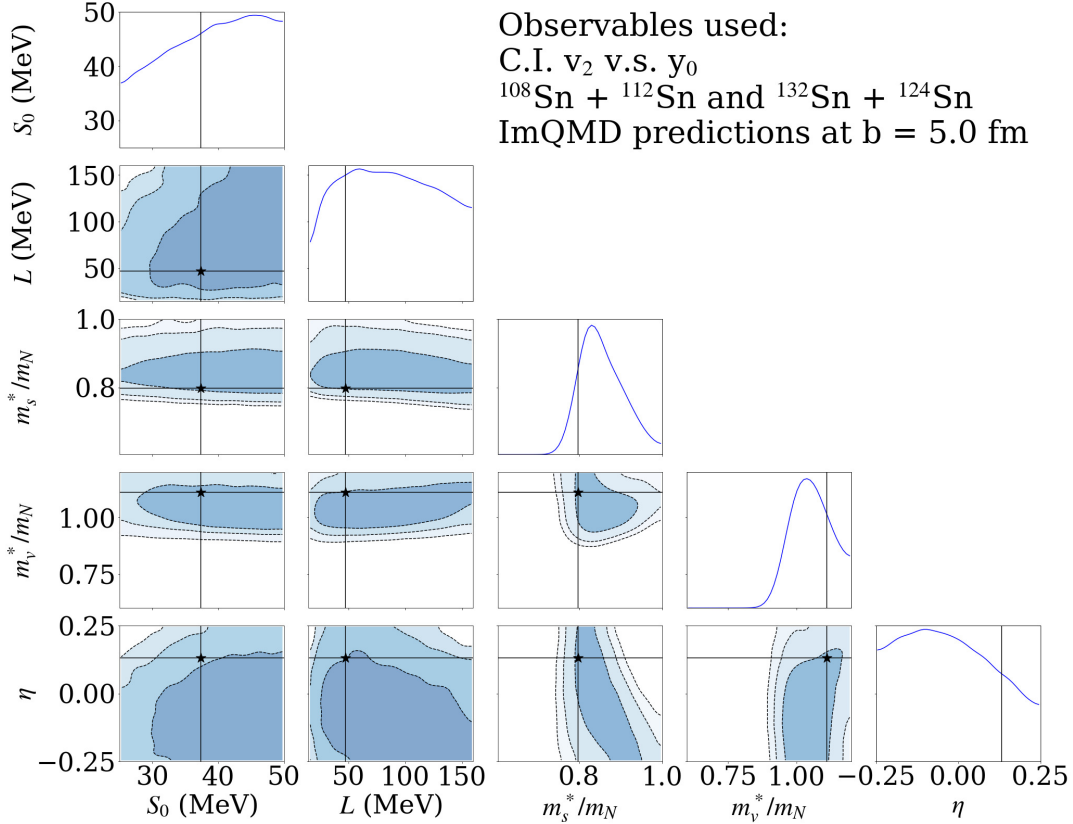
Figure 6.2: Same as Fig. 6.1 but only observables in group 2 (C.I. $v_2$) are being fitted.

contributions to momentum dependence.

The final group of observables to be tested is VarXZ from $^{108}$Sn + $^{112}$Sn and $^{112}$Sn + $^{124}$Sn at $b = 1$ fm. Previous studies showed that VarXZ is mostly sensitive to the in-medium cross-section, and closure test corroborates this finding with a narrow peak on $\eta$ in Fig. 6.3. The peaks of $m_s^*/m_N$ and $m_v^*/m_N$ are wider than those on Fig. 6.2, which indicates that the constraining power of VarXZ on effective masses is not as strong as $v_2$.

The maximum constraining power can be obtained by comparing all of the above observables simultaneously in one global fit. Posterior with all observables being compared are shown in Fig. 6.4. This shows that $m_s^*/m_N$, $m_v^*/m_N$ and $\eta$ can be recovered with reasonable accuracy while the sensitivity on $S_0$ and $L$ is lacking.
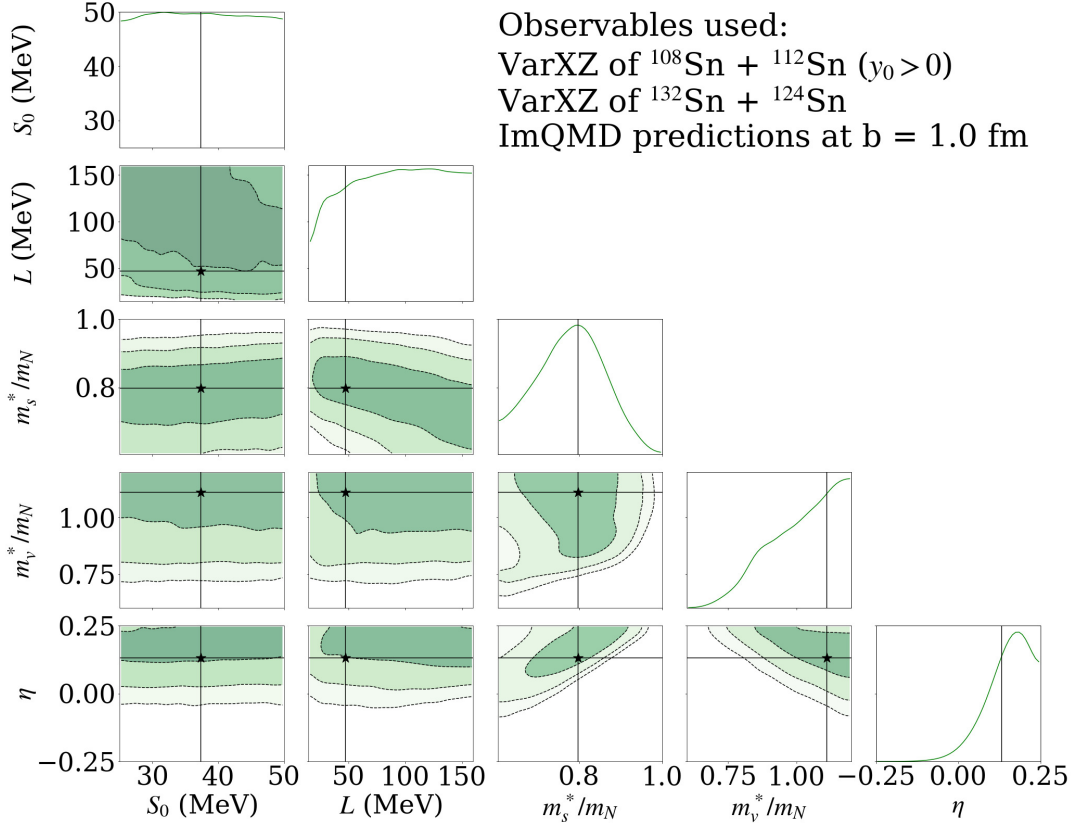
Figure 6.3: Same as Fig. 6.1 but only observables in group 3 (VarXZ) are being fitted.

### 6.5.2 Performance across parameter space

All posteriors in the previous section are analyzed on only one particular true parameter set, but the accuracy may change with parameter values. To understand the behavior of Bayesian analysis across the entire parameter space, closure test is repeated 18 times, each with a different randomly generated parameter set to cover the phase-space uniformly. The predicted values are plotted against the true values in Fig. 6.5. The error in the figure is the 68% confidence interval from the marginalized posterior distribution. Off-diagonal correlations between pairwise parameters are not shown for brevity. The red dotted $x = y$ line on each sub-plot represents the best possible performance where predicted values equal to true values. The sensitivities on $S_0$ and $L$ is lacking throughout the parameter space, but the sensitivities on $m_s^*/m_N$, $m_v^*/m_N$ and $\eta$ are quite good as the analysis is able to predict the correct values.
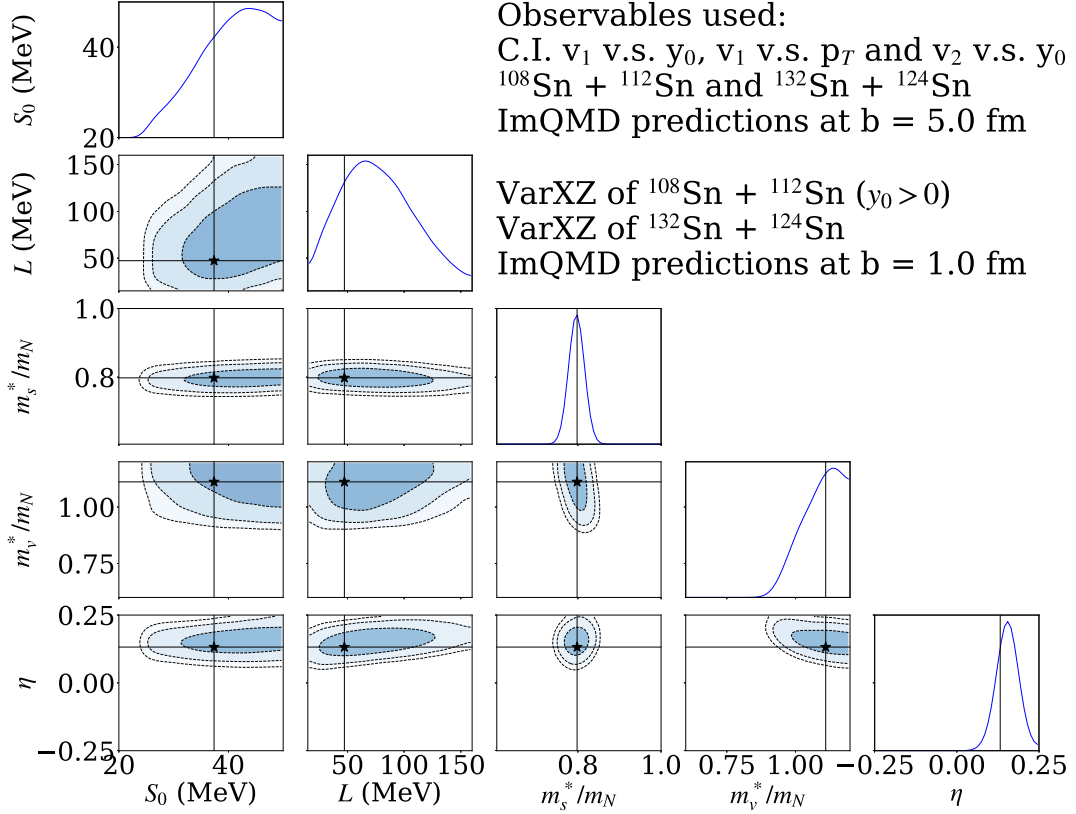
Figure 6.4: Same as Fig. 6.1, but all eight spectra across three groups of observables are used simultaneously in this analysis to demonstrate the maximal constraining power.

## 6.6 Constraints from experimental results

With the validity of the algorithms established, a comparison between ImQMD and experimental data from S$\pi$RIT experiment in Chapter 4 can be performed to constraint nuclear EoS parameters. Unlike in previous sections where priors of all parameters are uniform, Gaussian priors are used on $S_0 \sim \mathrm{Gaus}(\mu = 35.3, \sigma = 2.8)$ MeV and $L \sim \mathrm{Gaus}(\mu = 80, \sigma = 38)$ MeV. These priors come from the analysis of pion spectrum ratios in Section 4.4.2.

The centrality of the experimental data are selected with multiplicity gate and the selected events spans a range of impact parameters. The ranges of multiplicities are different across reactions and observables because multiplicity distributions for each system are different and centrality requirements for different observables are also different. The averaged impact parameters for each observable are $\langle b \rangle = 5.1$ fm in $^{108}$Sn + $^{112}$Sn reaction and $\langle b \rangle = 5.2$ fm in $^{132}$Sn + $^{124}$Sn reaction
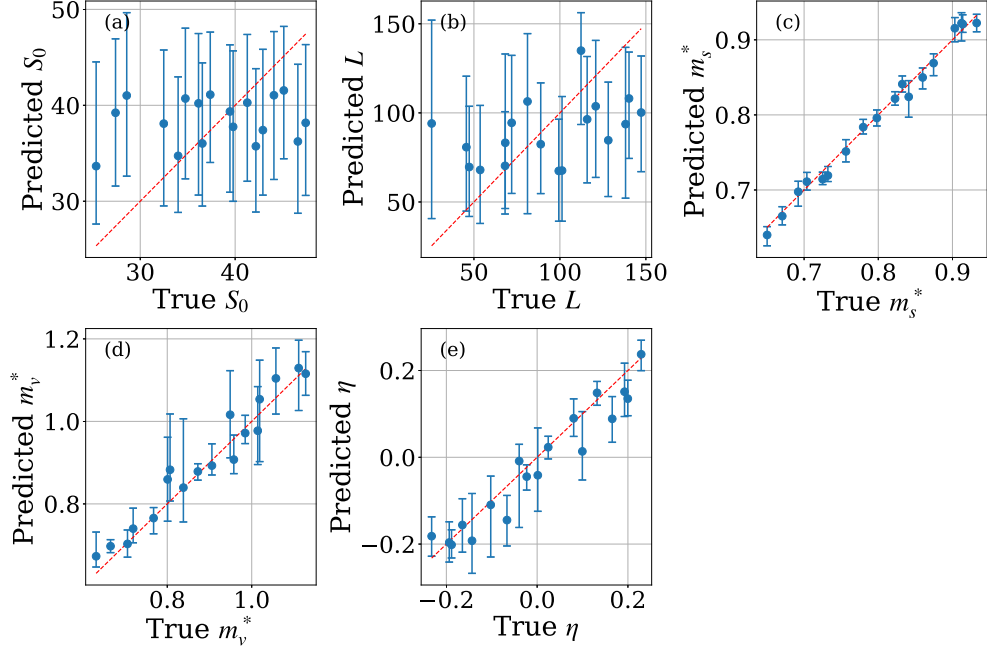
Figure 6.5: The predicted parameter values plotted against the true parameter value from the 18 closure tests. The markers and error bars indicate the medians and 68% (1-$\sigma$) confidence intervals from the marginalized probability distributions respectively. The red diagonal lines on all five plots are $x = y$ to indicate where each point should be if the algorithm performs with perfect accuracy and precision.

for $v_1$ and $v_2$, and $\langle b \rangle = 1.1\,\mathrm{fm}$ in $^{108}\mathrm{Sn} + ^{112}\mathrm{Sn}$ reaction and $\langle b \rangle = 1.0\,\mathrm{fm}$ in $^{112}\mathrm{Sn} + ^{124}\mathrm{Sn}$ reaction for VarXZ. The ImQMD predictions that the emulator is being trained on, however, are only calculated at impact parameter enumerated in Section 6.5 without spanning a range. The impact parameters in ImQMD calculations differ slightly from the average impact parameter of the selected events from the experiment, but given that the resolution of impact parameter determination with multiplicity is larger than 0.5 fm (see Section 5.9.3), this slight disagreement should be negligible.

The posterior is shown in Fig. 6.6. Tight constraints on $m_s^*/m_N$, $m_v^*/m_N$ and $\eta$ are achieved while the uncertainty of $S_0$ and $L$ remains large. The performance is consistent with our findings from closure test. The agreement between experimental spectra and emulated ImQMD predictions are shown in appendix A.4.

The results can be converted to a probability distribution on effective mass splitting $\Delta m_{np}^*/\delta$
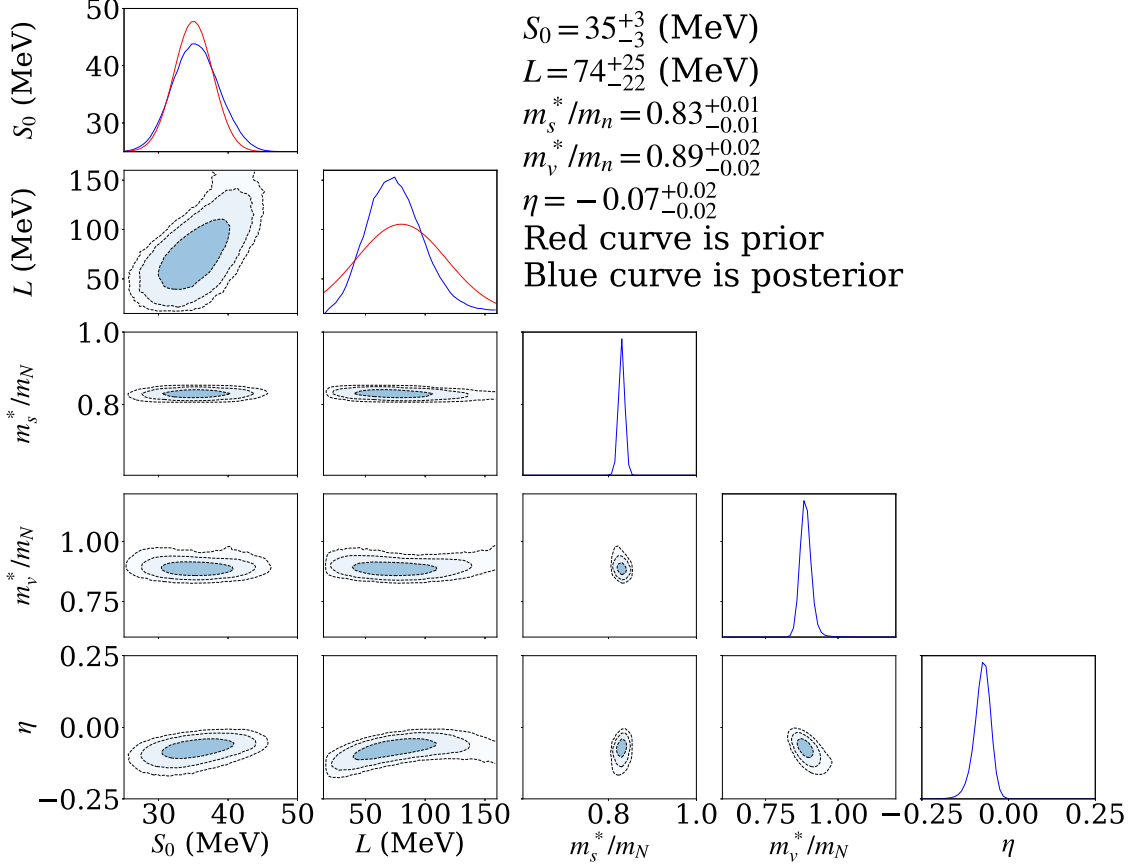
Figure 6.6: Posterior distribution when ImQMD is compared against experimental data from Chapter 4. All eight observables are used for Bayesian analysis. The values for median and 68% confidence interval of the marginalized distribution are tabulated on the upper right hand side of the figure.

with the following relation [155],

$$f_I = \frac{m_N}{m_s^*} - \frac{m_N}{m_v^*}$$
$$\frac{\Delta m_{np}^*}{\delta} \approx -2 f_I \left(\frac{m_s^*}{m_N}\right)^2. \tag{6.15}$$

Using this equation, we find that $\delta m_{np}^*/\delta = -0.11 \pm 0.04$. Analysis of n/p ratio using ImQMD at 120 AMeV shows that $\delta m_{np}^*/\delta = -0.05 \pm 0.09$ [155] while nuclear elastic collision shows that $\delta m_{np}^*/\delta = -0.25 \pm 0.27$ [192]. Previous analysis are inconclusive about the sign of effective mass splitting, but this analysis shows that $\delta m_{np}^*/\delta$ is most likely negative.

Although closure test shows that our analysis is not able to constrain $L$ reliably, this can
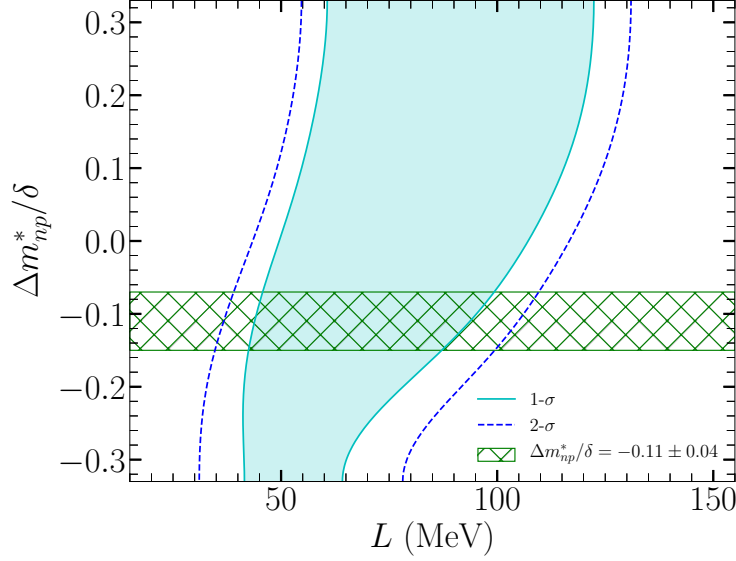
Figure 6.7: Same as Fig. 4.4, with $\delta m^*_{np}/\delta = -0.11 \pm 0.04$ overlay as green hatch.

still be achieve indirectly by invoking previous constraint from pion ratio spectra. The previous constraint shows a correlation between $\Delta m^*_{np}/\delta$ and $L$, therefore a tighter constraint on $L$ can be achieved with $\Delta m^*_{np}/\delta$ narrowed down, as Fig. 6.7 illustrates. The combined analysis of flows, stopping and pion ratios gives $L = 68 \pm 23$ MeV, which is 39% tighter than the previous pion ratios constraint. Since pion observables are sensitive to $\rho = 1.5\rho_0$ [138], our constraint should be place there instead of at $\rho_0$. Calculation with EoS in dcQMD shows that $S(1.5\rho_0) = 46 \pm 8$ MeV and $L(1.5\rho_0) = 61 \pm 51$ MeV.

To test the prediction power of our results, ImQMD is executed with the best fitted parameters ($S_0 = 35$ MeV, $L = 68$ MeV, $m^*_s/m_N = 0.83$, $m^*_v/m_N = 0.89$ and $\eta = -0.07$) to predict VarXZ for $^{197}$Au + $^{197}$Au and $^{129}$Xe + $^{133}$Cs reactions at 250 AMeV and $b = 1$ fm. $L = 68$ MeV comes from the analysis with pion constraints and all other parameter values are taken from Fig. 6.6. Experimental results on these systems have been published by FOPI group [36]. Their results covers a wide range of beam energy, but results of 250 AMeV is chosen for they are close to that of S$\pi$RIT experiment. As illustrated in Fig. 6.8, the agreement between model predictions (orange points) and experimental data (blue points) are reasonable. Our constraints are applicable to reactions near 270 MeV.
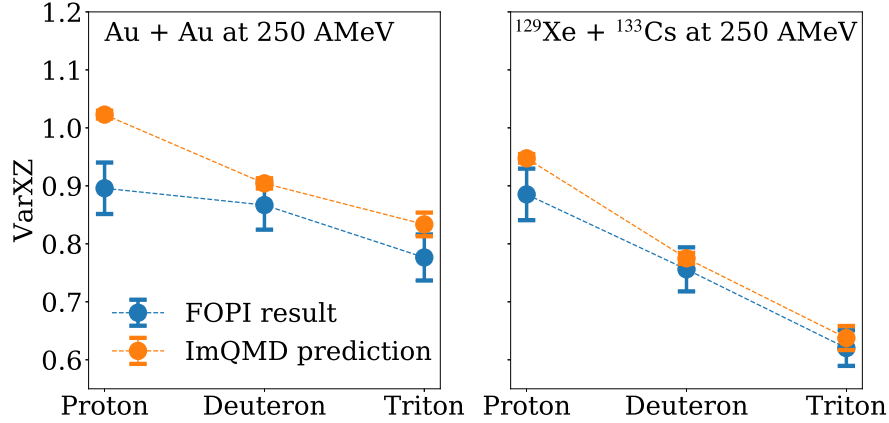
Figure 6.8: VarXZ of proton, Deuteron and Triton for Au + Au and $^{129}$Xe + $^{133}$Cs reactions at 250 AMeV when $b = 1$ fm. The orange points show ImQMD predictions using the best fitted parameter values. The blue points show experimental results from the FOPI data set.

Even though $K_0$ (another name for $K_{\text{sat}}$ in Eq. (1.4)) is known experimentally to be around 230 MeV, the dependence of effective mass constraints on $K_0$ should still be studied. Additional Bayesian analysis is done with $K_0$ included as a free parameter, ranging from 200 to 300 MeV. The prior for $K_0$ is a Gaussian distribution with mean = 237 MeV and standard deviation = 27 MeV. The values are taken from Table 2.1, which shows the statistics of $K_{\text{sat}}$ for commonly used Skyrme type EoSs. The posterior in Fig. 6.9 shows that our observables are not sensitive to $K_0$ as the marginalized posterior distribution for $K_0$ is almost identical to its prior. Furthermore, posterior distributions of $m_s^*/m_N$ and $m_v^*/m_N$ show no correlation with $K_0$ and peak at around the same values as in Fig. 6.6. Although $\eta$ correlates with $K_0$, it does not affect our constraint on effective masses.

## 6.7 Implications on NS properties

With the connection between EoS parameters and NS properties established in Chapter 2, the impact of SπRIT constraint on NS properties will be inspected.

Meta-modelling EoS from Section 2.3 is chosen for this analysis. These EoSs are randomly generated with $S$, $L$, $K$, $Q$ and $Z$ values distributed uniformly within two standard deviation from

$S_0 = 32^{+3}_{-3}$ (MeV)    $m_s^*/m_N = 0.81^{+0.01}_{-0.01}$
$L = 93^{+33}_{-30}$ (MeV)    $m_v^*/m_N = 0.93^{+0.04}_{-0.05}$
$K_0 = 240.49^{+23.63}_{-22.84}$    $\eta = -0.09^{+0.08}_{-0.10}$
Red curve is prior
Blue curve is posterior
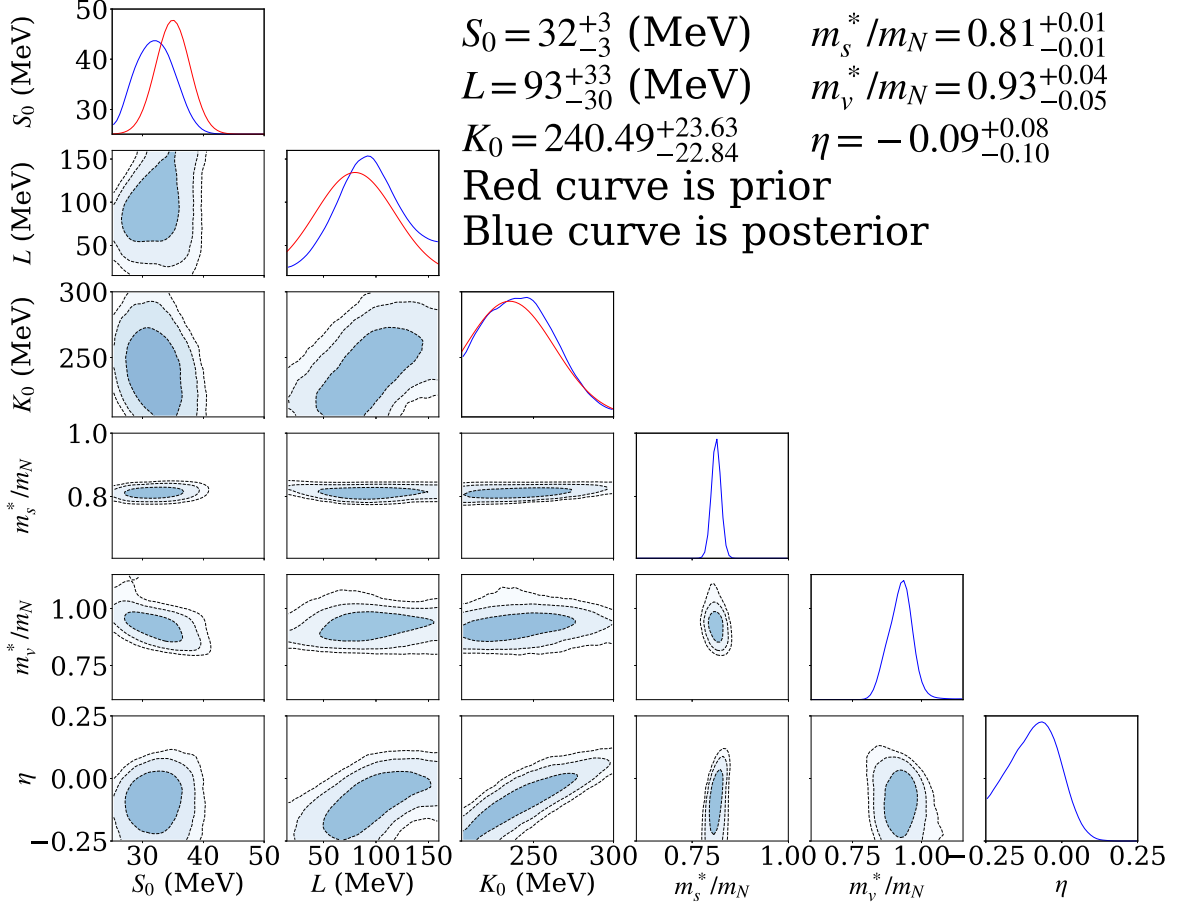
Figure 6.9: Same as Fig. 6.6, but $K_0$ is allowed to vary from 200 to 300 MeV.

the mean of all commonly used models in Table 2.1. Unlike in Section 2.3, however, Gaussian priors on $S$, $L$, $K$, $Q$ and $Z$ and constraint on $\Lambda$ from LIGO are not used as we want to test the constraining power of just the heavy-ion results.

We follow Eq. (2.7) to calculate posterior distribution. The EoSs that violate either maximum mass > $2.2M_\odot$ or causality will be discarded. The remaining EoSs are weighted with the product of three Gaussian distributions with means and standard deviations given by the following three constraints from heavy-ion collision: $L(1.5\rho_0) = 69 \pm 51$ MeV from analysis of S$\pi$RIT data, $S(0.67\rho_0) = 25 \pm 1$ MeV from nuclear mass [19, 20] and $L(0.67\rho_0) = 71 \pm 23$ MeV from neutron skin thickness measurement of $^{208}$Pb from PREX-II [193].

The pair-wise correlations and marginal distributions of the three constraining parameters, as well as radius and $\Lambda$ of $1.4M_\odot$ NS, are shown in in Fig. 6.10. The diagonal distributions show

| | Before | After |
|---|---|---|
| $S(0.67\rho_0)$ | $23.2^{+3.3}_{-3.1}$ | $24.9^{+1.0}_{-1.0}$ |
| $L(0.67\rho_0)$ | $62.2^{+15.0}_{-16.4}$ | $60.2^{+10.5}_{-12.5}$ |
| $L(1.5\rho_0)$ | $128.3^{+36.8}_{-64.2}$ | $84.9^{+37.6}_{-31.2}$ |
| $R(1.4M_\odot)$ | $13.8^{+0.4}_{-1.0}$ | $13.3^{+0.4}_{-0.6}$ |
| $\Lambda(1.4M_\odot)$ | $741.8^{+156.0}_{-209.5}$ | $646.1^{+119.6}_{-139.7}$ |
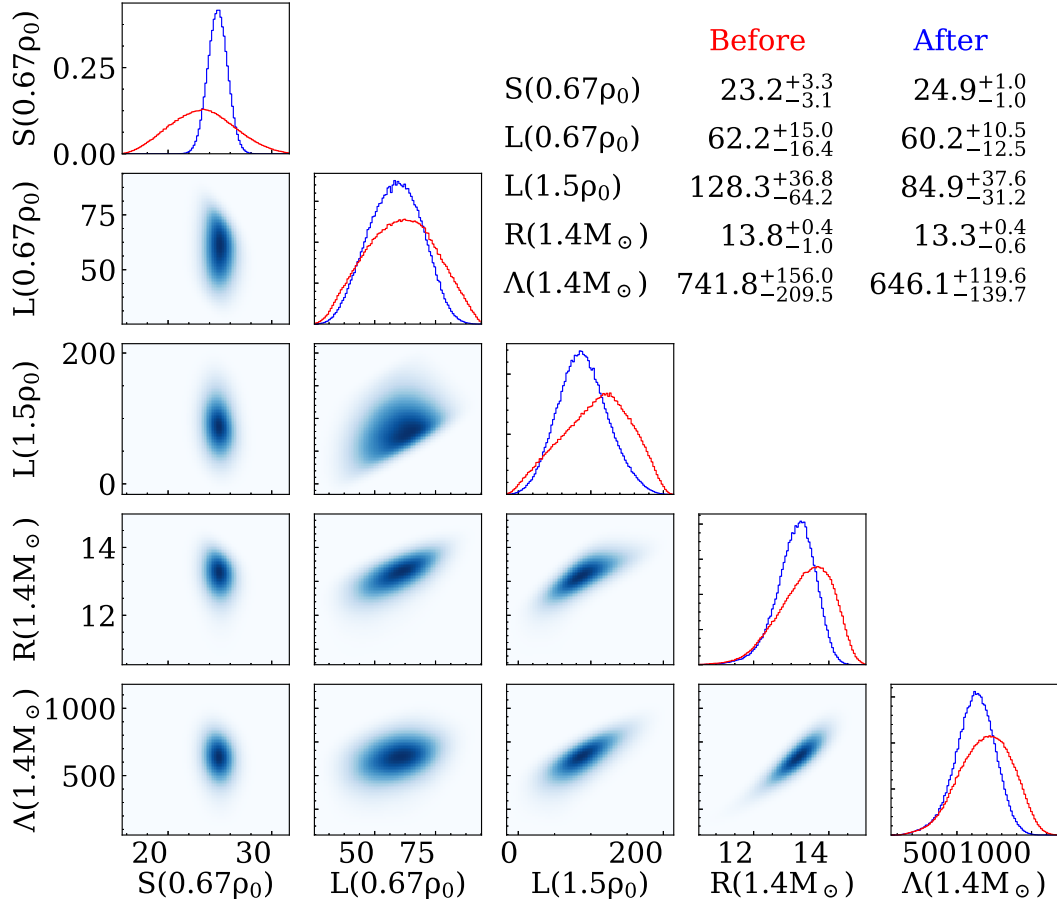
Figure 6.10: Posterior distributions for $S(0.67\rho_0)$, $L(0.67\rho_0)$, $L(1.5\rho_0)$, $R$ and $\Lambda$ of $1.4M_\odot$ NS. See text for details.

the marginal probability distributions from only maximum mass and causality conditions (red histograms), and with heavy-ion constraints included in addition to the previous two conditions (blue histogram). The off-diagonal pairwise correlation are plotted with heavy-ion constraints. The table in the upper right hand corner of the figure shows the ranges of parameter values by fitting the marginal distribution with asymmetric Gaussian. The numbers on the row labelled "Before" corresponds the fitted values for blue histograms and "After" for red histograms. Our calculations indicate that $R = 13.3^{+0.4}_{-0.6}$ km and $\Lambda = 646^{+120}_{-140}$ for $1.4M_\odot$ NS.

The 95% confidence interval (C.I.) of pressure as a function of density is plotted in Fig. 6.11a. Solid blue region and open dashed blue region are C.I. with and without using heavy-ion constraints respectively. The result is consistent with multimessenger constraints from the survey of NICER,
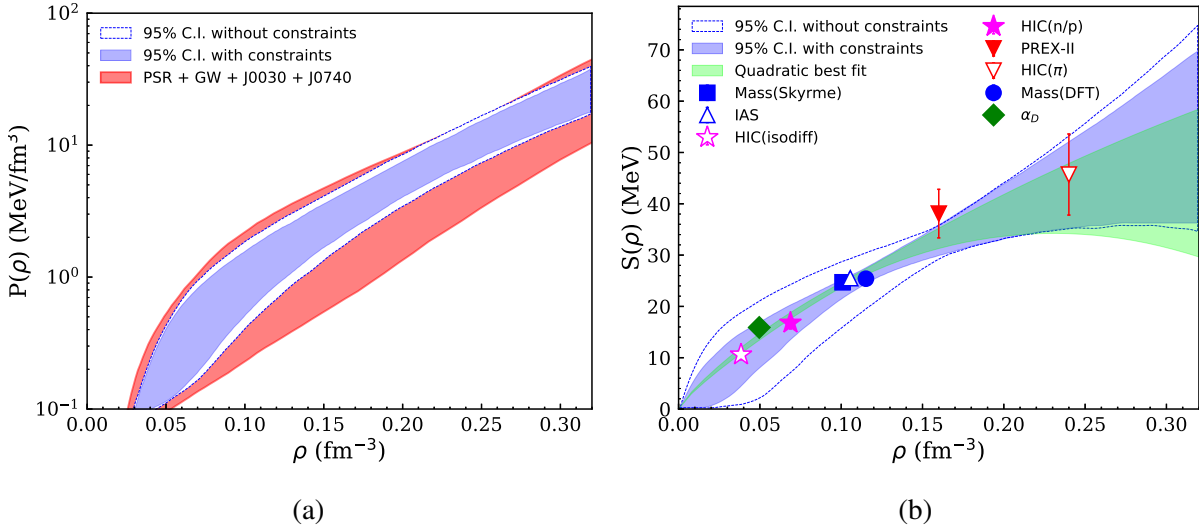
Figure 6.11: (a): Dependence of pressure on matter density. (b): Dependence of symmetric energy terms on matter density. See text for details.

gravitational wave and X-ray pulse PSR J0030 + 0740 [194] whose 90% C.I. predictions on pressure is shown as the solid red region on the figure.

Fig. 6.11b shows the 95% C.I. of symmetry energy term with (solid blue region) and without (dashed blue open region) heavy-ion constraints. Constraints from various analyses are also plotted on top for comparison. These analyses are: Neutron to proton ratio (n/p) [155], isospin diffusion (isodiff) [195–197], nuclear masses (Mass(Skyrme) [19] and Mass(DFT) [18]), isobaric analog states (IAS) [42], electric dipole polarizability [198] and neutron skin thickness of $^{208}$Pb [193]. The open red triangle labelled "HIC($\pi$)" corresponds to the refined constraint on $S(1.5\rho_0)$ from S$\pi$RIT experiment. The sensitive density for each experiment is extracted in Ref. [199] and the green region corresponds to $1\sigma$ region from fitting all of the constraints, excluding HIC($\pi$), with second order polynomial expended at $\rho = 0.67\rho_0$.

# CHAPTER 7

# SUMMARY

The properties of neutron stars depend strongly on high density part of symmetry energy term in nuclear equation of state. Equation of state is used as an input for Tolman–Oppenheimer–Volkoff equation to predict neutron star properties such as radius or Tidal deformability ($\Lambda$). This work demonstrates a strong correlation between $\Lambda$ and the slope parameter ($L$) in symmetry energy term with Skyrme type and Meta-modelling EoS.

To place constraints on nuclear EoS, the S$\pi$RIT TPC was constructed to probe symmetry energy term with the main goal of measuring pion emissions from heavy-ion collisions of rare neutron-rich isotopes. The production threshold of pion implies that pions originate from high density region where neutron star properties are most sensitive to. Four different reactions: $^{108}$Sn + $^{112}$Sn, $^{112}$Sn + $^{124}$Sn, $^{124}$Sn + $^{112}$Sn and $^{132}$Sn + $^{124}$Sn at 270 AMeV are preformed during the experimental campaign. $^{108}$Sn and $^{132}$Sn are radioactive.

To extract useful spectrum from S$\pi$RIT TPC, multiple steps are needed to recognize nuclear fragments, remove detector aberrations and correct for detector resolution and efficiency effects. Upstream bean detectors have to be calibrated and analyzed to isolate the desired isotopes from contamination. After corrections on detector aberrations such as space charge and pad saturation is done, the hit points are fitted with GENFIT package to reconstruct the $p/Z$ value for each fragments. The final steps in the analysis is to correct for detector efficiency with embedding and reaction plane resolution with sub-event methods.

To verify our understanding of detector response, Monte Carlo simulation of S$\pi$RIT TPC is developed to recreate aspects of experimental data. It shows that the sudden loss of tracking efficiency for particles emitting at $\phi = \pm 90°$ can be recreated by incorporating saturation modes of heavy residue. Discrepancies in momentum distributions between particles with positive $p_x$ and negative $p_x$ can be recreated by incorporating space charge effect and the shape of multiplicity distributions can be quantitatively reproduced with simulation of KYOTO and KATANA trigger

134

conditions.

By comparing experimental pion ratios with transport model dcQMD, a correlated constraints on $\Delta_{np}^*/\delta$ and $L$ can be imposed in Fig. 4.4. To reduce our uncertainty on $L$, a tighter constraint on $\Delta_{np}^*/\delta$ is needed. It is achieved in this work by utilizing the light fragment observables. The coalescence invariant direct and elliptical flow for $^{108}$Sn + $^{112}$Sn and $^{132}$Sn + $^{124}$Sn from peripheral events, and VarXZ for $^{108}$Sn + $^{112}$Sn and $^{112}$Sn + $^{124}$Sn from central events are reconstructed from S$\pi$RIT data. A global Bayesian fit is performed by comparing all these observables with predictions from transport model ImQMD.

$S_0$, $L$, $m_s^*/m_N$, $m_v^*/m_N$ and $\eta$ are compared simultaneously using Markov-Chain Monte Carlo (MCMC). It searches parameter space by sampling predictions from ImQMD thousands of time, but such calculations are too demanding even for supercomputers. As a work around, Gaussian process with Principal Component Analysis is employed to emulate the behavior of ImQMD from just 70 calculations as a surrogate model. To test the performance of such algorithms, closure test is performed on simulated data. It shows that our method is able to constraint $m_s^*/m_N$, $m_v^*/m_N$ and $\eta$ but not $S_0$ and $L$.

The final global fit with experimental data shows a tight constraint on $m_s^*/m_N$, $m_v^*/m_N$ and $\eta$. The predicting power of the constraints is verified by running ImQMD again with the best fitted parameters on Au + Au and Xe + Cs reactions at 250 AMeV. The predicted VarXZ agrees reasonable well with published results from FOPI. Our values of $m_s^*/m_N$ and $m_v^*/m_N$ are converted to $\Delta_{np}^*/\delta$ to give $\Delta_{np}^*/\delta = 0.11 \pm 0.04$. When imposed together with constraint from pion ratio, the constraint on $L$ can be tighten to $L = 68 \pm 25$ MeV and when calculated to the sensitive density of pion ratio at $1.5\rho_0$, we get $S(1.5\rho_0) = 45 \pm 9$ MeV and $L(1.5\rho_0) = 69 \pm 51$ MeV.

Overall the S$\pi$RIT experiment have successfully constrained nuclear EoS at high density. A major source of uncertainty comes from the limited statistics of pions. It is hoped that with improved analysis technique we can increase the statistics by relaxing the cut conditions. Furthermore, collaborative efforts from theorists are underway to better understand the effect of pion potential and ensure consistent model predictions. A better understanding of nuclear EoS is within reach as

theory converges and data from different experiments are being finalized.

**APPENDIX**

## A.1  TOV equation

The Tolman–Oppenheimer–Volkoff (TOV) equation set predicts the structure of a static spherical object under general relativity for any given EoS. The equations are:

$$\frac{dP(r)}{dr} = -\frac{(\mathcal{E}(r) + P(r))(M(r) + 4\pi r^3 P(r))}{r^2(1 - 2M(r)/r)},$$

$$\frac{dM(r)}{dr} = 4\pi r^2 \mathcal{E}(r). \tag{1}$$

Here geometrized units $G = c = 1$ are used, $\mathcal{E}(r)$ is the energy density given by EoS, $P(r)$ is the internal pressure at given depth and $M(r)$ is the integral of gravitational mass from the core up to radius $r$. The surface is defined as the radial distance $R$ at which $P(R) = 0$.

A list of equations whose solutions will lead to the value of $\Lambda$ from the above structural functions will be shown without derivation. Please refer to Refs. [31, 200] for details. To begin with, an auxiliary variable $y_R = y(R)$ is calculated,

$$r\frac{dy(r)}{dr} + y(r)^2 + y(r)F(r) + r^2 Q(r) = 0. \tag{2}$$

where

$$F(r) = \frac{r - 4\pi r^3(\mathcal{E}(r) - P(r))}{r - 2M(r)}. \tag{3}$$

$$Q(r) = \frac{4\pi r \left(5\mathcal{E}(r) + 9P(r) + \frac{\mathcal{E}+P(r)}{\partial P(r)/\partial \mathcal{E}} - \frac{6}{4\pi r^2}\right)}{r - 2M(r)}$$
$$- 4\left[\frac{(M(r) + 4\pi r^3 P(r))}{r^2(1 - 2M(r)/r)}\right]^2. \tag{4}$$

The tidal Love number $k_2$ can then be calculated with the following expression:

$$
\begin{aligned}
k_2 = &\frac{1}{20} \left(\frac{R_S}{R}\right)^5 \left(1 - \frac{R_S}{R}\right)^2 \left[2 - y_R + (y_R - 1)\frac{R_S}{R}\right] \\
&\times \left\{ \frac{R_S}{R}\left(6 - 3y_R + \frac{3R_S}{2R}(5y_R - 8) + \frac{1}{4}\left(\frac{R_S}{R}\right)^2 \right. \right. \\
&\times \left[26 - 22y_R + \frac{R_S(3y_R - 2)}{R} + \left(\frac{R_S}{R}\right)^2 (1 + y_R)\right] \right) \\
&+ 3\left(1 - \frac{R_S}{R}\right)^2 \left[2 - y_R + \frac{R_S(y_R - 1)}{R}\right] \\
&\times \ln\left(1 - \frac{R_S}{R}\right) \Bigg\}^{-1} .
\end{aligned}
\tag{5}
$$

In the above, $R_S = 2M$ is the Schwarzschild radius. The value of $\Lambda$ is then extracted with Eq. (1.9).

## A.2 Meta-modeling parameters and Taylor parameters mapping

ELFc energy functional is written as a sum of kinetic energy term and potential energy term:

$$
E_{EFLc}(\rho, \delta) = t^{FG*}(\rho, \delta) + v^N_{EFLc}(\rho, \delta),
\tag{6}
$$

where $\rho$ is the density and $\delta$ is the asymmetry parameter. The kinetic energy term $t^{FG*}(\rho, \delta)$ in the above is written as:

$$
\begin{aligned}
t^{FG*}(\rho, \delta) = &\frac{t^{FG}_{\text{sat}}}{2}\left(\frac{\rho}{\rho_0}\right)^{\frac{2}{3}} \left[\left(1 + \frac{\kappa_{\text{sat}}\rho}{\rho_0}\right)((1+\delta)^{\frac{5}{3}} + \right. \\
&(1-\delta)^{\frac{5}{3}}) + \frac{\kappa_{\text{sym}}\rho}{\rho_0}\delta((1+\delta)^{\frac{5}{3}} - (1-\delta)^{\frac{5}{3}}) \Bigg].
\end{aligned}
\tag{7}
$$

In the above, the parameters $t^{FG}_{\text{sat}} = 22.1\,\text{MeV}$ while $\kappa_{sym}$ and $\kappa_{sat}$ are effective mass parameters described in Eq. (2.3).

The potential energy term $v^N_{EFLc}(\rho, \delta)$ is written as:

$$
\begin{aligned}
v^N_{EFLc}(\rho, \delta) = &\sum_{i=0}^{4} \frac{1}{i!}(v_i^{is} + v_i^{iv}\delta^2)(1 - (-3)^{5-i}) \\
&\times \exp\left(-\frac{6.93\rho}{\rho_0}\right)x^i.
\end{aligned}
\tag{8}
$$

In the above, the parameters $v_i^{is}$ and $v_i^{iv}$ are free parameters. These 10 parameters can be uniquely mapped onto Taylor parameters using the following formulas (For a detailed derivation, please refer to Ref. [1]):

$$v_0^{is} = E_{\text{sat}} - t_{\text{sat}}^{FG}(1 + \kappa_{\text{sat}}), \tag{9}$$

$$v_1^{is} = -t_{\text{sat}}^{FG}(2 + 5\kappa_{\text{sat}}), \tag{10}$$

$$v_2^{is} = K_{\text{sat}} - 2t_{\text{sat}}^{FG}(-1 + 5\kappa_{\text{sat}}), \tag{11}$$

$$v_3^{is} = Q_{\text{sat}} - 2t_{\text{sat}}^{FG}(4 - 5\kappa_{\text{sat}}), \tag{12}$$

$$v_4^{is} = Z_{\text{sat}} - 8t_{\text{sat}}^{FG}(-7 + 5\kappa_{\text{sat}}), \tag{13}$$

$$v_0^{iv} = S_0 - \frac{5}{9}t_{\text{sat}}^{FG}(1 + (\kappa_{\text{sat}} + 3\kappa_{\text{sym}})), \tag{14}$$

$$v_1^{iv} = L - \frac{5}{9}t_{\text{sat}}^{FG}(2 + 5(\kappa_{\text{sat}} + 3\kappa_{\text{sym}})), \tag{15}$$

$$v_2^{iv} = K_{\text{sym}} - \frac{10}{9}t_{\text{sat}}^{FG}(-1 + 5(\kappa_{\text{sat}} + 3\kappa_{\text{sym}})), \tag{16}$$

$$v_3^{iv} = Q_{\text{sym}} - \frac{10}{9}t_{\text{sat}}^{FG}(4 - 5(\kappa_{\text{sat}} + 3\kappa_{\text{sym}})), \tag{17}$$

$$v_4^{iv} = Z_{\text{sym}} - \frac{40}{9}t_{\text{sat}}^{FG}(-7 + 5(\kappa_{\text{sat}} + 3\kappa_{\text{sym}})). \tag{18}$$

When exploring the parameter space, Taylor parameters will be translated to Meta-modeling EoS using the above formulas and NS features will then be calculated with TOV equation. Neutron star

properties will be examined to search for Taylor parameter spaces flavored by the observed tidal deformability.

## A.3  Full correlation between tidal deformability and parameters

The correlation between $L$, $K_{\text{sym}}$, $K_{\text{sat}}$, $Q_{\text{sym}}$, $Q_{\text{sat}}$, $Z_{\text{sym}}$, $Z_{\text{sat}}$, $\left(m_{\text{sat}}/m\right)$, $P(2\rho_0)$ and $\Lambda$ are shown in Fig. A.3.1. This is an extension of Fig. 2.9 where bivariate distributions of some selected parameters are shown. The organization is similar: Lower triangles show bivariate distributions between variables and marginal distribution of each variable is shown on the diagonal. The upper triangles shows Pearson correlation coefficients between each variable pairs if it is larger than 0.1 otherwise they are omitted for simplicity and 3 dots are put in its place.

## A.4  Best fit from ImQMD

The fitted results from Bayesian analysis are shown in Figs. A.3.2 and A.4.1.

Fig. A.3.2 shows results on direct and elliptical flow. Plots on the left column show results in $^{108}$Sn + $^{112}$Sn reaction and on the right show that of $^{132}$Sn + $^{124}$Sn reaction. From top to bottom, the three rows show $v_1$ as a function of $y_0$, $v_1$ as a function of $p_T$ (MeV) and $v_2$ as a function of $y_0$.

Fig. A.4.1 is similar to Fig. A.3.2 but with results of VarXZ being shown. Beware that the reaction on the right column is now $^{112}$Sn + $^{124}$Sn instead of $^{132}$Sn + $^{124}$Sn. Using symmetry arguments in Chapter 4, rapidity distributions are reflected along $y_0 = 0$ only in $^{108}$Sn + $^{112}$Sn reaction when VarXZ is calculated.

ImQMD calculations are done at $b = 5$ fm for flow results and at $b = 1$ fm for stopping results, and on both Figs. A.3.2 and A.4.1 the averaged impact parameter on the label of $y$-axis reflects the centrality gate on experimental data.
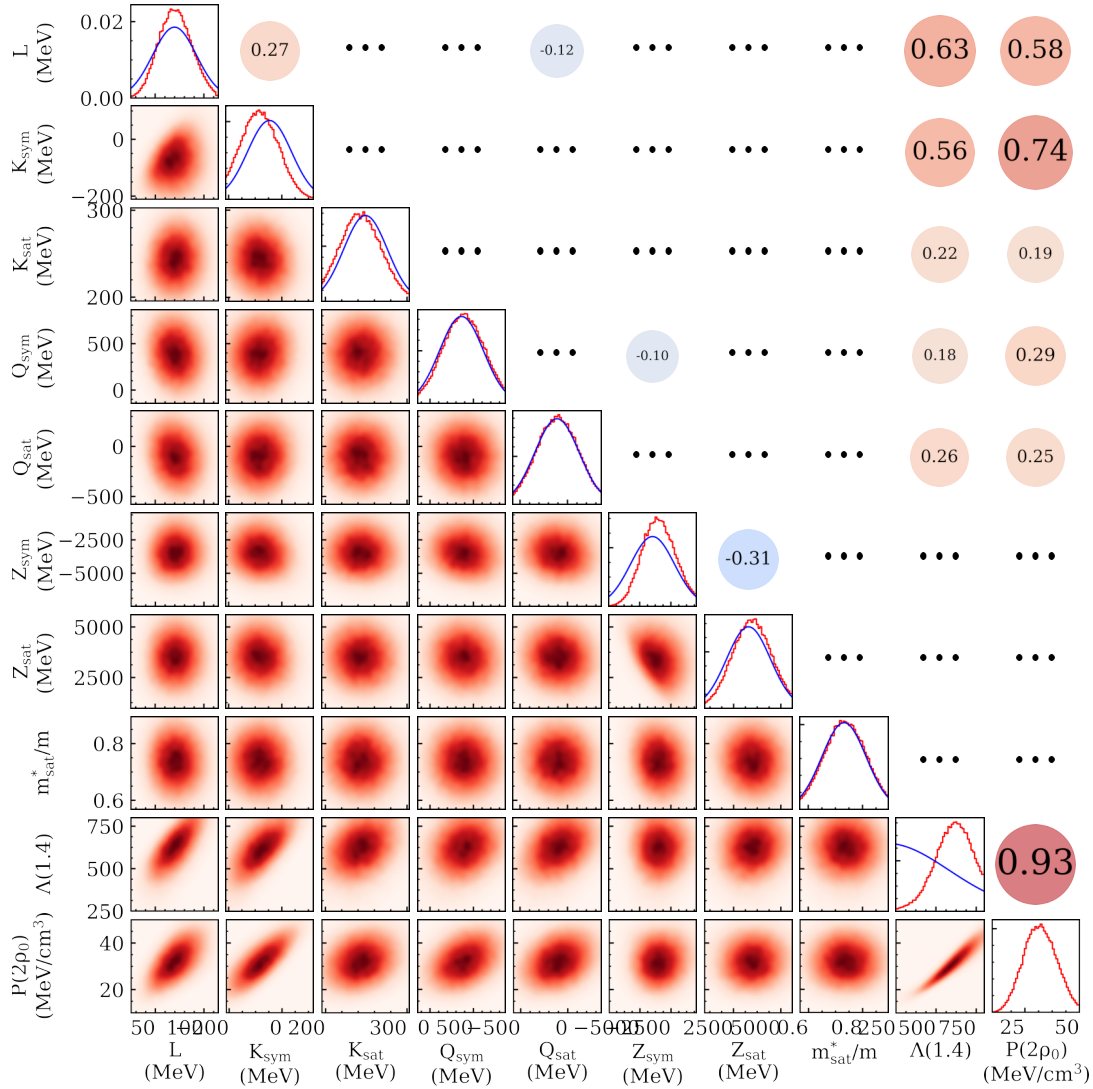
Figure A.3.1: Bivariate characteristics of posterior likelihood distributions. This is an extension to Fig. 2.6 and correlation pairs of all parameters pair are shown. Three regions can be distinguished. The lower triangle panels show likelihood distributions, with intensity proportional to distribution value, for pairs of Taylor parameters. The diagonal panels display marginalized distribution for each parameter. The upper triangular region shows Pearson correlation coefficient for parameter pairs, but when correlation in magnitude is less than 0.1, it is omitted and 3 dots are put in place of its value.
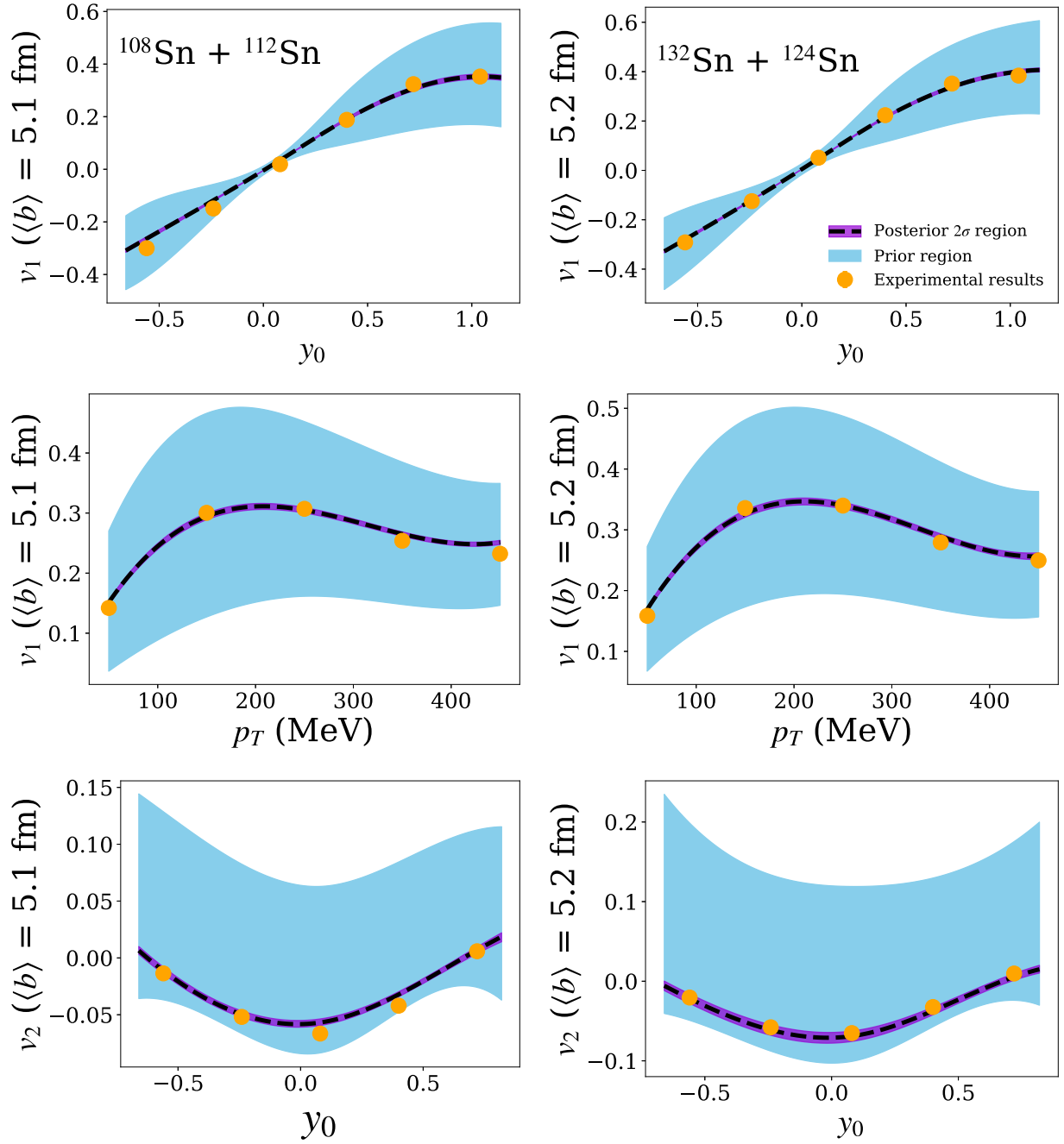
Figure A.3.2: Comparison of direct and elliptical flow between the best fitted ImQMD predictions and experimental results. The blue region shows the maximum range of prediction values from ImQMD with the parameter range in Table 6.1 and the purple region shows the $2\sigma$ confidence region of ImQMD's prediction after Bayesian analysis. The orange points show results from S$\pi$RIT experiment, which is identical to what is shown in Chapter 4. See text for details.
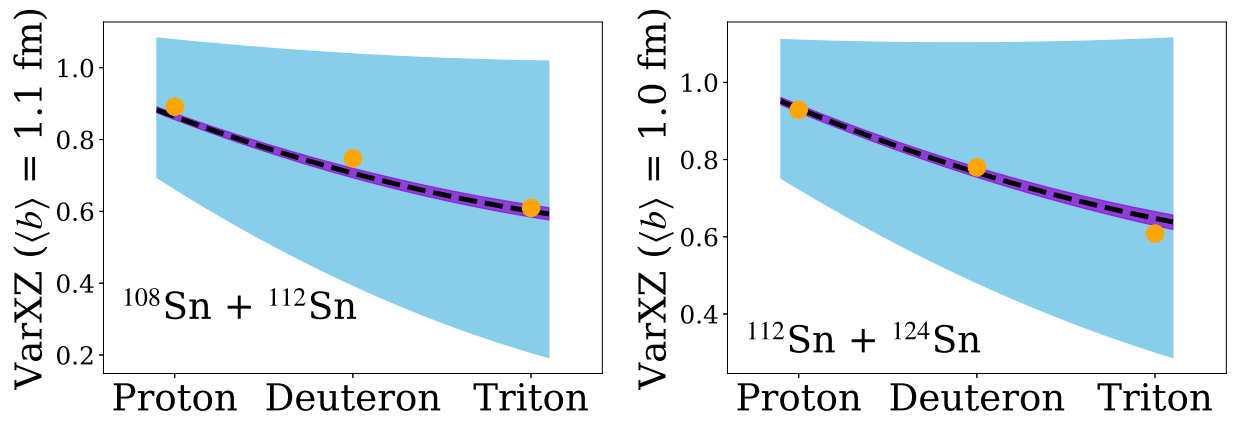
Figure A.4.1: Same as Fig. A.3.2, but with VarXZ of $^{108}$Sn + $^{112}$Sn on the left and that of $^{112}$Sn + $^{124}$Sn on the right.

**BIBLIOGRAPHY**

# BIBLIOGRAPHY

[1] J. Margueron, R. Hoffmann Casali, and F. Gulminelli, Phys. Rev. C **97**, 025805 (2018).

[2] J. Barney, *Charged Pion Emission from 112Sn + 124Sn and 124Sn + 112Sn Reactions with the SpiRIT Time Projection Chamber*, Ph.D. thesis, Michigan State U. (2019).

[3] M. Dutra, O. Lourenço, J. S. Sá Martins, A. Delfino, J. R. Stone, and P. D. Stevenson, Phys. Rev. C **85**, 035201 (2012).

[4] F. J. Fattoyev, J. Piekarewicz, and C. J. Horowitz, Phys. Rev. Lett. **120**, 172702 (2018).

[5] K. Yamada, T. Dantsuka, M. Fujimaki, T. Fujinawa, N. Fukunishi, A. Goto, H. Hasebe, Y. Higurashi, E. Ikezawa, O. Kamigaito, M. Kase, M. Kobayashi-Komiyama, H. Kuboki, K. Kumagai, T. Maie, M. Nagase, T. Nakagawa, J. Ohnishi, H. Okuno, and S. Yokouchi, Proceedings of HIAT09 (2009).

[6] G. Jhang, *Performance of the SπRIT TPC for the nuclear physics experiment at RIBF*, Ph.D. thesis, Korea University (2016).

[7] J. E. JBarney, *Charged Pion Emission from $^{112}Sn$ + $^{124}Sn$ and $^{124}Sn$ + $^{112}Sn$ Reactions with the SπRIT Time Projection Chamber*, Ph.D. thesis.

[8] J. Estee, *Constraining the high density nuclear symmetry energy with pions*, Ph.D. thesis, Michigan State University (2020).

[9] C. J. Horowitz, E. F. Brown, Y. Kim, W. G. Lynch, R. Michaels, A. Ono, J. Piekarewicz, M. B. Tsang, and H. H. Wolter, Journal of Physics G: Nuclear and Particle Physics **41**, 093001 (2014).

[10] A. H. Wapstra, "Atomic masses of nuclides," in *External Properties of Atomic Nuclei / Äussere Eigenschaften der Atomkerne*, edited by S. Flügge (Springer Berlin Heidelberg, Berlin, Heidelberg, 1958) pp. 1–37.

[11] P. Danielewicz, R. Lacey, and W. G. Lynch, Science **298**, 1592 (2002).

[12] C. Fuchs, Progress in Particle and Nuclear Physics **56**, 1 (2006).

[13] W. G. Lynch, M. B. Tsang, Y. Zhang, P. Danielewicz, M. Famiano, Z. Li, and A. W. Steiner, Progress in Particle and Nuclear Physics **62**, 427 (2009), heavy-Ion Collisions from the Coulomb Barrier to the Quark-Gluon Plasma.

[14] A. L. Fèvre, Y. Leifels, W. Reisdorf, J. Aichelin, and C. Hartnack, Nuclear Physics A **945**, 112 (2016).

[15] A. W. Steiner, J. M. Lattimer, and E. F. Brown, The Astrophysical Journal **765**, L5 (2013).

[16] C. Y. Tsang, M. B. Tsang, P. Danielewicz, F. J. Fattoyev, and W. G. Lynch, Physics Letters B **796**, 1 (2019).

[17] J. M. Lattimer and M. Prakash, The Astrophysical Journal **550**, 426 (2001).

[18] M. Kortelainen, T. Lesinski, J. Moré, W. Nazarewicz, J. Sarich, N. Schunck, M. V. Stoitsov, and S. Wild, Phys. Rev. C **82**, 024313 (2010).

[19] B. A. Brown, Phys. Rev. Lett. **111**, 232502 (2013).

[20] Z. Zhang and L.-W. Chen, Phys. Lett. **B726**, 234 (2013), arXiv:1302.5327 [nucl-th] .

[21] P. Danielewicz, P. Singh, and J. Lee, Nucl. Phys. **A958**, 147 (2017), arXiv:1611.01871 [nucl-th] .

[22] B.-A. Li, P. G. Krastev, D.-H. Wen, and N.-B. Zhang, The European Physical Journal A **55**, 117 (2019).

[23] M. Baldo and G. Burgio, Progress in Particle and Nuclear Physics **91** (2016), 10.1016/j.ppnp.2016.06.006.

[24] J. M. Lattimer, Annual Review of Nuclear and Particle Science **62**, 485 (2012), https://doi.org/10.1146/annurev-nucl-102711-095018 .

[25] M. Tsang, W. Lynch, P. Danielewicz, and C. Tsang, Physics Letters B **795**, 533 (2019).

[26] B. P. Abbott *et al.* (LIGO Scientific Collaboration and Virgo Collaboration), Phys. Rev. Lett. **119**, 161101 (2017).

[27] T. Damour, M. Soffel, and C. Xu, Phys. Rev. D **45**, 1017 (1992).

[28] E. E. Flanagan and T. Hinderer, Phys. Rev. D **77**, 021502 (2008).

[29] T. Damour, A. Nagar, and L. Villain, Phys. Rev. D **85**, 123007 (2012).

[30] T. Binnington and E. Poisson, Phys. Rev. D **80**, 084018 (2009).

[31] S. Postnikov, M. Prakash, and J. M. Lattimer, Phys. Rev. D **82**, 024016 (2010).

[32] J. Piekarewicz and F. J. Fattoyev, Phys. Rev. C **99**, 045802 (2019).

[33] B. P. Abbott *et al.* (The LIGO Scientific Collaboration and the Virgo Collaboration), Phys. Rev. Lett. **121**, 161101 (2018).

[34] W. Reisdorf, D. Best, A. Gobbi, N. Herrmann, K. Hildenbrand, B. Hong, S. Jeong, Y. Leifels, C. Pinkenburg, J. Ritman, D. Schüll, U. Sodan, K. Teh, G. Wang, J. Wessels, T. Wienold, J. Alard, V. Amouroux, Z. Basrak, N. Bastid, I. Belyaev, L. Berger, J. Biegansky, M. Bini, S. Boussange, A. Buta, R. Čaplar, N. Cindro, J. Coffin, P. Crochet, R. Dona, P. Dupieux, M. Dželalija, J. Erö, M. Eskef, P. Fintz, Z. Fodor, L. Fraysse, A. Genoux-Lubain, G. Goebels, G. Guillaume, Y. Grigorian, E. Häfele, S. Hölbling, A. Houari, M. Ibnouzahir, M. Joriot, F. Jundt, J. Kecskemeti, M. Kirejczyk, P. Koncz, Y. Korchagin, M. Korolija, R. Kotte,

C. Kuhn, D. Lambrecht, A. Lebedev, A. Lebedev, I. Legrand, C. Maazouzi, V. Manko, T. Matulewicz, P. Maurenzig, H. Merlitz, G. Mgebrishvili, J. Mösner, S. Mohren, D. Moisa, G. Montarou, I. Montbel, P. Morel, W. Neubert, A. Olmi, G. Pasquali, D. Pelte, M. Petrovici, G. Poggi, P. Pras, F. Rami, V. Ramillien, C. Roy, A. Sadchikov, Z. Seres, B. Sikora, V. Simion, K. Siwek-Wilczyńska, V. Smolyankin, N. Taccetti, R. Tezkratt, L. Tizniti, M. Trzaska, M. Vasiliev, P. Wagner, K. Wisniewski, D. Wohlfarth,  and A. Zhilin, Nuclear Physics A **612**, 493 (1997).

[35] W. Reisdorf, M. Stockmeier, A. Andronic, M. Benabderrahmane, O. Hartmann, N. Herrmann, K. Hildenbrand, Y. Kim, M. Kiš, P. Koczoń, T. Kress, Y. Leifels, X. Lopez, M. Merschmeyer, A. Schüttauf, V. Barret, Z. Basrak, N. Bastid, R. Čaplar, P. Crochet, P. Dupieux, M. Dželalija, Z. Fodor, Y. Grishkin, B. Hong, T. Kang, J. Kecskemeti, M. Kirejczyk, M. Korolija, R. Kotte, A. Lebedev, T. Matulewicz, W. Neubert, M. Petrovici, F. Rami, M. Ryu, Z. Seres, B. Sikora, K. Sim, V. Simion, K. Siwek-Wilczyńska, V. Smolyankin, G. Stoicea, Z. Tymiński, K. Wiśniewski, D. Wohlfarth, Z. Xiao, H. Xu, I. Yushmanov,  and A. Zhilin, Nuclear Physics A **781**, 459 (2007).

[36] W. Reisdorf, A. Andronic, R. Averbeck, M. Benabderrahmane, O. Hartmann, N. Herrmann, K. Hildenbrand, T. Kang, Y. Kim, M. Kiš, P. Koczoń, T. Kress, Y. Leifels, M. Merschmeyer, K. Piasecki, A. Schüttauf, M. Stockmeier, V. Barret, Z. Basrak, N. Bastid, R. Čaplar, P. Crochet, P. Dupieux, M. Dželalija, Z. Fodor, P. Gasik, Y. Grishkin, B. Hong, J. Kecskemeti, M. Kirejczyk, M. Korolija, R. Kotte, A. Lebedev, X. Lopez, T. Matulewicz, W. Neubert, M. Petrovici, F. Rami, M. Ryu, Z. Seres, B. Sikora, K. Sim, V. Simion, K. Siwek-Wilczyńska, V. Smolyankin, G. Stoicea, Z. Tymiński, K. Wiśniewski, D. Wohlfarth, Z. Xiao, H. Xu, I. Yushmanov,  and A. Zhilin, Nuclear Physics A **848**, 366 (2010).

[37] J. Estee, W. G. Lynch, C. Y. Tsang, J. Barney, G. Jhang, M. B. Tsang, R. Wang, M. Kaneko, J. W. Lee, T. Isobe, M. Kurata-Nishimura, T. Murakami, D. S. Ahn, L. Atar, T. Aumann, H. Baba, K. Boretzky, J. Brzychczyk, G. Cerizza, N. Chiga, N. Fukuda, I. Gasparic, B. Hong, A. Horvat, K. Ieki, N. Inabe, Y. J. Kim, T. Kobayashi, Y. Kondo, P. Lasko, H. S. Lee, Y. Leifels, J. Łukasik, J. Manfredi, A. B. McIntosh, P. Morfouace, T. Nakamura, N. Nakatsuka, S. Nishimura, H. Otsu, P. Pawłowski, K. Pelczar, D. Rossi, H. Sakurai, C. Santamaria, H. Sato, H. Scheit, R. Shane, Y. Shimizu, H. Simon, A. Snoch, A. Sochocka, T. Sumikama, H. Suzuki, D. Suzuki, H. Takeda, S. Tangwancharoen, H. Toernqvist, Y. Togano, Z. G. Xiao, S. J. Yennello, Y. Zhang,  and M. D. Cozma (S$\pi$RIT Collaboration), Phys. Rev. Lett. **126**, 162701 (2021).

[38] T. Malik, N. Alam, M. Fortin, C. Providência, B. K. Agrawal, T. K. Jha, B. Kumar,  and S. K. Patra, Phys. Rev. C **98**, 035804 (2018).

[39] H. Gil, Y.-M. Kim, C. H. Hyun, P. Papakonstantinou,  and Y. Oh, Phys. Rev. C **100**, 014312 (2019).

[40] Z. Carson, A. W. Steiner,  and K. Yagi, Phys. Rev. D **99**, 043010 (2019).

[41] Y. Lim and J. W. Holt, Phys. Rev. Lett. **121**, 062701 (2018).

[42] P. Danielewicz, P. Singh,  and J. Lee, Nuclear Physics A **958**, 147 (2017).

148

[43]  P. Haensel, A. Y. Potekhin,  and D. G. Yakovlev, *Neutron Stars I* (Springer, 2007).

[44]  C. J. Horowitz, M. A. Pérez-García,  and J. Piekarewicz, Phys. Rev. C **69**, 045804 (2004).

[45]  C. J. Horowitz, M. A. Pérez-García, J. Carriere, D. K. Berry,  and J. Piekarewicz, Phys. Rev. C **70**, 065806 (2004).

[46]  C. J. Horowitz, M. A. Pérez-García, D. K. Berry,  and J. Piekarewicz, Phys. Rev. C **72**, 035801 (2005).

[47]  G. Watanabe, K. Sato, K. Yasuoka,  and T. Ebisuzaki, Phys. Rev. C **68**, 035806 (2003).

[48]  G. Watanabe, T. Maruyama, K. Sato, K. Yasuoka,  and T. Ebisuzaki, Phys. Rev. Lett. **94**, 031101 (2005).

[49]  G. Watanabe, H. Sonoda, T. Maruyama, K. Sato, K. Yasuoka,  and T. Ebisuzaki, Phys. Rev. Lett. **103**, 121101 (2009).

[50]  A. S. Schneider, C. J. Horowitz, J. Hughto,  and D. K. Berry, Phys. Rev. C **88**, 065807 (2013).

[51]  C. J. Horowitz, D. K. Berry, C. M. Briggs, M. E. Caplan, A. Cumming,  and A. S. Schneider, Phys. Rev. Lett. **114**, 031102 (2015).

[52]  M. E. Caplan, A. S. Schneider, C. J. Horowitz,  and D. K. Berry, Phys. Rev. C **91**, 065802 (2015).

[53]  P. Magierski and P.-H. Heenen, Phys. Rev. C **65**, 045804 (2002).

[54]  N. Chamel, Nuclear Physics A **747**, 109  (2005).

[55]  W. G. Newton and J. R. Stone, Phys. Rev. C **79**, 055801 (2009).

[56]  B. Schuetrumpf and W. Nazarewicz, Phys. Rev. C **92**, 045806 (2015).

[57]  F. J. Fattoyev, C. J. Horowitz,  and B. Schuetrumpf, Phys. Rev. C **95**, 055804 (2017).

[58]  D. G. Ravenhall, C. J. Pethick,  and J. R. Wilson, Phys. Rev. Lett. **50**, 2066 (1983).

[59]  M. Hashimoto, H. Seki,  and M. Yamada, Prog. Theor. Phys. **71**, 320 (1984).

[60]  K. Oyamatsu, M.-a. Hashimoto,  and M. Yamada, Prog. Theor. Phys. **72**, 373 (1984).

[61]  V. A. Ambartsumyan and G. S. Saakyan, Soviet Astronomy **4**, 187 (1960).

[62]  D. Chatterjee and I. Vidaña, The European Physical Journal A **52**, 29 (2016).

[63]  C. Ducoin, J. Margueron, C. Providência,  and I. Vidaña, Phys. Rev. C **83**, 045810 (2011).

[64]  G. Baym, C. Pethick,  and P. Sutherland, Astrophys. J. **170**, 299 (1971).

[65]  F. Ji, J. Hu, S. Bao,  and H. Shen, Phys. Rev. C **100**, 045801 (2019).

[66]  L. Perot, N. Chamel,  and A. Sourie, Phys. Rev. C **101**, 015806 (2020).

[67] B. Margalit and B. D. Metzger, The Astrophysical Journal **850**, L19 (2017).

[68] I. Tews, J. Margueron, and S. Reddy, Phys. Rev. C **98**, 045804 (2018).

[69] H. Sotani, K. Iida, and K. Oyamatsu, Monthly Notices of the Royal Astronomical Society **470**, 4397 (2017), https://academic.oup.com/mnras/article-pdf/470/4/4397/19179395/stx1510.pdf .

[70] N.-B. Zhang, B.-A. Li, and J. Xu, The Astrophysical Journal **859**, 90 (2018).

[71] E. Khan, J. Margueron, and I. Vidaña, Phys. Rev. Lett. **109**, 092501 (2012).

[72] E. Khan, Physica Scripta **T152**, 014008 (2013).

[73] H. Guven, K. Bozkurt, E. Khan, and J. Margueron, (2020), arXiv:2001.10259 [nucl-th] .

[74] E. Lipparini and S. Stringari, Physics Reports **175**, 103 (1989).

[75] L. D. Landau and E. M. Lifshitz, *Fluid Mechanics* (Pergamonm Oxford, 1987) pp. 251–254.

[76] J. M. Lattimer and M. Prakash, Phys. Rept. **621**, 127 (2016), arXiv:1512.07820 [astro-ph.SR] .

[77] P. Demorest, T. Pennucci, S. Ransom, M. Roberts, and J. Hessels, Nature **467**, 1081 (2010), arXiv:1010.5788 [astro-ph.HE] .

[78] J. Antoniadis, P. C. C. Freire, N. Wex, T. M. Tauris, R. S. Lynch, M. H. van Kerkwijk, M. Kramer, C. Bassa, V. S. Dhillon, T. Driebe, J. W. T. Hessels, V. M. Kaspi, V. I. Kondratiev, N. Langer, T. R. Marsh, M. A. McLaughlin, T. T. Pennucci, S. M. Ransom, I. H. Stairs, J. van Leeuwen, J. P. W. Verbiest, and D. G. Whelan, Science **340** (2013), 10.1126/science.1233232.

[79] G. Baym, S. Furusawa, T. Hatsuda, T. Kojo, and H. Togashi, arXiv e-prints (2019), arXiv:1903.08963 [astro-ph.HE] .

[80] B.-A. Li, P. G. Krastev, D.-H. Wen, W.-J. Xie, and N.-B. Zhang, AIP Conference Proceedings **2127**, 020018 (2019), https://aip.scitation.org/doi/pdf/10.1063/1.5117808 .

[81] M. Shibata, S. Fujibayashi, K. Hotokezaka, K. Kiuchi, K. Kyutoku, Y. Sekiguchi, and M. Tanaka, Phys. Rev. D **96**, 123012 (2017).

[82] L. Rezzolla, E. R. Most, and L. R. Weih, The Astrophysical Journal **852**, L25 (2018).

[83] M. Ruiz, S. L. Shapiro, and A. Tsokaros, Phys. Rev. D **97**, 021501 (2018).

[84] E.-P. Zhou, X. Zhou, and A. Li, Phys. Rev. D **97**, 083015 (2018).

[85] J. Benesty, J. Chen, Y. Huang, and I. Cohen, *Pearson Correlation Coefficient. In: Noise Reduction in Speech Processing*, Vol. 2 (Springer, Berlin, Heidelberg, 2009) Chap. Pearson Correlation Coefficient.

[86]  B. P. Abbott *et al.* (LIGO Scientific, Virgo),  (2020), arXiv:2001.01761 [astro-ph.HE] .

[87]  I. Tews, J. Carlson, S. Gandolfi,  and S. Reddy, The Astrophysical Journal **860**, 149 (2018).

[88]  A. Maselli, V. Cardoso, V. Ferrari, L. Gualtieri,  and P. Pani, Phys. Rev. D **88**, 023007 (2013).

[89]  J. M. Lattimer, private communication.

[90]  J. Barney, J. Estee, W. G. Lynch, T. Isobe, G. Jhang, M. Kurata-Nishimura, A. B. McIntosh, T. Murakami, R. Shane, S. Tangwancharoen, M. B. Tsang, G. Cerizza, M. Kaneko, J. W. Lee, C. Y. Tsang, R. Wang, C. Anderson, H. Baba, Z. Chajecki, M. Famiano, R. Hodges-Showalter, B. Hong, T. Kobayashi, P. Lasko, J. Łukasik, N. Nakatsuka, R. Olsen, H. Otsu, P. Pawłowski, K. Pelczar, H. Sakurai, C. Santamaria, H. Setiawan, A. Taketani, J. R. Winkelbauer, Z. Xiao, S. J. Yennello, J. Yurkon,  and Y. Zhang, Review of Scientific Instruments **92** (2021), 10.1063/5.0041191.

[91]  H. Sato, T. Kubo, Y. Yano, K. Kusaka, J. Ohnishi, K. Yoneda, Y. Shimizu, T. Motobayashi, H. Otsu, T. Isobe, T. Kobayashi, K. Sekiguchi, T. Nakamura, Y. Kondo, Y. Togano, T. Murakami, T. Tsuchihashi, T. Orikasa,  and K. Maeta, IEEE Transactions on Applied Superconductivity **23**, 4500308 (2013).

[92]  C. Tsang, J. Estee, R. Wang, J. Barney, G. Jhang, W. Lynch, Z. Zhang, G. Cerizza, T. Isobe, M. Kaneko, M. Kurata-Nishimura, J. Lee, T. Murakami,  and M. Tsang, Nuclear Instruments and Methods in Physics Research Section A: Accelerators, Spectrometers, Detectors and Associated Equipment **959**, 163477 (2020).

[93]  R. Shane, A. B. McIntosh, T. Isobe, W. G. Lynch, H. Baba, J. Barney, Z. Chajecki, M. Chartier, J. Estee, M. Famiano, B. Hong, K. Ieki, G. Jhang, R. Lemmon, F. Lu, T. Murakami, N. Nakatsuka, M. Nishimura, R. Olsen, W. Powell, H. Sakurai, A. Taketani, S. Tangwancharoen, M. B. Tsang, T. Usukura, R. Wang, S. J. Yennello,  and J. Yurkon, Nuclear Instruments and Methods in Physics Research Section A: Accelerators, Spectrometers, Detectors and Associated Equipment **784**, 513  (2015), Symposium on Radiation Measurements and Applications 2014 (SORMA XV).

[94]  M. Kaneko, T. Murakami, T. Isobe, M. Kurata-Nishimura, W. G. Lynch, M. B. Tsang, J. Barney, J. Estee, G. Cerizza, C. Santamaria, G. Jhang, J. W. Lee, P. Lasko, J. Lukasik, P. Pawlowski,  and Y. Zhang, RIKEN Accel. Prog. Rep. **50**, 172 (2017).

[95]  P. Lasko, M. Adamczyk, J. Brzychczyk, P. Hirnyk, J. Łukasik, P. Pawłowski, K. Pelczar, A. Snoch, A. Sochocka, Z. Sosin, J. Barney, G. Cerizza, J. Estee, T. Isobe, G. Jhang, M. Kaneko, M. Kurata-Nishimura, W. Lynch, T. Murakami, C. Santamaria, M. Tsang,  and Y. Zhang, Nuclear Instruments and Methods in Physics Research Section A: Accelerators, Spectrometers, Detectors and Associated Equipment **856**, 92 (2017).

[96]  M. Al-Turany, D. Bertini, R. Karabowicz, D. Kresan, P. Malzacher, T. Stockmanns,  and F. Uhlig, Journal of Physics: Conference Series **396**, 022001 (2012).

[97] J. Lee, G. Jhang, G. Cerizza, J. Barney, J. Estee, T. Isobe, M. Kaneko, M. Kurata-Nishimura, W. Lynch, T. Murakami, C. Tsang, M. Tsang, R. Wang, B. Hong, A. McIntosh, H. Sakurai, C. Santamaria, R. Shane, S. Tangwancharoen, S. Yennello,  and Y. Zhang, Nuclear Instruments and Methods in Physics Research Section A: Accelerators, Spectrometers, Detectors and Associated Equipment **965**, 163840 (2020).

[98] J. Estee, W. Lynch, J. Barney, G. Cerizza, G. Jhang, J. Lee, R. Wang, T. Isobe, M. Kaneko, M. Kurata-Nishimura, T. Murakami, R. Shane, S. Tangwancharoen, C. Tsang, M. Tsang, B. Hong, P. Lasko, J. Łukasik, A. McIntosh, P. Pawłowski, K. Pelczar, H. Sakurai, C. Santamaria, D. Suzuki, S. Yennello,  and Y. Zhang, Nuclear Instruments and Methods in Physics Research Section A: Accelerators, Spectrometers, Detectors and Associated Equipment **944**, 162509 (2019).

[99] M. Anderson, J. Berkovitz, W. Betts, R. Bossingham, F. Bieser, R. Brown, M. Burks, M. Calderón de la Barca Sánchez, D. Cebra, M. Cherney, J. Chrin, W. Edwards, V. Ghazikhanian, D. Greiner, M. Gilkes, D. Hardtke, G. Harper, E. Hjort, H. Huang, G. Igo, S. Jacobson, D. Keane, S. Klein, G. Koehler, L. Kotchenda, B. Lasiuk, A. Lebedev, J. Lin, M. Lisa, H. Matis, J. Nystrand, S. Panitkin, D. Reichold, F. Retiere, I. Sakrejda, K. Schweda, D. Shuman, R. Snellings, N. Stone, B. Stringfellow, J. Thomas, T. Trainor, S. Trentalange, R. Wells, C. Whitten, H. Wieman, E. Yamamoto,  and W. Zhang, Nuclear Instruments and Methods in Physics Research Section A: Accelerators, Spectrometers, Detectors and Associated Equipment **499**, 659 (2003), the Relativistic Heavy Ion Collider Project:  RHIC and its Detectors.

[100] J. Rauch and T. Schlüter, Journal of Physics:  Conference Series **608**, 012042 (2015).

[101] W. Waltenberger, W. Mitaroff, F. Moser, B. Pflugfelder,  and H. Riedel, Journal of Physics:  Conference Series **119**, 032037 (2008).

[102] P. Sigmund, *Particle Penetration and Radiation Effect* (Springer-Verlag, 2006).

[103] J. Adam, D. Adamová, M. M. Aggarwal, G. Aglieri Rinella, M. Agnello, N. Agrawal, Z. Ahammed, S. Ahmad, S. U. Ahn, S. Aiola, A. Akindinov, S. N. Alam, D. S. D. Albuquerque, D. Aleksandrov, B. Alessandro, D. Alexandre, R. Alfaro Molina, A. Alici, A. Alkin, J. R. M. Almaraz, J. Alme, T. Alt, S. Altinpinar, I. Altsybeev, C. Alves Garcia Prado, C. Andrei, A. Andronic, V. Anguelov, T. Antičić, F. Antinori, P. Antonioli, L. Aphecetche, H. Appelshäuser, S. Arcelli, R. Arnaldi, O. W. Arnold, I. C. Arsene, M. Arslandok, B. Audurier, A. Augustinus, R. Averbeck, M. D. Azmi, A. Badalà, Y. W. Baek, S. Bagnasco, R. Bailhache, R. Bala, S. Balasubramanian, A. Baldisseri, R. C. Baral, A. M. Barbano, R. Barbera, F. Barile, G. G. Barnaföldi, L. S. Barnby, V. Barret, P. Bartalini, K. Barth, J. Bartke, E. Bartsch, M. Basile, N. Bastid, S. Basu, B. Bathen, G. Batigne, A. Batista Camejo, B. Batyunya, P. C. Batzing, I. G. Bearden, H. Beck, C. Bedda, N. K. Behera, I. Belikov, F. Bellini, H. Bello Martinez, R. Bellwied, R. Belmont, E. Belmont-Moreno, V. Belyaev, P. Benacek, G. Bencedi, S. Beole, I. Berceanu, A. Bercuci, Y. Berdnikov, D. Berenyi, R. A. Bertens, D. Berzano, L. Betev, A. Bhasin, I. R. Bhat, A. K. Bhati, B. Bhattacharjee, J. Bhom, L. Bianchi, N. Bianchi, C. Bianchin, J. Bielčík, J. Bielčíková, A. Bilandzic, G. Biro, R. Biswas, S. Biswas, S. Bjelogrlic, J. T. Blair, D. Blau, C. Blume, F. Bock, A. Bogdanov,

H. Bøggild, L. Boldizsár, M. Bombara, J. Book, H. Borel, A. Borissov, M. Borri, F. Bossú, E. Botta, C. Bourjau, P. Braun-Munzinger, M. Bregant, T. Breitner, T. A. Broker, T. A. Browning, M. Broz, E. J. Brucken, E. Bruna, G. E. Bruno, D. Budnikov, H. Buesching, S. Bufalino, P. Buncic, O. Busch, Z. Buthelezi, J. B. Butt, J. T. Buxton, J. Cabala, D. Caffarri, X. Cai, H. Caines, L. Calero Diaz, A. Caliva, E. Calvo Villar, P. Camerini, F. Carena, W. Carena, F. Carnesecchi, J. Castillo Castellanos, A. J. Castro, E. A. R. Casula, C. Ceballos Sanchez, J. Cepila, P. Cerello, J. Cerkala, B. Chang, S. Chapeland, M. Chartier, J. L. Charvet, S. Chattopadhyay, A. Chauvin, V. Chelnokov, M. Cherney, C. Cheshkov, B. Cheynis, V. Chibante Barroso, D. D. Chinellato, S. Cho, P. Chochula, K. Choi, M. Chojnacki, S. Choudhury, P. Christakoglou, C. H. Christensen, P. Christiansen, T. Chujo, S. U. Chung, C. Cicalo, L. Cifarelli, F. Cindolo, J. Cleymans, F. Colamaria, D. Colella, A. Collu, M. Colocci, G. Conesa Balbastre, Z. Conesa del Valle, M. E. Connors, J. G. Contreras, T. M. Cormier, Y. Corrales Morales, I. Cortés Maldonado, P. Cortese, M. R. Cosentino, F. Costa, P. Crochet, R. Cruz Albino, E. Cuautle, L. Cunqueiro, T. Dahms, A. Dainese, M. C. Danisch, A. Danu, D. Das, I. Das, S. Das, A. Dash, S. Dash, S. De, A. De Caro, G. de Cataldo, C. de Conti, J. de Cuveland, A. De Falco, D. De Gruttola, N. De Marco, S. De Pasquale, A. Deisting, A. Deloff, E. Dénes, C. Deplano, P. Dhankher, D. Di Bari, A. Di Mauro, P. Di Nezza, M. A. Diaz Corchero, T. Dietel, P. Dillenseger, R. Divià, Ø. Djuvsland, A. Dobrin, D. Domenicis Gimenez, B. Dönigus, O. Dordic, T. Drozhzhova, A. K. Dubey, A. Dubla, L. Ducroux, P. Dupieux, R. J. Ehlers, D. Elia, E. Endress, H. Engel, E. Epple, B. Erazmus, I. Erdemir, F. Erhardt, B. Espagnon, M. Estienne, S. Esumi, J. Eum, D. Evans, S. Evdokimov, G. Eyyubova, L. Fabbietti, D. Fabris, J. Faivre, A. Fantoni, M. Fasel, L. Feldkamp, A. Feliciello, G. Feofilov, J. Ferencei, A. Fernández Téllez, E. G. Ferreiro, A. Ferretti, A. Festanti, V. J. G. Feuillard, J. Figiel, M. A. S. Figueredo, S. Filchagin, D. Finogeev, F. M. Fionda, E. M. Fiore, M. G. Fleck, M. Floris, S. Foertsch, P. Foka, S. Fokin, E. Fragiacomo, A. Francescon, U. Frankenfeld, G. G. Fronze, U. Fuchs, C. Furget, A. Furs, M. Fusco Girard, J. J. Gaardhøje, M. Gagliardi, A. M. Gago, M. Gallio, D. R. Gangadharan, P. Ganoti, C. Gao, C. Garabatos, E. Garcia-Solis, C. Gargiulo, P. Gasik, E. F. Gauger, and T. A. Collaboration, The European Physical Journal Plus **131**, 168 (2016).

[104] J. Lee, Private Communication (2022).

[105] O. Tarasov and D. Bazin, Nuclear Instruments and Methods in Physics Research Section B: Beam Interactions with Materials and Atoms **376**, 185 (2016), proceedings of the XVIIth International Conference on Electromagnetic Isotope Separators and Related Topics (EMIS2015), Grand Rapids, MI, U.S.A., 11-15 May 2015.

[106] F. Rami, P. Crochet, R. Donà, B. de Schauenburg, P. Wagner, J. Alard, A. Andronic, Z. Basrak, N. Bastid, I. Belyaev, A. Bendarag, G. Berek, D. Best, R. Čaplar, A. Devismes, P. Dupieux, M. Dželalija, M. Eskef, Z. Fodor, A. Gobbi, Y. Grishkin, N. Herrmann, K. Hildenbrand, B. Hong, J. Kecskemeti, M. Kirejczyk, M. Korolija, R. Kotte, A. Lebedev, Y. Leifels, H. Merlitz, S. Mohren, D. Moisa, W. Neubert, D. Pelte, M. Petrovici, C. Pinkenburg, C. Plettner, W. Reisdorf, D. Schüll, Z. Seres, B. Sikora, V. Simion, K. Siwek-Wilczyńska, G. Stoicea, M. Stockmeier, M. Vasiliev, K. Wisniewski, D. Wohlfarth, I. Yushmanov, and A. Zhilin, Nuclear Physics A **646**, 367 (1999).

[107] A. Andronic, W. Reisdorf, J. P. Alard, V. Barret, Z. Basrak, N. Bastid, A. Bendarag, G. Berek, R. Čaplar, P. Crochet, A. Devismes, P. Dupieux, M. Dželalija, C. Finck, Z. Fodor, A. Gobbi, Y. Grishkin, O. N. Hartmann, N. Herrmann, K. D. Hildenbrand, B. Hong, J. Kecskemeti, Y. J. Kim, M. Kirejczyk, P. Koczon, M. Korolija, R. Kotte, T. Kress, R. Kutsche, A. Lebedev, Y. Leifels, W. Neubert, D. Pelte, M. Petrovici, F. Rami, B. de Schauenburg, D. Schüll, Z. Seres, B. Sikora, K. S. Sim, V. Simion, K. Siwek-Wilczyńska, V. Smolyankin, M. R. Stockmeier, G. Stoicea, P. Wagner, K. Wiśniewski, D. Wohlfarth, I. Yushmanov, and A. Zhilin, Phys. Rev. C **64**, 041604 (2001).

[108] De Filippo, E., Russotto, P., Acosta, L., Adamczyk, M., Al-Ajlan, A., Al-Garawi, M., Al-Homaidhi, S., Amorini, F., Auditore, L., Aumann, T., Ayyad, Y., Basrak, Z., Benlliure, J., Boisjoli, M., Boretzky, K., Brzychczyk, J., Budzanowski, A., Caesar, C., Cardella, G., Cammarata, P., Chajecki, Z., Chartier, M., Chbihi, A., Colonna, M., Cozma, M.D., Czech, B., Di Toro, M., Famiano, M., Gannon, S., Gaspari´c, I., Grassi, L., Guazzoni, C., Guazzoni, P., Heil, M., Heilborn, L., Introzzi, R., Isobe, T., Kezzar, K., Kis, M., Krasznahorkay, A., Kupny, S., Kurz, N., La Guidara, E., Lanzalone, G., Lasko, P., Le Fèvre, A., Leifels, Y., Lemmon, R.C., Li, Q.F., Lombardo, I., Lukasik, J., Lynch, W.G., Marini, P., Matthews, Z., May, L., Minniti, T., Mostazo, M., Pagano, A., Pagano, E.V., Papa, M., Pawlowski, P., Pirrone, S., Politi, G., Porto, F., Reviol, W., Riccio, F., Rizzo, F., Rosato, E., Rossi, D., Santoro, S., Sarantites, D.G., Simon, H., Skwirczynska, I., Sosin, Z., Stuhl, L., Trautmann, W., Trifirò, A., Trimarchi, M., Tsang, M.B., Verde, G., Veselsky, M., Vigilante, M., Wang, Yongjia, Wieloch, A., Wigg, P., Winkelbauer, J., Wolter, H.H., Wu, P., Yennello, S., Zambon, P., Zetta, L., and Zoric, M., EPJ Web Conf. **137**, 09002 (2017).

[109] A. M. Poskanzer and S. A. Voloshin, Phys. Rev. C **58**, 1671 (1998).

[110] P. Danielewicz and G. Odyniec, Physics Letters B **157**, 146 (1985).

[111] J. Barrette, R. Bellwied, S. Bennett, R. Bersch, P. Braun-Munzinger, W. C. Chang, W. E. Cleland, M. Clemen, J. Cole, T. M. Cormier, Y. Dai, G. David, J. Dee, O. Dietzsch, M. Drigert, K. Filimonov, S. C. Johnson, J. R. Hall, T. K. Hemmick, N. Herrmann, B. Hong, Y. Kwon, R. Lacasse, Q. Li, T. W. Ludlam, S. K. Mark, R. Matheus, S. McCorkle, J. T. Murgatroyd, D. Miśkowiec, E. O'Brien, S. Panitkin, T. Piazza, M. Pollack, C. Pruneau, M. N. Rao, E. Reber, M. Rosati, N. C. da Silva, S. Sedykh, U. Sonnadara, J. Stachel, E. M. Takagui, S. Voloshin, T. B. Vongpaseuth, G. Wang, J. P. Wessels, C. L. Woody, N. Xu, Y. Zhang, and C. Zou, Phys. Rev. C **56**, 3254 (1997).

[112] M. Colonna, Y.-X. Zhang, Y.-J. Wang, D. Cozma, P. Danielewicz, C. M. Ko, A. Ono, M. B. Tsang, R. Wang, H. Wolter, J. Xu, Z. Zhang, L.-W. Chen, H.-G. Cheng, H. Elfner, Z.-Q. Feng, M. Kim, Y. Kim, S. Jeon, C.-H. Lee, B.-A. Li, Q.-F. Li, Z.-X. Li, S. Mallik, D. Oliinychenko, J. Su, T. Song, A. Sorensen, and F.-S. Zhang, Phys. Rev. C **104**, 024603 (2021).

[113] C. Hartnack, L. Zhuxia, L. Neise, G. Peilert, A. Rosenhauer, H. Sorge, J. Aichelin, H. Stöcker, and W. Greiner, Nuclear Physics A **495**, 303 (1989).

[114] J. Aichelin, Physics Reports **202**, 233 (1991).

[115] A. Ono, Phys. Rev. C **59**, 853 (1999).

[116] H. Feldmeier, Nuclear Physics A **515**, 147 (1990).

[117] M. Colonna and P. Chomaz, Physics Letters B **436**, 1 (1998).

[118] A. Ono, H. Horiuchi, T. Maruyama, and A. Ohnishi, Progress of Theoretical Physics **87**, 1185 (1992), https://academic.oup.com/ptp/article-pdf/87/5/1185/5272175/87-5-1185.pdf .

[119] A. Ono, H. Horiuchi, T. Maruyama, and A. Ohnishi, Phys. Rev. Lett. **68**, 2898 (1992).

[120] M. Papa, T. Maruyama, and A. Bonasera, Phys. Rev. C **64**, 024612 (2001).

[121] Y. Zhang and Z. Li, Phys. Rev. C **74**, 014602 (2006).

[122] S. Ayik and C. Gregoire, Physics Letters B **212**, 269 (1988).

[123] Y. Abe, S. Ayik, P.-G. Reinhard, and E. Suraud, Physics Reports **275**, 49 (1996).

[124] J. Randrup and B. Remaud, Nuclear Physics A **514**, 339 (1990).

[125] P. Chomaz, M. Colonna, and J. Randrup, Physics Reports **389**, 263 (2004).

[126] P. Napolitani and M. Colonna, Physics Letters B **726**, 382 (2013).

[127] P. Napolitani and M. Colonna, Phys. Rev. C **92**, 034607 (2015).

[128] Y. Zhang and Z. Li, Phys. Rev. C **71**, 024604 (2005).

[129] Y. Zhang, P. Danielewicz, M. Famiano, Z. Li, W. Lynch, and M. Tsang, Physics Letters B **664**, 145 (2008).

[130] Z. Yingxun, L. Zhuxia, Z. Kai, L. Hang, and T. MB, NUCLEAR SCIENCE AND TECH-NIQUES) **24**, 50503 (2019).

[131] Y. Zhang, M. Tsang, Z. Li, and H. Liu, Physics Letters B **732**, 186 (2014).

[132] S. Bass, M. Belkacem, M. Bleicher, M. Brandstetter, L. Bravina, C. Ernst, L. Gerland, M. Hofmann, S. Hofmann, J. Konopka, G. Mao, L. Neise, S. Soff, C. Spieles, H. Weber, L. Winckelmann, H. Stöcker, W. Greiner, C. Hartnack, J. Aichelin, and N. Amelin, Progress in Particle and Nuclear Physics **41**, 255 (1998).

[133] Y. Wang, C. Guo, Q. Li, H. Zhang, Z. Li, and W. Trautmann, Phys. Rev. C **89**, 034606 (2014).

[134] Q. Li, Z. Li, S. Soff, M. Bleicher, and H. Stöcker, Journal of Physics G: Nuclear and Particle Physics **32**, 151 (2005).

[135] Q. Li, M. Bleicher, and H. Stöcker, Physics Letters B **659**, 525 (2008).

[136] Y. Wang, C. Guo, Q. Li, H. Zhang, Y. Leifels, and W. Trautmann, Phys. Rev. C **89**, 044603 (2014).

[137] L. Tong, P. Li, F. Li, Y. Wang, Q. Li, and F. Liu, Chinese Physics C **44**, 074103 (2020).

[138] Y. Liu, Y. Wang, Y. Cui, C.-J. Xia, Z. Li, Y. Chen, Q. Li, and Y. Zhang, Phys. Rev. C **103**, 014616 (2021).

[139] Y.-J. Wang and Q.-F. Li, Frontiers of Physics **15**, 44302 (2020).

[140] Y.-X. Zhang, N. Wang, Q.-F. Li, L. Ou, J.-L. Tian, M. Liu, K. Zhao, X.-Z. Wu, and Z.-X. Li, Frontiers of Physics **15**, 1 (2020).

[141] F. Li, Y. Wang, H. Lü, P. Li, Q. Li, and F. Liu, Journal of Physics G: Nuclear and Particle Physics **47**, 115104 (2020).

[142] D. T. Khoa, N. Ohtsuka, M. Matin, A. Faessler, S. Huang, E. Lehmann, and R. K. Puri, Nuclear Physics A **548**, 102 (1992).

[143] C. Fuchs, L. Sehn, E. Lehmann, J. Zipprich, and A. Faessler, Physical Review C **55**, 411 (1997).

[144] K. Shekhter, C. Fuchs, A. Faessler, M. Krivoruchenko, and B. Martemyanov, Phys. Rev. C **68**, 014904 (2003).

[145] M. Cozma, Physics Letters B **700**, 139 (2011).

[146] M. Cozma, Y. Leifels, W. Trautmann, Q. Li, and P. Russotto, Physical Review C **88**, 044912 (2013).

[147] G. Jhang, J. Estee, J. Barney, G. Cerizza, M. Kaneko, J. Lee, W. Lynch, T. Isobe, M. Kurata-Nishimura, T. Murakami, C. Tsang, M. Tsang, R. Wang, D. Ahn, L. Atar, T. Aumann, H. Baba, K. Boretzky, J. Brzychczyk, N. Chiga, N. Fukuda, I. Gasparic, B. Hong, A. Horvat, K. Ieki, N. Inabe, Y. Kim, T. Kobayashi, Y. Kondo, P. Lasko, H. Lee, Y. Leifels, J. Łukasik, J. Manfredi, A. McIntosh, P. Morfouace, T. Nakamura, N. Nakatsuka, S. Nishimura, R. Olsen, H. Otsu, P. Pawłowski, K. Pelczar, D. Rossi, H. Sakurai, C. Santamaria, H. Sato, H. Scheit, R. Shane, Y. Shimizu, H. Simon, A. Snoch, A. Sochocka, Z. Sosin, T. Sumikama, H. Suzuki, D. Suzuki, H. Takeda, S. Tangwancharoen, H. Toernqvist, Y. Togano, Z. Xiao, S. Yennello, J. Yurkon, Y. Zhang, M. Colonna, D. Cozma, P. Danielewicz, H. Elfner, N. Ikeno, C. M. Ko, J. Mohs, D. Oliinychenko, A. Ono, J. Su, Y. J. Wang, H. Wolter, J. Xu, Y.-X. Zhang, and Z. Zhang, Physics Letters B **813**, 136016 (2021).

[148] M. Cozma, Physics Letters B **753**, 166 (2016).

[149] A. Ono, Progress in Particle and Nuclear Physics **105**, 139 (2019).

[150] B. Dönigus, The European Physical Journal A **56**, 280 (2020).

[151] M. Kaneko, T. Murakami, T. Isobe, M. Kurata-Nishimura, A. Ono, N. Ikeno, J. Barney, G. Cerizza, J. Estee, G. Jhang, J. Lee, W. Lynch, C. Santamaria, C. Tsang, M. Tsang, R. Wang, D. Ahn, L. Atar, T. Aumann, H. Baba, K. Boretzky, J. Brzychczyk, N. Chiga, N. Fukuda, I. Gašparić, B. Hong, A. Horvat, T. Ichihara, K. Ieki, N. Inabe, Y. Kim, T. Kobayashi, Y. Kondo, P. Lasko, H. Lee, Y. Leifels, J. Łukasik, J. Manfredi, A. McIntosh, P. Morfouace, T. Nakamura, N. Nakatsuka, S. Nishimura, R. Olsen, H. Otsu, P. Pawłowski, K. Pelczar,

D. Rossi, H. Sakurai, H. Sato, H. Scheit, R. Shane, Y. Shimizu, H. Simon, T. Sumikama, D. Suzuki, H. Suzuki, H. Takeda, S. Tangwancharoen, Y. Togano, H. Törnqvist, Z. Xiao, S. Yennello, J. Yurkon, and Y. Zhang, Physics Letters B **822**, 136681 (2021).

[152] B.-A. Li, Phys. Rev. Lett. **88**, 192701 (2002).

[153] M. D. Cozma and M. B. Tsang, The European Physical Journal A **57**, 309 (2021).

[154] Q. Li, C. Shen, C. Guo, Y. Wang, Z. Li, J. Lukasik, and W. Trautmann, Phys. Rev. C **83**, 044617 (2011).

[155] P. Morfouace, C. Tsang, Y. Zhang, W. Lynch, M. Tsang, D. Coupland, M. Youngs, Z. Chajecki, M. Famiano, T. Ghosh, G. Jhang, J. Lee, H. Liu, A. Sanetullaev, R. Showalter, and J. Winkelbauer, Physics Letters B **799**, 135045 (2019).

[156] T. Gaitanos, C. Fuchs, and H. Wolter, Physics Letters B **609**, 241 (2005).

[157] F. Rami, Y. Leifels, B. de Schauenburg, A. Gobbi, B. Hong, J. P. Alard, A. Andronic, R. Averbeck, V. Barret, Z. Basrak, N. Bastid, I. Belyaev, A. Bendarag, G. Berek, R. Čaplar, N. Cindro, P. Crochet, A. Devismes, P. Dupieux, M. Dželalija, M. Eskef, C. Finck, Z. Fodor, H. Folger, L. Fraysse, A. Genoux-Lubain, Y. Grigorian, Y. Grishkin, N. Herrmann, K. D. Hildenbrand, J. Kecskemeti, Y. J. Kim, P. Koczon, M. Kirejczyk, M. Korolija, R. Kotte, M. Kowalczyk, T. Kress, R. Kutsche, A. Lebedev, K. S. Lee, V. Manko, H. Merlitz, S. Mohren, D. Moisa, J. Mösner, W. Neubert, A. Nianine, D. Pelte, M. Petrovici, C. Pinkenburg, C. Plettner, W. Reisdorf, J. Ritman, D. Schüll, Z. Seres, B. Sikora, K. S. Sim, V. Simion, K. Siwek-Wilczyńska, A. Somov, M. R. Stockmeier, G. Stoicea, M. Vasiliev, P. Wagner, K. Wiśniewski, D. Wohlfarth, J. T. Yang, I. Yushmanov, and A. Zhilin (FOPI Collaboration), Phys. Rev. Lett. **84**, 1120 (2000).

[158] S. Agostinelli, J. Allison, K. Amako, J. Apostolakis, H. Araujo, P. Arce, M. Asai, D. Axen, S. Banerjee, G. Barrand, F. Behner, L. Bellagamba, J. Boudreau, L. Broglia, A. Brunengo, H. Burkhardt, S. Chauvie, J. Chuma, R. Chytracek, G. Cooperman, G. Cosmo, P. Degtyarenko, A. Dell'Acqua, G. Depaola, D. Dietrich, R. Enami, A. Feliciello, C. Ferguson, H. Fesefeldt, G. Folger, F. Foppiano, A. Forti, S. Garelli, S. Giani, R. Giannitrapani, D. Gibin, J. Gómez Cadenas, I. González, G. Gracia Abril, G. Greeniaus, W. Greiner, V. Grichine, A. Grossheim, S. Guatelli, P. Gumplinger, R. Hamatsu, K. Hashimoto, H. Hasui, A. Heikkinen, A. Howard, V. Ivanchenko, A. Johnson, F. Jones, J. Kallenbach, N. Kanaya, M. Kawabata, Y. Kawabata, M. Kawaguti, S. Kelner, P. Kent, A. Kimura, T. Kodama, R. Kokoulin, M. Kossov, H. Kurashige, E. Lamanna, T. Lampén, V. Lara, V. Lefebure, F. Lei, M. Liendl, W. Lockman, F. Longo, S. Magni, M. Maire, E. Medernach, K. Minamimoto, P. Mora de Freitas, Y. Morita, K. Murakami, M. Nagamatu, R. Nartallo, P. Nieminen, T. Nishimura, K. Ohtsubo, M. Okamura, S. O'Neale, Y. Oohata, K. Paech, J. Perl, A. Pfeiffer, M. Pia, F. Ranjard, A. Rybin, S. Sadilov, E. Di Salvo, G. Santin, T. Sasaki, N. Savvas, Y. Sawada, S. Scherer, S. Sei, V. Sirotenko, D. Smith, N. Starkov, H. Stoecker, J. Sulkimo, M. Takahata, S. Tanaka, E. Tcherniaev, E. Safai Tehrani, M. Tropeano, P. Truscott, H. Uno, L. Urban, P. Urban, M. Verderi, A. Walkden, W. Wander, H. Weber, J. Wellisch, T. Wenaus, D. Williams,

D. Wright, T. Yamada, H. Yoshida, and D. Zschiesche, Nuclear Instruments and Methods in Physics Research Section A: Accelerators, Spectrometers, Detectors and Associated Equipment **506**, 250 (2003).

[159] H. Schindler, *Garfield++ Usser Guide*, CERN.

[160] K. Masanori, *TBD*, Ph.D. thesis, Kyoto University (2022).

[161] C. Adler, Z. Ahammed, C. Allgower, J. Amonett, B. D. Anderson, M. Anderson, G. S. Averichev, J. Balewski, O. Barannikova, L. S. Barnby, J. Baudot, S. Bekele, V. V. Belaga, R. Bellwied, J. Berger, H. Bichsel, A. Billmeier, L. C. Bland, C. O. Blyth, B. E. Bonner, A. Boucham, A. Brandin, A. Bravar, R. V. Cadman, H. Caines, M. Calderón de la Barca Sánchez, A. Cardenas, J. Carroll, J. Castillo, M. Castro, D. Cebra, P. Chaloupka, S. Chattopadhyay, Y. Chen, S. P. Chernenko, M. Cherney, A. Chikanian, B. Choi, W. Christie, J. P. Coffin, T. M. Cormier, J. G. Cramer, H. J. Crawford, W. S. Deng, A. A. Derevschikov, L. Didenko, T. Dietel, J. E. Draper, V. B. Dunin, J. C. Dunlop, V. Eckardt, L. G. Efimov, V. Emelianov, J. Engelage, G. Eppley, B. Erazmus, P. Fachini, V. Faine, J. Faivre, K. Filimonov, E. Finch, Y. Fisyak, D. Flierl, K. J. Foley, J. Fu, C. A. Gagliardi, N. Gagunashvili, J. Gans, L. Gaudichet, M. Germain, F. Geurts, V. Ghazikhanian, O. Grachov, V. Grigoriev, M. Guedon, E. Gushin, T. J. Hallman, D. Hardtke, J. W. Harris, T. W. Henry, S. Heppelmann, T. Herston, B. Hippolyte, A. Hirsch, E. Hjort, G. W. Hoffmann, M. Horsley, H. Z. Huang, T. J. Humanic, G. Igo, A. Ishihara, Y. I. Ivanshin, P. Jacobs, W. W. Jacobs, M. Janik, I. Johnson, P. G. Jones, E. G. Judd, M. Kaneta, M. Kaplan, D. Keane, J. Kiryluk, A. Kisiel, J. Klay, S. R. Klein, A. Klyachko, A. S. Konstantinov, M. Kopytine, L. Kotchenda, A. D. Kovalenko, M. Kramer, P. Kravtsov, K. Krueger, C. Kuhn, A. I. Kulikov, G. J. Kunde, C. L. Kunz, R. K. Kutuev, A. A. Kuznetsov, L. Lakehal-Ayat, M. A. C. Lamont, J. M. Landgraf, S. Lange, C. P. Lansdell, B. Lasiuk, F. Laue, J. Lauret, A. Lebedev, R. Lednický, V. M. Leontiev, M. J. LeVine, Q. Li, S. J. Lindenbaum, M. A. Lisa, F. Liu, L. Liu, Z. Liu, Q. J. Liu, T. Ljubicic, W. J. Llope, G. LoCurto, H. Long, R. S. Longacre, M. Lopez-Noriega, W. A. Love, T. Ludlam, D. Lynn, J. Ma, R. Majka, S. Margetis, C. Markert, L. Martin, J. Marx, H. S. Matis, Y. A. Matulenko, T. S. McShane, F. Meissner, Y. Melnick, A. Meschanin, M. Messer, M. L. Miller, Z. Milosevich, N. G. Minaev, J. Mitchell, V. A. Moiseenko, C. F. Moore, V. Morozov, M. M. de Moura, M. G. Munhoz, J. M. Nelson, P. Nevski, V. A. Nikitin, L. V. Nogach, B. Norman, S. B. Nurushev, G. Odyniec, A. Ogawa, V. Okorokov, M. Oldenburg, D. Olson, G. Paic, S. U. Pandey, Y. Panebratsev, S. Y. Panitkin, A. I. Pavlinov, T. Pawlak, V. Perevoztchikov, W. Peryt, V. A. Petrov, M. Planinic, J. Pluta, N. Porile, J. Porter, A. M. Poskanzer, E. Potrebenikova, D. Prindle, C. Pruneau, J. Putschke, G. Rai, G. Rakness, O. Ravel, R. L. Ray, S. V. Razin, D. Reichhold, J. G. Reid, G. Renault, F. Retiere, A. Ridiger, H. G. Ritter, J. B. Roberts, O. V. Rogachevski, J. L. Romero, A. Rose, C. Roy, V. Rykov, I. Sakrejda, S. Salur, J. Sandweiss, A. C. Saulys, I. Savin, J. Schambach, R. P. Scharenberg, N. Schmitz, L. S. Schroeder, A. Schüttauf, K. Schweda, J. Seger, D. Seliverstov, P. Seyboth, E. Shahaliev, K. E. Shestermanov, S. S. Shimanskii, V. S. Shvetcov, G. Skoro, N. Smirnov, R. Snellings, P. Sorensen, J. Sowinski, H. M. Spinka, B. Srivastava, E. J. Stephenson, R. Stock, A. Stolpovsky, M. Strikhanov, B. Stringfellow, C. Struck, A. A. P. Suaide, E. Sugarbaker, C. Suire, M. Šumbera, B. Surrow, T. J. M. Symons, A. Szanto de Toledo, P. Szarwas, A. Tai, J. Takahashi, A. H. Tang, J. H. Thomas, M. Thompson, V. Tikhomirov, M. Tokarev,

M. B. Tonjes, T. A. Trainor, S. Trentalange, R. E. Tribble, V. Trofimov, O. Tsai, T. Ullrich, D. G. Underwood, G. V. Buren, A. M. VanderMolen, I. M. Vasilevski, A. N. Vasiliev, S. E. Vigdor, S. A. Voloshin, F. Wang, H. Ward, J. W. Watson, R. Wells, G. D. Westfall, C. Whitten, H. Wieman, R. Willson, S. W. Wissink, R. Witt, J. Wood, N. Xu, Z. Xu, A. E. Yakutin, E. Yamamoto, J. Yang, P. Yepes, V. I. Yurevich, Y. V. Zanevski, I. Zborovský, H. Zhang, W. M. Zhang, R. Zoulkarneev,  and A. N. Zubarev (STAR Collaboration), Phys. Rev. Lett. **90**, 032301 (2003).

[162] V. D. Elvira, Physics Reports **695** (2017), 10.1016/j.physrep.2017.06.002.

[163] N. Ikeno, A. Ono, Y. Nara,  and A. Ohnishi, Phys. Rev. C **93**, 044612 (2016).

[164] N. Ikeno, A. Ono, Y. Nara,  and A. Ohnishi, Phys. Rev. C **101**, 034607 (2020).

[165] M. Cozma, Phys. Lett. B **753**, 166 (2016).

[166] M. D. Cozma, Phys. Rev. C **95**, 014601 (2017).

[167] C. Hartnack, R. K. Puri, J. Aichelin, J. Konopka, S. Bass, H. Stoecker,  and W. Greiner, Euro. Phys. J. A **1**, 151 (1998).

[168] A. Le Fevre, Y. Leifels, W. Reisdorf, J. Aichelin,  and C. Hartnack, Nucl. Phys. A **945**, 112 (2016).

[169] Y. Zhang, M. Tsang, Z. Li,  and H. Liu, Phys. Lett. B **732**, 186 (2014).

[170] J. Xu, L.-W. Chen, M. B. Tsang, H. Wolter, Y.-X. Zhang, J. Aichelin, M. Colonna, D. Cozma, P. Danielewicz, Z.-Q. Feng, A. Le Fèvre, T. Gaitanos, C. Hartnack, K. Kim, Y. Kim, C.-M. Ko, B.-A. Li, Q.-F. Li, Z.-X. Li, P. Napolitani, A. Ono, M. Papa, T. Song, J. Su, J.-L. Tian, N. Wang, Y.-J. Wang, J. Weil, W.-J. Xie, F.-S. Zhang,  and G.-Q. Zhang, Phys. Rev. C **93**, 044609 (2016).

[171] Y.-X. Zhang, Y.-J. Wang, M. Colonna, P. Danielewicz, A. Ono, M. B. Tsang, H. Wolter, J. Xu, L.-W. Chen, D. Cozma, Z.-Q. Feng, S. Das Gupta, N. Ikeno, C.-M. Ko, B.-A. Li, Q.-F. Li, Z.-X. Li, S. Mallik, Y. Nara, T. Ogawa, A. Ohnishi, D. Oliinychenko, M. Papa, H. Petersen, J. Su, T. Song, J. Weil, N. Wang, F.-S. Zhang,  and Z. Zhang, Phys. Rev. C **97**, 034625 (2018).

[172] C. E. Rasmussen and C. K. I. Williams, in [180], Chap. 4, pp. 7–32.

[173] J. E. Jackson (Wiley-Interscience, 2003) Chap. 1.4.

[174] S. Sharma, Annual Review of Astronomy and Astrophysics **55**, 213 (2017), https://doi.org/10.1146/annurev-astro-082214-122339 .

[175] A. Patil, D. Huard,  and C. J. Fonnesbeck, Journal of statistical software **35**, 1 (2010), 21603108[pmid].

[176] R. von Mises (Academic Press, 1964) Chap. 9.3.

[177] C. E. Rasmussen and C. K. I. Williams, in [180], Chap. 4, pp. 79–104.

[178] C. E. Rasmussen and C. K. I. Williams, in [180], Chap. 5, pp. 105–128.

[179] D. P. Kingma and J. Ba, "Adam: A Method for Stochastic Optimization," (2017), arXiv:1412.6980 [cs.LG] .

[180] C. E. Rasmussen and C. K. I. Williams, "Gaussian Processes for Machine Learning (Adaptive Computation and Machine Learning)," (2005).

[181] Z. Chen, J. Fan, and K. Wang, "Remarks on multivariate Gaussian Process," (2021), arXiv:2010.09830 [math.ST] .

[182] H. Petersen, C. Coleman-Smith, S. A. Bass, and R. Wolpert, Journal of Physics G: Nuclear and Particle Physics **38**, 045102 (2011).

[183] B.-A. Li, Phys. Rev. C **69**, 064602 (2004).

[184] B. Liu, V. Greco, V. Baran, M. Colonna, and M. Di Toro, Phys. Rev. C **65**, 045201 (2002).

[185] K. Brueckner, Physical Review **97**, 1353 (1955), cited By 388.

[186] C. Mahaux, P. Bortignon, R. Broglia, and C. Dasso, Physics Reports **120**, 1 (1985).

[187] F. Hofmann, C. M. Keil, and H. Lenske, Phys. Rev. C **64**, 034314 (2001).

[188] V. Greco, M. Colonna, M. Di Toro, and F. Matera, Phys. Rev. C **67**, 015203 (2003).

[189] M. Farine, J. Pearson, and F. Tondeur, Nuclear Physics A **696**, 396 (2001).

[190] X. Chen, Y. Zhang, and Z. li, Chinese Physics C (2021), 10.1088/1674-1137/abfb51.

[191] J. Cugnon, D. L'Hôte, and J. Vandermeulen, Nuclear Instruments and Methods in Physics Research, Section B: Beam Interactions with Materials and Atoms **111**, 215 (1996), cited By 95.

[192] B.-A. Li and X. Han, Physics Letters B **727**, 276 (2013).

[193] D. Adhikari, H. Albataineh, D. Androic, K. Aniol, D. S. Armstrong, T. Averett, C. Ayerbe Gayoso, S. Barcus, V. Bellini, R. S. Beminiwattha, J. F. Benesch, H. Bhatt, D. Bhatta Pathak, D. Bhetuwal, B. Blaikie, Q. Campagna, A. Camsonne, G. D. Cates, Y. Chen, C. Clarke, J. C. Cornejo, S. Covrig Dusa, P. Datta, A. Deshpande, D. Dutta, C. Feldman, E. Fuchey, C. Gal, D. Gaskell, T. Gautam, M. Gericke, C. Ghosh, I. Halilovic, J.-O. Hansen, F. Hauenstein, W. Henry, C. J. Horowitz, C. Jantzi, S. Jian, S. Johnston, D. C. Jones, B. Karki, S. Katugampola, C. Keppel, P. M. King, D. E. King, M. Knauss, K. S. Kumar, T. Kutz, N. Lashley-Colthirst, G. Leverick, H. Liu, N. Liyange, S. Malace, R. Mammei, J. Mammei, M. McCaughan, D. McNulty, D. Meekins, C. Metts, R. Michaels, M. M. Mondal, J. Napolitano, A. Narayan, D. Nikolaev, M. N. H. Rashad, V. Owen, C. Palatchi, J. Pan, B. Pandey, S. Park, K. D. Paschke, M. Petrusky, M. L. Pitt, S. Premathilake, A. J. R. Puckett, B. Quinn, R. Radloff, S. Rahman, A. Rathnayake, B. T. Reed, P. E. Reimer, R. Richards,

S. Riordan, Y. Roblin, S. Seeds, A. Shahinyan, P. Souder, L. Tang, M. Thiel, Y. Tian, G. M. Urciuoli, E. W. Wertz, B. Wojtsekhowski, B. Yale, T. Ye, A. Yoon, A. Zec, W. Zhang, J. Zhang, and X. Zheng (PREX Collaboration), Phys. Rev. Lett. **126**, 172502 (2021).

[194] I. Legred, K. Chatziioannou, R. Essick, S. Han, and P. Landry, Phys. Rev. D **104**, 063003 (2021).

[195] M. B. Tsang, Y. Zhang, P. Danielewicz, M. Famiano, Z. Li, W. G. Lynch, and A. W. Steiner, Phys. Rev. Lett. **102**, 122701 (2009).

[196] M. B. Tsang, T. X. Liu, L. Shi, P. Danielewicz, C. K. Gelbke, X. D. Liu, W. G. Lynch, W. P. Tan, G. Verde, A. Wagner, H. S. Xu, W. A. Friedman, L. Beaulieu, B. Davin, R. T. de Souza, Y. Larochelle, T. Lefort, R. Yanez, V. E. Viola, R. J. Charity, and L. G. Sobotka, Phys. Rev. Lett. **92**, 062701 (2004).

[197] T. X. Liu, W. G. Lynch, M. B. Tsang, X. D. Liu, R. Shomin, W. P. Tan, G. Verde, A. Wagner, H. F. Xi, H. S. Xu, B. Davin, Y. Larochelle, R. T. d. Souza, R. J. Charity, and L. G. Sobotka, Phys. Rev. C **76**, 034603 (2007).

[198] A. Tamii, I. Poltoratska, P. von Neumann-Cosel, Y. Fujita, T. Adachi, C. A. Bertulani, J. Carter, M. Dozono, H. Fujita, K. Fujita, K. Hatanaka, D. Ishikawa, M. Itoh, T. Kawabata, Y. Kalmykov, A. M. Krumbholz, E. Litvinova, H. Matsubara, K. Nakanishi, R. Neveling, H. Okamura, H. J. Ong, B. Özel-Tashenov, V. Y. Ponomarev, A. Richter, B. Rubio, H. Sakaguchi, Y. Sakemi, Y. Sasamoto, Y. Shimbara, Y. Shimizu, F. D. Smit, T. Suzuki, Y. Tameshige, J. Wambach, R. Yamada, M. Yosoi, and J. Zenihiro, Phys. Rev. Lett. **107**, 062502 (2011).

[199] W. G. Lynch and M. B. Tsang, "Decoding the Density Dependence of the Nuclear Symmetry Energy," (2021), arXiv:2106.10119 [nucl-th] .

[200] F. J. Fattoyev, J. Carvajal, W. G. Newton, and B.-A. Li, Phys. Rev. C **87**, 015806 (2013).